Synthesis, characterization and evaluation of the photocatalytic activity of several composites using two dimensional geomimetics for environmental remediation

チティフォン, チャイチャム

https://doi.org/10.15017/2534417

九州大学
KYUSHU UNIVERSITY

Synthesis, characterization and evaluation of the photocatalytic activity of several composites using two dimensional geomimetics for environmental remediation

By

Chitiphon Chuaicham

A thesis submitted to Kyushu University
for the degree of Doctor of Engineering

Department of Earth Resources Engineering
Graduate School of Engineering
Kyushu University
Fukuoka, Japan

September 2019

Abstract

Nowadays, contamination of organic and heavy metal in wastewater create major environmental problems and the treatment process of that pollutant associated with worldwide economic growth is an alarming research subject for different fields of researchers. Photocatalysis is a remarkable methodology which is popular and applied in the different interdisciplinary area of the research such as, degradation of several organic and reduction of hazardous metal ions due to eco-friendly, low cost, easy to operation and energy shortages problem. According to that fact, this thesis represents the development of high-quality photocatalytic materials for the degradation of organic pollutants and reduction of hexavalent chromium (Cr(VI)) under the UV and visible light irradiation.

In **chapter 1**, the introduction, including principle, mechanism, the background of the photocatalyst materials and objectives of this study were explained. All of the photocatalytic application in this work focuses on wastewater treatment (organic and inorganic wastes).

In **chapter 2**, synthsis, chareacterization and application of photocatalysts in this work were described.

Nowadays, two-dimensional/two-dimensional (2D/2D) composites have been received considerable attention for photocatalytic application because it has high electron-hole mobility across the heterojunction interface, which can impede the electron-hole recombination rate. In **chapter 3,** ZnTi layered double hydroxide/montmorillonite composite (ZTL/MT) were prepared via a hydrothermal method by varying the weight percent of MT (10 %, 20 %, and 30 %). The

photocatalytic activity of the obtained samples was investigated by reduction of Cr(VI) under UV light irradiation. The ZTL/MT composites displayed higher photocatalytic performance than pristine samples of ZnTi layered double hydroxide (ZTL) and montmorillonite (MT), and ZTL/MT20% exhibited the highest photocatalytic efficiency. The synergistic effect between ZTL and MT can avoid the recombination of photogenerated electron-hole pairs. The probability of electron-hole recombination in ZTL/MT composites could be significantly decreased because of the formation of an interfacial combination between ZTL and MT heterojunction. The photocatalytic mechanism for Cr(VI) reduction over the ZTL/MT composites was proposed. The ZTL/MT composites can be potential catalysts for the removal of heavy metal pollutants in wastewater.

Moreover, Zn-Ti mixed metal oxide derived from ZnTi layered double hydroxides has been used as a heterogeneous catalyst, in which charge separation efficiency of photogenerated electron-hole pairs was improved within this heterojunction for prolonging organic compounds decomposition. In **chapter 4**, ZnTi mixed metal oxides (ZTM) was synthesized as photocatalysts derived from ZnTi layered double hydroxides, and the phase transformations were systematically studied by varying the molar ratio of Zn/Ti, synthetic method and calcination temperatures. The three-dimensional distribution of Ti ion in the nanocomposite network structure greatly influenced the photocatalytic efficiency of the products. The ZTM synthesized at 500 °C with the different Zn/Ti ratios showed similar energy-resolved density of electron traps (ERDT) patterns, suggesting that the products are composed of ZnO, and $ZnTiO_3$. Powder X-Ray diffraction (PXRD) for some products did not show the existence of crystalline $ZnTiO_3$, but ERDT pattern suggested the co-existence of

amorphous $ZnTiO_3$. The above series of products showed similar photocatalytic activities in the degradation of phenol. Also, the similar ERDT patterns have a high electron accumulation level near conduction band bottom (CBB) which are close to the one-electron transfer of superoxide radical formation. However, the ZTM calcined at 600°C, in which the phase of Zn_2TiO_4 is formed together, have shown different ERDT patterns with lower electron accumulation level near CBB, resulting in lower photocatalytic efficiency. The enhanced photocatalytic performance of ZTM photocatalyst could be attributed to heterojunction among ZnO, TiO_2 and $ZnTiO_3$ to facilitate the electron transfer in the composites and may be caused by avoiding the charge recombination and adsorption characteristics of wider light wavelengths by $ZnTiO_3$ phase.

Graphitic carbon nitrides with two-dimensional (2D) topology have attracted for photocatalytic degradation for organic pollutants in the visible light region due to its effective use of solar light radiation. In **chapter 5**, a series of porous oxygen-doped carbon nitride (OCN) have been successfully synthesized via thermal polycondensation of melamine with different amounts of polyoxyethylene stearyl ether at 500°C for 2 hours under air condition. The photocatalytic activity of the obtained samples was investigated by rhodamine B degradation under visible light irradiation (>400 nm). The sample with a 1 mg of polyoxyethylene stearyl ether showed the highest photocatalytic performance for rhodamine B degradation visible light irradiation among all these OCN samples. Moreover, the electron-hole recombination of OCN sample exhibited lower than normal graphitic carbon nitride that was confirmed by PL results. The improved photocatalytic activity of the OCN samples could be attributed to improving light absorption ability and reduced the

recombination rate of $e^{-}h^{+}$ pair. The OCN samples can be potential catalysts for the removal of heavy metal pollutants in wastewater. However, the fast recombination of photo-generated charge carriers of graphitic carbon nitrides results in low photocatalytic efficiency. In **chapter 6**, C_3N_4/ZnTi mixed metal composites (CN/ZTM) with various weight percentages of ZTM were fabricated via calcination of C_3N_4/ZnTi-layered double hydroxide composites at 400 °C. The photocatalytic activity of the CN/ZTM composites has been demonstrated via the degradation of rhodamine B under visible light irradiation and found to highly depend on the loading of ZTM. The CN/ZTM with the C_3N_4 weight loading of 5% represented the highest decolorization efficiency, which is nearly twice of the pure CN. The enhanced activity of CN/ZTM composites could be ascribed to the synergistic effect between CN and ZTM that restraint of the electron-hole recombination. A synergistic photocatalysis mechanism between CN and ZTM was proposed.

Furthermore, the formation of intermediate oxidative species during the rhodamine B photocatalytic reactions was investigated by quenching. The superoxide anion radical is a main active species for rhodamine B degradation. The CN/ZTM composites can be potential catalysts for the degradation of organic pollutants in wastewater.

In order to study organic dye degradation by natural clay, the photocatalytic activity of sepiolite was examined for the degradation of several dye compounds under visible light irradiation. In **chapter 7**, higher adsorption capacities and more excellent photocatalytic performance of cationic dyes (rhodamine B and methylene blue) were observed on sepiolite, in comparison with anionic dyes (orange II and trypan blue). Superiority in the photocatalytic activity of cationic dyes is attributed to the strong

electrostatic attraction and photosensitization properties of cationic dye molecules. Sepiolite has degraded 45.3% rhodamine B within 120 min, which is the greatest photocatalytic degradation efficiency when compared with other dyes. Subsequently, the reusability of spent sepiolite after adsorption of rhodamine B was evaluated by the degradation of trypan blue under the visible light irradiation. The photocatalytic degradation performance of trypan blue by spent sepiolite after adsorption of rhodamine B increased about twice as much as with pristine sepiolite, indicating that the dye-sensitized photocatalytic process could enhance the photocatalytic degradation ability of sepiolite. Through radical scavenger tests, it was found that a superoxide radical is mainly responsible for rhodamine B degradation. The possible mechanism of rhodamine B degradation under visible light irradiation was proposed. The sepiolite could be a potential catalyst for the degradation of organic pollutants in wastewater under solar light.

Based on the above finding of dye-sensitized property on the surface of sepiolite, the sepiolite based composites were synthesized. In **chapter 8**, the composite of natural sepiolite clay and synthetic graphitic carbon nitride (CN) along with dispersed palladium nanoparticles were developed for the efficient photodegradation of rhodamine B dye. Several analytical techniques were utilized to thoroughly characterization of original sepiolite, CN, and composite materials. Here in the composite, the natural sepiolite showed an essential role as a space controller for the CN, as well as beneficial for an electron transfer between rhodamine B and CN. The additional optimized decoration of Pd(0) nanoparticles on the sepiolite-CN composite further enhanced the visible light photocatalytic activity for degradation of rhodamine B. The reason can be explained as the well-dispersed Pd-nanoparticles

collectively advantageous to dye degradation by avoiding the recombination between photogenerated electrons and holes in Sepiolite/CN composite. The added amount of Pd was optimized to 1wt% in the composite from the excellent photocatalytic degradation efficiency of rhodamine B, which was found consistent with a decrease in photoluminescence intensity. Finally, the photocatalytic degradation mechanism was proposed concerning the electron transfer from the conduction band of CN to the surface of Pd(0) nanoparticles through the heterojunction. The traditional scavenger test experiments confirmed this phenomenon. Additionally, the first time mechanism was proved by the novel reversed double-beam photoacoustic spectroscopy (RDB-PAS) technique. The developed sepiolite/CN/Pd(0) composite can be a potential catalyst for the degradation of positively charged organic pollutants in wastewater under the visible light.

In **chapter 9**, the conclusions of all chapters were summarized.

Contents

List of tables

List of figures

Chapter 1

Introduction

1.1 Introduction

1.1.1 Basic principle of photocatalysis for wastewater treatment

Water pollutions, which come from urbanization and industrialization, has become a hot topic among academic researchers, which affects human life and environments [1]. Wastewater can be treated by different methods such as adsorption, coagulation/flocculation, and biodegradation. However, these processes have some disadvantages. For example, the requirement of further treatment of contaminated sorbents or sludge waste; the requirement of extremely high energy; and it is a very time-consuming process.

The researchers of this study believe that "photocatalysis" is a notable method, which is a popular method for the degradation of various inorganic/organic hazardous contaminants in wastewater. When compared with other environmental remedial approaches, this method is gaining more consideration by researchers as a viable alternative to existing techniques. Increased research into this field has occurred because it is a natural solar-powered approach, which has the potential to deliver a solution to assist remediation.

The definition of photocatalysis is the amalgamation of photochemistry and catalysis. Photocatalysis is a compound word composed of photo and catalysis, that can be defined as catalysis driven acceleration of a light-induced reaction.

Photocatalysis is a sustainable process, which has strong potential to develop many technologies, related to overcoming the present and future issues related to energy conversion and environmental remediation (Including diminishing the persistence of organic and inorganic pollutants from the aqueous systems).

This process has several advantages over competing processes, such as complete mineralization. Advantages include the fact that there is no waste disposal problem; the cost is low; and it needs mild conditions only.

Several semiconducting materials are used as photocatalysts such as CdSe, Fe_2O_3, WO_3, Bi_2WO_6, $BiVO_4$, TiO_2, ZnO, CdS, TaNO, Si, Cu_2O SnO_2, and CeO_2 (**Fig. 1.1**). This is because of the favorable combination of electronic structures, which are characterized by a filled valence band (VB) and an empty conduction band (CB); light absorption properties; charge transport characteristics; and has an excited states lifetime [2].

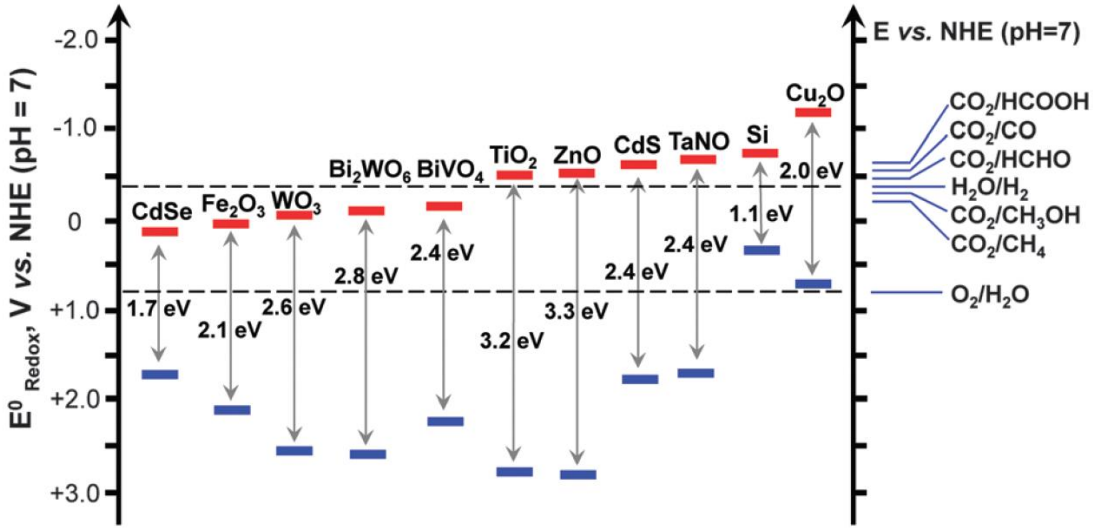

Fig. 1.1 Band-edge positions of some typical semiconductor photocatalysts [2].

1.1.2 Photocatalytic mechanism for wastewater treatment

In general, a photocatalytic reaction occurs based on the catalyst and the photon energy from light. The photocatalysts (semiconductors) are used as light sensitizers for the irradiation of light stimulated redox process because it is filled with an electron

in the valence band and an empty, vacant conduction band. The photocatalytic mechanism of a photocatalytic semiconductor is shown in **Fig. 1.2**.

Under light irradiation to the surface of the photocatalytic semiconductor, if the energy of incident light is equivalent or more than the bandgap energy of the photocatalytic semiconductor, the electrons in the VB of the photocatalytic semiconductor are excited by photons of light to the CB. At the same time, holes are also produced in the VB of the photocatalytic semiconductor. The electrons in the conduction band of the photocatalytic semiconductor can reduce the dissolved O_2 in water to form superoxide radical ions ($^{\bullet}O_2^-$), while the generated hole in the valence band also can react with water molecules to produce hydroxyl radicals ($^{\bullet}OH$). The $^{\bullet}O_2^-$ and $^{\bullet}OH$ have strong oxidizing power responsible for the degradation of adsorbed pollutants on the surface of the s photocatalytic semiconductor.

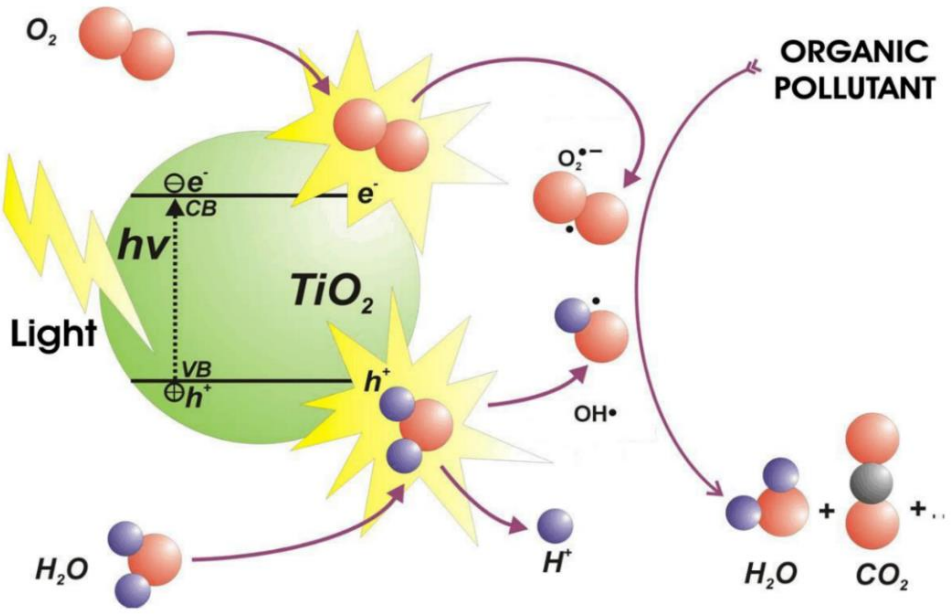

Fig. 1.2 Schematic of semiconductor excitation by bandgap illumination leading to the creation of "electrons" in the conduction band and "holes" in the valance band [3].

1.1.3 Challenging of photocatalysis for wastewater treatment

The challenge in the photocatalysis research field is to design, and development high-quality photocatalytic materials, which must fulfill essential criteria such as must be photoactive; able to utilize visibility and near-UV light; biologically and chemically inert; inexpensive; nontoxic; and have high chemical/photochemical stability. These factors remain essential elements of the research.

At present, researchers are interested in the utilization of solar light due to its huge availability, sustainability, and cleanliness. **Fig. 1.3** shows the solar spectrum constitutes about 3–5% UV ($\lambda < 400$ nm) and about 47% visible light ($400 > \lambda < 700$ nm) [4]. However, the ways and means to harvest and utilize solar energy for photocatalytic treatment of wastewater are one of the focusing points of the development of photocatalyst.

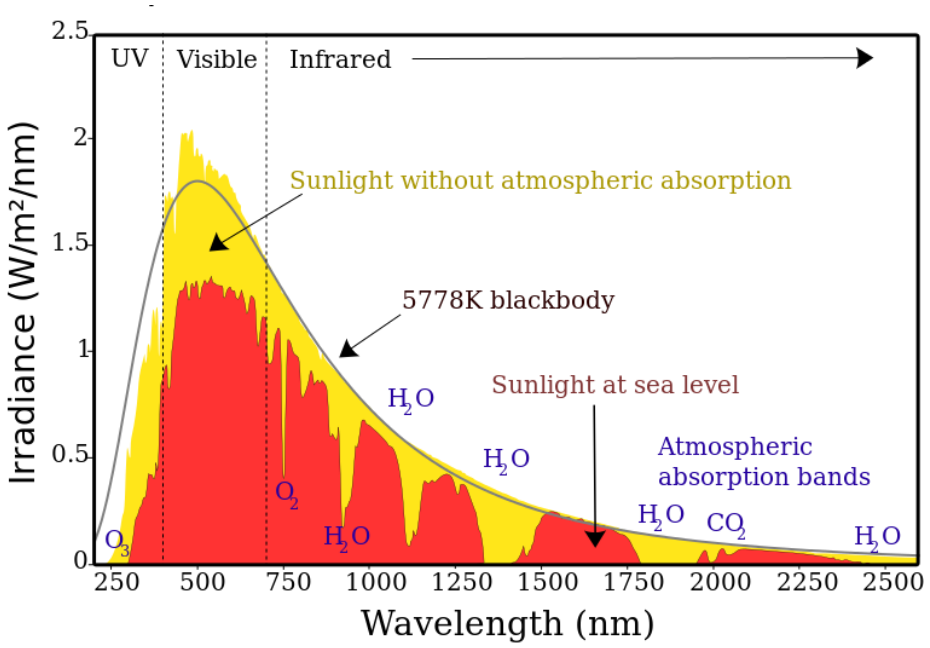

Fig. 1.3 The solar spectrum [5].

1.2 Nanocomposite and its importance in photocatalytic degradation of organic pollutants

The major requirement of photocatalysis is a semiconductor material that can produce radical species during its excitation by light irradiation. Originally, the light energy falls on the surface of a catalyst; the valence band electrons are agitated; and move to the conduction band. Holes would be left in the valance band of the catalyst. These holes in the valence band can oxidize donor molecules and react with water molecules to generate hydroxyl radicals. In these regards already several materials have been used as photocatalysts, but there are some disadvantages related to the use of pure semiconductor materials. This is because s photocatalyst like charge carrier recombination happens within nanoseconds, and the band edge absorption threshold does not allow for the utilization of visible light.

To overcome these restrictions, new nanocomposite materials have been applied to expand the light absorption behavior and elongate the lifetime of the photocatalyst materials. The formation of a well-defined heterojunction between two semiconductors with matching electronic band structures can improve the separation of electrons and holes [6]. **Fig. 1.4.** shows the separation mechanism of electron and hole, through the heterojunction between two semiconductors.

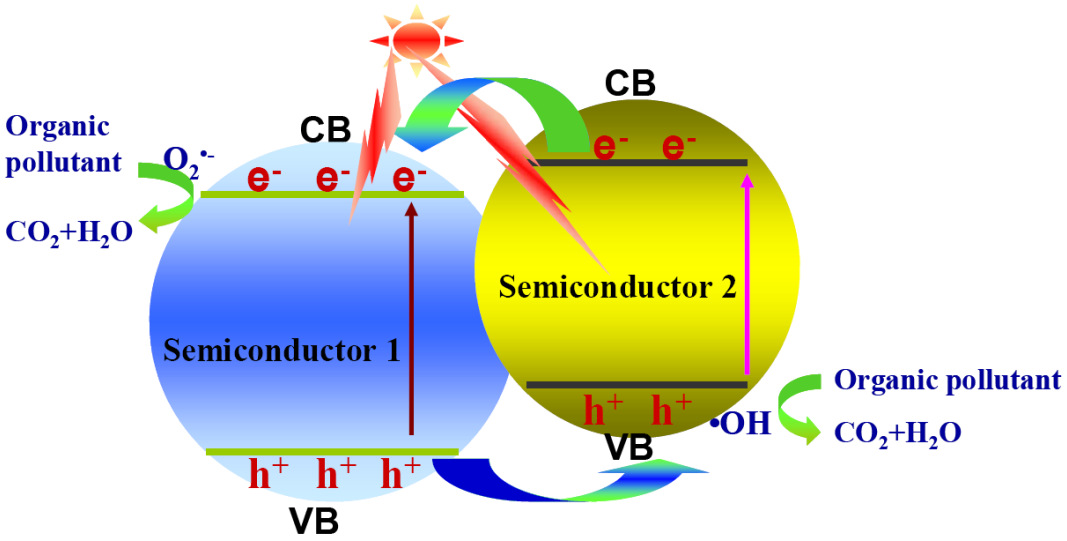

Fig. 1.4 The separation mechanism of electron and hole through the heterojunction between two semiconductors [6].

The p-n heterojunction of the acceptor p-type and the donor n-type semiconductor is a tropical junction which can avoid the recombination of photogenerated charge carriers (electron and hole) as shown in **Fig. 1.5**. The different concentrations of negatively and positively charged ions of the p-type and n-type semiconductor generates the strong local electric field near the junction which can enhance the mobility and charge separation leading to the high quantum efficiency of the photocatalytic reactions.

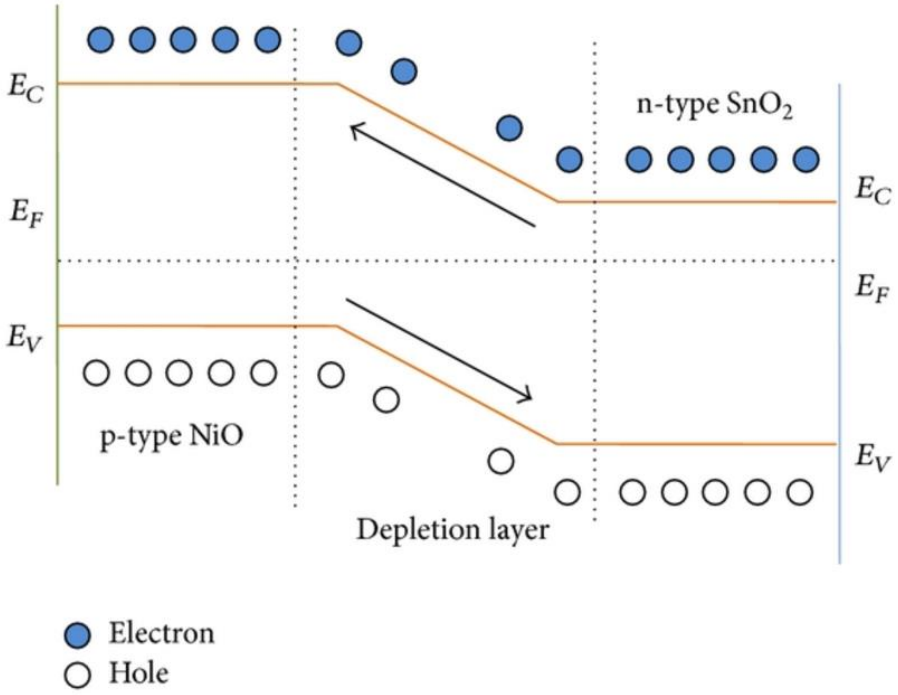

Fig. 1.5 The schematic diagram represents the role of the p-n heterojunction in enhancing the separation of electron-hole pairs [7].

Other types of heterojunctions could also be used for separation of photogenerated charge carrier in a photocatalyst. For instance, Z-scheme heterojunctions between different semiconductors with matching electronic band structures can also improve the photocatalytic activity by enhancing the lifetime of the electron and hole pair by the recombination of an electron from the CB of one semiconductor with a hole from the VB of another semiconductor as shown in **Fig. 1.6**.

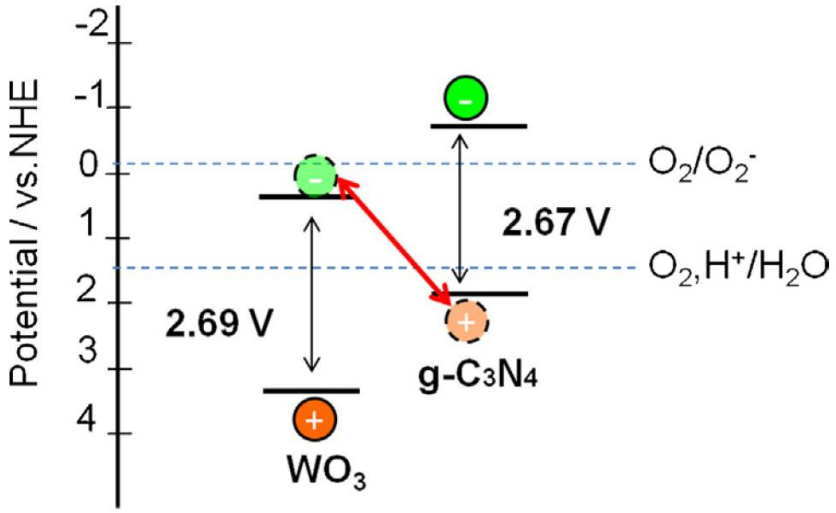

Fig. 1.6 The Z-schematic band structure of two semiconductors [8].

Moreover, the loading to metal nanoparticle on the surface of the photocatalyst is interesting due to the enhancing of the photocatalytic activity. The metal nanoparticles, such as Au, Ag, Pd, and Pt, on the surface of the photocatalyst, can induce the oscillation of the conducted electrons with a resonance frequency, called the surface plasmon resonance, which can improve the visible light absorption ability. Also, the separation of the photogenerated electron and hole of the photocatalyst can also be improved through the Schottky barrier [9], which is the heterojunction between the photocatalytic semiconductor and metal nanoparticle (**Fig. 1.7**). Thus, engineering the junction between semiconductors is essential for improving photocatalytic activity.

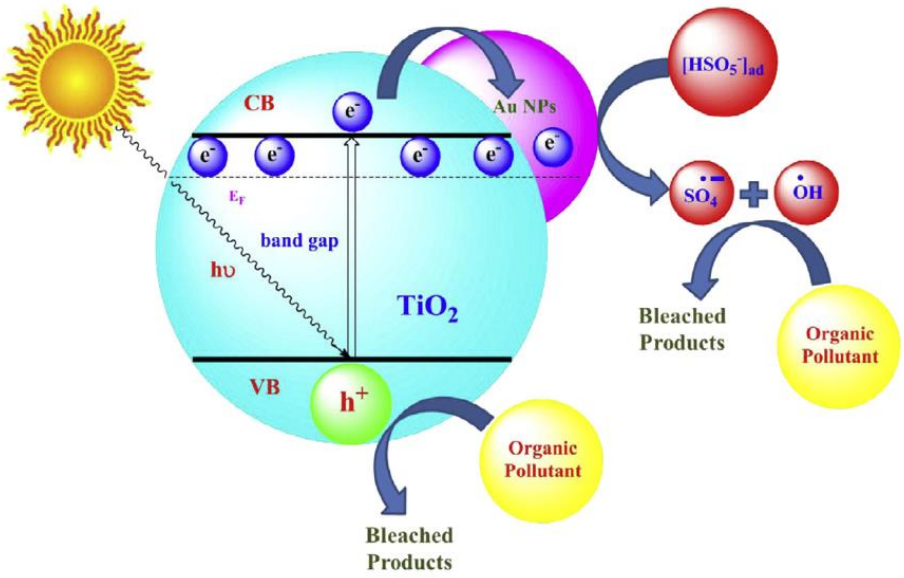

Fig. 1.7 The schematic diagram represents the role of the Schottky barrier in enhancing the separation of electron-hole pairs [9].

Two-dimensional/two-dimensional (2D/2D) composites have been extensively developed for use as a photocatalyst, due to its greater electron-hole mobility across the interface of 2D/2D heterojunction, which can decrease the distance and time of charge migration to inhibit the recombination of photogenerated electron and hole.

1.3 Layered double hydroxide (LDH)

1.3.1 Basic structure of LDH

The layered double hydroxide (LDH) has been widely used as a photocatalyst for photocatalytic oxidation of organic pollutants and the photocatalytic reduction of chromium (VI) in wastewater. LDH is a class of two-dimensional anionic clay, which can be expressed by the general formula $[M^{2+}_{1-x}M^{3+}_{x}(OH)_2]^{z+}(A^n)_{z/n}\cdot yH_2O$ (M^{2+} and M^{3+}, divalent and trivalent metal cations respectively; A^n is the interlayer anion between the layer compensating for positive charge of the layer). The crystal structure

of LDH is shown in **Fig. 1.8**.

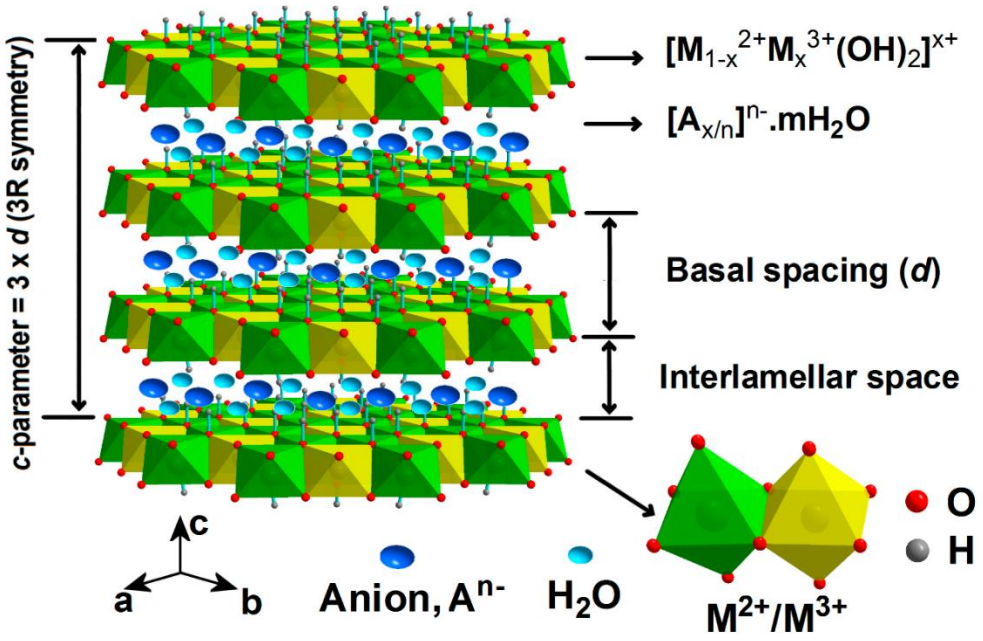

Fig. 1.8 Schematic representation of the classical LDH structure [10].

1.3.2 Photocatalytic application of LDH

Zinc and titanium contained in the octahedral sheet of LDH have been extensively used as photocatalyst for wastewater treatment and water-splitting [11-14]. **Xin-Rui** et al. reported that ZnTi-LDH is more suitable as a safe UV-shielding material. **Mingfei Shao et al.** reported the synthesis of hierarchical Zn–Ti layered double hydroxide for efficient visible-light photocatalysis for solar photocatalytic degradation of methylene blue (MB) in wastewater, and it showed higher photocatalytic activity than common photocatalyst (P25, TiO_2, and ZnO) as shown in **Fig. 1.9**.

However, a similar problem of photocatalyst also occurs in LDH materials, with a high recombination rate of electron and hole. Thus, the formation of heterojunction between LDH and other materials has been performed to separate the

photogenerated charge carrier, leading to avoiding the recombination. **Das** et al. reported Au-loaded $CaFe_2O_4$/CoAl LDH p–n junction composite with improved photocatalytic activity for chromium reduction. **Xiaoya Yuan et al.** reported mixed metal oxide derived from ZnAl layered double hydroxide for photocatalytic reduction of hexavalent chromium. Yanping Zhu et al. developed Zn/Ti-LDH via hybridizing with C60 and utilized for simultaneous photocatalytic degradation of Orange II (OII) dye. Yufei Zhao et al. developed highly dispersed TiO_6 units in a layered double hydroxide, and the catalyst was tested as photocatalysts for water splitting. The LDH based photocatalysts were summarised in **Table 1.1**.

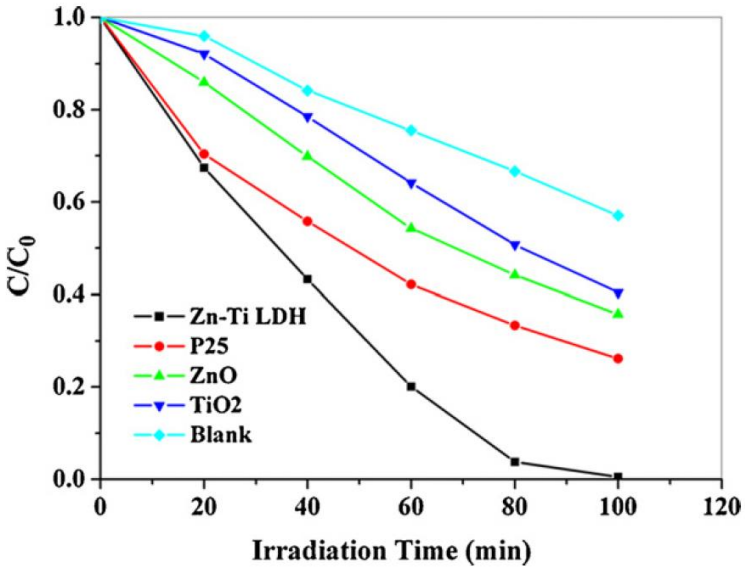

Fig. 1.9 Photodegradation of MB monitored as the normalized concentration vs. irradiation time under visible-light irradiation with the presence of different photocatalysts [11].

Table 1.1. LDH based photocatalysts

Catalyst	Active compound	Target	C_0	Loading (g/L)	Efficacy (%)	Time (min)	Ref.
$CaFe_2O_4$/CoAl LDH@Au	$CaFe_2O_4$/CoAl LDH@Au	Cr(VI)	20ppm	1.0	95	60	[15]
Ag@NiAl LDH/g-C_3N_4	Ag@NiAl LDH/g-C_3N_4	RhB	5 ppm	0.25	85	60	[16]
O doped g-C_3N_4/CoAl LDH	O doped g-C_3N_4/CoAl LDH	MO	20 ppm	0.3	100	60	[17]
Mn/Co/Ti LDH	Mn/Co/Ti LDH	RhB	1 x 10-5 M	0.1	80	60	[18]
CeO_2/ZnTi LDH	CeO_2/ZnTi LDH	acid red 14	50 ppm	1.0	100	100	[19]
Co, Cu/ZnAl LDH	Co, Cu/ZnAl LDH	Orange II	30 ppm	0.5	80	360	[20]
ZnAl LDH	ZnAl LDH	MB	3 ppm	3.5	10	180	[21]
LDH-VB9-TiO_2	LDH-VB9-TiO_2	MB	10 ppm	1.0	100	400	[22]
ZnTi LDH	ZnTi LDH	RhB	5 ppm	0.66	100	120	[23]
Fe_3O_4/ZnCr LDH	Fe_3O_4/ZnCr LDH	MO	50 ppm	0.66	80	1500	[24]
ZnFe LDH	ZnFe LDH	methyl violet	100 ppm	1.0	100	120	[25]
ZnFe LDH	ZnFe LDH	malachite green	100 ppm	1.0	100	120	[25]
Ag coated Zn/Ti-LDH	Ag coated Zn/Ti-LDH	RhB	10 ppm	1.0	83	30	[26]

Table 1.1. LDH based photocatalysts (continued)

Catalyst	Active compound	Target	C_0	Loading (g/L)	Efficacy (%)	Time (min)	Ref.
Fe_3O_4/ZnCr LDH	Fe_3O_4/ZnCr LDH	MB	5 ppm	1.0	90	180	[27]
ZnCr LDH	ZnCr LDH	RhB	100 ppm	1.0	95	60	[28]
BiOCl/TiO_2/ZnCr LDH	BiOCl/TiO_2/ZnCr LDH	RhB	100 ppm	0.37	100	30	[29]
NiTi LDH	NiTi LDH	MB	1 x 10^{-6} M	-	92	75	[30]

1.4 Mixed metal oxide (MMO) derived from LDH

1.4.1 Background of mixed metal oxide (MMO) derived from LDH

Mixed metal oxide (MMO) has gained enormous attention among nanotechnologists due to their excellent physiochemical properties. The MMO exhibits improved photocatalytic activity due to the formation of a heterojunction between two different metal oxides, which can suppress the recombination of electron and hole. Moreover, it might absorb a wide range of visible light. The mixed metal oxide nanocomposite can be obtained by various synthesis methods such as the sol-gel method; the hydrothermal method; the precipitation method; and spray pyrolysis techniques.

Until now, the topotactic transformation from LDH to MMO has been considered to be an effective photocatalyst for wastewater treatment, including as an organic dye. This method provides more advantageous properties of MMO than other methods, such as being grafted within an amorphous matrix; has high dispersion of immobilized semiconductor nanoparticles; has a large specific surface area; and there are possible synergistic effects between the components of MMO.

1.4.2 Photocatalytic application of MMO

Sanghoon Kim et al. suggested the Cu, Co-doped ZnAl based mixed metal oxides derived from layered double hydroxides, because of an improved visible-light-induced photocatalytic activity for dye degradation [31]. Guangshan Zhang et al. reported the enhancing of p-nitrophenol degradation by ZnNiAl-layered double hydroxides with calcination treatment under visible-light irradiation [32]. Fei Ji et al.

developed hierarchical C-doped BiPO4/ZnCoAl-MMO hybrid composite and it was utilized for simultaneous photocatalytic degradation of methylene blue (MB) [33]. Liting Ju et al. developed Fullerene modified ZnAlTi-MMO, and the catalyst is tested as photocatalysts for Bisphenol A under simulated visible light irradiation [34]. Cornelia-Magda Puscasu and Jun developed ZnTi LDH and the derived mixed oxides as mesoporous nanoarchitectonics showed higher photocatalytic activity for the degradation of phenol [35]. The MMO based photocatalysts were summarised in **Table 1.2**.

Table 1.2 MMO photocatalysts

Catalyst	Active compound	Target	C_0	Loading (g/L)	Efficacy (%)	Time (min)	Ref.
ZnNiAl MMO	ZnNiAl MMO	p-nitrophenol	5 ppm	1.0	100	180	[32]
ZnCoAl-MMO	ZnCoAl-MMO	MB	2 ppm	0.625	73.5	120	[33]
ZnO/$ZnTi_2TiO_4$	ZnO/$ZnTi_2TiO_4$	phenol	50 ppm	0.1	80	450	[36]
ZnO/$ZnCr_2O_4$	ZnO/$ZnCr_2O_4$	phenol	50 ppm	0.1	98	210	[36]
ZnO/$ZnAl_2O_4$	ZnO/$ZnAl_2O_4$	phenol	50 ppm	0.1	98	300	[36]
$BiPO_4$/ZnCoAl-MMO	$BiPO_4$/ZnCoAl-MMO	MB	2 ppm	0.625	55.5	120	[33]
C-doped $BiPO_4$/ZnCoAl-MMO	C-doped $BiPO_4$/ZnCoAl-MMO	MB	2 ppm	0.625	93.7	120	[33]
ZnAlTi-MMO	ZnAlTi-MMO	Bisphenol A	10 ppm	0.5	60	300	[34]
Fullerene modified ZnAlTi-MMO	Fullerene modified ZnAlTi-MMO	Bisphenol A	10 ppm	0.5	80	300	[34]
RGO/NiFe MMO	RGO/NiFe MMO	MB	5 ppm	1.0	100	180	[37]
g-C_3N_4/CuONP/ZnAl-MMO	g-C_3N_4/CuONP/ZnAl-MMO	phenol	20 ppm	1.0	65	1440	[38]
BiOCl-TiO_2	BiOCl-TiO_2	phenol	50 ppm	1.0	25	360	[39]

Table 1.2 MMO photocatalysts (continued)

Catalyst	Active compound	Target	C_0	Loading (g/L)	Efficacy (%)	Time (min)	Ref.
ZnAl-MMO	ZnAl-MMO	Cr(VI)	10 ppm	2.0	100	300	[40]
RGO/TiO_2	RGO/TiO_2	Cr(VI)	12ppm	0.2	180	240	[41]
ZnTi MMO	ZnTi MMO	phenol	50 ppm	0.5	90	250	[35]
ZnFeAl-LDO	ZnFeAl-LDO	MB	3 ppm	3.5	60	180	[21]
ZnAl-LDO	ZnAl-LDO	MB	3 ppm	3.5	23	180	[21]
ZnAl MMO	ZnAl MMO	Orange II	0.23 mM	0.2	35	360	[31]
Co doped ZnAl MMO	Co doped ZnAl MMO	Orange II	0.23 mM	0.2	95	360	[31]
Cu doped ZnAl MMO	Cu doped ZnAl MMO	Orange II	0.23 mM	0.2	95	360	[31]

1.5 Graphitic carbon nitride (g-C_3N_4)

1.5.1 Basic structure of g-C_3N_4

Over the last decade, a graphitic carbon nitride (g-C_3N_4) as a metal-free conjugated semiconductor photocatalyst has attracted massive attention in the photocatalysis literature [34]. This material (g-C_3N_4) has some interesting properties that give it advantages over traditional semiconductor photocatalyst materials. Most importantly, it is composed of the highly abundant earth elements of carbon and nitrogen and has a structural arrangement similar to graphene. This provides high physicochemical stability; it is a simple synthesis approach to solving the cost issues; and the absorption band is favorably placed in the visible light region (the development of photocatalyst which works in the visible light region is also a big challenge) [34]. A variety of surface defects on the surface of the g-C_3N_4 affect the properties of this material (**Fig. 1.10**). The CNH_2 and C_2NH functional group on the edges of g-C_3N_4 could be generated by a small quantity of hydrogen impurities, due to the incomplete thermal condensation [34, 42, 43]. Thus, the surface defects of g-C_3N_4 and electron-rich properties provide H-bonding motifs leading to enhancing the facilitation of an electron in catalysis [43]. The functional groups of NH, N, NH_2, and NC on the surface of g-C_3N_4 are beneficial for the removal of toxic acidic molecules through electrostatic interactions [44]. Moreover, the hydrophobic part of g-C_3N_4 can control the electron separation and surface electrocatalytic reactions because of the weak interacted interfacial layer [45-50]. The occurrence of hydroxyl groups and carboxyl groups on the surface of g-C_3N_4 through chemical oxidation improve the dispersion in the aqueous solutions and further enhance the interfacial coupling and photocatalytic activities.

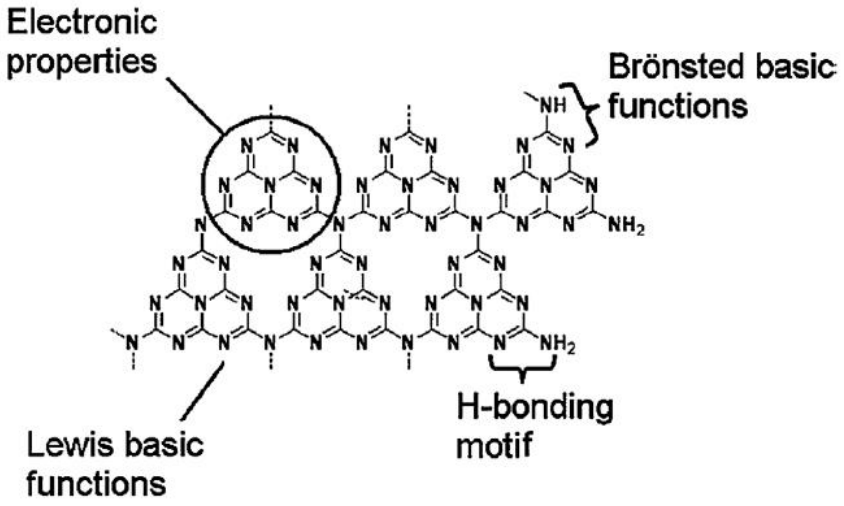

Fig. 1.10 Multiple functional surface properties of polymeric g-C_3N_4 material with defects [34].

Taking into account the features described above, g-C_3N_4 has rapidly become a popular material in photocatalysis. However, the main intrinsic limitation in practical applications of the use of original g-C_3N_4 are due to the high recombination rate of photogenerated electron-hole pairs; low electronic conductivity; and small specific surface areas. Thus, researchers have made considerable efforts to modify g-C_3N_4 by modifying different aspects, such as by ions doping, noble metals deposition; construction with other semiconductors; and heterojunction construction.

1.5.2 Photocatalytic application of g-C_3N_4

So far g-C_3N_4 and g-C_3N_4 composites have been used as an effective transporter in the photocatalytic treatment of several types of pollutants including an organic dye. Fan Dong et al. reported g-C_3N_4/g-C_3N_4 metal-free heterojunction with improved visible-light-induced photocatalytic removal of NO [51]. Li Fu et al. reported reduced graphene oxide coupled with g-C_3N_4 nanodots as 2D/0D

nanocomposites for enhanced photocatalytic activity [52]. Anise Akhundi et al. developed ternary magnetic g-C_3N_4/Fe_3O_4/AgI nanocomposites for degradation of Rhodamine B (RhB). Yun Zheng et al. developed sulfur-doped carbon nitride polymers, and the catalyst was tested for RhB degradation and reduction of Cr(VI) [53]. Ran You et al. developed graphitic carbon nitride, with S and O co-doping for enhanced visible light photocatalytic performance, which showed higher photocatalytic activity for the degradation of RhB in aqueous solution than pristine g-C_3N_4 nanosheets [54]. D.B.Hernández-Uresti et al. successfully used a polymeric g-C_3N_4 photocatalyst, and the as-prepared samples showed an efficient photocatalytic activity for the degradation of pharmaceutical pollutants under UV–vis irradiation [55]. Bifu Luo et al. investigated the photocatalytic property of the g-C_3N_4/Bi_3TaO_7 nanocomposite composites in the treatment of tetracycline [56].

The photocatalytic activity of g-C_3N_4 improved with the above-mentioned modifications, even though it needs additional improvement to avoid fast recombination of electron-hole pairs, low degradation efficiency; difficulty in separation; and low adsorption ability [57]. Bearing in mind these difficulties, researchers have focused on hybridizing g-C_3N_4 with the natural minerals diatomite, zeolite, and have included several recognized clay minerals, such as kaolinite [58], palygorskite [59], montmorillonites [60, 61], bentonite [62], and rectorite [63].

These reports suggest that these minerals could be useful as carrier support and are able to avoid a recombination of electron and hole due to the interfacial charge transfer between the positively photogenerated hole and the negatively charged electron on the clay surfaces. The g-C_3N_4 based photocatalysts were summarised in **Table 1.3**.

Table 1.3 g-C_3N_4 based photocatalysts

Catalyst	Active compound	Target	C_0	Loading (g/L)	Efficacy (%)	Time (min)	Ref.
g-C_3N_4/ZnAl-MMO	g-C_3N_4/ZnAl-MMO	phenol	20 ppm	1.0	75	1440	[38]
g-C_3N_4/CuONP/ZnAl-MMO	g-C_3N_4/CuONP/ZnAl-MMO	phenol	20 ppm	1.0	65	1440	[38]
g-C_3N_4/Fe_3O_4/AgI	g-C_3N_4/Fe_3O_4/AgI	RhB	2.5 x 10^{-5} M	0.4	98	270	[64]
g-C_3N_4/TiO_2 films	g-C_3N_4/TiO_2 films	MB	10 ppm	-	68	180	[65]
TiO_2/g-C_3N_4 films	TiO_2/g-C_3N_4 films	phenol	5 ppm	-	100	180	[66]
Ag@NiAl LDH/g-C_3N_4	Ag@NiAl LDH/g-C_3N_4	RhB	5 ppm	0.25	85	60	[16]
O doped g-C_3N_4/CoAl LDH	O doped g-C_3N_4/CoAl LDH	MO	20 ppm	0.3	100	60	[17]
Ti-SBA15-g-C_3N_4 (Ti-SBA15-CN)	Ti-SBA15-CN	Cr(VI)	10 ppm	1.0	25	120	[67]
Acid-treated g-C_3N_4 with citric acid	Acid-treated g-C_3N_4 with citric acid	Cr(VI)	50 ppm	1.0	100	240	[8]
α-Fe_2O_3/g-C_3N_4	α-Fe_2O_3/g-C_3N_4	Cr(VI)	10 ppm	2.0	100	160	[68]
ZnO-g-C_3N_4	ZnO-g-C_3N_4	Cr(VI)	10 ppm	-	70	240	[69]
Ag@Ag_3PO_4/g-C_3N_4/NiFe	Ag@Ag_3PO_4/g-C_3N_4/NiFe	Cr(VI)	20 ppm	1.0	95	120	[70]

Table 1.3 g-C_3N_4 based photocatalysts (continued)

Catalyst	Active compound	Target	C_0	Loading (g/L)	Efficacy (%)	Time (min)	Ref.
Porous g-C_3N_4	Porous g-C_3N_4	p-chlorophenol	20 ppm	1.0	100	60	[71]
NiS_2 nanoparticles/sulfur-doped g-C_3N_4	NiS_2 nanoparticles/sulfur-doped g-C_3N_4	RhB	8 ppm	1.0	90	180	[72]
S doped g-C_3N_4	S doped g-C_3N_4	RhB	1 x 10^{-5} M	1.0	90	20	[53]
O functionalized S–P codoped g-C_3N_4 nanorods	O functionalized S–P codoped g-C_3N_4 nanorods	RhB	10 ppm	0.25	100	120	[73]
g-C_3N_4 nanodots as 2D/0D	g-C_3N_4 nanodots as 2D/0D	MB	12 ppm	0.2	90	60	[52]
S and O codoped g-C_3N_4	S and O codoped g-C_3N_4	RhB	10 ppm	0.1	75	180	[54]
Oxygen self-doped g-C_3N_4	Oxygen self-doped g-C_3N_4	RhB	1 x 10^{-5} M	0.5	100	45	[74]
O doped g-C_3N_4	O doped g-C_3N_4	MO	20 ppm	0.3	20	60	[17]
S doped mesoporous g-C_3N_4	S doped mesoporous g-C_3N_4	RhB	11 ppm	0.7	100	90	[57]
BiOCl/g-C_3N_4/kaolinite	BiOCl/g-C_3N_4/kaolinite	RhB	10 ppm	3.0	95	360	[58]
g-C_3N_4/TiO_2/kaolinite	g-C_3N_4/TiO_2/kaolinite	Ciprofloxacin	10 ppm	2.0	90	240	[33]
g-C_3N_4/illite	g-C_3N_4/illite	RhB	10 ppm	2.0	80	360	[75]

Table 1.3 g-C_3N_4 based photocatalysts (continued)

Catalyst	Active compound	Target	C_0	Loading (g/L)	Efficacy (%)	Time (min)	Ref.
Oxygen self-doped g-C_3N_4	Oxygen self-doped g-C_3N_4	RhB	1 x 10^{-5} M	0.5	100	45	[74]
g-C_3N_4/montmorillonite	g-C_3N_4/montmorillonite	RhB	30 ppm	2.0	85	360	[60]
Dark orange montmorillonite/ g-C_3N_4	Dark orange montmorillonite/ g-C_3N_4	MB	20 ppm	0.5	95	150	[76]
Au-Pd@g-C_3N_4	Au-Pd@g-C_3N_4	phenol	0.5 mM	0.5	95	120	[77]
g-C_3N_4/Ag_3VO_4	g-C_3N_4/Ag_3VO_4	Bbasic fuchsin	10 ppm	1.0	95	150	[78]
Pd/CeO_2/ g-C_3N_4	Pd/CeO_2/ g-C_3N_4	Cr(VI)	0.1 mM	0.5	100	40	[79]
Cyanuric Acid Modified g-C_3N_4/Kaolinite	Cyanuric Acid Modified g-C_3N_4/Kaolinite	RhB	10 ppm	2.0	93	420	[80]
Ag/GO/g-C_3N_4	Ag/GO/g-C_3N_4	RhB	10 ppm	1.2	100	120	[81]
Pd/g-C_3N_4/Bi_2MoO_6	Pd/g-C_3N_4/Bi_2MoO_6	RhB	10 ppm	0.2	100	40	[82]
Au/Pt/g-C_3N_4	Au/Pt/g-C_3N_4	RhB	10 ppm	0.2	90	180	[83]
Au/g-C_3N_4	Au/g-C_3N_4	bisphenol A	5 ppm	1.0	100	70	[84]
Pd/g-C_3N_4	Pd/g-C_3N_4	bisphenol A	5 ppm	1.0	100	60	[84]

1.6 Clay-based photocatalyst

Nowadays, the composites of photocatalyst from different two semiconductors have been applied to expand the light absorption behavior and elongate the lifetime of the photocatalyst materials. In this regard cost effective supported photocatalysts on many porous adsorbent materials, such as silica gels, zeolites, carbons, and clay minerals are utilized to immobilized photocatalytic materials.

In recent years, natural abundant 2:1 smectite clay materials have been extensively used as support materials for semiconductors/another photocatalyst due to the abundant natural availability and characteristic features, such as fibrous/layered morphology; large specific surface areas; superior cation exchange capacity; negative surface charge, and an -OH ion decorated surface. Collectively all these natural properties can be utilized for several types of organic /inorganic types of modification, which are beneficial to the development of clay-based photocatalyst.

1.6.1 Sepiolite

1.6.1.1 Basic structure of sepiolite

Currently, natural sepiolite, belonging to the 2:1 type of clay minerals, has gained significant interest in different fields of application, including the development of photocatalyst materials. In **Fig. 1.11**, sepiolite is a hydrous magnesium silicate that is widespread due to its unusual fibrous morphology and intracrystalline tunnels, which are different from layered phyllosilicate clays. Sepiolite is a widespread hydrous magnesium silicate due to its unusual fibrous morphology and intracrystalline tunnels. The ideal structural formula is $Si_{12}Mg_8O_{30}(OH)_4(OH_2)_4 \cdot 8H_2O$ for a half-unit cell.

Sepiolite shows an alternation of blocks and tunnels that grow up in the fiber direction. Each structural block is composed of two tetrahedral silica sheets and a central octahedral sheet containing magnesium.

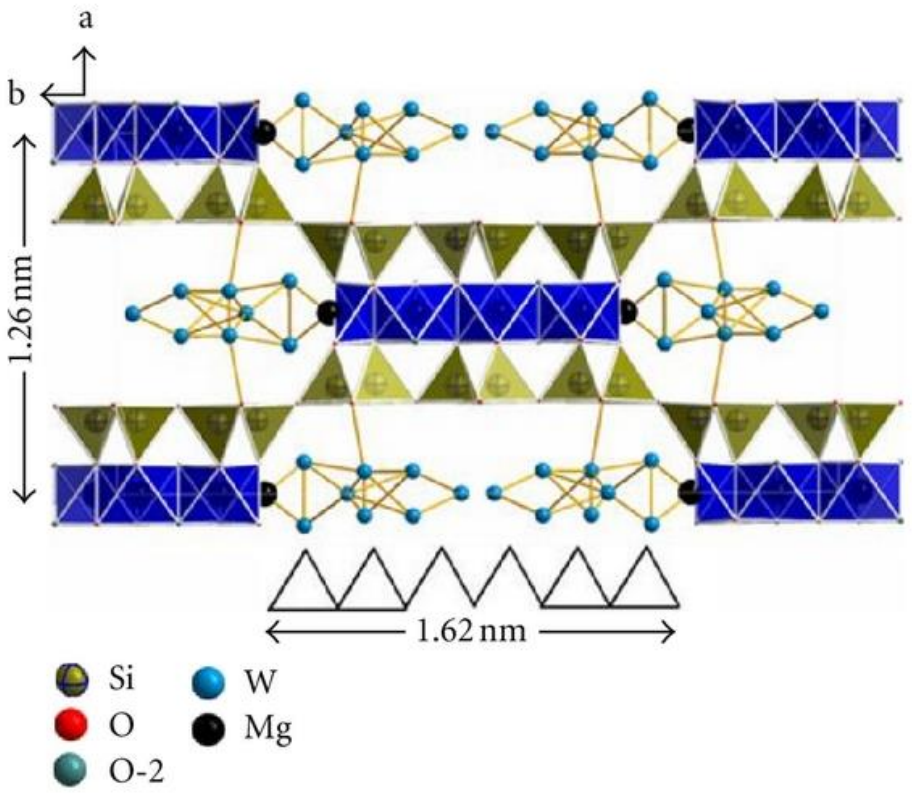

Fig. 1.11 Sepiolite structure [85].

1.6.1.2 Photocatalytic application of sepiolite-based photocatalyst

Sepiolite is a fibrous, hydrated Mg–Al silicate clay mineral and formed by an alternation of blocks and tunnels that grow up in the fiber direction (c-axis). Each structural block is composed of two tetrahedral silica sheets and a central octahedral sheet containing magnesium. The structure of sepiolite results in zeolite-like channels. The peculiar pore structure with interior channels contributes to adsorb organic

molecules and ions. It has a 2:1 layered structure which is constituted. Also, these channels might contain zeolitic water and exchangeable metal cations (Ca^{2+} and Mg^{2+}). The structural and textural physicochemical properties of sepiolite offer its exclusive role compared to other clay materials. So far, Sepiolite has been considered to be an effective transporter in the photocatalytic treatment of several types of pollutants, including an organic dye. Xiaolong Hu et al. report the synthesis of novel ternary heterogeneous BiOCl/TiO_2/sepiolite composite with improved visible-light-induced photocatalytic activity for tetracycline degradation [86]. Akkari, M, et al. report ZnO/sepiolite heterostructured materials for solar photocatalytic degradation of pharmaceuticals in wastewater [87]. Li Jin et al. developed in situ synthesis of Sepiolite@LDH composite and utilized for simultaneous photocatalytic degradation of methyl orange (MO) and methylene blue (MB) dye [88]. Sepiolite-TiO_2 nanocomposites utilized for the Orange-G dye [89]. Akkari, M, et al. developed a ternary ZnO/Fe_3O_4-sepiolite nanostructured material, and the catalyst was tested as photocatalysts for methylene blue dye degradation [90]. Wenguo Xu et l developed quantum-sized ZnO particles sepiolite, which showed a higher photocatalytic activity for the degradation of Reactive Blue 4 in aqueous solution [91]. Yalei Zhang et al. successfully synthesized the TiO_2/sepiolite composites at low temperature, and the as-prepared samples showed an efficient photocatalytic activity for the degradation of acid red G and 4-nitrophenol under UV light irradiation [92]. Ugurlu and Karaoglu (2011) developed TiO_2/sepiolite composites for photocatalytic treatment of phenol [93].

So far, from the reported results, it is observed that generally sepiolite was utilized as an efficient, supportive material for well-known semiconductors, or other

types of photo-catalytically active species. As far as we know, there are still no reports on pristine natural sepiolite material (photocatalyst) application for rhodamine B dye degradation upon visible light irradiation.

The two-dimensional clay surface offers a rigid active surface for the adsorption dye species through electrostatic interaction or a complexation mechanism. Successful surface adsorption of dye species on a clay surface is generally benefited by a photochemical reaction. In some cases, the adsorbed dye particles on the clay surface are responsible for the formation of a photon-responsive composite material. The same phenomenon is possible in the case of the sepiolite clay due to the anomalous fibrous and other structural features. If we consider the structure of the outer surface of sepiolite, it is decorated with siloxane bonds, whereas its lateral surface contains broken and terminated Si–O, Mg–O bonds. These unprotected metal cations at the edges are electron-deficient, which are recognized as natural electron acceptors. The adsorbed dye species around the broken surface are responsible for generating a radical dye species. It is predictable that the formed dye radical can react with active oxygen species present within the system, which may lead to a disintegration of the dyes. Also, it is well-known that the highly polar surface of the clay material is advantageous because it can stabilize the generated radicles' species, which prolong the lifetime and is ultimately responsible for the better photocatalytic performance.

1.6.2 Montmorillonites

1.6.2.1 Basic structure of montmorillonites

Montmorillonite (MT), as a cationic exchanged 2D clay mineral belonging to the 2:1 type of clay minerals, has attracted much interest as a promising photocatalyst due to natural abundance; high surface area; low cost; high thermal and chemical stability; non-toxicity; and is environmentally friendly. The structure of MT (**Fig. 1.12**) is composed of a negatively charged layer and the cationic ion intercalated between the layer to stabilize the negative charge of MT.

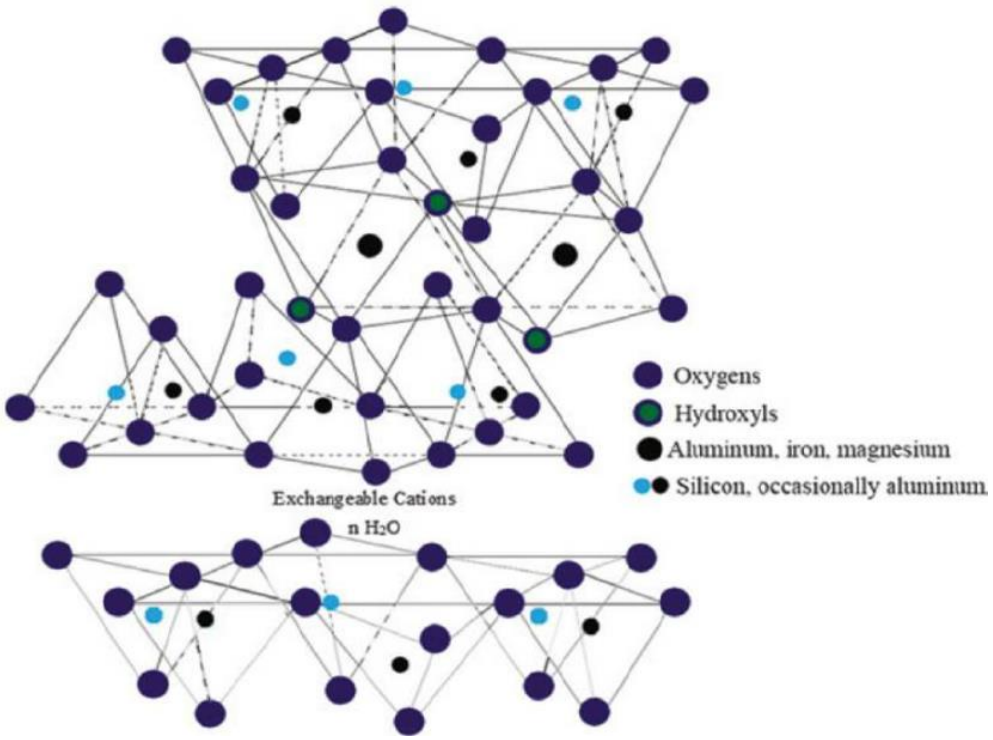

Fig. 1.12 Montmorillonite structure [94].

1.6.2.2 Photocatalytic application of montmorillonite composite

There are some reports about MT composites with enhancing photocatalytic performance by suppressing the electron-hole recombination. However, the mechanism is not well understood. So far, montmorillonite has been considered as an effective transporter in the photocatalytic treatment of several types of pollutants, including organic dyes. Boualem Damardji et al. reported TiO_2-pillared montmorillonite with improved photocatalytic activity for azo dye degradation [95, 96]. Beatriz González et al. developed the Ti doped-pillared montmorillonite for degradation of trimethoprim [97]. Ondřej Kozák et al. report ZnS nanoparticles deposited on montmorillonite and utilized for the reduction of carbon dioxide [98]. Yajie Wang et al. report that Natural montmorillonite is utilized for the photooxidation of As(III) in aqueous suspensions [99]. Jianjun Liu et al. developed TiO2/montmorillonite by solvothermal, and the catalyst is tested as photocatalysts for MB dye degradation [100]. Li Chunquan et al. developed C_3N_4/montmorillonite composite, which showed higher photocatalytic activity for the degradation of RhB in aqueous solution under visible light irradiation [60]. JixiangXu and coauthors successfully synthesized the montmorillonite-hybridized g-C_3N_4 composite modified by NiCoP cocatalyst, and the as-prepared samples showed an efficient photocatalytic activity for the production of hydrogen evolution under visible-light light irradiation [61]. Nur Fajrina and Muhammad Tahir investigated the photocatalytic property of the 2D-montmorillonite-dispersed g-C_3N_4/TiO_2 2D/0D nanocomposite in H_2 evolution from a glycerol-water mixture [101]. The clay-based photocatalysts were summarised in **Table 1.4**.

Table 1.4. Clay-based photocatalysts

Catalyst	Active compound	Target	C_0	Loading (g/L)	Efficacy (%)	Time (min)	Ref.
BiOCl/g-C_3N_4/kaolinite	BiOCl/g-C_3N_4	RhB	10 ppm	3.0	95	360	[58]
g-C_3N_4/TiO_2/kaolinite	g-C_3N_4/TiO_2	ciprofloxacin	10 ppm	2.0	90	240	[33]
kaolinite/g-C_3N_4	g-C_3N_4	RhB	10 ppm	3.0	95	360	[102]
g-C_3N_4/kaolinite	g-C_3N_4	RhB	10 ppm	2.0	95	360	[75]
g-C_3N_4/illite	g-C_3N_4	RhB	10 ppm	2.0	80	360	[75]
g-C_3N_4/montmorillonite	g-C_3N_4	RhB	30 ppm	2.0	85	360	[60]
Dark orange montmorillonite/g-C_3N_4	g-C_3N_4	MB	20 ppm	0.5	95	150	[76]
Cyanuric Acid Modified g-C_3N_4/Kaolinite	Cyanuric Acid Modified g-C_3N_4	RhB	10 ppm	2.0	93	420	[80]
TiO_2-montmorillonite	TiO_2	Cr(VI)	30 ppm	0.2	~15	240	[103]
TiO_2-montmorillonite with tartaric acid	TiO_2 with tartaric acid	Cr(VI)	30 ppm	0.2	100	120	[103]
Bi_2O_3/sepiolite	Bi_2O_3	Malachite green	14×10^{-5}	0.5	98.2	180	[104]
Sepiolite-TiO_2	TiO_2	Orange G	2.2×10^{-5}	0.8	97.8	150	[105]

Table 1.4. Clay-based photocatalysts (continued)

Catalyst	Active compound	Target	C_0	Loading (g/L)	Efficacy (%)	Time (min)	Ref.
Sepiolite/Cu_2O/Cu	Cu_2O/Cu	Congo red	1.4×10^{-5}	0.2	95.1	50	[106]
Eu-TiO_2/sepiolite	Eu-TiO_2	Orange G	2.2×10^{-5}	0.8	~70	600	[107]
ZnCr LDH/Sepiolite	ZnCr LDH	MB	3.1×10^{-5}	1.25	93.1	120	[108]
Sepiolite –TiO_2	TiO_2	RhB	8.3×10^{-5}	0.85	~80	120	[109]
Sepiolite	Adsorbed MB on sepiolite	MB	2.0×10^{-5}	0.25	83.3	120	[110]
Sepiolite	Adsorbed RhB on sepiolite	RhB	2.0×10^{-5}	0.25	65.5	120	[110]

1.7 Photocatalytic treatment of wastewater

Nowadays, industrial processes and excessive amounts of pollutants cause seepages into waterways and soils, leading to widespread environmental degradation. Effective treatment processes of wastewater is an important step for the industry to treat effluent. In this study, the focus is on the photocatalytic removal of the contaminated organic compounds and hexavalent chromium Cr(VI), which have become serious problems for humans, animals, and the environment.

1.7.1 Photocatalytic degradation of organic pollutant

Synthetic organic compounds and dyes are an essential constituent in the dyeing, printing, petroleum refineries, coal gasification operations, liquefication processes, dye synthesis units, pulp ,paper mills and pharmaceutical industries and textile industries. During processing, disorganization in dyeing result in huge quantities of the dyestuff being directly lost to the wastewater; which ultimately finds its way into the environment. The wastewater containing organic waste and dyes is responsible for the adverse effects on the aquatic biota and public health. The treatment of organic waste and dyes in wastewater before discharge into the environment is an important step for industries.

Substantial research has been carried out on the treatment of various types of wastewater, including into several types of dyes through adsorption; coagulation; flocculation; oxidation; precipitation; filtration; and electrochemical processes. All these techniques have some benefits and limitations. Limitations include high operating costs; and an incapability to treat pollutants totally. The photocatalytic

oxidation is an interesting reprocess for contaminated organic decomposition in wastewater. Under light irradiation, the photogenerated charge carriers (electron and hole) are generated and separated at different electronic states; the photogenerated electron will move to CB leaving the photogenerated hole in the VB. In this way, an electron in the CB could reduce the dissolved O_2 to $^{\bullet}O_2^-$. At the same time, the H_2O also can react with h^+ in the VB to produce $^{\bullet}OH$. Thus, the generated reactive species ($^{\bullet}O_2^-$ and $^{\bullet}OH$) and h^+ in the VB of photocatalyst decomposed organic compounds into small and harmless byproducts (**Fig. 1.13**).

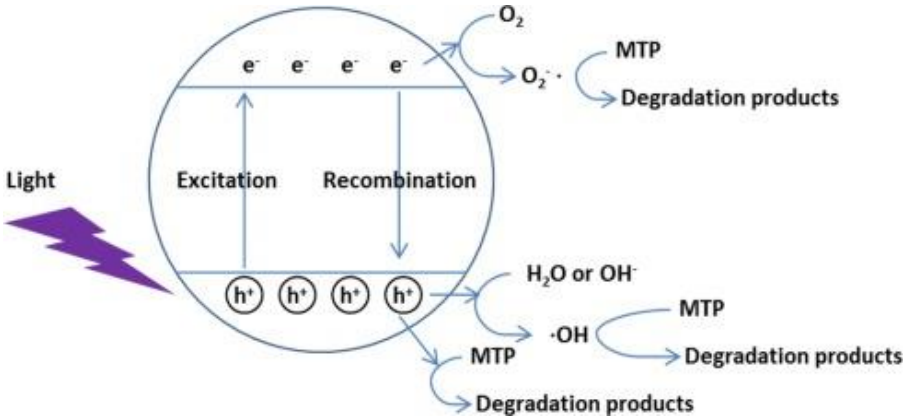

Fig. 1.13 Mechanism for photocatalytic degradation of organic pollutant [111].

1.7.1.1 Photocatalytic degradation of Rhodamine B

Rhodamine B (RhB, $C_{28}H_{31}ClN_2O_3$) is one of the famous dyes and is widely used as a colorant in foodstuffs and textiles due to its high stability [112]. It is [9-(2-carboxyphenyl)-6-diethylamino-3- xanthenylidene]-diethylammonium chloride [113]. The carcinogenic behavior of RhB dye can irritate the eyes and skin; damage the respiratory, reproductive, and nervous system [114, 115]. Discharging RhB into the aquatic environment makes it a highly toxic and low transparent. Moreover, RhB is

harmful even at very low concentrations, and the later should be removed from wastewater effluent to lessen the effects of the environment before discharging [116]. **Fig. 1.14** show the chemical structure of RhB.

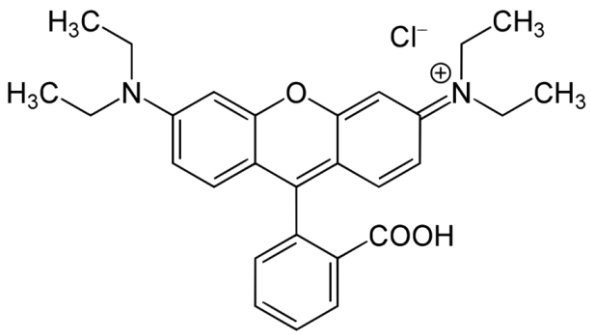

Fig. 1.14 Structure of Rhodamine B.

For the photocatalytic degradation of RhB under light irradiation (**Fig. 1.15**), RhB was adsorbed on the surface of the photocatalyst, and then the electrons of RhB were excited under the visible light to generate the excited electrons. The electrons in the LUMO of RhB ($E_{LUMO} = -1.10$ eV versus NHE) can be transferred to the CB of a photocatalyst to generate the superoxide radical. The photoexcited electron on the CB of sepiolite could reduce the dissolved O_2 to $^{\bullet}O_2^-$. Then, the oxidation of RhB by $^{\bullet}O_2^-$ occurred to degrade RhB to smaller molecules. The photocatalytic degradation of RhB was summarised in **Table 1.5.**

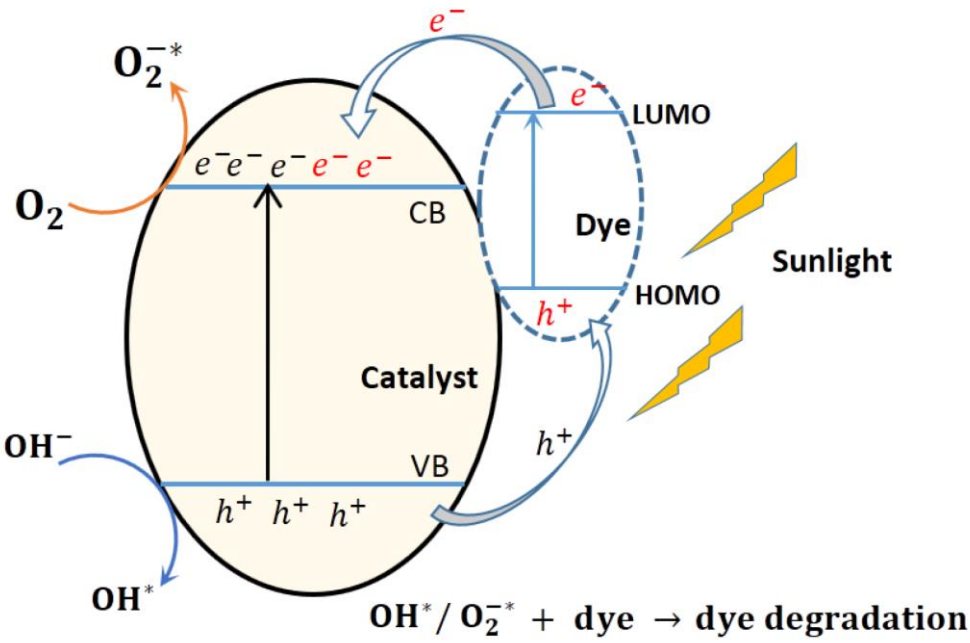

Fig. 1.15 Dye-sensitized visible light photocatalytic mechanism [117].

Table 1.5. Photocatalytic degradation of RhB

Catalyst	Active compound	Target	C_0	Loading (g/L)	Efficacy (%)	Time (min)	Ref.
g-C_3N_4/Fe_3O_4/AgI	g-C_3N_4/Fe_3O_4/AgI	RhB	2.5 x 10^{-5} M	0.4	98	270	[64]
NiS_2 nanoparticles/sulfur-doped g-C_3N_4	NiS_2 nanoparticles/sulfur-doped g-C_3N_4	RhB	8 ppm	1.0	90	180	[72]
S doped g-C_3N_4	S doped g-C_3N_4	RhB	1 x 10^{-5} M	1.0	90	20	[53]
O functionalized S–P codoped g-C_3N_4nanorods	O functionalized S–P codoped g-C_3N_4nanorods	RhB	10 ppm	0.25	100	120	[73]
Ag@NiAl LDH/g-C_3N_4	Ag@NiAl LDH/g-C_3N_4	RhB	5 ppm	0.25	85	60	[16]
S and O codoped g-C_3N_4	S and O codoped g-C_3N_4	RhB	10 ppm	0.1	75	180	[54]
Oxygen self-doped g-C_3N_4	Oxygen self-doped g-C_3N_4	RhB	1 x 10^{-5} M	0.5	100	45	[74]
BiOCl/g-C_3N_4/kaolinite	BiOCl/g-C_3N_4/kaolinite	RhB	10 ppm	3.0	95	360	[58]
S doped mesoporous g-C_3N_4	S doped mesoporous g-C_3N_4	RhB	11 ppm	0.7	100	90	[57]
kaolinite/g-C_3N_4	kaolinite/g-C_3N_4	RhB	10 ppm	3.0	95	360	[102]
g-C_3N_4/kaolinite	g-C_3N_4/kaolinite	RhB	10 ppm	2.0	95	360	[75]
g-C_3N_4/illite	g-C_3N_4/illite	RhB	10 ppm	2.0	80	360	[75]

Table 1.5. Photocatalytic degradation of RhB (continued)

Catalyst	Active compound	Target	C_0	Loading (g/L)	Efficacy (%)	Time (min)	Ref.
g-C_3N_4/montmorillonite	g-C_3N_4/montmorillonite	RhB	30 ppm	2.0	85	360	[60]
Cyanuric Acid Modified g-C_3N_4/Kaolinite	Cyanuric Acid Modified g-C_3N_4/Kaolinite	RhB	10 ppm	2.0	93	420	[80]
Mn/Co/Ti LDH	Mn/Co/Ti LDH	RhB	1 x 10^{-5} M	0.1	80	60	[18]
ZnCr LDH	ZnCr LDH	RhB	100 ppm	1.0	95	60	[28]
BiOCl/TiO_2/ZnCr LDH	BiOCl/TiO_2/ZnCr LDH	RhB	100 ppm	0.37	100	30	[29]
Ag coated Zn/Ti-LDH	Ag coated Zn/Ti-LDH	RhB	10 ppm	1.0	83	30	[26]
Ag/GO/g-C_3N_4	Ag/GO/g-C_3N_4	RhB	10 ppm	1.2	100	120	[81]
Pd/g-C_3N_4/Bi_2MoO_6	Pd/g-C_3N_4/Bi_2MoO_6	RhB	10 ppm	0.2	100	40	[82]
Au/Pt/g-C_3N_4	Au/Pt/g-C_3N_4	RhB	10 ppm	0.2	90	180	[83]
Sepiolite –TiO_2	Sepiolite –TiO_2	RhB	8.3×10^{-5}	0.85	~80	120	[109]
Sepiolite	Sepiolite	RhB	2.0×10^{-5}	0.25	65.5	120	[110]
Oxygen self-doped g-C_3N_4	Oxygen self-doped g-C_3N_4	RhB	1 x 10^{-5} M	0.5	100	45	[74]

1.7.1.2 Photocatalytic degradation of phenol

Phenol (C_6H_5OH) is one of the phenolic compounds which is used to manufacture a wide variety of products (**Fig. 1.16**). Many industrial processes rely on the use of phenol, such as the petrochemical industry, petroleum refineries, coal gasification operations, liquefication processes, dye synthesis units, pulp, and paper mills and pharmaceutical industries. In addition, phenolic resins are critical in the plywood, construction, automotive, and appliance industries [118]. Its usages can be found in adhesives and sealant chemicals, flame retardants, ion exchange agents, and odor agents. Consumer uses of phenol include wood products, cleaning and furnishing care products, floor coverings, and paints and coatings [119]. Due to the wide range and abundant use of phenol, it is critical to be aware of the dangers of the chemical and effective techniques for disposal.

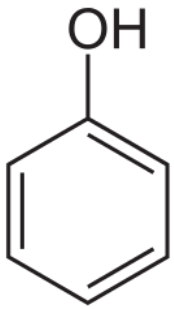

Fig. 1.16 Structure of phenol.

Phenol is a contaminant to the environment and difficult to remove from wastewater due to its nonbiodegradable nature. Pollution in wastewater effluvia from phenol and phenolic compounds is a common occurrence in many industrial manufacturing plants. Phenol is a highly corrosive nerve poisoning agent and is known to have harmful short-term and long-term effects on human beings. It is also toxic to

aquatic wildlife. The toxic levels range between 10-24mg/L for humans and 9-25mg/L for fish. The lethal blood concentration for humans is approximately 150 mg/100ml [118]. As a result of the toxic and harmful nature 2 of phenol, it is imperative that phenol is properly removed/decomposed from wastewater before wastewater streams are returned to the environment.

For the photocatalytic degradation of phenol under light irradiation (**Fig. 1.17**), The excited electrons in the CB of photocatalyst can react with O_2 to produce the $^{\bullet}O_2^-$. Then, the oxidation of RhB by $^{\bullet}O_2^-$ occurred to degrade RhB to smaller molecules. The photocatalytic reduction of Cr(VI)degradation phenol was summarised in **Table 1.6**.

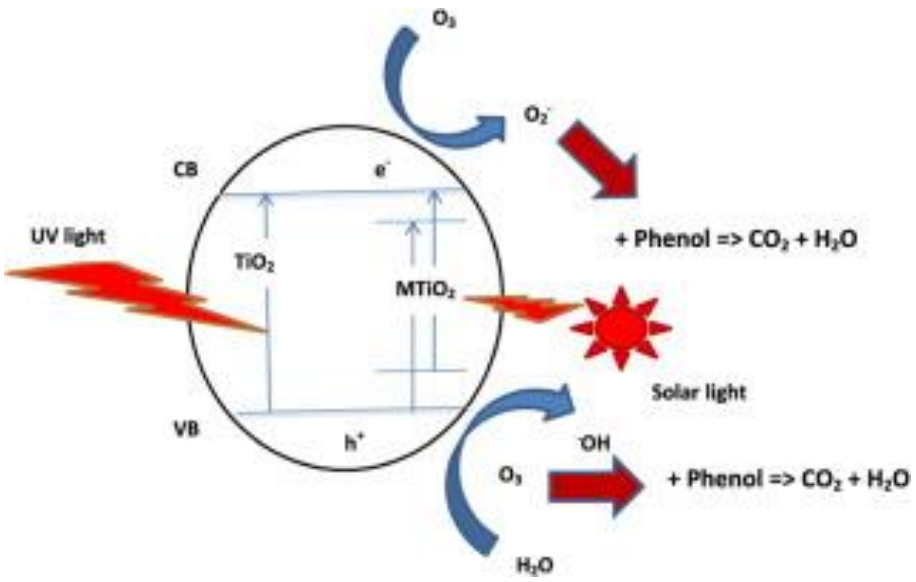

Fig. 1.17 Photocatalytic degradation of phenol [120].

Table 1.6 Photocatalytic degradation of phenol and phenolic compounds

Catalyst	Active compound	Target	C_0	Loading (g/L)	Efficacy (%)	Time (min)	Ref.
$ZnO/ZnTi_2TiO_4$	$ZnO/ZnTi_2TiO_4$	phenol	50 ppm	0.1	80	450	[36]
$ZnO/ZnCr_2O_4$	$ZnO/ZnCr_2O_4$	phenol	50 ppm	0.1	98	210	[36]
ZnO/ZnAl2O4	ZnO/ZnAl2O4	phenol	50 ppm	0.1	98	300	[36]
g-C_3N_4/CuONP/ZnAl-MMO	g-C_3N_4/CuONP/ZnAl-MMO	phenol	20 ppm	1.0	65	1440	[38]
BiOCl-TiO_2	BiOCl-TiO_2	phenol	50 ppm	1.0	25	360	[39]
ZnTi MMO	ZnTi MMO	phenol	50 ppm	0.5	90	250	[35]
g-C_3N_4/ZnAl-MMO	g-C_3N_4/ZnAl-MMO	phenol	20 ppm	1.0	75	1440	[38]
g-C_3N_4/CuONP/ZnAl-MMO	g-C_3N_4/CuONP/ZnAl-MMO	phenol	20 ppm	1.0	65	1440	[38]
TiO_2/g-C_3N_4films	TiO_2/g-C_3N_4films	phenol	5 ppm	-	100	180	[66]
Au-Pd@ g-C_3N_4	Au-Pd@ g-C_3N_4	phenol	0.5 mM	0.5	95	120	[77]
Ag /activated carbon doped ZnO	Ag /activated carbon doped ZnO	Bisphenol A	25 ppm	1.2	100	100	[121]
Fullerene modified ZnAlTi-MMO	Fullerene modified ZnAlTi-MMO	Bisphenol A	10 ppm	0.5	80	300	[34]

Table 1.6 Photocatalytic degradation of phenol and phenolic compounds (continued)

Catalyst	Active compound	Target	C_0	Loading (g/L)	Efficacy (%)	Time (min)	Ref.
ZnAlTi-MMO	ZnAlTi-MMO	Bisphenol A	10 ppm	0.5	60	300	[34]
ZnNiAl MMO	ZnNiAl MMO	p-nitrophenol	5 ppm	1.0	100	180	[32]
Porous g-C_3N_4	Porous g-C_3N_4	p-chlorophenol	20 ppm	1.0	100	60	[71]
Au/g-C_3N_4	Au/g-C_3N_4	bisphenol A	5 ppm	1.0	100	70	[84]
Pd/g-C_3N_4	Pd/g-C_3N_4	bisphenol A	5 ppm	1.0	100	60	[84]
Ag/g-C_3N_4	Ag/g-C_3N_4	bisphenol A	5 ppm	1.0	100	60	[84]

1.7.2 Photocatalytic reduction of hexavalent chromium Cr(VI)

Hexavalent chromium ((Cr(VI)), which is released from certain manufacturing processes is a very toxic heavy metal, causing carcinogenic and mutagenic diseases. In contrast, the Cr(III) species is less toxic and more mobile in water. The appropriate way for Cr(VI) remediation in wastewater is the reduction of Cr(VI) to Cr(III). Various methods have been utilized for the treatment of the toxic Cr(VI) in an aqueous solution such as adsorption, precipitation, microbial, and membrane filtration. Nevertheless, all these techniques have some benefits and limitations. These include high operating costs; an incapability to treat pollutants totally; there are difficulties in the development of actual industrial arrangement. Photocatalysis is one of the interesting methods for Cr(VI) reduction in recent years due to mild temperature and pressure conditions; low costs; and it is environmentally friendly. The requirements in the photocatalysis is a semiconductor material that can produce an electron-hole pair during light irradiation. The excited electron can be applied as a redox system for Cr(VI) reduction in water, as shown in **Fig. 1.18**. The photocatalytic reduction of Cr(VI) was summarised in **Table 1.7**.

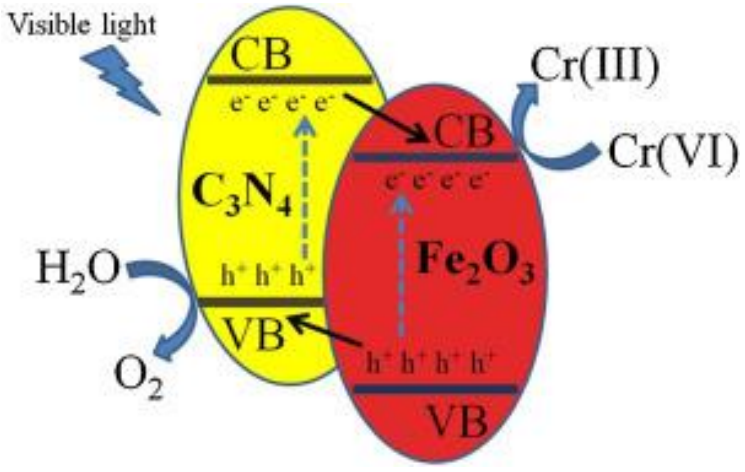

Fig. 1.18 Mechanism for photocatalytic reduction of Cr(VI) [68].

Table 1.7 Comparison of photocatalytic efficiency for Cr(VI) reduction

Catalyst	Active compound	Target	C_0	Loading (g/L)	Efficacy (%)	Time (min)	Ref.
TiO2-montmorillonite	TiO2-montmorillonite	Cr(VI)	30 ppm	0.2	~15	240	[103]
TiO2-montmorillonite with tartaric acid	TiO2-montmorillonite with tartaric acid	Cr(VI)	30 ppm	0.2	100	120	[103]
$BiVO_4$	$BiVO_4$	Cr(VI)	0.1 mM	1.0	50	180	[122]
ZnAl-MMO	ZnAl-MMO	Cr(VI)	10 ppm	2.0	100	300	[40]
Ti-SBA15-g-C_3N_4 (Ti-SBA15-CN)	Ti-SBA15-g-C_3N_4 (Ti-SBA15-CN)	Cr(VI)	10 ppm	1.0	25	120	[67]
TiO_2 with methanol (100ppm)	TiO_2 with methanol (100ppm)	Cr(VI)	20 ppm	1.0	90	300	[123]
α-Fe_2O_3/g-C_3N_4	α-Fe_2O_3/g-C_3N_4	Cr(VI)	10 ppm	2.0	100	160	[68]
TiO_2	TiO_2	Cr(VI)	10 ppm	-	20	120	[124]
ZnO	ZnO	Cr(VI)	10 ppm	-	34	240	[69]
ZnO-g-C_3N_4	ZnO-g-C_3N_4	Cr(VI)	10 ppm	-	70	240	[69]
Ag@Ag_3PO_4/g-C_3N_4/NiFe	Ag@Ag_3PO_4/g-C_3N_4/NiFe	Cr(VI)	20 ppm	1.0	95	120	[70]
$CaFe_2O_4$/CoAl LDH@Au	$CaFe_2O_4$/CoAl LDH@Au	Cr(VI)	20ppm	1.0	95	60	[15]

Table 1.7 Comparison of photocatalytic efficiency for Cr(VI) reduction (continued)

Catalyst	Active compound	Target	C_0	Loading (g/L)	Efficacy (%)	Time (min)	Ref.
Acid-treated g-C_3N_4	Acid-treated g-C_3N_4	Cr(VI)	50 ppm	1.0	5	300	[8]
Acid-treated g-C_3N_4 with citric acid	Acid-treated g-C_3N_4 with citric acid	Cr(VI)	50 ppm	1.0	100	240	[8]
RGO/TiO_2	RGO/TiO_2	Cr(VI)	12ppm	0.2	180	240	[41]
Pd/CeO_2/g-C_3N_4	Pd/CeO_2/g-C_3N_4	Cr(VI)	0.1 mM	0.5	100	40	[79]
$CaFe_2O_4$/CoAl LDH@Au	$CaFe_2O_4$/CoAl LDH@Au	Cr(VI)	20ppm	1.0	95	60	[15]

1.8 Objectives of this thesis and outline

Various types of heavy metal and organic pollutants which create potential risk to human health are unintendedly released into the natural water system and groundwater by many industries. The wastewater containing organic waste and dyes is responsible for the adverse effects on the aquatic biota and public health. The treatment of organic waste and dyes in wastewater before discharge into the environment is an important step for industries. Moreover, Cr(VI) which are released from manufacturing is very toxic heavy metal, causing the carcinogenic and mutagenic, whereas Cr(III) species is less toxic and mobility in water. The treatment of Cr(VI) containing wastewater before discharge in the environment by the development of an effective and economical technique is an alarming research subject for different fields of researchers.

Recently, photocatalysis is a remarkable methodology for heavy metal and organic pollutants treatment in recent years due to mild temperature/ pressure conditions, low cost, and environmentally friendly. The requirements in the photocatalysis is a semiconductor material that can produce electron-hole pair during light irradiation. However, it has some disadvantage related to the use of pure semiconductor material as photocatalyst like charge carrier recombination. To overcome these restrictions, a composite of two kinds of semiconductor composite has been focused on the environmental application because it can avoid the photogenerated charge recombination thought the charge transfer between a couple of materials.

Therefore, this study established the newly two dimensional geomimetics based photocatalyst composites due to it has greater electron-hole mobility across the

interface of the heterojunction, which can decrease the distance and time of charge migration to inhibit the recombination of photogenerated electron and hole. Through the electronic structure of the composition in the photocatalyst, the photocatalytic mechanism for organic pollutants degradation or Cr(VI) reduction was investigated. The role of two dimensional geomimetics in the composite was examined and compared with the previous reports.

Furthermore, the newly reversed double-beam photoacoustic spectroscopy (RDB-PAS) technique which is a powerful technique to characterization of the photocatalyst, including crystallinity and amorphous phase was utilized to investigate the surface and electronic properties of the pristine and synthetic products. This method has used for the identification of photocatalyst in the solid phase by observation of the pattern of energy-resolved distribution of electron traps (ERDT), combined with conduction band bottom position (CBB). The obtained ERDT include the surface structure and bulk structure, which may be the characteristic of metal oxide. The combined result of ERDT with CBB was used as a fingerprint of photocatalyst, based on the degree of coincidence for a given pair of samples. In this thesis, the RDB-PAS technique was used for investigation the ZnTi mixed metal oxide samples from different preparation condition in order to understand the phase component, including amorphous phase which cannot be observed by XRD technique.

The objectives of the work presented in this thesis are:

In **chapter 3**, the series of 2D/2D ZnTi LDH/MT composite were prepared precipitation method, and the obtained products were used as a photocatalyst for Cr(VI) reduction. Moreover, the electronic level and migration of electron between

ZnTi LDH and MT were studded by density functional theory calculation (DFT) in order to better understand the photocatalytic mechanism of the composite. The role of radical species in photocatalytic decomposition of organic pollutant was investigated by the radical scavenger tests.

In **chapter 4**, the preparation of $ZnTiO_3$ in ZnTi mixed metal oxide (ZTM) for photocatalyst derived from ZnTi layered double hydroxides and systematic study by varying molar ratios of Zn/Ti , synthetic methods and calcination temperatures. This is the first report about the surface electronic property of ZTM using ERDT, related to the phase compositions and photocatalytic performances. The obtained ERDT patterns confirmed the electrical characteristic of the products including the surface and bulk which combing ERDT results with conduction band bottom (CBB), which was used as a fingerprint of a metal oxide including the amorphous phase.

In **chapter 5**, the series of porous oxygen-doped graphitic carbon nitride (OCN) have been successfully synthesized via thermal polycondensation of melamine with a different amount of polyoxyethylene stearyl ether. The photocatalytic performance was also examined for the degradation of RhB as a model under visible light irradiation.

In order to enhance the photocatalytic degradation efficiency of g-C_3N_4, in **chapter 6**, The new composite of ZnTi MMO and g-C_3N_4 composites were prepared by hydrothermal followed by calcination method. The obtained composites were utilized as photocatalyst for RhB degradation under visible light irradiation. Furthermore, the characterization of material and photocatalytic degradation mechanism are also discussed in detail.

In **chapter 7**, the understanding of natural sepiolite as a dye-sensitized photocatalyst for dyes degradation was investigated. The observed phenomenon was proved by several physiochemical and photocatalytic experimental studies in the presence of different dyes with various size and charges, e.g., anionic or cation colorants organic pollutants.

In **chapter 8**, we have developed for the first time a natural sepiolite/g-C_3N_4 by varying the compositions of well-dispersed Pd nanoparticles to enable the efficient photodegradation RhB. The structural properties, optical properties, and photocatalytic efficiency of products were characterized. The possible mechanism of the enhanced photocatalyst was proposed. Moreover, RDB-PAS was applied to interpret the charge transfer in the composite.

References

[1] Y. Teng, J. Yang, R. Zuo, J. Wang, Impact of urbanization and industrialization upon surface water quality: A pilot study of Panzhihua mining town, Journal of Earth Science, 22 (2011) 658-668.

[2] S. Xie, Q. Zhang, G. Liu, Y. Wang, Photocatalytic and photoelectrocatalytic reduction of CO_2 using heterogeneous catalysts with controlled nanostructures, Chem Commun (Camb), 52 (2016) 35-59.

[3] A.O. Ibhadon, P. Fitzpatrick, Heterogeneous Photocatalysis: Recent Advances and Applications, Catalysts, 3 (2013) 189-218.

[4] L.V. Bora, R.K. Mewada, Visible/solar light active photocatalysts for organic effluent treatment: Fundamentals, mechanisms and parametric review, Renewable and Sustainable Energy Reviews, 76 (2017) 1393-1421.

[5] I. Pvps, Task 13: PV Performance Modeling Methods and Practices, (2017).

[6] C. Yu, W. Zhou, J.C. Yu, H. Liu, L. Wei, Design and fabrication of heterojunction photocatalysts for energy conversion and pollutant degradation, Chinese Journal of Catalysis, 35 (2014) 1609-1618.

[7] C. Wei, B. Bo, F. Tao, Y. Lu, S. Peng, W. Song, Q. Zhou, Hydrothermal Synthesis and Structural Characterization of NiO/SnO_2 Composites and Hydrogen Sensing Properties, Journal of Spectroscopy, 2015 (2015) 1-6.

[8] Y. He, L. Zhang, M. Fan, X. Wang, M.L. Walbridge, Q. Nong, Y. Wu, L. Zhao, Z-scheme SnO_2^{-x}/g-C_3N_4 composite as an efficient photocatalyst for dye degradation and photocatalytic CO_2 reduction, Solar Energy Materials and Solar Cells, 137 (2015) 175-184.

[9] L. Gomathi Devi, R. Kavitha, A review on plasmonic metal TiO_2 composite for generation, trapping, storing and dynamic vectorial transfer of photogenerated electrons across the Schottky junction in a photocatalytic system, Applied Surface Science, 360 (2016) 601-622.

[10] T. Li, H.N. Miras, Y.-F. Song, Polyoxometalate (POM)-Layered Double Hydroxides (LDH) Composite Materials: Design and Catalytic Applications, Catalysts, 7 (2017) 260, 1-17.

[11] X.-R. Wang, Y. Li, L.-P. Tang, W. Gan, W. Zhou, Y.-F. Zhao, D.-S. Bai, Fabrication of Zn-Ti layered double hydroxide by varying cationic ratio of Ti^{4+} and its application as UV absorbent, Chinese Chemical Letters, 28 (2017) 394-399.

[12] M. Shao, J. Han, M. Wei, D.G. Evans, X. Duan, The synthesis of hierarchical Zn–Ti layered double hydroxide for efficient visible-light photocatalysis, Chemical Engineering Journal, 168 (2011) 519-524.

[13] Y. Zhu, M. Laipan, R. Zhu, T. Xu, J. Liu, J. Zhu, Y. Xi, G. Zhu, H. He, Enhanced photocatalytic activity of Zn/Ti-LDH via hybridizing with C60, Molecular Catalysis, 427 (2017) 54-61.

[14] Y. Zhao, P. Chen, B. Zhang, D.S. Su, S. Zhang, L. Tian, J. Lu, Z. Li, X. Cao, B. Wang, M. Wei, D.G. Evans, X. Duan, Highly dispersed TiO_6 units in a layered double hydroxide for water splitting, Chemistry, 18 (2012) 11949-11958.

[15] S. Das, S. Patnaik, K.M. Parida, Fabrication of a Au-loaded $CaFe_2O_4$/CoAl LDH p–n junction based architecture with stoichiometric H_2&O_2 generation and Cr(Vi) reduction under visible light, Inorganic Chemistry Frontiers, 6 (2019) 94-109.

[16] S. Tonda, W.-K. Jo, Plasmonic Ag nanoparticles decorated NiAl-layered double hydroxide/graphitic carbon nitride nanocomposites for efficient visible-light-driven photocatalytic removal of aqueous organic pollutants, Catalysis Today, 315 (2018) 213-222.

[17] Y. Wu, H. Wang, Y. Sun, T. Xiao, W. Tu, X. Yuan, G. Zeng, S. Li, J.W. Chew, Photogenerated charge transfer via interfacial internal electric field for significantly improved photocatalysis in direct Z-scheme oxygen-doped carbon nitrogen/CoAl-layered double hydroxide heterojunction, Applied Catalysis B: Environmental, 227 (2018) 530-540.

[18] P. Roy Chowdhury, K.G. Bhattacharyya, Synthesis and characterization of Mn/Co/Ti LDH and its utilization as a photocatalyst in visible light assisted degradation of aqueous Rhodamine B, RSC Adv, 6 (2016) 112016-112034.

[19] S.-j. Xia, X.-b. Zhou, W. Shi, G.-x. Pan, Z.-m. Ni, Photocatalytic property and mechanism studies on acid red 14 by M_xO_y/ZnTi–layered double hydroxides (M=Fe, Sn, Ce), Journal of Molecular Catalysis A: Chemical, 392 (2014) 270-277.

[20] S. Kim, J. Fahel, P. Durand, E. André, C. Carteret, Ternary Layered Double Hydroxides (LDHs) Based on Co-, Cu-Substituted ZnAl for the Design of Efficient Photocatalysts, European Journal of Inorganic Chemistry, 2017 (2017) 669-678.

[21] S. Xia, L. Zhang, G. Pan, P. Qian, Z. Ni, Photocatalytic degradation of methylene blue with a nanocomposite system: synthesis, photocatalysis and degradation pathways, Phys Chem Chem Phys, 17 (2015) 5345-5351.

[22] S. Mallakpour, M. Hatami, LDH-VB_9-TiO_2 and LDH-VB_9-TiO_2/crosslinked PVA nanocomposite prepared via facile and green technique and their photo-degradation application for methylene blue dye under ultraviolet illumination, Applied Clay Science, 163 (2018) 235-248.

[23] S.J. Xia, F.X. Liu, Z.M. Ni, J.L. Xue, P.P. Qian, Layered double hydroxides as efficient photocatalysts for visible-light degradation of Rhodamine B, J Colloid Interface Sci, 405 (2013) 195-200.

[24] D. Chen, Y. Li, J. Zhang, W. Li, J. Zhou, L. Shao, G. Qian, Efficient removal of dyes by a novel magnetic Fe_3O_4/ZnCr-layered double hydroxide adsorbent from heavy metal wastewater, J Hazard Mater, 243 (2012) 152-160.

[25] K.M. Parida, L. Mohapatra, Carbonate intercalated Zn/Fe layered double hydroxide: A novel photocatalyst for the enhanced photo degradation of azo dyes, Chemical Engineering Journal, 179 (2012) 131-139.

[26] Y. Zhu, R. Zhu, G. Zhu, M. Wang, Y. Chen, J. Zhu, Y. Xi, H. He, Plasmonic Ag coated Zn/Ti-LDH with excellent photocatalytic activity, Applied Surface Science, 433 (2018) 458-467.

[27] D. Chen, Y. Li, J. Zhang, J.-z. Zhou, Y. Guo, H. Liu, Magnetic Fe_3O_4/ZnCr-layered double hydroxide composite with enhanced adsorption and photocatalytic activity, Chemical Engineering Journal, 185-186 (2012) 120-126.

[28] L. Mohapatra, K.M. Parida, Zn–Cr layered double hydroxide: Visible light responsive photocatalyst for photocatalytic degradation of organic pollutants, Separation and Purification Technology, 91 (2012) 73-80.

[29] Q. Liu, J. Ma, K. Wang, T. Feng, M. Peng, Z. Yao, C. Fan, S. Komarneni, BiOCl and TiO_2 deposited on exfoliated ZnCr-LDH to enhance visible-light photocatalytic decolorization of Rhodamine B, Ceramics International, 43 (2017) 5751-5758.

[30] P. Roy Chowdhury, K.G. Bhattacharyya, Ni/Ti layered double hydroxide: synthesis, characterization and application as a photocatalyst for visible light degradation of aqueous methylene blue, Dalton Trans, 44 (2015) 6809-6824.

[31] S. Kim, P. Durand, E. André, C. Carteret, Enhanced photocatalytic ability of Cu, Co doped ZnAl based mixed metal oxides derived from layered double hydroxides, Colloids and Surfaces A: Physicochemical and Engineering Aspects, 524 (2017) 43-52.

[32] G. Zhang, L. Hu, R. Zhao, R. Su, Q. Wang, P. Wang, Microwave-assisted synthesis of ZnNiAl-layered double hydroxides with calcination treatment for enhanced PNP photo-degradation under visible-light irradiation, Journal of Photochemistry and Photobiology A: Chemistry, 356 (2018) 633-641.

[33] F. Ji, J. Li, X. Cui, J. Liu, X. Bing, P. Song, Hierarchical C-doped $BiPO_4$ /ZnCoAl-LDO hybrid with enhanced photocatalytic activity for organic pollutants degradation, Applied Clay Science, 162 (2018) 182-191.

[34] J. Wen, J. Xie, X. Chen, X. Li, A review on g-C_3N_4-based photocatalysts, Applied Surface Science, 391 (2017) 72-123.

[35] C.-M. Puscasu, E.M. Seftel, M. Mertens, P. Cool, G. Carja, ZnTiLDH and the Derived Mixed Oxides as Mesoporous Nanoarchitectonics with Photocatalytic Capabilities, Journal of Inorganic and Organometallic Polymers and Materials, 25 (2015) 259-266.

[36] C.M. Puscasu, G. Carja, M. Mureseanu, C. Zaharia, Mixed oxides derived from layered double hydroxides as novel catalysts for phenol photodegradation, IOP Conference Series: Materials Science and Engineering, 227 (2017) 012105, 1-8.

[37] G. Zhao, C. Li, X. Wu, J. Yu, X. Jiang, W. Hu, F. Jiao, Reduced graphene oxide modified NiFe-calcinated layered double hydroxides for enhanced photocatalytic removal of methylene blue, Applied Surface Science, 434 (2018) 251-259.

[38] M. Mureseanu, T. Radu, R.-D. Andrei, M. Darie, G. Carja, Green synthesis of g-C_3N_4/CuONP/LDH composites and derived g-C_3N_4/MMO and their photocatalytic performance for phenol reduction from aqueous solutions, Applied Clay Science, 141 (2017) 1-12.

[39] D. Sánchez-Rodríguez, M.G. Méndez Medrano, H. Remita, V. Escobar-Barrios, Photocatalytic properties of BiOCl-TiO_2 composites for phenol photodegradation, Journal of Environmental Chemical Engineering, 6 (2018) 1601-1612.

[40] X. Yuan, Q. Jing, J. Chen, L. Li, Photocatalytic Cr(VI) reduction by mixed metal oxide derived from ZnAl layered double hydroxide, Applied Clay Science, 143 (2017) 168-174.

[41] Y. Zhao, D. Zhao, C. Chen, X. Wang, Enhanced photo-reduction and removal of Cr(VI) on reduced graphene oxide decorated with TiO_2 nanoparticles, J Colloid Interface Sci, 405 (2013) 211-217.

[42] J. Zhu, P. Xiao, H. Li, S.A. Carabineiro, Graphitic carbon nitride: synthesis, properties, and applications in catalysis, ACS Appl Mater Interfaces, 6 (2014) 16449-16465.

[43] A. Thomas, A. Fischer, F. Goettmann, M. Antonietti, J.-O. Müller, R. Schlögl, J.M. Carlsson, Graphitic carbon nitride materials: variation of structure and morphology and their use as metal-free catalysts, Journal of Materials Chemistry, 18 (2008) 4893-4899.

[44] E. Haque, J.W. Jun, S.N. Talapaneni, A. Vinu, S.H. Jhung, Superior adsorption capacity of mesoporous carbon nitride with basic CN framework for phenol, Journal of Materials Chemistry, 20 (2010) 10801-10803.

[45] J. Liu, W. Li, L. Duan, X. Li, L. Ji, Z. Geng, K. Huang, L. Lu, L. Zhou, Z. Liu, W. Chen, L. Liu, S. Feng, Y. Zhang, A Graphene-like Oxygenated Carbon Nitride Material for Improved Cycle-Life Lithium/Sulfur Batteries, Nano Lett, 15 (2015) 5137-5142.

[46] J. Oh, R.J. Yoo, S.Y. Kim, Y.J. Lee, D.W. Kim, S. Park, Oxidized carbon nitrides: water-dispersible, atomically thin carbon nitride-based nanodots and their performances as bioimaging probes, Chemistry, 21 (2015) 6241-6246.

[47] S.Y. Kim, J. Oh, S. Park, Y. Shim, S. Park, Production of Metal-Free Composites Composed of Graphite Oxide and Oxidized Carbon Nitride Nanodots and Their Enhanced Photocatalytic Performances, Chemistry, 22 (2016) 5142-5145.

[48] L. Ming, H. Yue, L. Xu, F. Chen, Hydrothermal synthesis of oxidized g-C_3N_4 and its regulation of photocatalytic activity, J. Mater. Chem. A, 2 (2014) 19145-19149.

[49] G. Dong, Z. Ai, L. Zhang, Efficient anoxic pollutant removal with oxygen functionalized graphitic carbon nitride under visible light, RSC Advances, 4 (2014) 5553-5560.

[50] H.J. Li, B.W. Sun, L. Sui, D.J. Qian, M. Chen, Preparation of water-dispersible porous g-C_3N_4 with improved photocatalytic activity by chemical oxidation, Phys Chem Chem Phys, 17 (2015) 3309-3315.

[51] F. Dong, Z. Zhao, T. Xiong, Z. Ni, W. Zhang, Y. Sun, W.K. Ho, In situ construction of g-C_3N_4/g-C_3N_4 metal-free heterojunction for enhanced visible-light photocatalysis, ACS Appl Mater Interfaces, 5 (2013) 11392-11401.

[52] L. Fu, X. Xiao, A. Wang, Reduced graphene oxide coupled with g-C_3N_4 nanodots as 2D/0D nanocomposites for enhanced photocatalytic activity, Journal of Physics and Chemistry of Solids, 122 (2018) 104-108.

[53] Y. Zheng, Z. Yu, F. Lin, F. Guo, K.A. Alamry, L.A. Taib, A.M. Asiri, X. Wang, Sulfur-Doped Carbon Nitride Polymers for Photocatalytic Degradation of Organic Pollutant and Reduction of Cr(VI), Molecules, 22 (2017) 572, 1-17.

[54] R. You, H. Dou, L. Chen, S. Zheng, Y. Zhang, Graphitic carbon nitride with S and O codoping for enhanced visible light photocatalytic performance, RSC Advances, 7 (2017) 15842-15850.

[55] D.B. Hernández-Uresti, A. Vázquez, D. Sanchez-Martinez, S. Obregón, Performance of the polymeric g-C_3N_4 photocatalyst through the degradation of pharmaceutical pollutants under UV–vis irradiation, Journal of Photochemistry and Photobiology A: Chemistry, 324 (2016) 47-52.

[56] B. Luo, M. Chen, Z. Zhang, J. Xu, D. Li, D. Xu, W. Shi, Highly efficient visible-light-driven photocatalytic degradation of tetracycline by a Z-scheme g-C_3N_4/Bi_3TaO_7 nanocomposite photocatalyst, Dalton Trans, 46 (2017) 8431-8438.

[57] M. Jourshabani, Z. Shariatinia, A. Badiei, Sulfur-Doped Mesoporous Carbon Nitride Decorated with Cu Particles for Efficient Photocatalytic Degradation under Visible-Light Irradiation, The Journal of Physical Chemistry C, 121 (2017) 19239-19253.

[58] X. Dong, Z. Sun, X. Zhang, C. Li, S. Zheng, Construction of BiOCl/g-C_3N_4 /kaolinite composite and its enhanced photocatalysis performance under visible-light irradiation, Journal of the Taiwan Institute of Chemical Engineers, 84 (2018) 203-211.

[59] J. Zhang, N. Gao, F. Chen, T. Zhang, G. Zhang, D. Wang, X. Xie, D. Cai, X. Ma, L. Wu, Z. Wu, Improvement of Cr (VI) photoreduction under visible-light by g-C_3N_4 modified by nano-network structured palygorskite, Chemical Engineering Journal, 358 (2019) 398-407.

[60] C. Li, Z. Sun, W. Huang, S. Zheng, Facile synthesis of g-C_3N_4/montmorillonite composite with enhanced visible light photodegradation of rhodamine B and tetracycline, Journal of the Taiwan Institute of Chemical Engineers, 66 (2016) 363-371.

[61] J. Xu, Y. Qi, W. Wang, L. Wang, Montmorillonite-hybridized g-C_3N_4 composite modified by NiCoP cocatalyst for efficient visible-light-driven photocatalytic hydrogen evolution by dye-sensitization, International Journal of Hydrogen Energy, 44 (2019) 4114-4122.

[62] A. Mishra, A. Mehta, S. Kainth, S. Basu, Effect of g-C_3N_4 loading on TiO_2/Bentonite nanocomposites for efficient heterogeneous photocatalytic

degradation of industrial dye under visible light, Journal of Alloys and Compounds, 764 (2018) 406-415.

[63] Z. Sun, X. Zhang, R. Zhu, X. Dong, J. Xu, B. Wang, Facile Synthesis of Visible Light-Induced g-C_3N_4/Rectorite Composite for Efficient Photodegradation of Ciprofloxacin, Materials (Basel), 11 (2018) 2452, 1-15.

[64] A. Akhundi, A. Habibi-Yangjeh, Ternary magnetic g-C_3N_4/Fe_3O_4/AgI nanocomposites: Novel recyclable photocatalysts with enhanced activity in degradation of different pollutants under visible light, Materials Chemistry and Physics, 174 (2016) 59-69.

[65] N. Boonprakob, N. Wetchakun, S. Phanichphant, D. Waxler, P. Sherrell, A. Nattestad, J. Chen, B. Inceesungvorn, Enhanced visible-light photocatalytic activity of g-C_3N_4/TiO_2 films, J Colloid Interface Sci, 417 (2014) 402-409.

[66] Z. Wei, F. Liang, Y. Liu, W. Luo, J. Wang, W. Yao, Y. Zhu, Photoelectrocatalytic degradation of phenol-containing wastewater by TiO_2/g-C_3N_4 hybrid heterostructure thin film, Applied Catalysis B: Environmental, 201 (2017) 600-606.

[67] M. Epifani, S. Kaciulis, A. Mezzi, D. Altamura, C. Giannini, R. Díaz, C. Force, A. Genç, J. Arbiol, P. Siciliano, E. Comini, I. Concina, Inorganic Photocatalytic Enhancement: Activated RhB Photodegradation by Surface Modification of SnO_2 Nanocrystals with V_2O_5-like species, Scientific Reports, 7 (2017) 44763-44770.

[68] D. Xiao, K. Dai, Y. Qu, Y. Yin, H. Chen, Hydrothermal synthesis of α-Fe_2O_3/g-C_3N_4 composite and its efficient photocatalytic reduction of Cr(VI) under visible light, Applied Surface Science, 358 (2015) 181-187.

[69] X. Yuan, C. Zhou, Q. Jing, Q. Tang, Y. Mu, A.K. Du, Facile Synthesis of g-C_3N_4 Nanosheets/ZnO Nanocomposites with Enhanced Photocatalytic Activity in Reduction of Aqueous Chromium(VI) under Visible Light, Nanomaterials (Basel), 6 (2016) 173, 1-12.

[70] S. Nayak, K.M. Parida, Dynamics of Charge-Transfer Behavior in a Plasmon-Induced Quasi-Type-II p–n/n–n Dual Heterojunction in Ag@Ag_3PO_4/g-C_3N_4/NiFe LDH Nanocomposites for Photocatalytic Cr(VI) Reduction and Phenol Oxidation, ACS Omega, 3 (2018) 7324-7343.

[71] Z. Zeng, K. Li, K. Wei, Y. Dai, L. Yan, H. Guo, X. Luo, Fabrication of porous g-C_3N_4 and supported porous g-C_3N_4 by a simple precursor pretreatment strategy and

their efficient visible-light photocatalytic activity, Chinese Journal of Catalysis, 38 (2017) 498-507.

[72] M. Jourshabani, Z. Shariatinia, G. Achari, C.H. Langford, A. Badiei, Facile synthesis of NiS_2 nanoparticles ingrained in a sulfur-doped carbon nitride framework with enhanced visible light photocatalytic activity: two functional roles of thiourea, Journal of Materials Chemistry A, 6 (2018) 13448-13466.

[73] S. Hu, L. Ma, Y. Xie, F. Li, Z. Fan, F. Wang, Q. Wang, Y. Wang, X. Kang, G. Wu, Hydrothermal synthesis of oxygen functionalized S-P codoped g-C_3N_4 nanorods with outstanding visible light activity under anoxic conditions, Dalton Trans, 44 (2015) 20889-20897.

[74] F. Wei, Y. Liu, H. Zhao, X. Ren, J. Liu, T. Hasan, L. Chen, Y. Li, B.L. Su, Oxygen self-doped g-C_3N_4 with tunable electronic band structure for unprecedentedly enhanced photocatalytic performance, Nanoscale, 10 (2018) 4515-4522.

[75] Z. Sun, C. Li, X. Du, S. Zheng, G. Wang, Facile synthesis of two clay minerals supported graphitic carbon nitride composites as highly efficient visible-light-driven photocatalysts, J Colloid Interface Sci, 511 (2018) 268-276.

[76] P. Li, L. Huang, Y. Li, Y. Xu, S. Huang, D. Yuan, H. Xu, H. Li, Synthesis of dark orange montmorillonite/g-C_3N_4 composites and their applications in the environment, Journal of Physics and Chemistry of Solids, 107 (2017) 131-139.

[77] G. Darabdhara, M.R. Das, Bimetallic Au-Pd nanoparticles on 2D supported graphitic carbon nitride and reduced graphene oxide sheets: A comparative photocatalytic degradation study of organic pollutants in water, Chemosphere, 197 (2018) 817-829.

[78] S. Wang, D. Li, C. Sun, S. Yang, Y. Guan, H. He, Synthesis and characterization of g-C_3N_4/Ag_3VO_4 composites with significantly enhanced visible-light photocatalytic activity for triphenylmethane dye degradation, Applied Catalysis B: Environmental, 144 (2014) 885-892.

[79] K. Saravanakumar, R. Karthik, S.M. Chen, J. Vinoth Kumar, K. Prakash, V. Muthuraj, Construction of novel Pd/CeO_2/g-C_3N_4 nanocomposites as efficient visible-light photocatalysts for hexavalent chromium detoxification, J Colloid Interface Sci, 504 (2017) 514-526.

[80] Z. Sun, F. Yuan, X. Li, C. Li, J. Xu, B. Wang, Fabrication of Novel Cyanuric Acid Modified g-C_3N_4/Kaolinite Composite with Enhanced Visible Light-Driven Photocatalytic Activity, Minerals, 8 (2018) 437, 1-15.

[81] Y. Zhang, J. Wu, Y. Deng, Y. Xin, H. Liu, D. Ma, N. Bao, Synthesis and visible-light photocatalytic property of Ag/GO/g-C_3N_4 ternary composite, Materials Science and Engineering: B, 221 (2017) 1-9.

[82] M. Wang, Y. Zhang, C. Jin, Z. Li, T. Chai, T. Zhu, Fabrication of novel ternary heterojunctions of Pd/g-C_3N_4/Bi_2MoO_6 hollow microspheres for enhanced visible-light photocatalytic performance toward organic pollutant degradation, Separation and Purification Technology, 211 (2019) 1-9.

[83] J. Xue, S. Ma, Y. Zhou, Z. Zhang, M. He, Facile Photochemical Synthesis of Au/Pt/g-C_3N_4 with Plasmon-Enhanced Photocatalytic Activity for Antibiotic Degradation, ACS Appl Mater Interfaces, 7 (2015) 9630-9637.

[84] C.H. Hak, L.C. Sim, K.H. Leong, P.F. Lim, Y.H. Chin, P. Saravanan, M/g-C_3N_4 (M=Ag, Au, and Pd) composite: synthesis via sunlight photodeposition and application towards the degradation of bisphenol A, Environ Sci Pollut Res Int, 25 (2018) 25401-25412.

[85] Q. Tang, F. Wang, M. Tang, J. Liang, C. Ren, Study on Pore Distribution and Formation Rule of Sepiolite Mineral Nanomaterials, Journal of Nanomaterials, 2012 (2012) 1-6.

[86] X. Hu, Z. Sun, J. Song, G. Zhang, C. Li, S. Zheng, Synthesis of novel ternary heterogeneous BiOCl/TiO_2/sepiolite composite with enhanced visible-light-induced photocatalytic activity towards tetracycline, J Colloid Interface Sci, 533 (2019) 238-250.

[87] M. Akkari, P. Aranda, C. Belver, J. Bedia, A. Ben Haj Amara, E. Ruiz-Hitzky, ZnO/sepiolite heterostructured materials for solar photocatalytic degradation of pharmaceuticals in wastewater, Applied Clay Science, 156 (2018) 104-109.

[88] L. Jin, H.-Y. Zeng, S. Xu, C.-R. Chen, H.-Z. Duan, J.-Z. Du, G. Hu, Y.-X. Sun, Facile preparation of sepiolite@LDH composites for the visible-light degradation of organic dyes, Chinese Journal of Catalysis, 39 (2018) 1832-1841.

[89] F. Zhou, C. Yan, T. Liang, Q. Sun, H. Wang, Photocatalytic degradation of Orange G using sepiolite-TiO_2 nanocomposites: Optimization of physicochemical parameters and kinetics studies, Chemical Engineering Science, 183 (2018) 231-239.
[90] M. Akkari, P. Aranda, A. Mayoral, M. Garcia-Hernandez, A. Ben Haj Amara, E. Ruiz-Hitzky, Sepiolite nanoplatform for the simultaneous assembly of magnetite and zinc oxide nanoparticles as photocatalyst for improving removal of organic pollutants, J Hazard Mater, 340 (2017) 281-290.
[91] W.G. Xu, S.F. Liu, S.X. Lu, S.Y. Kang, Y. Zhou, H.F. Zhang, Photocatalytic degradation in aqueous solution using quantum-sized ZnO particles supported on sepiolite, J Colloid Interface Sci, 351 (2010) 210-216.
[92] Y. Zhang, D. Wang, G. Zhang, Photocatalytic degradation of organic contaminants by TiO_2/sepiolite composites prepared at low temperature, Chemical Engineering Journal, 173 (2011) 1-10.
[93] M. Uğurlu, M.H. Karaoğlu, TiO_2 supported on sepiolite: Preparation, structural and thermal characterization and catalytic behaviour in photocatalytic treatment of phenol and lignin from olive mill wastewater, Chemical Engineering Journal, 166 (2011) 859-867.
[94] E. Maina, H. Wanyika, A. Gacanja, Natural Pyrethrum Extracts Photo-stabilized with Organo Clays, Journal of Scientific Research and Reports, 9 (2016) 1-20.
[95] B. Damardji, H. Khalaf, L. Duclaux, B. David, Preparation of TiO_2-pillared montmorillonite as photocatalyst Part I. Microwave calcination, characterisation, and adsorption of a textile azo dye, Applied Clay Science, 44 (2009) 201-205.
[96] B. Damardji, H. Khalaf, L. Duclaux, B. David, Preparation of TiO_2-pillared montmorillonite as photocatalyst Part II, Applied Clay Science, 45 (2009) 98-104.
[97] B. González, R. Trujillano, M.A. Vicente, V. Rives, S.A. Korili, A. Gil, Photocatalytic degradation of trimethoprim on doped Ti-pillared montmorillonite, Applied Clay Science, 167 (2019) 43-49.
[98] O. Kozak, P. Praus, K. Koci, M. Klementova, Preparation and characterization of ZnS nanoparticles deposited on montmorillonite, J Colloid Interface Sci, 352 (2010) 244-251.

[99] Y. Wang, J. Xu, J. Li, F. Wu, Natural montmorillonite induced photooxidation of As(III) in aqueous suspensions: roles and sources of hydroxyl and hydroperoxyl/superoxide radicals, J Hazard Mater, 260 (2013) 255-262.

[100] J. Liu, M. Dong, S. Zuo, Y. Yu, Solvothermal preparation of TiO_2/montmorillonite and photocatalytic activity, Applied Clay Science, 43 (2009) 156-159.

[101] N. Fajrina, M. Tahir, 2D-montmorillonite-dispersed g-C_3N_4/TiO_2 2D/0Dnanocomposite for enhanced photo-induced H_2 evolution from glycerol-water mixture, Applied Surface Science, 471 (2019) 1053-1064.

[102] Z. Sun, G. Yao, X. Zhang, S. Zheng, R.L. Frost, Enhanced visible-light photocatalytic activity of kaolinite/g-C_3N_4 composite synthesized via mechanochemical treatment, Applied Clay Science, 129 (2016) 7-14.

[103] R. Djellabi, M.F. Ghorab, C.L. Bianchi, G. Cerrato, S. Morandi, Recovery of hexavalent chromium from water using photoactive TiO_2-montmorillonite under sunlight, Mediterranean Journal of Chemistry, 5 (2016) 442-449.

[104] L. Guishui, C. Lijun, Z. Bing, L. Yi, Novel Bi_2O_3 loaded sepiolite photocatalyst: Preparation and characterization, Materials Letters, 168 (2016) 143-145.

[105] F. Zhou, C.J. Yan, T. Liang, Q. Sun, H.Q. Wang, Photocatalytic degradation of Orange G using sepiolite-TiO_2 nanocomposites: Optimization of physicochemical parameters and kinetics studies, Chemical Engineering Science, 183 (2018) 231-239.

[106] P.S. Wang, C.X. Qi, L.Y. Hao, P.C. Wen, X. Xu, Sepiolite/Cu_2O/Cu photocatalyst: Preparation and high performance for degradation of organic dye, Journal of Materials Science & Technology, 35 (2019) 285-291.

[107] F. Zhou, C.J. Yan, Q. Sun, S. Komarneni, TiO_2/Sepiolite nanocomposites doped with rare earth ions: Preparation, characterization and visible light photocatalytic activity, Microporous and Mesoporous Materials, 274 (2019) 25-32.

[108] L. Jin, H.Y. Zeng, S. Xu, C.R. Chen, H.Z. Duan, J.Z. Du, G. Hu, Y.X. Sun, Facile preparation of sepiolite@LDH composites for the visible-light degradation of organic dyes, Chinese Journal of Catalysis, 39 (2018) 1832-1841.

[109] D. Papoulis, D. Panagiotaras, P. Tsigrou, K.C. Christoforidis, C. Petit, A. Apostolopoulou, E. Stathatos, S. Komarneni, I. Koukouvelas, Halloysite and sepiolite

–TiO_2 nanocomposites: Synthesis characterization and photocatalytic activity in three aquatic wastes, Materials Science in Semiconductor Processing, 85 (2018) 1-8.
[110] C. Chuaicham, R. Pawar, K. Sasaki, Dye-sensitized Photocatalyst of Sepiolite for Organic Dye Degradation, Catalysts, 9 (2019) 235, 1-16.
[111] Y. Ye, Y. Feng, H. Bruning, D. Yntema, H.H.M. Rijnaarts, Photocatalytic degradation of metoprolol by TiO_2 nanotube arrays and UV-LED: Effects of catalyst properties, operational parameters, commonly present water constituents, and photo-induced reactive species, Applied Catalysis B: Environmental, 220 (2018) 171-181.
[112] Y. Wang, Z. Yan, X. Wang, Photocatalytic Degradation of Rhodamine B Dye over Novel Porous TiO_2-SnO_2 Nanocomposites Prepared by Hydrothermal Method, International Journal of Photoenergy, 2014 (2014) 1-7.
[113] D.A. Jahagirdar, Z. Ahmed, N. Donappa, N. Bhushana, B. Nagabhushana, Photocatalytic degradation of rhodamine B using nanocrystalline α-Fe_2O_3, Journal of Material and Environmental Sciences, 5 (2014) 1426-1433.
[114] A.I. Borhan, P. Samoila, V. Hulea, A.R. Iordan, M.N. Palamaru, Effect of Al^{3+} substituted zinc ferrite on photocatalytic degradation of Orange I azo dye, Journal of Photochemistry and Photobiology A Chemistry, 279 (2014) 17-23.
[115] P. Nuengmatcha, S. Chanthai, R. Mahachai, W.-C. Oh, Visible light-driven photocatalytic degradation of rhodamine B and industrial dyes (texbrite BAC-L and texbrite NFW-L) by ZnO-graphene-TiO_2 composite, Journal of Environmental Chemical Engineering, 4 (2016) 2170-2177.
[116] X. Li, Y. Hou, Q. Zhao, L. Wang, A general, one-step and template-free synthesis of sphere-like zinc ferrite nanostructures with enhanced photocatalytic activity for dye degradation, J Colloid Interface Sci, 358 (2011) 102-108.
[117] D.R. Shinde, P.S. Tambade, M.G. Chaskar, K.M. Gadave, Photocatalytic degradation of dyes in water by analytical reagent grades ZnO: a comparative study, Drinking Water Engineering and Science, 10 (2017) 109-117.
[118] S.J. Kulkarni, J.P. Kaware, Review on research for removal of Phenol from wastewater, Inter. J. Sci. Res. Publ, 3 (2013) 1-4.
[119] J. Prince, F. Tzompantzi, G. Mendoza-Damián, F. Hernández-Beltrán, J.S. Valente, Photocatalytic degradation of phenol by semiconducting mixed oxides

derived from Zn(Ga)Al layered double hydroxides, Applied Catalysis B: Environmental, 163 (2015) 352-360.

[120] A.C. Mecha, M.S. Onyango, A. Ochieng, C.J.S. Fourie, M.N.B. Momba, Synergistic effect of UV–vis and solar photocatalytic ozonation on the degradation of phenol in municipal wastewater: A comparative study, Journal of Catalysis, 341 (2016) 116-125.

[121] K. Intarasuwan, P. Amornpitoksuk, S. Suwanboon, P. Graidist, S. Maungchanburi, C. Randorn, Effect of Ag loading on activated carbon doped ZnO for bisphenol A degradation under visible light, Advanced Powder Technology, 29 (2018) 2608-2615.

[122] B. Xie, H. Zhang, P. Cai, R. Qiu, Y. Xiong, Simultaneous photocatalytic reduction of Cr(VI) and oxidation of phenol over monoclinic $BiVO_4$ under visible light irradiation, Chemosphere, 63 (2006) 956-963.

[123] X. Zhang, L. Song, X. Zeng, M. Li, Effects of Electron Donors on the TiO_2 Photocatalytic Reduction of Heavy Metal Ions under Visible Light, Energy Procedia, 17 (2012) 422-428.

[124] S.G. Schrank, H.J. José, R.F.P.M. Moreira, Simultaneous photocatalytic Cr(VI) reduction and dye oxidation in a TiO_2 slurry reactor, Journal of Photochemistry and Photobiology A: Chemistry, 147 (2002) 71-76.

Chapter 2

Methodology

2.1 Characterization methods

2.1.1 X-ray diffraction (XRD)

The crystal phases of the original and the composite materials were characterized by powder X-ray diffraction (PXRD) on Ultima IV diffractometer (Rigaku, Akishima, Japan), using Cu Kα radiation with 40 kV acceleration voltage and 40 mA applied current at a 2°/min scanning speed and 0.02° step size. Obtained XRD patterns were identified based on International Centre for Diffraction Data (ICDD) using powder diffraction analysis software PDXL (Rigaku).

2.1.2 X-ray fluorescence spectroscopy (XRF)

The elemental compositions of sepiolite were determined by X-ray fluorescence (XRF) spectroscopy Rigaku ZSX Primus II in the wavelength dispersive mode (Akishima, Japan). The experimental conditions are the Rh-anode, 3kW or 4 kW, 60kV, and wavelength dispersive type.

2.1.3 Scanning electron microscopy (SEM)

Morphology of the synthetic products were observed on a scanning electron microscopy (VE-9800, KEYENCE). The sample preparation for SEM observation were fixed on carbon tape, and Au-Pd magnetron sputtered (MSP-1S, Vacuum Device). Magnification was optimized based on the required image observation.

2.1.4 Transmission electron microscopy (TEM-EDX)

TEM images of the original and composite samples were observed on a transmission electron microscope (JEM-2100HCKM, JEOL (Akishima, Japan). The sample preparation for TEM observation was prepared by the grid dispersion method. The solid sample was dispersed with ethanol. After sonication for 20 minutes to minimize aggregation, the suspension was dropped on the Cu grid and completely dried at room temperature in a desiccator for 2 h.

2.1.5 Fourier transforms infrared spectroscopy (FT-IR)

The functional groups of the original and the composite materials were characterized by FTIR on Jasco FTIR-670 Plus (Tokyo, Japan). FT-IR spectra of precipitates were obtained by KBr pellet method (sample 1% (w/v)) using FT/IR-670 (JASCO) in the range of 360–4000 cm^{-1} (resolution: 4 cm^{-1}).

2.1.6 Specific surface area (BET method)

The specific surface area of original and composite samples was measured using the BET (Brunauer–Emmett–Teller) theory (BEL-Max, Microtrac BEL) based on adsorption isotherms using N_2 gas at −196°C. Adsorbed water and gases were removed under vacuum at 150°C for 10 hours before measurement.

2.1.7 UV–vis diffuse reflectance spectroscopy (DRS)

The light absorption and optical properties of synthetic products were UV–vis diffuse reflectance spectroscopy (DRS). The sample was pressed into a sample cup using a glass rod, and with the sample cup placed in the ISR-2600Plus integrating sphere attachment, the diffuse reflectance was measured from 350nm - 800 nm, using barium sulfate as the standard, scan speed medium, 5 nm step width, 1.0 nm sampling pitch.

2.1.8 Fluorescence spectroscopy (PL)

Photoluminescence spectroscopy is a useful technique to investigate the efficiency of photogenerated charge carries separation and lifetime of the photocatalyst. In basically, the low PL intensity may indicate low recombination of photogenerated electron and hole during light irradiation. In the experiment, the solid sample was pressed into a sample holder, and placed in the FP-6600 spectrofluorometer (JASCO, Tokyo, Japan), the Photoluminescence spectrum was measured from 300nm - 600 nm, using emission spectrum mode, Excitation wavelength in the range of 330 - 400 nm.

2.1.9 X-ray photoelectron spectroscopy (XPS)

The X-ray photoelectron spectroscopy (XPS) for the essential materials were collected on an ESCA 5800 (ULVAC-PHI, Inc. Kanagawa, Japan) using a monochromated Al Kα X-ray source at 200 W. The data analysis was performed by

Casa XPS software (version 2.3.12.8). Binding energy was calibrated using E_B[C 1s] = 284.6 eV assigned to the contamination peak derived from vacuum oil in the apparatus. The shirley background was used in the analysis. A line is drawn tangent to the point of inflection on the curve of XPS spectrum, and the binding energy at the point of intersection of the tangent line and the horizontal axis is the valence band.

2.1.10 Reversed double-beam photoacoustic spectroscopy (RDB-PAS)

Reversed double-beam photoacoustic spectroscopy (RDB-PAS) is a powerful technique to characterization of metal-oxide, including crystallinity and amorphous phase [1]. This method has used for the identification of metal-oxide in the solid phase by observation of the pattern of energy-resolved distribution of electron traps (ERDT), combined with conduction band bottom position (CBB). For a brief principle of this technique, the electron from the valence-band (VB) was excited by continuous scanned light and accumulated in the electron trap (ETs). During the irradiation of continuous scanned light, the photoacoustic signal (PA) was detected by modulated LED light (625nm), and the signal intensity was converted to the absolute density of ETs. The obtained ERDT include the surface structure and bulk structure, which may be the characteristic of metal oxide. The combined result of ERDT with CBB was used as a fingerprint of metal oxide, based on the degree of a coincidence for a given pair of samples. In this work, the RDB-PAS technique was used for investigation the ZnTi mixed metal oxide samples from different preparation condition in order to understand the phase component, including amorphous phase which cannot be observed by XRD

technique. The novel reversed double-beam photoacoustic spectroscopy (RDB-PAS) technique was utilized for characterizing energy resolved distribution of electron trap (ERDT) patterns of the composites. In details, 200 mg of powder sample was set into a PAS cell equipped with an electret condenser microphone and a quartz window. Moreover, the upper side under N_2 flow was saturated with methanol vapor for at least 30 min, and a light beam from a xenon lamp with a grating monochromator modulated at 80 Hz. A light chopper was irradiated from 650 nm to 350 nm through the cell window to detect the PAS signal using a digital lock-in amplifier, and then photoacoustic (PA) spectra were recorded concerning a PA spectrum of graphite for calibration. ERDT pattern can be obtained by determining the amount of photo-absorption change for accumulated electrons. The setup for RDB-PAS was as follows (Fig. 2.1).

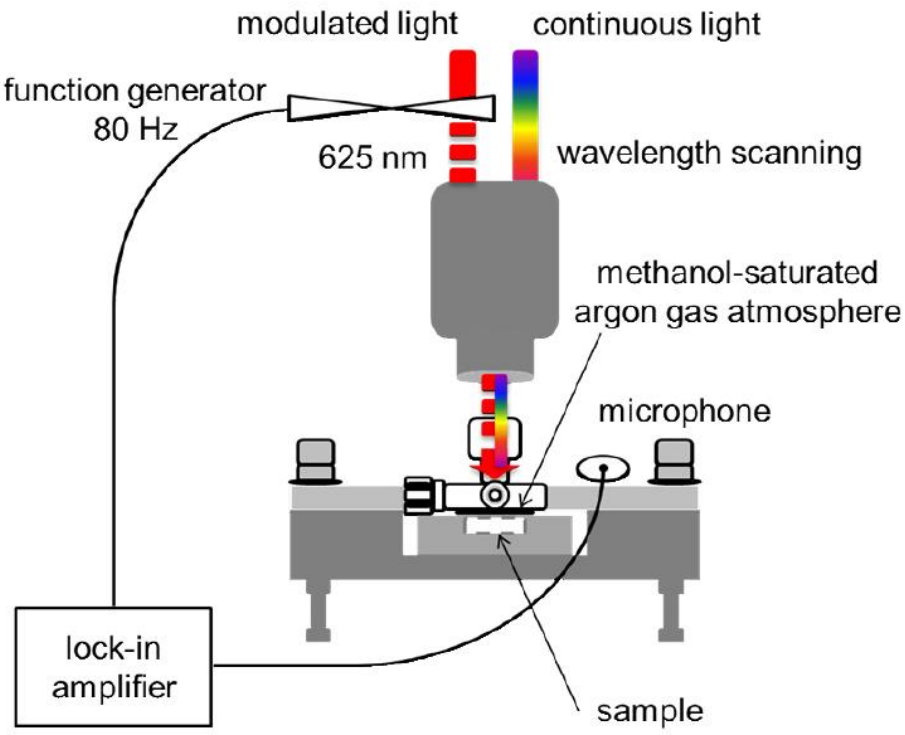

Fig. 2.1 Schematic representation of the setup for RDB-PAS [1].

2.2 Photocatalytic reaction tests

The photocatalytic performances of the original and developed composites were evaluated under the UV or visible light ($\lambda > 400$ nm) irradiation by using filter cut-off. In details, the synthesized composite was added into the wastewater solution and was magnetically stirred in the dark condition for 30 min to reach the adsorption-desorption equilibrium. The suspensions were then irradiated using a 500 W Xe lamp with or without a cut-off filter. During the light illumination, the wastewater solutions were collected and filtrated by 0.45 µm membrane filters to remove the suspended particles. The concentrations of the remaining concentration of pollutant were determined. The photocatalytic experimental setup was shown in **Fig. 2.2**.

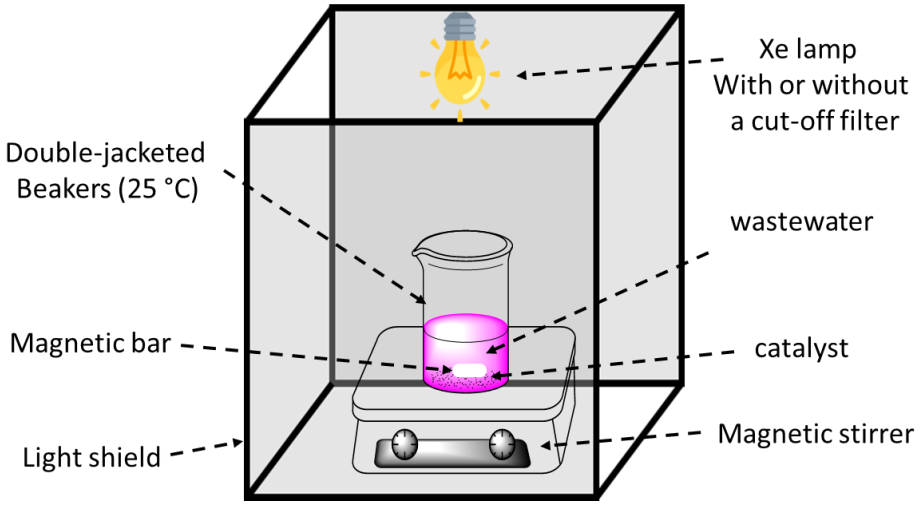

Fig. 2.2 Schematic of the photocatalytic experimental setup.

2.3 Hexavalent chromium determination

The concentration of hexavalent chromium determination was determined by Diphenylcarbazide method [2]. For the measurement, 30 µL of 1.8 M H_2SO_4 was added to some wells of 96-well measuring plate, following by adding 30 µL of liquid

Cr(VI) samples to the wells. Then, 30 µL of the mixed reagent of diphenyl carbazide solution (1% (w/v) 1, 5 diphenyl carbon hydrazide and 60% (v/v) acetone solubilized in distilled water) was added to the wells and adjusted the total volume to 300 µL by distilled water. The mixture was shacked for 10 min and measured absorbance at 530 nm using spectrophotometer (Multiskan Go, Thermo Scientific).

2.4 Radical scavenger tests

The role of reactive species, superoxide radical ($^{\cdot}O_2^-$), hydroxyl radical ($^{\cdot}OH$) and hole (h^+), in photocatalytic degradation of RhB under visible light irradiation were examined through the radical scavenger tests [2]. The 0.1 mmol of isopropyl alcohol (IPA), p-benzoquinone (BQ) and ethylenediaminetetraacetic acid disodium salt (EDTA-2Na) were added to the RhB solution in order to remove the superoxide radical ($^{\cdot}O_2^-$), hydroxyl radical ($^{\cdot}OH$) and hole (h^+), respectively. The trapping reaction of each scavenger was shown in **equation 2.1-2.3.**

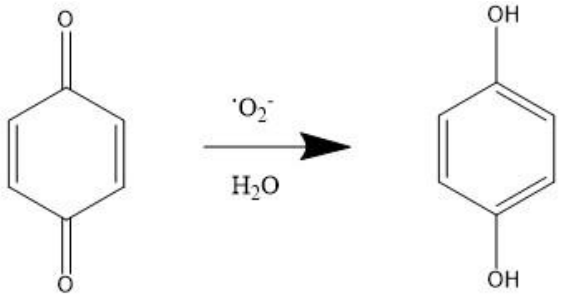

(2.1)

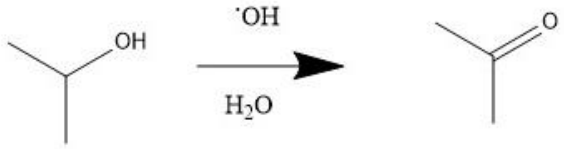

(2.2)

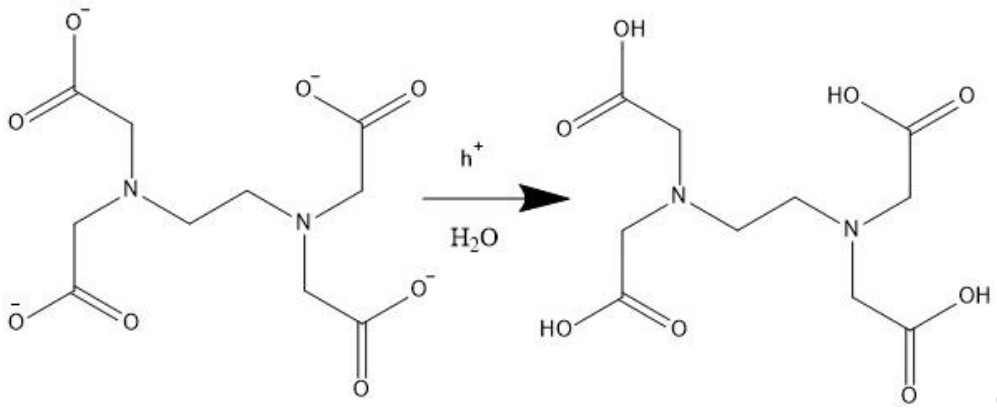

(2.3)

2.5 Band gap energy (*E*g) calculation

The band gap energy (*E*g) of a semiconductor photocatalyst can be evaluated by using the Kubelka–Munk equation [3]:

$$\alpha h\nu = A\,(h\nu - Eg)^{n/2} \tag{2.4}$$

where α, *h*, ν, *E*g, and *A* are the absorption coefficient, Planck constant, light frequency, band gap energy, and the proportionality constant, respectively. In addition, *n* is dependent on the type of optical transition of semiconductor (*n* = 1 for direct transition and *n* = 4 for indirect transition). The band gap energy value was calculated by the linear part of the $(\alpha h\nu)^2$ versus energy (*E*g) plot.

2.6 Kinetic calculation

To evaluate the kinetics of photocatalytic reaction, the photocatalytic removal results after the light irradiation were fitted to the pseudo-first-order equation (Equation (2)):

$$\ln\left(\frac{C_t}{C_0}\right) = kt \tag{2.5}$$

where C_0 is the initial concentration of organic poluutant or Cr(VI), C is the remaining concentration of organic poluutant or Cr(VI) at time t (min), and k is the pseudo-first-order rate constant (min^{-1}) [4-6]. The plots of reaction time (t) versus $-\ln(C/C_0)$ provided a linear line.

References

[1] A. Nitta, M. Takase, M. Takashima, N. Murakami, B. Ohtani, A fingerprint of metal-oxide powders: energy-resolved distribution of electron traps, Chem Commun (Camb), 52 (2016) 12096-12099.

[2] M. Noroozifar, M. Khorasani-Motlagh, Specific extraction of chromium as tetrabutylammonium-chromate and spectrophotometric determination by diphenylcarbazide: Speciation of chromium in effluent streams, Anal Sci, 19 (2003) 705-708.

[3] T. Liu, L. Wang, X. Lu, J. Fan, X. Cai, B. Gao, R. Miao, J. Wang, Y. Lv, Comparative study of the photocatalytic performance for the degradation of different dyes by $ZnIn_2S_4$: adsorption, active species, and pathways, RSC Advances, 7 (2017) 12292-12300.

[4] Z. Li, M. Chen, Z.Q. Ai, L. Wu, Q.W. Zhang, Mechanochemical synthesis of CdS/MgAl LDH-precursor as improved visible-light driven photocatalyst for organic dye, Applied Clay Science, 163 (2018) 265-272.

[5] Q. Feng, S.Y. Li, W.H. Ma, H.J. Fan, X.H. Wan, Y. Lei, Z.J. Chen, J. Yang, B. Qin, Synthesis and characterization of Fe_3O_4/ZnO-GO nanocomposites with improved

photocatalytic degradation methyl orange under visible light irradiation, Journal of Alloys and Compounds, 737 (2018) 197-206.

[6] Z. Wei, D. Benlin, Z. Fengxia, T. Xinyue, X. Jiming, Z. Lili, L. Shiyin, D.Y.C. Leung, C. Sun, A novel 3D plasmonic p-n heterojunction photocatalyst: Ag nanoparticles on flower-like p-Ag_2S/n-$BiVO_4$ and its excellent photocatalytic reduction and oxidation activities, Applied Catalysis B: Environmental, 229 (2018) 171-180.

[7] F. Xu, H. Chen, C. Xu, D. Wu, Z. Gao, Q. Zhang, K. Jiang, Ultra-thin Bi_2WO_6 porous nanosheets with high lattice coherence for enhanced performance for photocatalytic reduction of Cr(VI), J Colloid Interface Sci, 525 (2018) 97-106.

Chapter 3

A Z-scheme of 2D/2D ZnTi layered double hydroxide/Fe-contained montmorillonite heterojunction with improved photocatalytic reduction of Cr (VI)

3.1. Introduction

Now a day, the rapid development of industry and technology produce a toxic chemical into water and soil, leading to being environmental problems. Hexavalent chromium ((Cr(VI)) which are released from manufacturing is very toxic heavy metal, causing the carcinogenic and mutagenic, whereas Cr(III) species is less toxic and mobility in water [1]. The wastewater containing Cr(VI) is not only appealingly offensive but also responsible for the adverse effect on the aquatic biota and public health. Hence, considering the negative impact on the planet and subsequent hazards to public well-being. The treatment of Cr(VI) containing wastewater before discharge in the environment by the development of an effective and economical technique is an alarming research subject for different fields of researchers. The appropriate way for Cr(VI) remediation in wastewater is the reduction of Cr(VI) to Cr(III). Various methods have been utilized for the treatment of the toxic Cr(VI) in an aqueous solution such as adsorption, precipitation, microbial, and membrane filtration. Nevertheless, all these techniques have some benefits and limitations involving high operating costs, incapability to treatment pollutants totally, difficulties in the development of actual industrial arrangement. Photocatalysis is a remarkable methodology for Cr(VI) reduction in recent years due to mild temperature/ pressure conditions, low cost, and environmentally friendly. The requirements in the photocatalysis is a semiconductor material that can produce electron-hole pair during light irradiation. The excited electron can be applied as a redox system for Cr(VI) reduction in water.

Several materials are used as photocatalysts such as TiO_2 and ZnO. However, there is some disadvantage related to the use of pure semiconductor material as photocatalyst like charge carrier recombination. To overcome on these restrictions, a

composite of two kinds of two-dimensional material (2D/2D) photocatalyst composite has been focused on the environmental application because it has high contract area which can avoid the photogenerated charge recombination thought the charge transfer between a couple of materials [2-4].

Layered double hydroxide (LDH) has been widely used as a photocatalyst for photocatalytic oxidation of organic pollutant and photocatalytic of heavy metal in wastewater. LDH is a class of two-dimensional anionic clay which can be expressed by the general formula $[M^{2+}_{1-x}M^{3+}_{x}(OH)_2]^{z+}(A^n)_{z/n}\cdot yH_2O$ (M^{2+} and M^{3+}, divalent and trivalent metal cations respectively; A^n is the interlayer anion between the layer compensating for positive charge of the layer) [5, 6]. Zinc and titanium contained in the octahedral sheet of LDH have extensively used as photocatalyst for wastewater treatment and water-splitting [7-9]. However, the similar problem of photocatalyst also happen in LDH materials, the high recombination rate of electron and hole. Thus, the formation of heterojunction between LDH and another material has been performed to separate the photogenerated charge carrier, leading to avoiding the recombination. Das and coauthors reported Au-loaded $CaFe_2O_4$/CoAl LDH p–n junction composite with improved photocatalytic activity for chromium reduction. Li and coworker reported mixed metal oxide derived from ZnAl layered double hydroxide for photocatalytic reduction of hexavalent chromium [10].

Two-dimensional/two-dimensional (2D/2D) composite have been extensively developed for use as a photocatalyst due to it has greater electron-hole mobility across the interface of 2D/2D heterojunction, which can decrease the distance and time of charge migration to inhibit the recombination of photogenerated electron and hole. In the recent year, montmorillonite (MT) as a cationic exchanged 2D clay mineral has

attracted much interest as a promising photocatalyst due to natural abundance, high surface area, low cost, high thermal and chemical stability, non-toxic and environmentally friendly [11-13]. There are some reports about MT composites with enhancing photocatalytic performance by suppressing the electron-hole recombination. However, the mechanism is not well understood. In this work, the series of 2D/2D ZnTi LDH/MT composite were prepared precipitation method, and the obtained products were used as a photocatalyst for Cr(VI) reduction. The as-prepared materials were characterization by XRD, UV-Vis/DRS, PL XPS, and TEM-EDX. Moreover, the electronic level and migration of electron between ZnTi LDH and MT were studded by density functional theory calculation (DFT) in order to better understand the photocatalytic mechanism of the composite.

The previous reports regarding of photocatalytic reduction of Cr(VI) were summarized in Table 3.1 to compare with the present work. From the comparative results, we observed that ZTM/MT material could show a comparable reduction of Cr(VI). We believe that the present finding might be useful for a detailed understanding of the upcoming research scope of the 2D/2D LDH/MT photocatalyst materials for Cr(VI) reduction.

Table 3.1 Comparison of photocatalytic efficiency for Cr(VI) reduction

Catalyst	Active compound	Target	C_0	Loading (g/L)	Efficacy (%)	Time (min)	Ref.
TiO_2-montmorillonite	TiO_2	Cr(VI)	30 ppm	0.2	~15	240	[14]
TiO_2-montmorillonite with tartaric acid	TiO_2	Cr(VI)	30 ppm	0.2	100	120	[14]
$BiVO_4$	$BiVO_4$	Cr(VI)	0.1 mM	1.0	50	180	[15]
ZnAl-MMO	ZnAl-MMO	Cr(VI)	10 ppm	2.0	100	300	[16]
Ti-SBA15-carbon nitride (Ti-SBA15-CN)	Ti-SBA15-CN	Cr(VI)	10 ppm	1.0	25	120	[17]
TiO_2 with methanol (100ppm)	TiO_2	Cr(VI)	20 ppm	1.0	90	300	[18]
α-Fe_2O_3/g-C_3N_4	α-Fe_2O_3/g-C_3N_4	Cr(VI)	10 ppm	2.0	100	160	[19]
TiO_2	TiO_2	Cr(VI)	10 ppm	-	20	120	[20]
ZnO	ZnO	Cr(VI)	10 ppm	-	34	240	[21]
ZnO-C_3N_4	ZnO-C_3N_4	Cr(VI)	10 ppm	-	70	240	[21]
Ag@Ag_3PO_4/g-C_3N_4/NiFe	Ag@Ag_3PO_4/g-C_3N_4/NiFe	Cr(VI)	20 ppm	1.0	95	120	[22]
$CaFe_2O_4$/CoAl LDH@Au	$CaFe_2O_4$/CoAl LDH@Au	Cr(VI)	20ppm	1.0	95	60	[10]

Table 3.1 Comparison of photocatalytic efficiency for Cr(VI) reduction (continued)

Catalyst	Active compound	Target	C_0	Loading (g/L)	Efficacy (%)	Time (min)	Ref.
Acid-treated g-C_3N_4	Acid-treated g-C_3N_4	Cr(VI)	50 ppm	1.0	5	300	[23]
Acid-treated g-C_3N_4 with citric acid	Acid-treated g-C_3N_4	Cr(VI)	50 ppm	1.0	100	240	[23]
RGO/TiO_2	RGO/TiO_2	Cr(VI)	12ppm	0.2	180	240	[24]
Pd/CeO2/g-C_3N_4	Pd/CeO2/g-C_3N_4	Cr(VI)	0.1 mM	0.5	100	40	[25]
$CaFe_2O_4$/CoAl LDH@Au	$CaFe_2O_4$/CoAl LDH@Au	Cr(VI)	20ppm	1.0	95	60	[10]
ZTL/MT	ZTL/MT	Cr(VI)	10 ppm	1.0	100	300	This work

3.2. Materials and Methods

3.2.1. Materials and reagents

Montmorillonite (MT, Kunipia-F) which are cationic exchanged clay mineral was obtained from Kunimine Industries Co. Ltd., Japan which the chemical formula was $(Na_{0.97}Ca_{0.08})^{+1.13}(Si_{7.68}Al_{0.32})(Al_{2.94}Fe^{III}_{0.25}Fe^{II}_{0.03}Mg_{0.78})O_{20}(OH)_4^{-1.13}\cdot nH_2O$ [26]. Sodium Chromate tetrahydrate ($Na_2CrO_4\cdot 4H_2O$), zinc nitrate hexahydrate ($Zn(NO_3)_2\cdot 6H_2O$), Titanium(IV) Chloride ($TiCl_4$) and urea ($CO(NH_2)_2$) were obtained from Wako Chemicals (Osaka, Japan). All the chemicals were used directly without further purification.

3.2.2. Preparation of ZnTi layered double hydroxide (ZTL)

ZnTi layered double hydroxides with Zn^{2+}/Ti^{4+} molar ratio of 4:1 (ZTL) was synthesized by a co-precipitation refluxing method. In a typical synthesis, 1.19g of $Zn(NO_3)_2\cdot 6H_2O$ and 0.11 mL $TiCl_4$ were dissolved in the 50 mL of deionized water, followed by the addition of 1.5 g of urea. The mixed metal solution was heated under gentle reflux with vigorous stirring at 130 °C for 24h. The solid white product was obtained, separated by flirtation and washed with deionized water several times. Finally, the ZnTi layered double hydroxides (denoted as ZTL) was obtained by drying at 75 °C for 24 h in an oven.

3.2.3. Preparation of ZnTi layered double hydroxide/montmorillonite composites (ZTL/MT)

ZnTi layered double hydroxide/montmorillonite composites (ZTL/MT) were prepared by a similar method with ZTL, refluxing method. Firstly, 1.19g of $Zn(NO_3)_2 \cdot 6H_2O$ and 0.11 mL $TiCl_4$ were added into the 50 mL of deionized water, followed by the addition of 1.5 g of urea. The mixed metal solution was heated under gentle reflux with vigorous stirring at 130 °C for 12h. The different required amounts of montmorillonite (MT) (10, 20 and 30 % wt. in composite) was added into the above solution, followed by sonicated for 3h. Afterward, the suspended solution was continuously refluxed for 12 h. The products were collected by filtered and washed several times with the deionized water. Finally, the white colored powders were obtained after dried at 75 °C for 24 h in an oven. The obtained products are denoted as ZTL/MTX%, where X stands for a weight percent of MT in the composites.

3.2.4. Characterizations

The characterizations of the solid samples were carried out by X-ray diffraction (XRD), X-ray fluorescence spectroscopy (XRF), UV–vis diffuse reflectance spectroscopy (DRS), transmission electron microscopy (TEM-EDX), X-ray photoelectron spectroscopy (XPS) and photoluminescence spectroscopy (PL). Detailes are described in **Chapter 2**.

In addition, the electronic-structure calculations of ZTL and Fe-bearing MT were calculated by density functional theory (DFT). In this calculation, we performed self-consistent-field calculations with the PW code of the open-source Quantum-

Espresso software. All the calculations were carried out at the semilocal Perdew-Burke-Ernzerhof level with van der Waals corrections following the DFT-D parameterization of long-range interactions between fluctuating dipoles. The ionic cores were represented by ultrasoft pseudopotentials. Kinetic energy cutoffs were set to 60 and 480 Ry for the reciprocal-space expansion of the wave functions and charge density, respectively. A Marzari-Vanderbilt smearing of 0.005 Ry was employed for the sampling of the Brillouin zone with 6×4×4 and 4×8×4 Monkhorst-Pack grids for the ZTL and MT, respectively. The Hubbard *U* correction was applied to the Ti and Fe sites to account for electron correlations (U_{Ti} = 6.0eV and U_{Fe} = 1.9 eV), as suggested by previous work. Atomic positions and lattice vectors were optimized for both ZTL and MT until the residual force on each atom was smaller than 0.01 eV/Å and the residual pressure was lower than 0.5 kbar.

3.2.5. Photocatalytic test

Photocatalytic activity tests were evaluated toward the photocatalytic reduction of Cr(VI). In a typical procedure, 50 mg of catalysts were dispersed in the 50 mL of 10 ppm of Cr(VI) aqueous solution in the dark condition for 30 min to establish the adsorption-desorption equilibrium. The pH of suspension solutions was adjusted by 0.5 M HCl and NaOH in order to maintain the pH value at three before the photocatalytic reaction. Then, the suspensions were irradiated using a 500 W Xe lamp. During the light illumination, suspensions were taken out and filtrated by 0.45 μm membrane filters to separate the catalyst. The remaining concentrations of Cr(VI) was

determined by a diphenyl carbazide colorimetric method with a UV-VIS spectrometry at 554 nm [27].

3.3. Results and Discussion

3.3.1. Characterizations

Fig. 3.1 shows the XRD patterns of MT, ZTL, ZTL/MT10%, ZTL/MT20% and ZTL/MT30% composites. It can be seen that ZTL showed the strong diffraction peaks at 2θ = 13.2°, which is attributed to the (003) basal plane of LDH. Moreover, the other peaks located at 2θ values of 24.3°, 35.4°, 31.2°, 33.0° and 36.1°, corresponding to planes (006), (012), (100), (101) and (009), respectively, indicating to ZnTi layered double hydroxide phase [9]. The diffraction peaks of ZTL/MT with different MT content are resembled the ZTL, indicating the presence of MT in the composite would not change the backbone structure of ZnTi layered double hydroxide. The MT exhibits five strong diffraction peaks at 7.3°, 19.8°, 28.6°, 35.0°, and 61.9°, which correspond to the (001), (100), (004), (110) and (300) planes of montmorillonite. As for the composite, the broad peak at 2θ = 7.3° can be found, and the peak intensity becomes stronger with the increasing of MT content, suggesting the presence of MT in the composite.

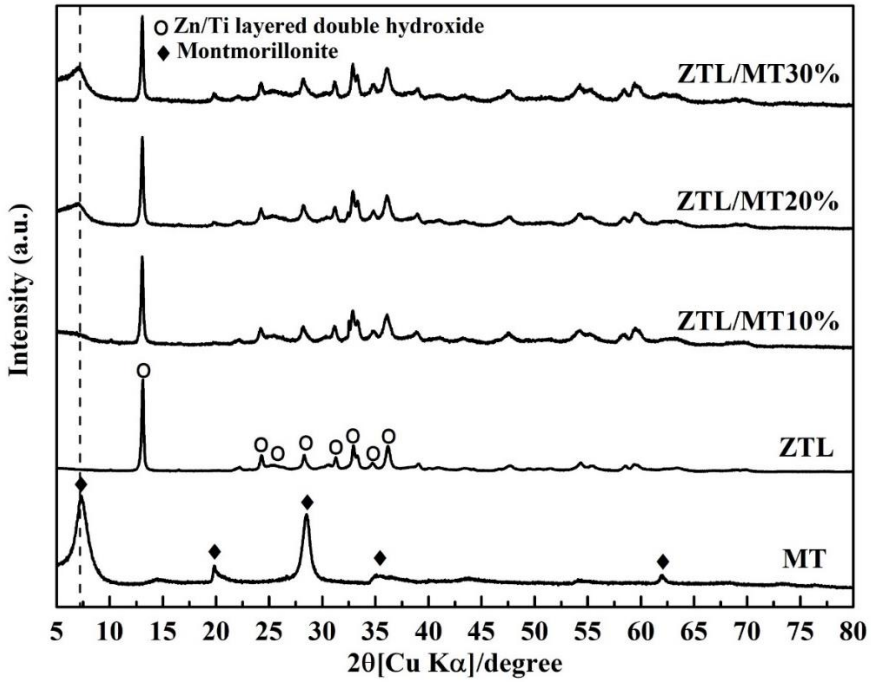

Fig. 3.1 XRD patterns of MT, ZTL, and ZTL/MT composites.

Also, the chemical composition of MT was examined by XRF, and the results were shown in **Table 3.2**. The main elements in the MT are Si, Al, Mg, Na, and O, which confirms the Na-type montmorillonite. It also has some transition metal impurities such as Fe that might be affected by the optical and photocatalytic properties of MT and ZTL/MT composites.

Table 3.2 The elemental compositions of MT in wt%.

Component	**C**	**O**	**F**	**Na**	**Mg**	**Al**	**Si**	**P**	**S**	**C**
wt.%	1.900	53.04	0.098	2.374	1.941	11.280	26.70	0.007	0.102	1.901
Component	**Cl**	**K**	**Ca**	**Ti**	**Mn**	**Fe**	**Zn**	**Ga**	**Sr**	**Y**
wt.%	0.018	0.066	0.551	0.089	0.018	1.779	0.007	0.0021	0.008	0.002

To investigate the electronic and optical properties of ZTL and ZTL/MT composites, UV-Vis diffuse reflectance spectrum (DRS) were collected, as shown in **Fig. 3.2a** The adsorption spectra of ZTL, MT and ZTL/MT composites existence the strong adsorption of light in the 300-400 nm regions, suggesting the ZTL, MT and ZTL/MT composites can be activated by UV light. Compared to ZTL, The ZTL/MT composites exhibited higher light absorption ability in near visible light region, implied that the composite could generate more electron-hole pair under light irradiation, which might play an important role for reduction of Cr(VI). Moreover, the increasing of light adsorption ability might be due to the vibration produced from the interfacial combination of ZTL and MT [11]. The band gap energies estimated by the linear part of the $(\alpha h\nu)^2$ versus the energy of absorbed light affords the Eg plot as shown in **Fig. 3.2b**. The multiple-transition state of MT can be observed around 2.13 eV, 2.65 eV, 2.94 eV, and 3.78 eV, which might be due to the Fe impurity in the structure of MT. The calculated band gap energy of ZTL, ZTL/MT10%, ZTL/MT20%, and ZTL/MT30% were 3.41, 3.39, 3.36 and 3.33 eV, respectively, lower than as-prepared ZTL. Thus, the formation of 2D/2D heterojunction between ZTL and MT provides the narrowed band gap energy of the composite which can improve the utilization of UV light leading to enhancing of photocatalytic activity for Cr(VI) reduction.

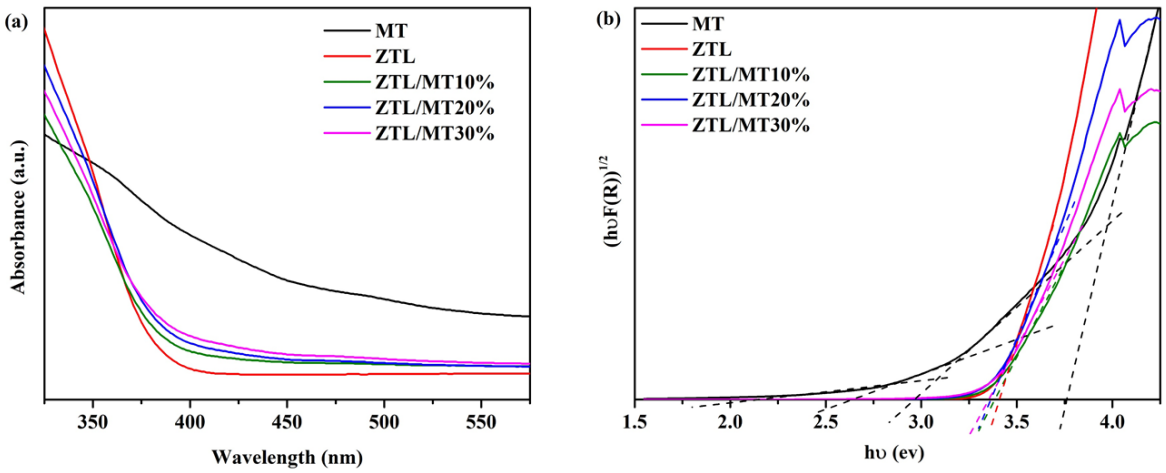

Fig. 3.2 (a) UV–vis diffuse reflectance spectra and (b) Tauc spectra bandgap (Eg) analyses of MT, ZTL and ZTL/MT composites.

Fig. 3.3a and 3b present the typical bright-field and dark-field TEM images of ZTL/MT20% composite, respectively. It is clear that the ZTL/MT20% composite shows the lowly crystallinity and shapeless structure with several hundred nanometers. The location of the MT and ZTL in the ZTL/MT20% composite was further confirmed by TEM-EDX elemental mapping analysis. As illustrated in **Fig. 3.3c**, the mapping results shows that O, Zn, and Ti element is a central component of the ZTL/MT20% composite, which are attributed to ZnTi layered double hydroxide phase. Meanwhile, the Al, Si, and Mg elements (indicating montmorillonite) are homogeneously distributed in a similar position with ZTL throughout the whole composite. Thus, the clear observation of the overlap of ZTL and MT confirm the formation of 2D/2D heterojunction structure.

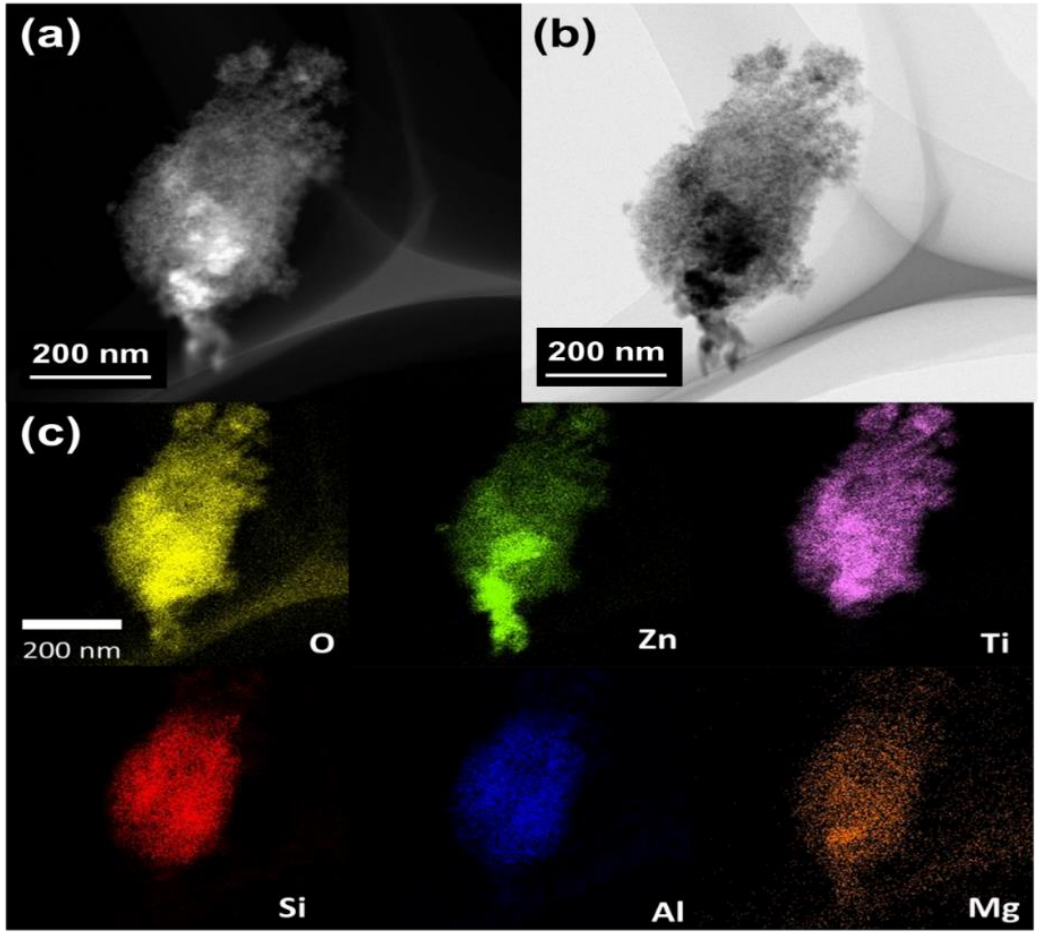

Fig. 3.3 TEM images of ZTL/MT20% (a) bright-field and (b) dark-field, scale bars indicate 200 nm and (c) TEM-EDX elemental mapping of O, Zn, Ti, Si, Al and Mg in ZTL/MT20%.

The surface chemical composition and oxidation states of each element in ZTL/MT20% composite were investigated by XPS analysis, as shown in **Fig. 3.4**. As can be seen in **Fig. 3.4a**, the survey spectrum of the ZTL/MT20% composite displays peaks of Zn, Ti, O, Si and Al orbital which can confirm the presence of ZnTi layered double hydroxide and montmorillonite in the composite. The XPS spectra in **Fig. 3. 4b** shows the binding energy values of $Zn2p_{5/2}$ and $Zn2p_{3/2}$ at 1021.5 eV and 1044.6 eV, respectively, which can be attributed to Zn^{2+} ion. Meanwhile, the high-resolution Ti 2p in **Fig. 3.4c** show characteristic peaks located at 457.13 eV and 462.83 eV which are corresponding to Ti $2p_{3/2}$ and Ti $2p_{3/2}$ orbital, respectively, of Ti^{4+} ion. In **Fig. 3.4d,** the two weak peaks at 712.9 eV and 725.3 eV could be assigned to Fe $2p_{3/2}$ and Fe $2p_{1/2}$ of Fe^{3+} ion which indicate a low concentration of Fe impurity in MT. Furthermore, the valence band (VB) of ZTL and MT were investigated in order to better understand the photocatalytic mechanism of the ZTL/MT composite. The measured XPS VB potential of ZTL **(Fig. 3.4e)** and MT **(Fig. 3.4f)** are 1.44 eV and 2.70 eV, respectively. According to their energy band gap value, the conduction band (CB) of ZTL and MT are calculated to be -1.97 eV and -1.08 eV, respectively.

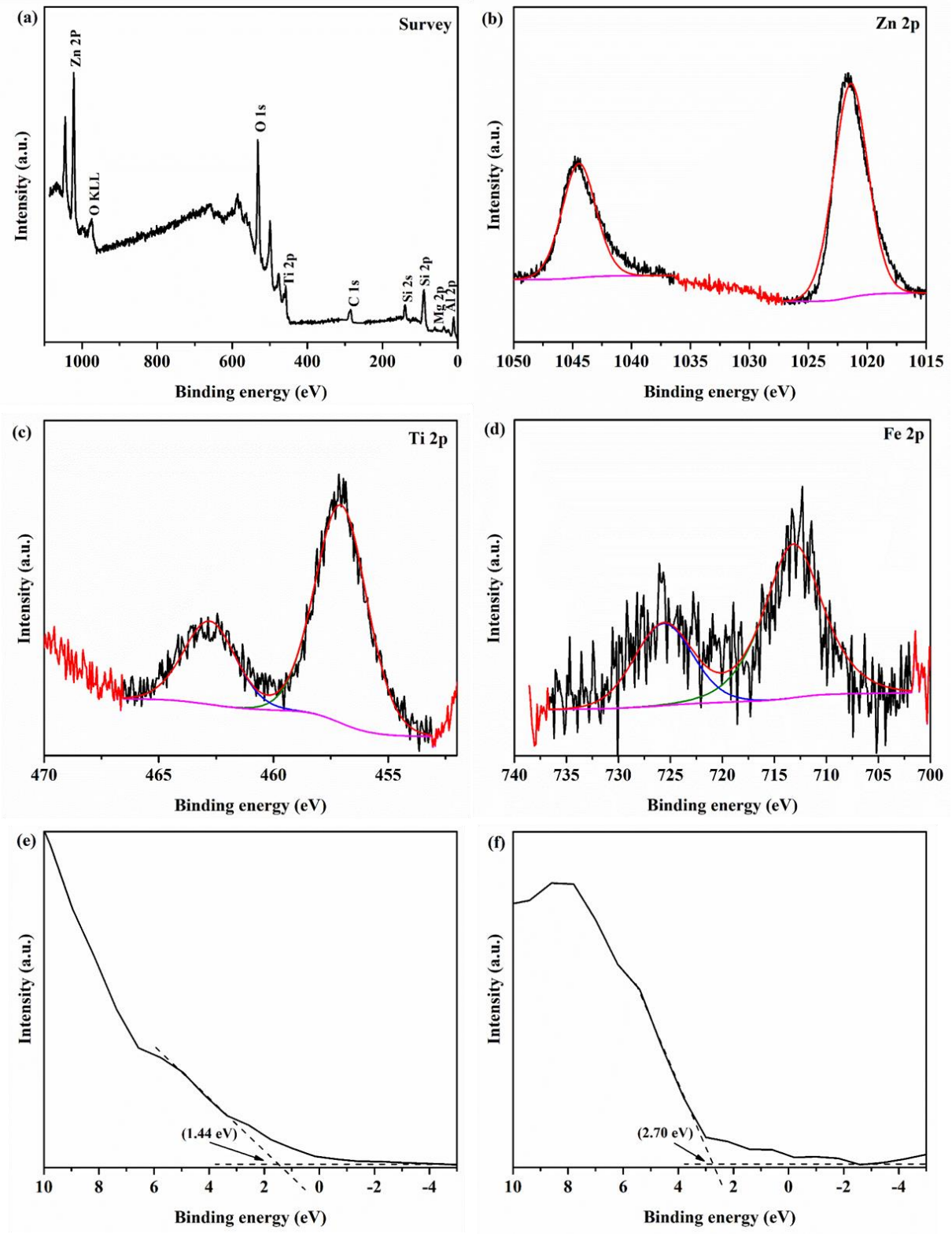

Fig. 3.4 XPS spectra of ZTL/MT20% (a-d): (a) survey, (b) Zn 2p, (c) Ti 2p, (d) Fe 2p, (e) valence band energy region of ZTL and (f) valence band energy region of MT.

It is known that one of the main problems of the photocatalytic process is the recombination of photogenerated charge carrier (electron and hole). Thus, the heterojunction between semiconductor can avoid the recombination process and maintain photogenerated electro, which is the main contribution for photocatalytic reduction of Cr(VI). The photoluminescence analysis (PL) are used to study the recombination rate of the electron-hole pair of the photocatalyst. As can be seen from **Fig. 3.5**, compared with the pure ZTL, the luminous intensity of ZTL/MT20% shown significantly decreased which are suggested to the separation of electron and hole could be enhanced through the interfacial 2D/2D heterojunction between ZTL and MT. In additions, the ZTL/MT20% shown blue-shift, indicating that the excellent transfer of an electron between the 2D/2D hybrid heterojunction structure [28, 29].

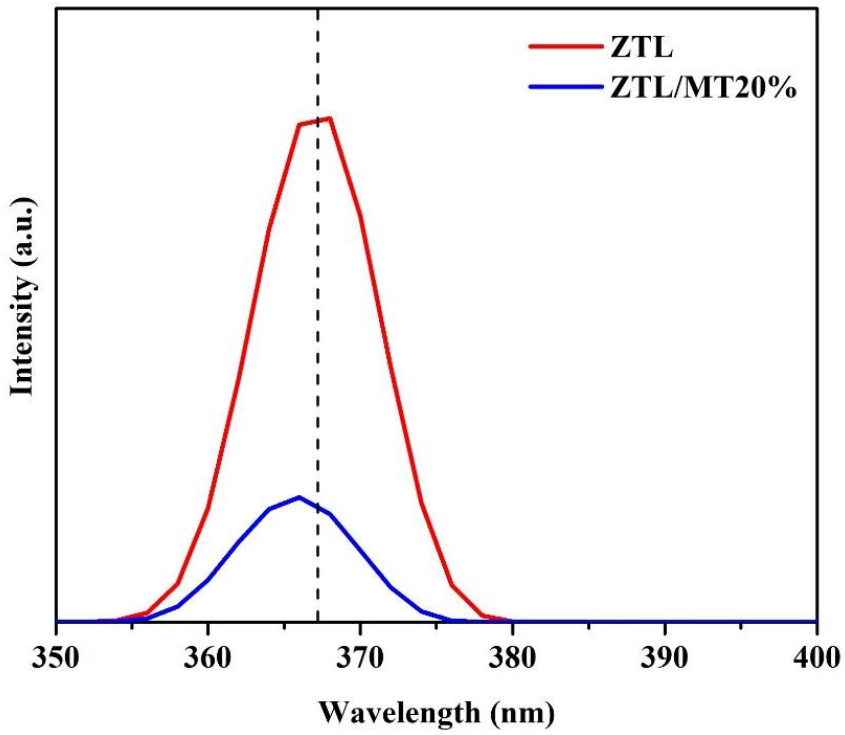

Fig. 3.5 Photoluminescence spectra of ZTL and ZTL/MT20%.

3.3.2 Photocatalytic reduction of Cr(VI)

It has been reported that ZnTi layered double hydroxide (ZTL) can catalyze the decomposition of an organic compound such as azo dyes [30, 31]. To evaluate the photocatalytic ability of ZTL and ZTL/MT20% composite without dye-sensitized property, photocatalytic reduction of *Cr(VI)* were performed in aqueous solution after reaching of the adsorption-desorption equilibrium at pH 3, and the results are displayed in **Fig. 3.6a**. Under light irradiation, the pristine MT showed negligibly decreasing of Cr(VI) concentration, while the ZTL can work well for reducing the Cr(VI). The result is suggesting that the ZTL base photocatalyst can be used as photocatalyst for Cr(VI) reduction instead of ZnO or TiO_2 due to it had low photocatalytic activity [16]. Moreover, the ZTL/MT10% and ZTL/MT20% possess higher photocatalytic reduction of Cr(VI) compared with pure ZTL. The improvement of the photocatalytic efficiency of the composites should be attributed to the significantly suppressing of recombination of electron-hole pair through 2D/2D interface heterojunction of ZTL and MT. However, when the MT content in the composite was up to 30%, the photocatalytic reduction performance would exhibit a decrease, which might be due to the reducing of the active area of ZTL by the excess of the amount of MT. The highest photocatalytic reduction of Cr(VI) was obtained about 99% over ZTL/MT20% composite after 300 min.

Fig. 3.6b displayed the kinetics plot of photocatalytic reduction of Cr(VI) over ZTL and ZTL/MT composites under light irradiation. The results of the photocatalytic reduction of Cr(VI) followed well with the first-order kinetics model, and the rate constants of each sample were also compared. It is clear that the rate constants of ZTL/MT20% are higher than that of the other photocatalyst, which is consistent with

the reduction efficiency in **Fig. 3.6a**. From the above results, the essential factors to improve the photocatalytic reduction of Cr(VI) for the ZTL/MT composites should be the decreasing of recombination rate of photogenerated charge carrier via 2D/2D interfacial heterojunction between ZTL and MT.

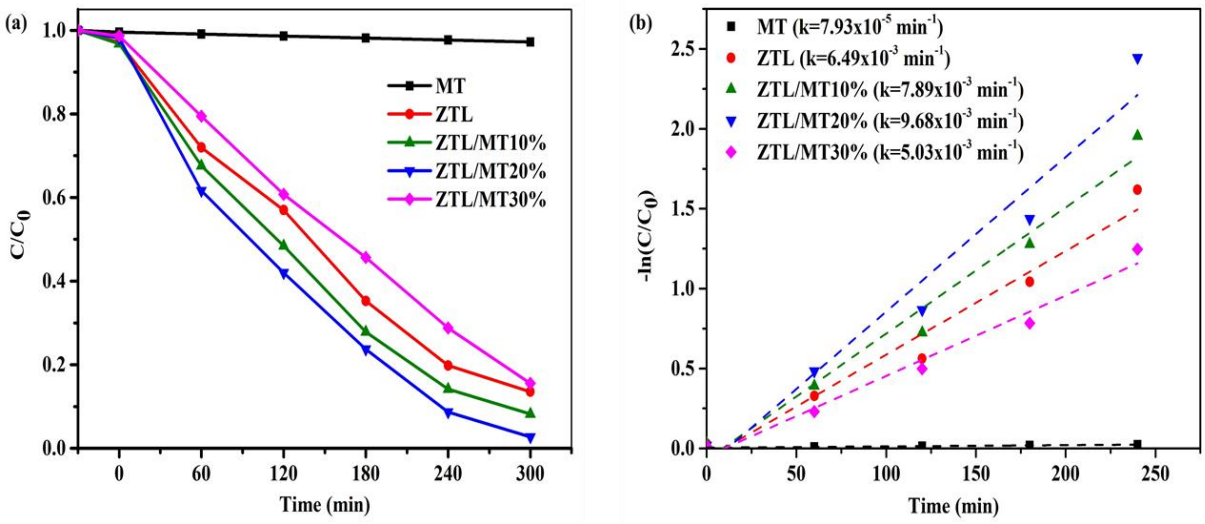

Fig. 3.6 (a) Photocatalytic reduction of Cr(VI) with time and (b) kinetic linear fitting curves of MT, ZTL and ZTL/MT with various MT contents; pH 3.0, initial [Cr(VI)] =10 ppm, catalyst loading= 1g/L at 25°C.

One of the critical factors of photocatalyst material is stability. The photocatalytic stability of ZTL/MT20% for Cr(VI) reduction was studied by the recycling test for three times. As shown in **Fig. 3.7a**, the photocatalytic reduction of Cr(VI) over ZTL/MT20% slightly decrease might be due to the some of ZTL transform in an acid condition. To confirmed the stability of ZTL after the reaction, spent ZTL/MT20% was collected after 1cycle of photocatalytic reduction of Cr(VI) under light irradiation. As illustrated in **Fig. 3.7b**, the main diffraction peak of ZTLstill remains in the XRD pattern of spent ZTL/MT20%, indicating that the ZTL structure did not change so much after photocatalytic reduction of Cr(VI). However, the interlayer peak of montmorillonite (MT) was shifted to the lower diffraction angle,

from 7.3° to 6.0°, after the photocatalytic reaction leading to the expansion of interlayer space of montmorillonite, from 12.48Å to 14.57Å. From the previous reports, it has been known that MT had an excellent cationic exchange capacity and organic adsorption from aqueous solution [32, 33]. Thus, the Cr(III), produced after photocatalytic reduction of Cr(VI) should be intercalated between the layer of montmorillonite by cationic exchange with Na^+ in MT, and it can expand the interlayer space of MT because the hydrated ion size of Cr(III) is larger than Na^+ ion [34].

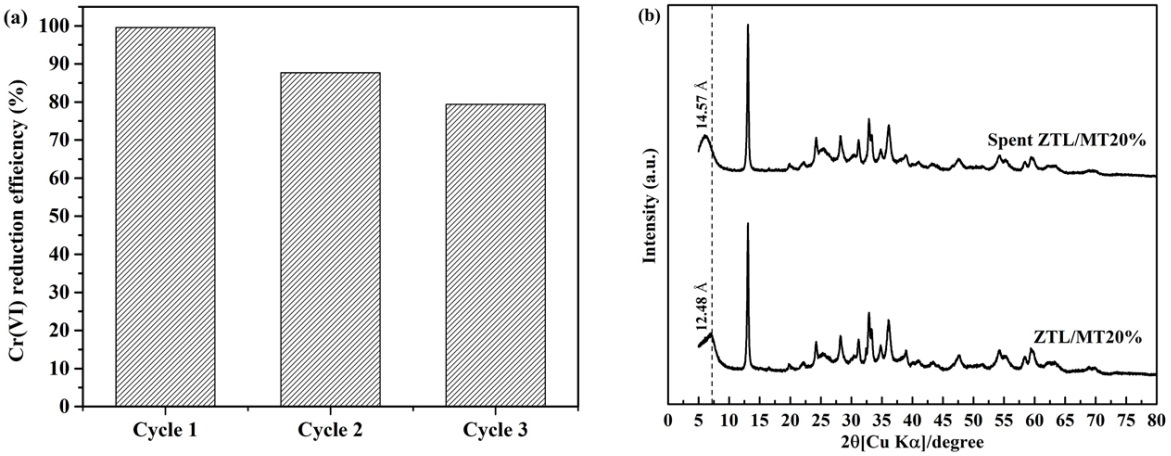

Fig 3.7 (a) Recycling test in the photocatalytic reduction of Cr(VI) over ZTL/MT20% and (b) XRD patterns of the fresh and spent ZTL/MT20%.

The chemical state of the elements in spent ZTL/MT20% also was investigated using XPS analysis. **Fig. 3.8a** displays the survey spectra of spent ZTL/MT20%, The sharp peaks of Zn 2p, Ti 2p, and O 1s orbital were detected in the full spectrum of the sample. Moreover, the tiny peak of Cr 2p was also founded, suggesting that it might have some Cr ion precipitate on the surface or intercalated between the layer of MT in ZTL/MT20% composite. In the Zn 2p region (**Fig.8b**), the spectrum could be separated into two peaks of zinc that corresponding to Zn $2p_{3/2}$ and Zn $2p_{1/2}$ of Zn^{2+} ion.

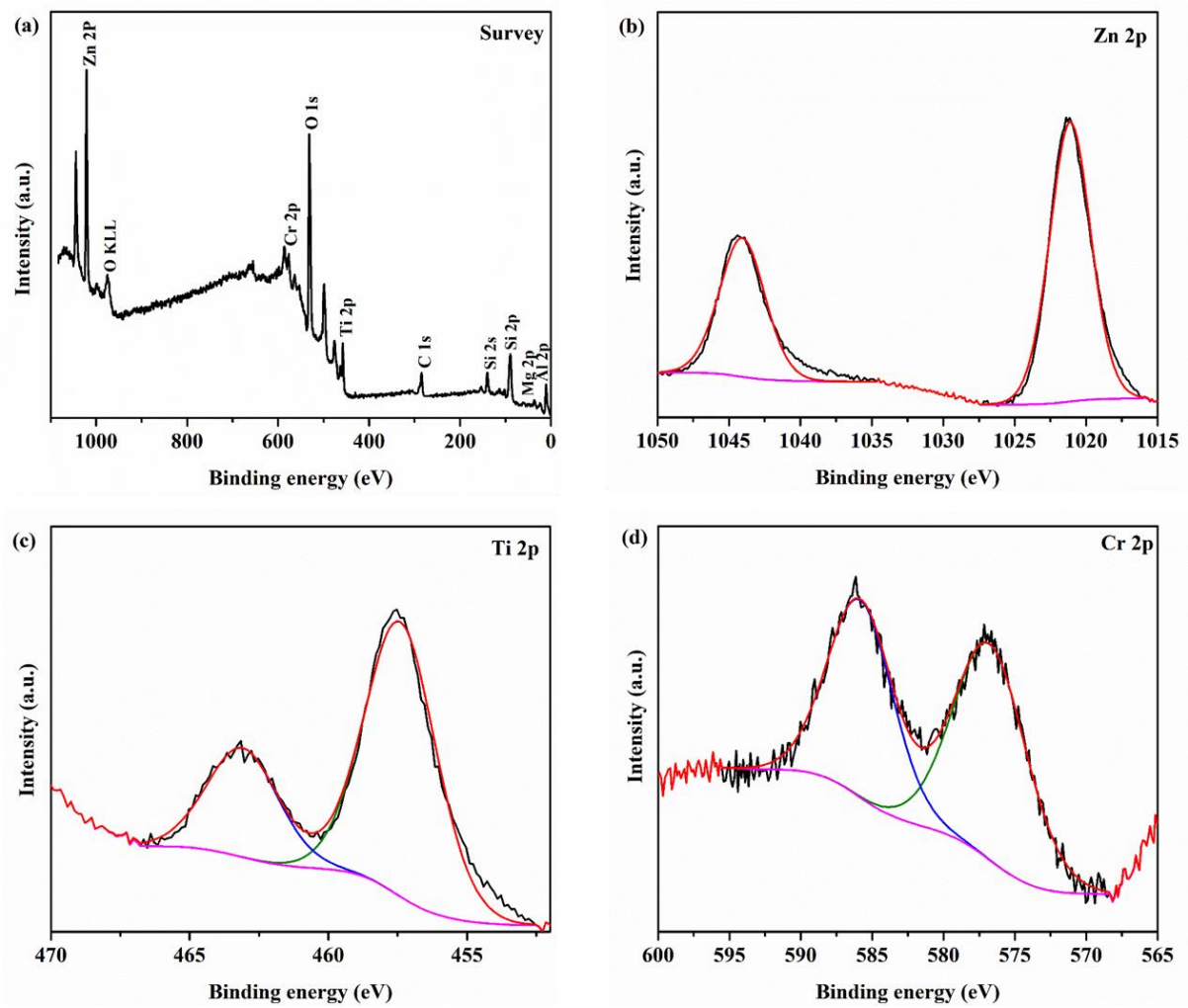

Fig. 3.8. XPS spectra for the spent ZTL/MT20%: (a) survey, (b) Zn 2p, (c) Ti 2p and (d) Cr 2p.

Meanwhile, **Fig. 3.8c** shown two distinct peaks at 457.5 eV and 463.1 eV, belonging to Ti $2p_{3/2}$ and Ti $2p_{1/2}$, consistent with Ti^{4+} ion. These results suggest that the oxidation state of Zn and Ti did not change after the reaction, which confirms the stability of ZTL in the composite after the photocatalytic reaction. Moreover, the spectrum of Cr 2p was recorded (**Fig. 8d**), and the peaks of Cr $2p_{3/2}$ and Cr $2p_{1/2}$ at 476.76 and 585.79, respectively, were indicated to Cr(III) ion which confirms the photocatalytic reduction of Cr(VI) under light irradiation.

Also, the distribution of Cr in spent ZTL/MT20%, TEM mapping of the spent catalyst was observed, and the results were shown in **Fig. 3.9**. The mapping results exhibited the presence of Cr element in the spent catalyst, and it was dispersed in a similar location with ZTL and MT. Thus, Form the XRD, XPS and TEM mapping results, it could be concluded that the produced Cr(III) after photocatalytic reduction of Cr(VI) might be intercalated or precipitated between the layer of MT.

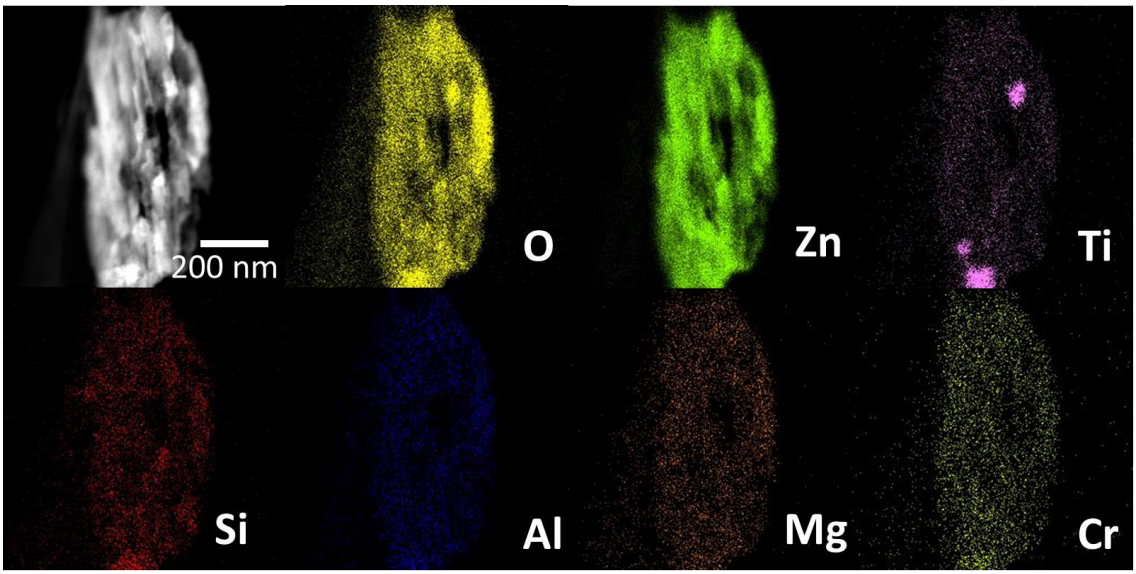

Fig. 3.9 TEM-EDX elemental mapping of O, Zn, Ti, Si, Al and Mg in spent ZTL/MT20%.

3.3.3 Photocatalytic mechanism of Cr(VI) reduction over ZTL/MT

It is well known that electron-hole pairs separation is importance for photocatalytic activity of photocatalysts. The ZTL/MT20% composites showed higher photocatalytic performance than ZTL and MT, suggesting that the heterojunction between the ZTL and MT can avoid the recombination of electron and hole pairs. To understand the charge transfer in the ZTL/MT composite, the energy band structure and density of states for ZTL and MT were calculated by density functional theory (DFT), respectively as shown in **Fig. 3. 10**, considering 1.78% Fe is substituted (Table 3.2). From the DOS results of MT and ZTL, the contributions of each atom in the VB and CB of ZTL and MT were also examined. The VB edge of ZTL was mainly composed of Zn orbits, while the CB edge of ZTL was contributed by Ti orbital. The VB edge of MT was mainly composed of O orbits, while the CB edge was contributed by Fe orbital, which is an impurity in the structure of MT. The ZTL was a band gap structure around 2.8 eV, while MT showed the large energy band gap about 5.1 eV. It was in good agreement with the experimental values by DSR spectra. The Fe impurity in the layer structure generates the middle state level between the VB and CB leading to provide the multigap state in MT. The electron in the mid-gap state can be excited by light and moved to the CB of MT. Thus, the electrons in the CB of MT can be recombined with h^+ in the VB of ZTL to avoid the recombination of electron-hole pair of ZTL.

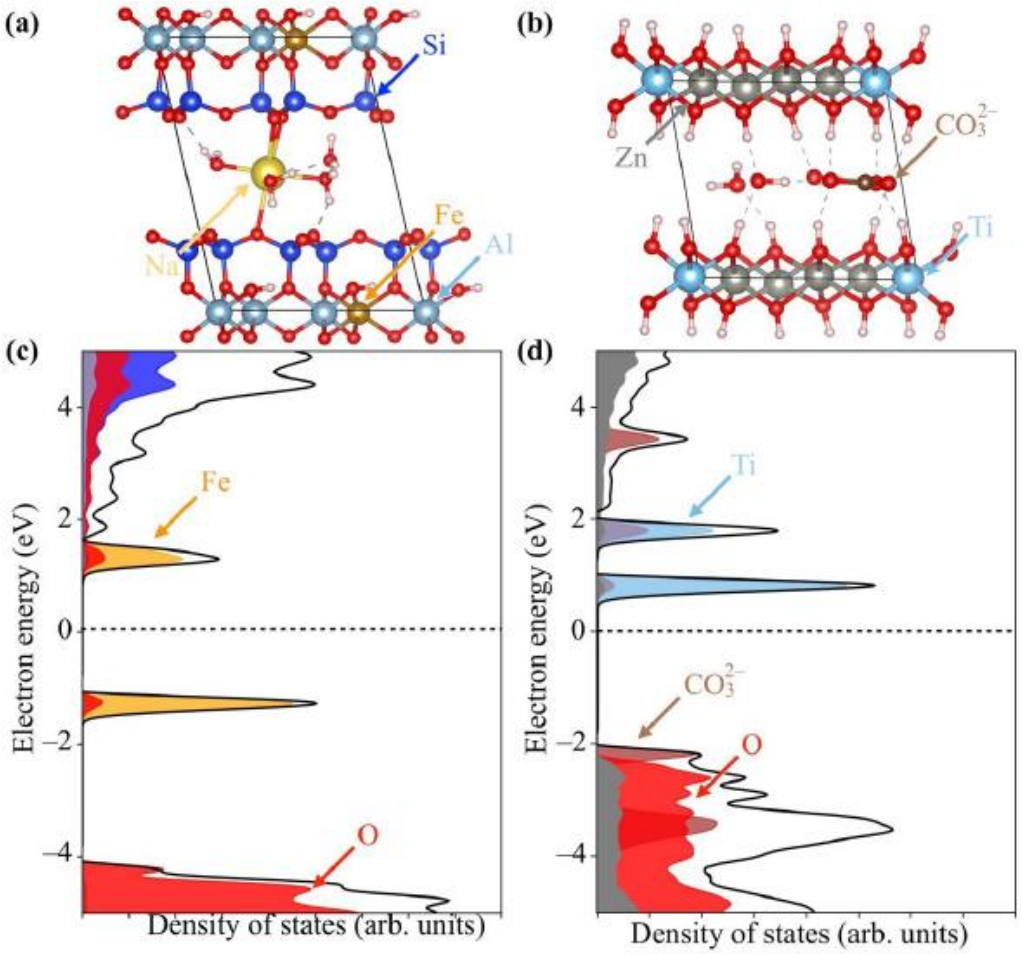

Fig. 3.10. (a) Crystal structure and (c) density of states (DOS) of MT, where Fe is substituted. (b) Crystal structure and (b) density of states (DOS) of ZTL.

The ZTL/MT20% composite shown the higher photocatalytic performance than pure ZTL and MT, suggesting the 2D/2D heterojunction between the ZTL and MT might be formed, leading to suppress the electron-hole recombination. According to the above results, a Z-scheme photocatalytic mechanism of charge transfer in ZTL/MT20% was proposed, as shown in **Fig. 3.11** and **Eq. 3.1-3.4**. Upon light irradiation, the ZTL can absorb photons and then produce photogenerated electron and hole in the CB and VB, respectively, while the electron from the mid-gap state from Fe orbital of MT was excited to the CB of MT. The photogenerated electron in CB of

MT can transfer to VB of ZTL due to the more positive energy level of VB state of ZTL (1.455 eV) compared with CB state of MT (-1.275 eV). The recombination electron and hole from the above process could promote the separation of photogenerated charge carrier of ZTL and maintain the electron in the CB of ZTL. The dissolved Cr(VI) in the solution can react with an electron in CB of ZTL and reduced it into Cr(III). Furthermore, the Cr(III) could be intercalated between the layer of MT via cationic exchange process with Na^+ ion, which can be decreased the mobility of toxic Cr(III) into the solid phase. From the above discussions, the photocatalytic reduction of Cr(VI) could be described as the following reaction of (3.1) - (3.4).

$$ZTL/MT + h\nu \rightarrow ZTL(h^+ + e^-)/MT\ (h^+ + e^-) \quad (3.1)$$

$$ZTL(h^+)/MT\ (e^-) \rightarrow ZTL/MT \quad (3.2)$$

$$HCrO_4^- + 7H^+ + ZTL(3e^-) \rightarrow Cr^{3+} + 4H_2O + ZTL \quad (3.3)$$

$$ZTL(h^+)/MT + 2H_2O + 4h^+ \rightarrow ZTL/MT \quad (3.4)$$

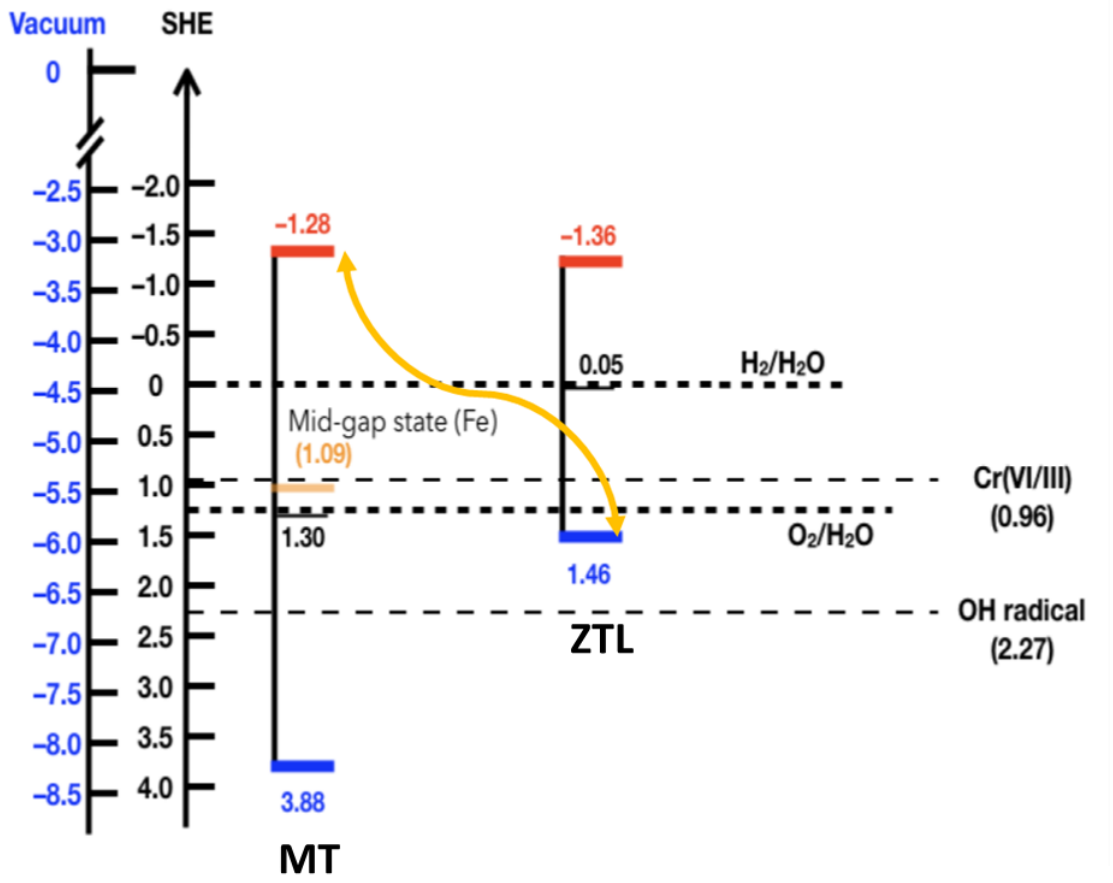

Fig. 3.11 Photocatalytic reductive adsorption of Cr(VI) over ZTL/MT composite.

3.4. Conclusions

The ZnTi layer double hydroxide/montmorillonite composites (ZTL/MT) were prepared a simply precipitation method and utilized the composites as a photocatalyst for the photocatalytic reduction of Cr(VI). The ZTL/MT20% composite displayed the highest reduction efficiency and reaction rate constant for Cr(VI), which could be attributed to the efficient light adsorption ability and low recombination rate of electron and hole in ZTL. The electrons from the CB of MT can be recombined with an electron in VB of ZTL, enhancing the charge separation of ZTL which enhance the

photocatalytic activity. Moreover, the role of MT is not only to suppress the recombination of photogenerated charge carrier of ZTL but also adsorb the Cr(III) after photocatalytic reduction. Cr(III) could be adsorbed or intercalated between the layer of MT, which can eliminate the toxic Cr(III) from the water.

References

[1] M. Shirzad-Siboni, M. Farrokhi, R. Darvishi Cheshmeh Soltani, A. Khataee, S. Tajassosi, Photocatalytic Reduction of Hexavalent Chromium over ZnO Nanorods Immobilized on Kaolin, Industrial & Engineering Chemistry Research, 53 (2014) 1079-1087.

[2] N. Tian, Y. Zhang, C. Liu, S. Yu, M. Li, H. Huang, g-C_3N_4/$Bi_4O_5I_2$ 2D–2D heterojunctional nanosheets with enhanced visible-light photocatalytic activity, RSC Advances, 6 (2016) 10895-10903.

[3] Y.-J. Yuan, Z. Shen, S. Wu, Y. Su, L. Pei, Z. Ji, M. Ding, W. Bai, Y. Chen, Z.-T. Yu, Z. Zou, Liquid exfoliation of g-C_3N_4 nanosheets to construct 2D-2D MoS_2/g-C_3N_4 photocatalyst for enhanced photocatalytic H_2 production activity, Applied Catalysis B: Environmental, 246 (2019) 120-128.

[4] Y.-J. Yuan, D. Chen, J. Zhong, L.-X. Yang, J. Wang, M.-J. Liu, W.-G. Tu, Z.-T. Yu, Z.-G. Zou, Interface engineering of a noble-metal-free 2D–2D MoS_2/Cu-$ZnIn_2S_4$ photocatalyst for enhanced photocatalytic H_2 production, Journal of Materials Chemistry A, 5 (2017) 15771-15779.

[5] Y. Zhao, X. Jia, G.I.N. Waterhouse, L.-Z. Wu, C.-H. Tung, D. O'Hare, T. Zhang, Layered Double Hydroxide Nanostructured Photocatalysts for Renewable Energy Production, Advanced Energy Materials, 6 (2016) 1501974, 1-20.

[6] C.G. Silva, Y. Bouizi, V. Fornés, H. García, Layered Double Hydroxides as Highly Efficient Photocatalysts for Visible Light Oxygen Generation from Water, Journal of the American Chemical Society, 131 (2009) 13833-13839.

[7] M.J. Wu, J.Z. Wu, J. Zhang, H. Chen, J.Z. Zhou, G.R. Qian, Z.P. Xu, Z. Du, Q.L. Rao, A review on fabricating heterostructures from layered double hydroxides for

enhanced photocatalytic activities, Catalysis Science & Technology, 8 (2018) 1207-1228.

[8] C.-M. Puscasu, E.M. Seftel, M. Mertens, P. Cool, G. Carja, ZnTiLDH and the Derived Mixed Oxides as Mesoporous Nanoarchitectonics with Photocatalytic Capabilities, Journal of Inorganic and Organometallic Polymers and Materials, 25 (2015) 259-266.

[9] Y. Zhu, R. Zhu, G. Zhu, M. Wang, Y. Chen, J. Zhu, Y. Xi, H. He, Plasmonic Ag coated Zn/Ti-LDH with excellent photocatalytic activity, Applied Surface Science, 433 (2018) 458-467.

[10] S. Das, S. Patnaik, K.M. Parida, Fabrication of a Au-loaded $CaFe_2O_4$/CoAl LDH p–n junction based architecture with stoichiometric H_2 & O_2 generation and Cr(vi) reduction under visible light, Inorganic Chemistry Frontiers, 6 (2019) 94-109.

[11] C. Li, Z. Sun, W. Huang, S. Zheng, Facile synthesis of g-C_3N_4 /montmorillonite composite with enhanced visible light photodegradation of rhodamine B and tetracycline, Journal of the Taiwan Institute of Chemical Engineers, 66 (2016) 363-371.

[12] I. Fatimah, S. Wang, D. Wulandari, ZnO/montmorillonite for photocatalytic and photochemical degradation of methylene blue, Applied Clay Science, 53 (2011) 553-560.

[13] P. Li, L. Huang, Y. Li, Y. Xu, S. Huang, D. Yuan, H. Xu, H. Li, Synthesis of dark orange montmorillonite/g-C_3N_4 composites and their applications in the environment, Journal of Physics and Chemistry of Solids, 107 (2017) 131-139.

[14] R. Djellabi, M.F. Ghorab, C.L. Bianchi, G. Cerrato, S. Morandi, Recovery of hexavalent chromium from water using photoactive TiO_2-montmorillonite under sunlight, Mediterranean Journal of Chemistry, 5 (2016) 442-449.

[15] B. Xie, H. Zhang, P. Cai, R. Qiu, Y. Xiong, Simultaneous photocatalytic reduction of Cr(VI) and oxidation of phenol over monoclinic $BiVO_4$ under visible light irradiation, Chemosphere, 63 (2006) 956-963.

[16] X. Yuan, Q. Jing, J. Chen, L. Li, Photocatalytic Cr(VI) reduction by mixed metal oxide derived from ZnAl layered double hydroxide, Applied Clay Science, 143 (2017) 168-174.

[17] M. Epifani, S. Kaciulis, A. Mezzi, D. Altamura, C. Giannini, R. Díaz, C. Force, A. Genç, J. Arbiol, P. Siciliano, E. Comini, I. Concina, Inorganic Photocatalytic Enhancement: Activated RhB Photodegradation by Surface Modification of SnO_2 Nanocrystals with V_2O_5-like species, Scientific Reports, 7 (2017) 44763-44770.

[18] X. Zhang, L. Song, X. Zeng, M. Li, Effects of Electron Donors on the TiO_2 Photocatalytic Reduction of Heavy Metal Ions under Visible Light, Energy Procedia, 17 (2012) 422-428.

[19] D. Xiao, K. Dai, Y. Qu, Y. Yin, H. Chen, Hydrothermal synthesis of α-Fe_2O_3/g-C_3N_4 composite and its efficient photocatalytic reduction of Cr(VI) under visible light, Applied Surface Science, 358 (2015) 181-187.

[20] S.G. Schrank, H.J. José, R.F.P.M. Moreira, Simultaneous photocatalytic Cr(VI) reduction and dye oxidation in a TiO_2 slurry reactor, Journal of Photochemistry and Photobiology A: Chemistry, 147 (2002) 71-76.

[21] X. Yuan, C. Zhou, Q. Jing, Q. Tang, Y. Mu, A.K. Du, Facile Synthesis of g-C_3N_4 Nanosheets/ZnO Nanocomposites with Enhanced Photocatalytic Activity in Reduction of Aqueous Chromium(VI) under Visible Light, Nanomaterials (Basel), 6 (2016) 173, 1-12.

[22] S. Nayak, K.M. Parida, Dynamics of Charge-Transfer Behavior in a Plasmon-Induced Quasi-Type-II p–n/n–n Dual Heterojunction in Ag@Ag_3PO_4/g-C_3N_4/NiFe LDH Nanocomposites for Photocatalytic Cr(VI) Reduction and Phenol Oxidation, ACS Omega, 3 (2018) 7324-7343.

[23] Y. He, L. Zhang, M. Fan, X. Wang, M.L. Walbridge, Q. Nong, Y. Wu, L. Zhao, Z-scheme SnO_{2-x}/g-C_3N_4 composite as an efficient photocatalyst for dye degradation and photocatalytic CO_2 reduction, Solar Energy Materials and Solar Cells, 137 (2015) 175-184.

[24] Y. Zhao, D. Zhao, C. Chen, X. Wang, Enhanced photo-reduction and removal of Cr(VI) on reduced graphene oxide decorated with TiO_2 nanoparticles, J Colloid Interface Sci, 405 (2013) 211-217.

[25] K. Saravanakumar, R. Karthik, S.M. Chen, J. Vinoth Kumar, K. Prakash, V. Muthuraj, Construction of novel Pd/CeO_2/g-C_3N_4 nanocomposites as efficient visible-light photocatalysts for hexavalent chromium detoxification, J Colloid Interface Sci, 504 (2017) 514-526.

[26] W. Luo, K. Sasaki, T. Hirajima, Surfactant-modified montmorillonite by benzyloctadecyldimethylammonium chloride for removal of perchlorate, Colloids and Surfaces A: Physicochemical and Engineering Aspects, 481 (2015) 616-625.
[27] Z.A. Zakaria, Z. Zakaria, S. Surif, W.A. Ahmad, Hexavalent chromium reduction by Acinetobacter haemolyticus isolated from heavy-metal contaminated wastewater, J Hazard Mater, 146 (2007) 30-38.
[28] Z. Wei, F. Liang, Y. Liu, W. Luo, J. Wang, W. Yao, Y. Zhu, Photoelectrocatalytic degradation of phenol-containing wastewater by TiO_2/g-C_3N_4 hybrid heterostructure thin film, Applied Catalysis B: Environmental, 201 (2017) 600-606.
[29] X. Bai, L. Wang, Y. Wang, W. Yao, Y. Zhu, Enhanced oxidation ability of g-C_3N_4 photocatalyst via C60 modification, Applied Catalysis B: Environmental, 152-153 (2014) 262-270.
[30] S.-J. Xia, F.-X. Liu, Z.-M. Ni, W. Shi, J.-L. Xue, P.-P. Qian, Ti-based layered double hydroxides: Efficient photocatalysts for azo dyes degradation under visible light, Applied Catalysis B: Environmental, 144 (2014) 570-579.
[31] M. Shao, J. Han, M. Wei, D.G. Evans, X. Duan, The synthesis of hierarchical Zn–Ti layered double hydroxide for efficient visible-light photocatalysis, Chemical Engineering Journal, 168 (2011) 519-524.
[32] L. Charlet, C. Tournassat, Fe(II)-Na(I)-Ca(II) Cation Exchange on Montmorillonite in Chloride Medium: Evidence for Preferential Clay Adsorption of Chloride – Metal Ion Pairs in Seawater, Aquatic Geochemistry, 11 (2005) 115-137.
[33] Y.L. Ma, Z.R. Xu, T. Guo, P. You, Adsorption of methylene blue on Cu(II)-exchanged montmorillonite, J Colloid Interface Sci, 280 (2004) 283-288.
[34] J. Kielland, Individual Activity Coefficients of Ions in Aqueous Solutions, Journal of the American Chemical Society, 59 (1937) 1675-1678.

Chapter 4

Synthesis and characterization of ZnTi-mixed metal oxide composites including $ZnTiO_3$ as a photocatalyst

4.1. Introduction

It is challenging for human society to satisfy the concept of renewable energy and environmental issues at the same time [1]. Recently, researchers have focused on solar energy source for the sustainable clean environment and renewable energy sources. Thus, photocatalysts are promising and attractive for a clean environment, renewable fuels [2], CO_2 conversion into solar fuels [3], fine chemical production [4], solar cells via utilizing solar energy. So far, titanium oxide (TiO_2) is only one photocatalyst successfully implemented industries at present [5] because of their superior photocatalytic activity, highest chemical stability, and economic availability [6]. However, TiO_2 photocatalyst has limitations which can work only in the ultraviolet region of light wavelength (i.e., about 5% of total solar energy) due to its wide band gap [7]. The visible light-active materials have been focused on developing. As one of them, Zn-Ti mixed metal oxide has been used as a heterogeneous catalyst, in which charge separation efficiency of photogenerated electron-hole pairs were improved within this intra heterojunction for prolonging organic compounds decomposition [8-11]. $ZnTiO_3$ perovskites is an environmentally friendly promising material for a variety of applications including dehydrogenation reactions, microelectronics, optics, low temperature co-fired ceramics, and potential photocatalysis [12-14]. Different synthetic strategies like co-doping improved $ZnTiO_3$ perovskites photocatalytic activity towards application in a visible light region [15]. Niasari et al. [16] have reported that in the sol-gel method, $ZnTiO_3$ perovskite photocatalyst has shown the high photocatalytic efficiency for methyl orange degradation under UV light. The photocatalytic activity was enhanced by keeping the photogenerated charge separation and effective distribution of hydroxyl radical on the

surface of $ZnTiO_3$. The visible light-active of $ZnTiO_3$ photocatalyst has been reported by modified alcoholysis method [17].

Here, we report the preparation of $ZnTiO_3$ in ZnTi mixed metal oxide (ZTM) for photocatalyst derived from ZnTi layered double hydroxides and systematic study by varying molar ratios of Zn/Ti , synthetic methods and calcination temperatures. This is the first report about the surface electronic property of ZTM using the energy-resolved distribution of electron traps pattern (ERDT) [18], related to the phase compositions and photocatalytic performances. The obtained ERDT patterns confirmed the electrical characteristic of the products including the surface and bulk which combing ERDT results with conduction band bottom (CBB), which was used as a fingerprint of a metal oxide including the amorphous phase.

The previous reports regarding of photocatalytic degradation of phenol were summarized in **Table 4.1** to compare with the present work. From the comparative results, we observed that ZTM4-500H could show comparable degradation of phenol. We believe that the present finding might be useful for a detailed understanding of the upcoming research scope of the mixed metal oxide derived from layered double hydroxides photocatalyst for the degradation of phenol.

Table 4.1 Comparison of photocatalytic degradation of phenol

Catalyst	Active compound	Target	C_0	Loading (g/L)	Efficacy (%)	Time (min)	Ref.
$ZnO/ZnTi_2TiO_4$	$ZnO/ZnTi_2TiO_4$	phenol	50 ppm	0.1	80	450	[19]
$ZnO/ZnCr_2O_4$	$ZnO/ZnCr_2O_4$	phenol	50 ppm	0.1	98	210	[19]
$ZnO/ZnAl_2O_4$	$ZnO/ZnAl_2O_4$	phenol	50 ppm	0.1	98	300	[19]
g-C_3N_4/CuONP/ZnAl-MMO	g-C_3N_4/CuONP/ZnAl-MMO	phenol	20 ppm	1.0	65	1440	[20]
BiOCl-TiO_2	BiOCl-TiO_2	phenol	50 ppm	1.0	25	360	[21]
ZnTi MMO	ZnTi MMO	phenol	50 ppm	0.5	90	250	[22]
g-C_3N_4/ZnAl-MMO	g-C_3N_4/ZnAl-MMO	phenol	20 ppm	1.0	75	1440	[20]
g-C_3N_4/CuONP/ZnAl-MMO	g-C_3N_4/CuONP/ZnAl-MMO	phenol	20 ppm	1.0	65	1440	[20]
TiO_2/g-C_3N_4 films	TiO_2/g-C_3N_4 films	phenol	5 ppm	-	100	180	[23]
Au-Pd@g-C_3N_4	Au-Pd@g-C_3N_4	phenol	0.5 mM	0.5	95	120	[24]
ZTM4-500H	ZTM4-500H	phenol	10 ppm	1.0	85	180	This work

4.2. Materials and Methods

4.2.1. Materials and reagents

Zinc nitrate hexahydrate ($Zn(NO_3)_2 \cdot 6H_2O$), titanium chloride ($TiCl_4$), urea ($CO(NH_2)_2$) and phenol (C_6H_5OH) were purchased from Wako Chemicals (Osaka, Japan), and all the chemicals were used without further purification. Ultrapure water was used to prepare synthetic solutions.

4.2.2. Synthesis of ZnTi mixed metal oxides (ZTM)

The ZTM samples were synthesized by varying three different factors such as the molar ratio of Zn/Ti, calcination temperature, and synthetic pathways. Typically, 1.5 g of urea was dissolved in 50 ml of mixed solution of $TiCl_4$ and $Zn(NO_3)_2 \cdot 6H_2O$ with different molar ratios of Zn/Ti (2/1, 4/1 and 6/1) under vigorous stirring, the total molar concentration of [Zn^{2+}] and [Ti^{4+}] is set to 0.25 M in all cases. The above mixture was aged at 130 °C for 24 h. The obtained solid products were separated by filtration, washed several times with de-ionized water, and dried at 75 °C for 24 h. Afterward, the synthetic products were calcined at different temperatures at 400 °C, 500 °C, and 600 °C under air for 2 h. The calcined products were denoted as ZTMx-yz, where x is the initial molar ratio of Zn/Ti (2, 4 and 6), y is the calcination temperature (400 °C, 500 °C and 600 °C) and z is the symbol from the synthetic method (hydrothermal (H) or refluxing (R)).

4.2.3. Characterizations

The characterizations of the solid samples were carried out by X-ray diffraction (XRD), UV–vis diffuse reflectance spectroscopy (DRS), specific surface area (BET method), scanning electron microscopy (SEM), transmission electron microscopy (TEM-EDX), and X-ray photoelectron spectroscopy (XPS). Detailes are described in **Chapter 2**.

4.2.4. Reversed double-beam photoacoustic spectroscopy (RDB-PAS)

Synthetic samples (~200 mg) were set in an order-made PAS cell equipped with an electret condenser microphone and a quartz window on the upper side under N_2 flow saturated with methanol vapor for at least 30 min. A light beam from a Xe lamp with a grating monochromator modulated at 80 Hz by a light chopper was irradiated from 650 nm to 350 nm through the cell window to detect the PAS signal using a digital lock-in amplifier. Energy-resolved distribution of electron traps patterns (ERDT) were obtained by determining the amount of photo-absorption change for accumulated electrons. The combination of ERDT and conduction band bottom (CBB) position (ERDT/CBB patterns) can be used as a fingerprint of samples for comparison of identicalness/similarity/differentness of sample pairs could be quantitatively calculated by the degree of coincidence (Γ). Detailes are described in section 2.1.10.

4.2.5. Photocatalytic test

Photocatalytic performances of synthetic ZTM samples were evaluated by the photocatalytic degradation of phenol under the visible light irradiation. Typically, 50 mg of samples were magnetically stirred in 50 mL of 10 ppm aqueous phenol solution in the dark condition for 30 min to reach the adsorption-desorption equilibrium. The suspensions were irradiated using a 500 W Xe lamp with a cut-off filter. Then, the light source was turned on, and the photoreactor was cooled at 25° C throughout the reaction using a cooling circulator water bath. During the light illumination reaction at different time intervals, the suspension was withdrawn with a syringe and filtrated through a 0.45 μm membrane filter to remove the solid samples. The remaining concentrations of phenol and by-product were determined on a JASCO LC-netII/ADC high-performance liquid chromatography (HPLC) system PU-2089 plus pump, C0-2065 plus column oven and UV-2075 plus detector equipped with a C18 column (K009450, Shodex, Japan). The mobile phase was prepared by mixing deionized water and methanol with the volumetric ratio of 3:7.

Moreover, the radical scavenger test can be seen in chapter 2.4.

4.3. Results and discussion

4.3.1. Characterizations

The crystalline phase of ZTM samples via diverse synthetic conditions were characterized by X-ray diffraction, as shown in **Fig. 4.1a.** The XRD pattern of synthesized ZTM samples showed the main diffraction peaks of ZnO (JCPDS 36-1451). Calcination temperature influenced the phase transformation of ZTMs. The

$ZnTiO_3$ (JCPDS 39-0190) can be observed at 500 °C for ZTM2-500H, ZTM4-500H, and ZTM4-600H, while Zn_2TiO_4 (JCPDS 25-1164) was observed after calcination at 600 °C. These results confirm the transformation of $ZnTiO_3$ to Zn_2TiO_4 at high temperature. The main diffraction peak of $ZnTiO_3$ at 35.3° in 2θ can be indicted to *d*-value about 2.5 Å. In addition, TiO_2 anatase (JCPDS 21-1272) was found at 400°C and 500°C of calcination temperature, and it was transformed to rutile (JCPDS 21-1276) at 600 °C. The hydrothermal product (ZTM4-500H) showed the bimetallic phase of $ZnTiO_3$, which cannot be observed in refluxing method, suggesting that the condition of hydrothermal synthesis (high pressure) promoted the formation of $ZnTiO_3$. The Rietveld analysis determined the quantitative phase composition, as summarized in **Table. 4.2.**

It has shown a trend that the ZnO phase content increased with an increase in the molar ratio of Zn/Ti (ZTM2-500H, ZTM4-500H, ZTM6-500H). It's clear that the increasing of calcination temperature from 400 °C to 600 °C (ZTM4-400H, ZTM4-500H, ZTM4-600H), the phase composition of ZnO decreases due to the transformation of ZnO and TiO_2 to $ZnTiO_3$ and Zn_2TiO_4 [25]. Moreover, the ZTM4-500H showed lower content of ZnO than ZTM4-500R because some of ZnO might be transformed to $ZnTiO_3$.

Table 4.2. Physicochemical characterizations and phase component of ZTM samples

Sample ID	ZnO (%)	$ZnTiO_3$ (%)	Zn_2TiO_4 (%)	TiO_2 (anatase, %)	TiO_2 (rutile, %)	SSA ($m^2 \cdot g^{-1}$)	Eg (eV)	Zn/Ti*
ZTM2-500H	81.8	5.6	-	12.6	-	36.5	3.18	3.34
ZTM4-500H	73.7	17.5	-	8.8	-	31.0	3.17	5.40
ZTM6-500H	99.2	-	-	7.8	-	25.6	3.17	4.20
ZTM4-400H	85.6	-	-	17.4	-	48.6	3.22	5.03
ZTM4-600H	47.7	28.8	20.8	-	2.7	9.30	3.20	4.54
ZTM4-500R	88.7	-	-	11.3	-	38.8	3.18	5.09

* obtained from XPS.

UV–visible absorption spectra of ZTM samples were recorded, as shown in **Fig. 4.1b**. The absorption spectra of ZTM samples synthesized under different synthetic conditions showed the different absorption bands, suggesting that the different synthetic conditions provided the different band gap energies (*E*g). The increasing of calcination temperature (from 400 °C to 600 °C) and the molar ratio of Zn/Ti (2~6) improved the light absorption ability in visible light. The ZTM4-500H showed the strongest light absorption in a visible light region, suggesting that this sample might show the highest photocatalytic activity. In **Fig. 4.1c**, *E*g of the ZTM samples were calculated through the Kubelka–Munk equation. The calculated band gap energy of ZTMs are summarized in **Table 4.2**, showing that the calcination product at 500 °C in hydrothermal method (ZTM2-500H, ZTM4-500H, ZTM6-500H) exhibited the lower *E*g than others. Thus, these products might show higher photocatalytic performance than others (ZTM4-400H, ZTM4-600H, ZTM4-500R).

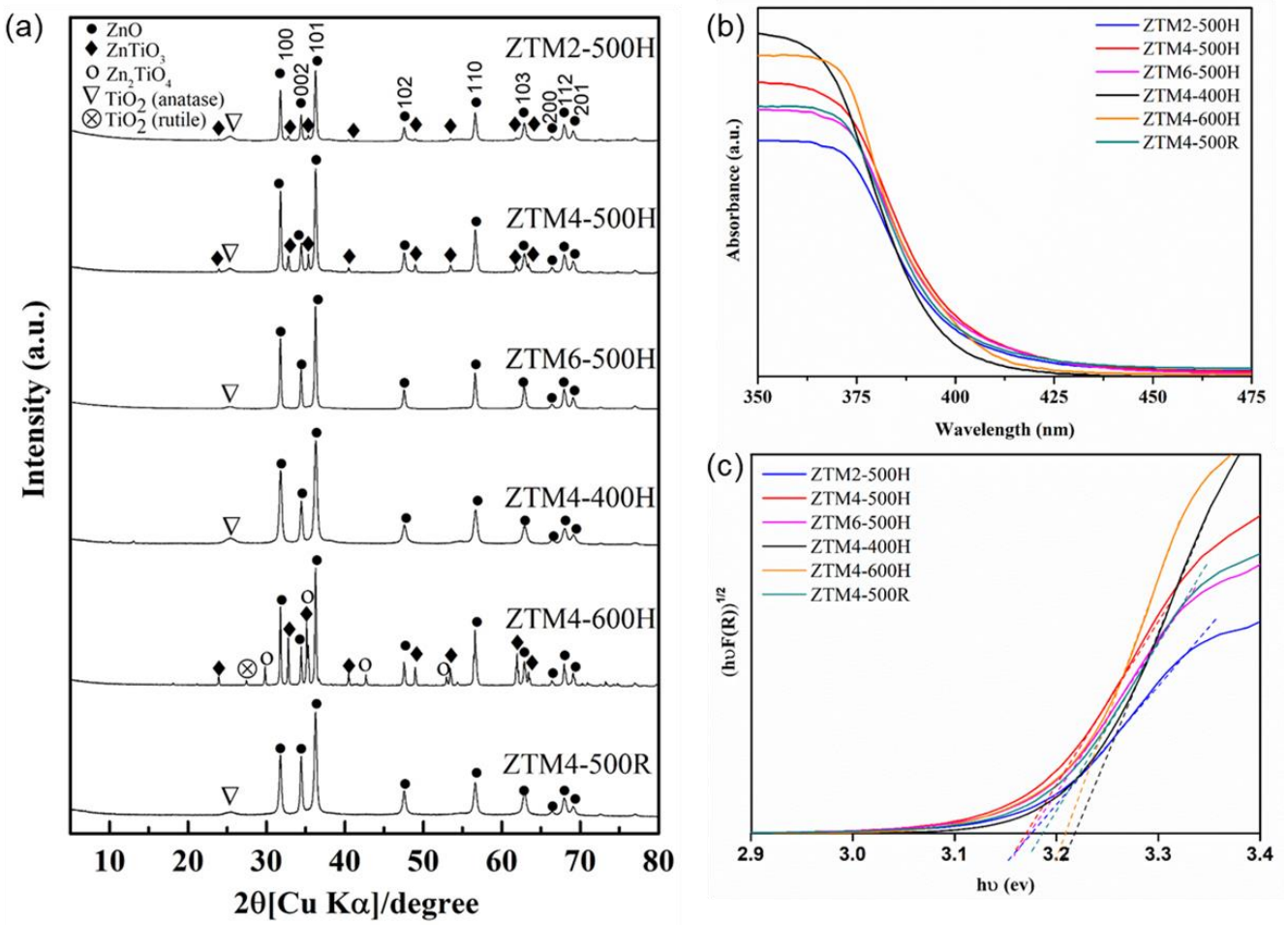

Fig. 4.1 a) PXRD patterns of ZTM samples, **b**) diffuse reflectance UV-visible spectra of ZTM samples, and c) plots between $(h\nu F(R))^{1/2}$ vs. hν (eV) for ZTM samples.

The specific surface areas (SSA) and the average pore size of ZTMs were determined using N_2 adsorption-desorption isotherms, as shown in **Fig. 4.2a** and summarized in **Table 4.2**. The adsorption-desorption isotherms of all samples revealed the IV isotherm types and H1 types, implying mesoporous materials with the average pore size around 8-10 nm. The increasing of the calcination temperatures from 400 °C to 600 °C reduced the SSA from 48.6 m^2g^{-1} to 9.3 m^2g^{-1} (ZTM4-400H, ZTM4-500H, and ZTM4-600H) due to the increasing of particle sizes which are in good agreement with the SEM results (**Fig. 4.4a-f**) even similar surface roughness (**Fig. 4.4g-l**) [26]. The smaller particle size might show photocatalytic performance due to the high SSA and high mobility, leading to enhancement of the separation of photogenerated charge carriers [27].

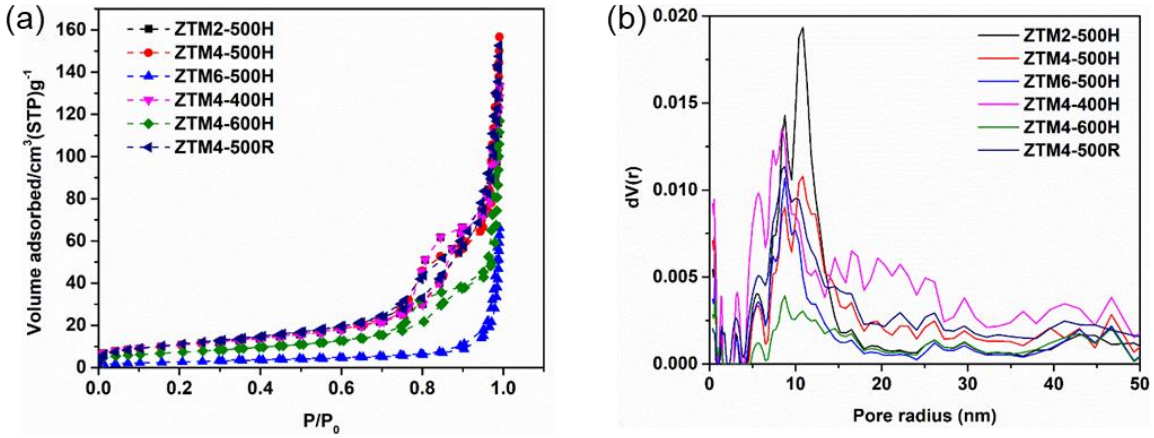

Fig. 4.2 (a) N_2 adsorption-desorption isotherm and (b) average pore size of ZTM sample.

The surface molar ratios of Zn/Ti in all samples were determined by XPS analysis, as summarized in **Table 4.2.** It was found that all of the samples except for ZTM6-500H exhibit the Zn rich on the surface. Moreover, the XPS spectra (**Fig. 4.3**)

for all showed the peak at E_B[Zn $2p_{3/2}$] = 1020.7±0.5 eV, assigned to ZnO [22], and the peak at E_B[Ti $2p_{3/2}$] = 457.8±0.7 eV, assigned to TiO_2 [28, 29].

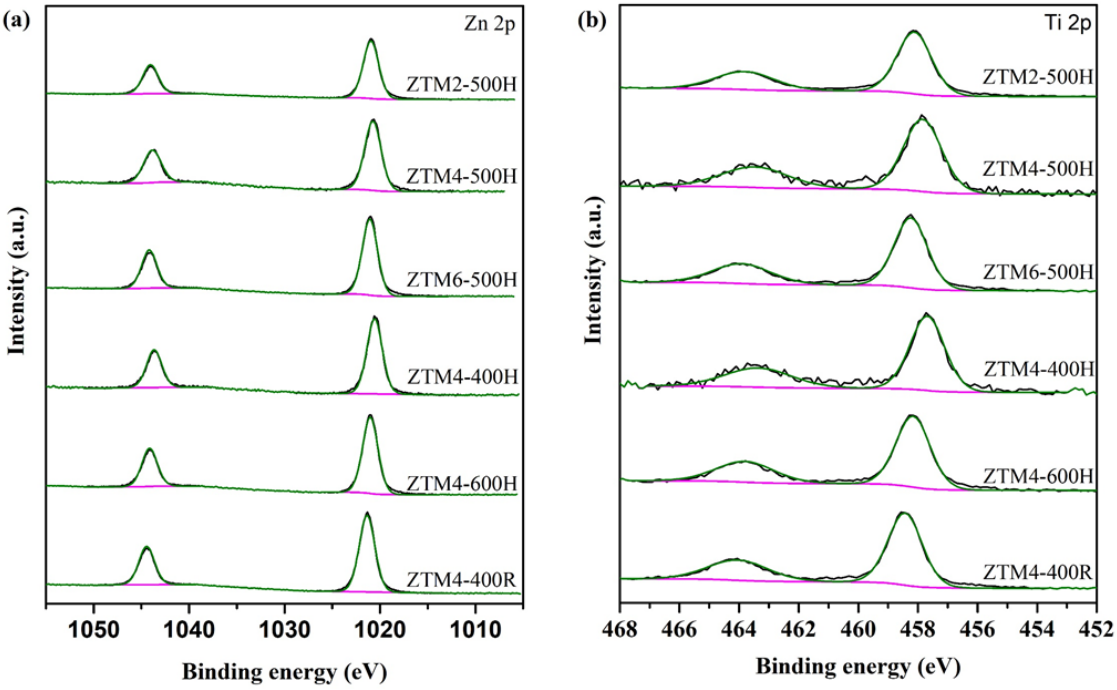

Fig. 4.3 XPS spectra of (a) Zn 2p and (b) Ti 2p of ZTM samples.

SEM images of ZTMs were observed, as shown in **Fig. 4.4a-l**. The hydrothermal synthesis provided the hierarchical structure in ZTM2-500H, ZTM4-500H, ZTM6-500H, ZTM4-400H, ZTM4-600H (**Fig. 4.4a-e, g-k)**, while the plate-like structure of ZTM4-500R can be obtained from refluxing method (**Fig. 4.4f, l)**. The hierarchical structures of ZTM products from hydrothermal synthesis can avoid the recombination of electron and hole, to improve the photocatalytic efficiency. Moreover, the different calcination temperatures and the molar ratios of Zn/Ti did not influence to form a hierarchical structure of the ZTMs in hydrothermal synthesis.

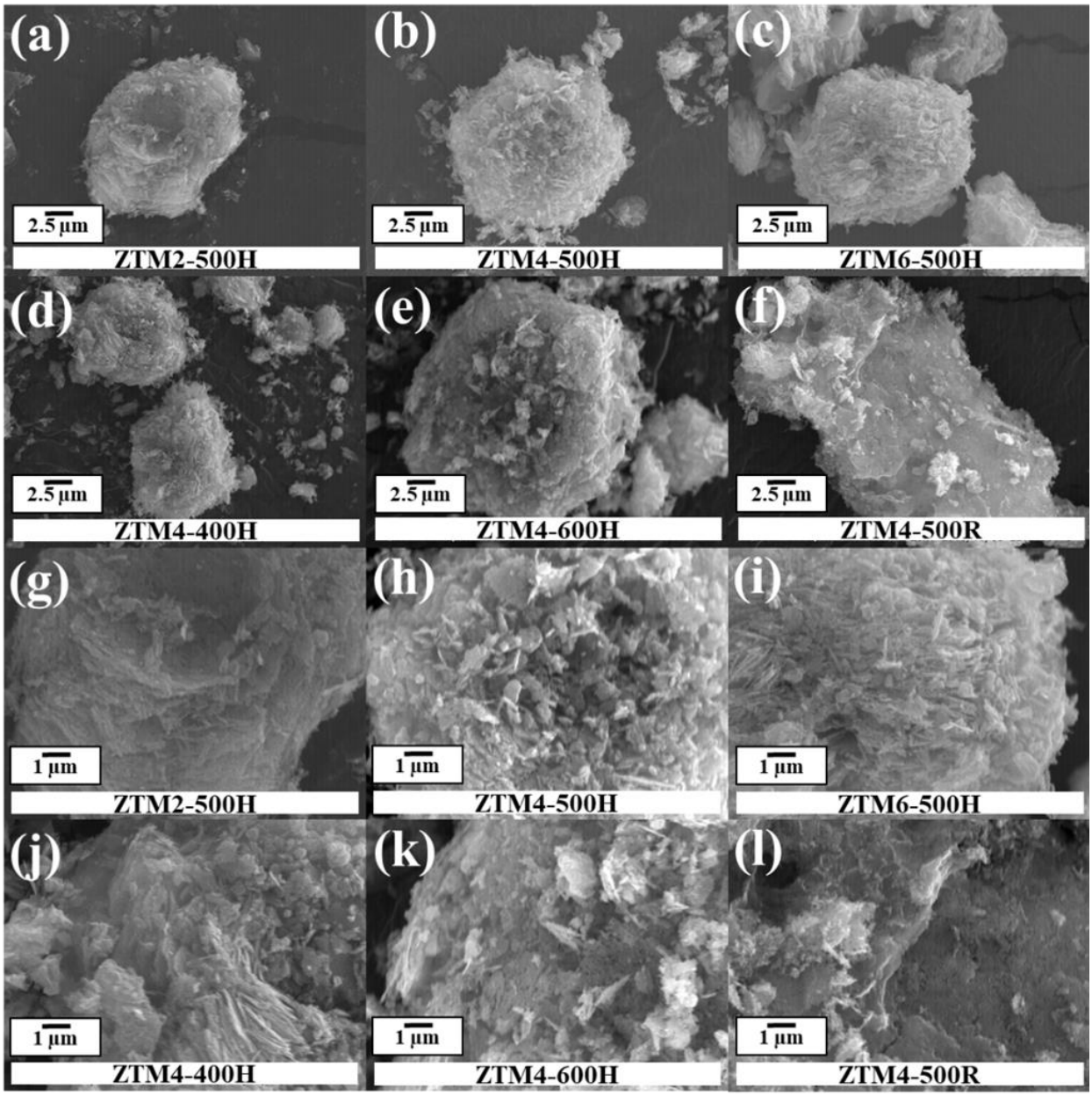

Fig. 4.4 SEM images of (a, g) ZTM2-500H, (b, h) ZTM4-500H, (c, i) ZTM6-500H, (d, j) ZTM4-400H, (e, k) ZTM4-600H and (f, l) ZTM4-500R.

Fig. 4.5 exhibits the HR-TEM images of ZTM4-500H and ZTM4-500R**.** The ZTM4-500H showed better-connected structure than the ZTM4-500R (individual particle) with an average particle size was 30 - 50 nm. The well-connected structure of ZTM4-500H could be implied to the formation of heterojunction, which can enhance

the photogenerated charge separation in the composite. In addition, the presence of $ZnTiO_3$ phase also was confirmed by *d*-spacing around 0.25 nm (**Fig. 4.5c**), which are in good agreement with XRD results (**Fig. 4.1a**).

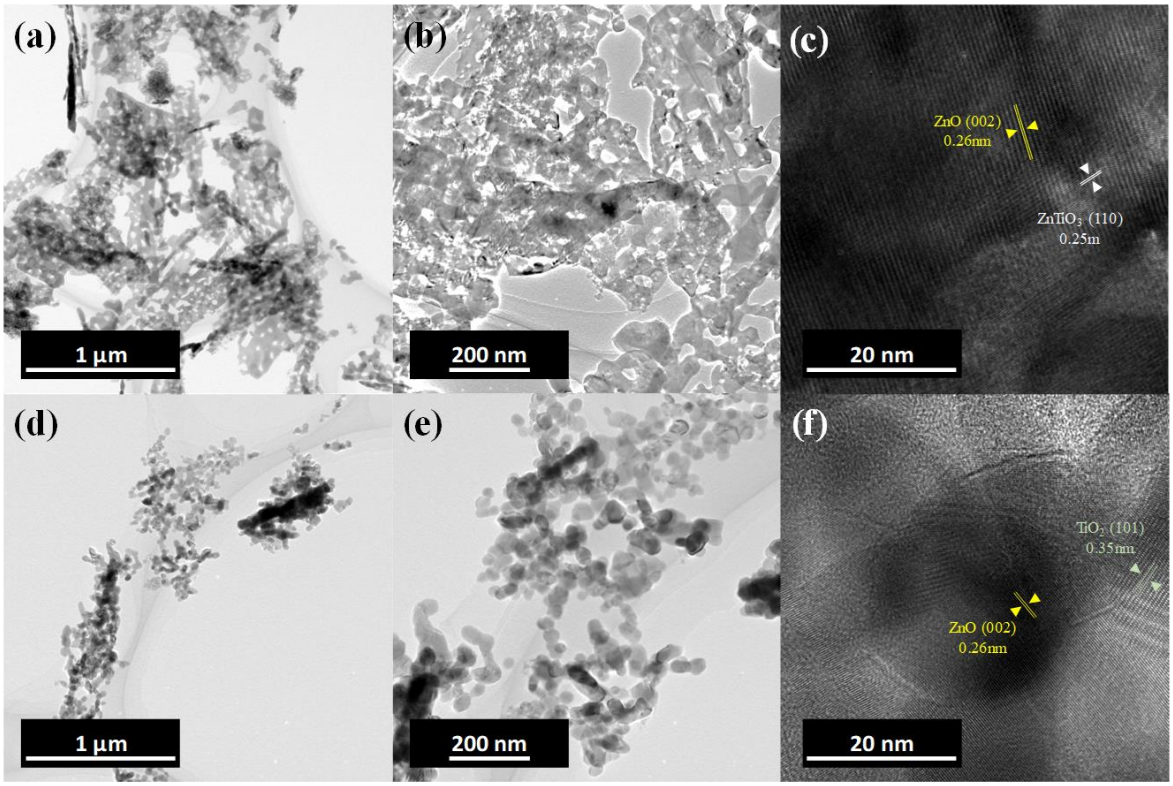

Fig. 4.5 TEM images of (a-c) ZTM4-500H and (d-f) ZTM4-500R.

Furthermore, based on TEM-EDX results of ZTM4-500H (**Fig. 4.6**), three phases of ZnO, $ZnTiO_3$, and TiO_2 are connected, confirming the well-connected phases in ZTM4-500H.

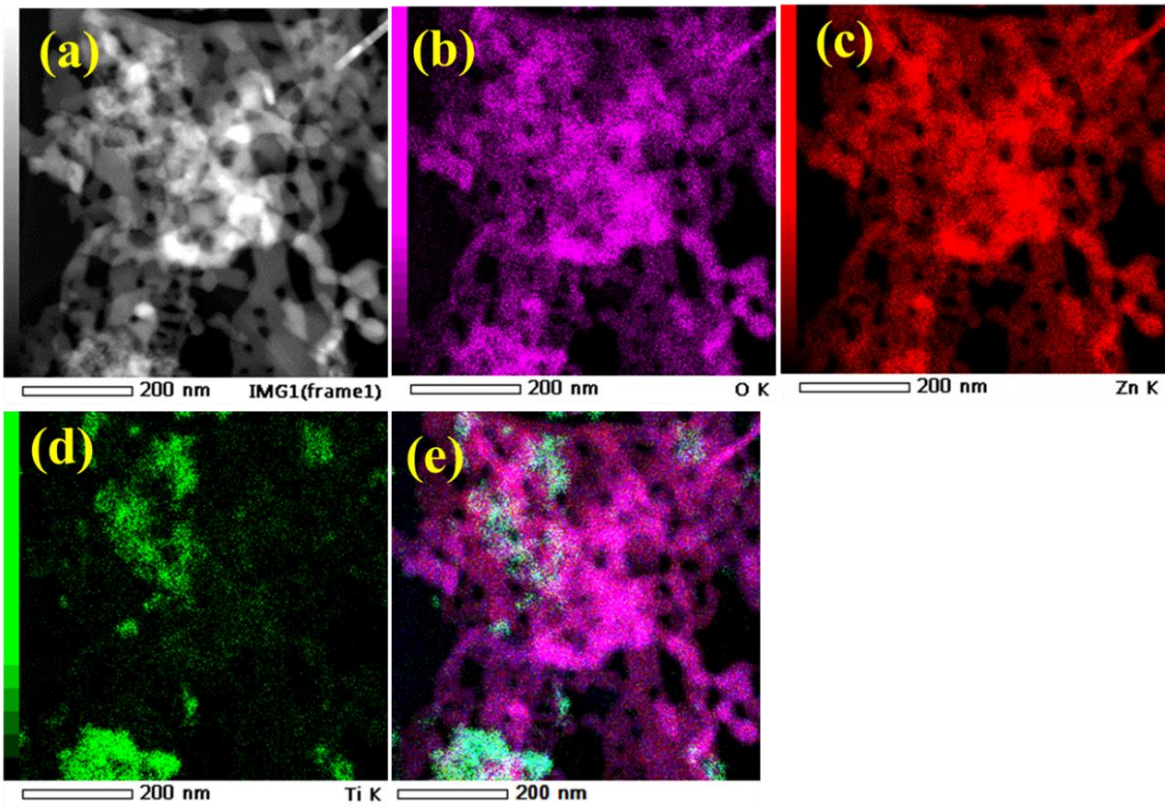

Fig. 4.6 TEM-EDX elemental mapping of (b) O, (c) Zn and (d) Ti in ZTM4-500H.

4.3.2. Photocatalytic degradation of phenol

Photocatalytic performances of synthesized ZTM samples were investigated using phenol degradation, which is a model prototypical organic pollutant [30]. Phenol has negligible absorbance in a region of the visible light and does not cause the photosensitization, which in turn hinder mechanistic insight and performance in benchmarking under the visible light [31]. In **Fig. 4.7a**, the photocatalytic activity was evaluated under irradiation of visible light for net amounts of photodegraded phenol (without catalyst), only <10%, because of photolysis. This indicates that the auto-oxidation of phenol was not significant under light irradiation, suggesting that both

photocatalyst and light irradiation were required for the successfully complete elimination of phenol.

The photocatalytic activities to degrade phenol were in the order of 82.07 % (ZnTM4-500H) > 81.76% (ZnTM6-500H) > 80.27 % (ZnTM2-500H) > 57.36% (ZnTM4-400H) > 55.91% (ZnTM4-600H) > 51.31 % (ZnTM4-500R) at 180 min under visible light irradiation. These samples can be categorized into two groups with high activity (ZnTM2-500H, ZnTM4-500H, ZnTM6-500H) and low activity (ZTM4-400H, ZTM4-600H, ZTM4-500R). ZnTM4-500H consists of ZnO and $ZnTiO_3$, which can make high charge carrier separation of photoinduced electron-hole pairs heterojunction. However, in ZTM6-500H, there is no evidence of the presence of $ZnTiO_3$ phase in XRD. However, the presence of a large amount of $ZnTiO_3$ phase (28.8%) in the ZnTM4-600H photocatalytic efficiency drastically reduced, suggesting that the presence of Zn_2TiO_4 phase (20.8%) is heavily influenced to phenol decomposition by either bulk electronic properties and/or the surface-active species.

Moreover, the excellent photocatalytic activity to degrade phenol on ZTM samples described using the reaction rates. The degradation rate constant for photocatalytic decomposition of phenol was evaluated using pseudo-first-order kinetics and by plotting ln C_0/C_t vs. time (**Eq. 2.2**). The photocatalytic degradation efficiency of phenol was determined using the reaction rates **(Fig. 4.7b)**. Notably, photocatalytic reaction rate constants were significantly larger in high rate group (ZnTM2-500H, ZnTM4-500H, ZnTM6-500H) than in low rate group (ZTM4-400H, ZTM4-600H, ZTM4-500R).

Fig. 4.7c presents the results of radical trapping tests using different scavengers. This suggests that the phenol removal rate declaimed from 85% (no scavenger) to 20% when using IPA and BQ. This significant reduction rate in ZTM-4-500H is due to decreasing in the concentration of both $^{\bullet}OH$ and $^{\bullet}O_2^-$, which play an important role in photocatalytic degradation of phenol.

Many kinds of literature [32-36] hypothetically reported complete mineralization of organic compounds, but it's very important whether degraded by-products are toxic or non-toxic to the environment. Reaction intermediates were identified by HPLC **(Fig. 4.7d).** The main by-products are p-benzoquinone and fumaric acid during 180 min. As expected, benzoquinone is main by-products for all ZTM catalysts for phenol decomposition, and the production also continued during reactions, whereas fumaric acid is the secondary product formed throughout the reaction. Beata et al. [37] reported that the catechol is the primary by-product of phenol mineralization instead of benzoquinone and/or hydroquinone for subsequent formation of carboxylic acid and following mineralization.

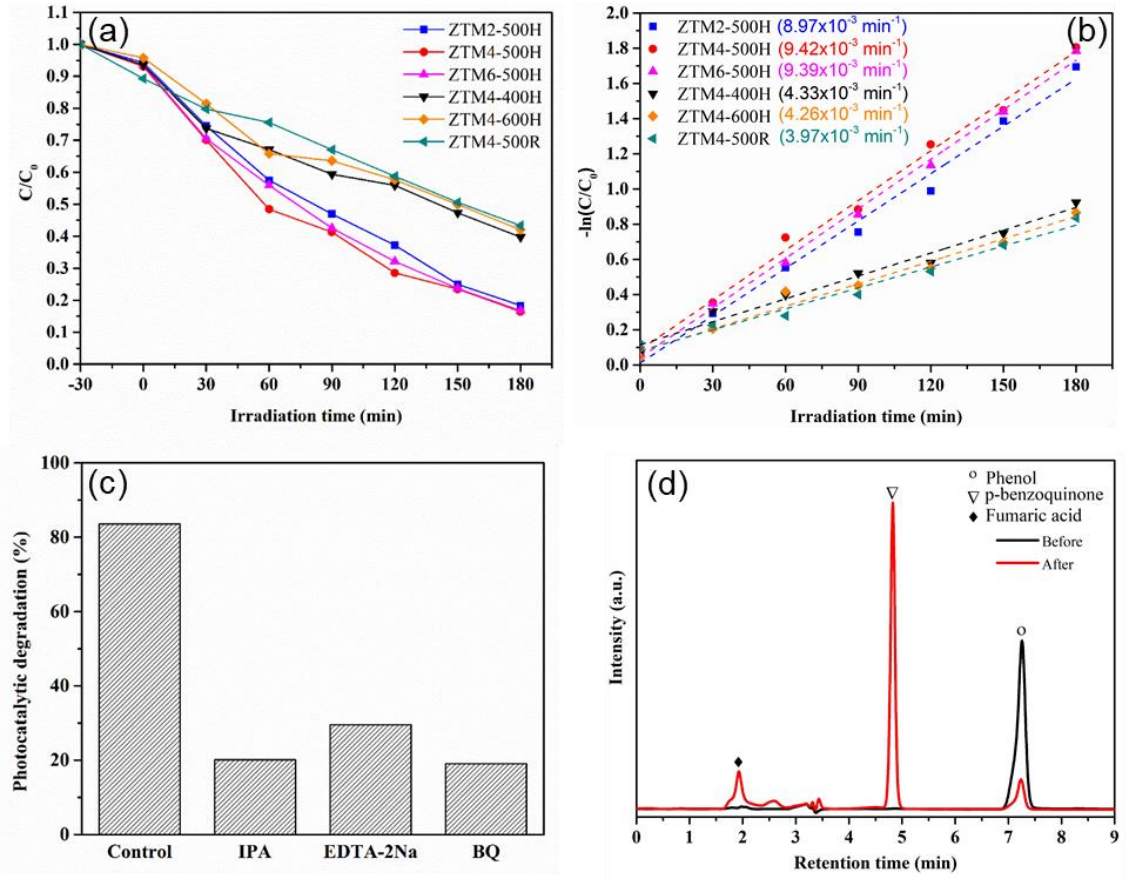

Fig. 4.7 a) Phenol photodegradation by ZTM samples at different time intervals, b) pseudo-first-order kinetics plots, c) photocatalytic phenol degradation over ZTM4-500H in the presence of radical scavengers and d) HPLC spectra of before and after of photocatalytic degradation of phenol over ZTM4-500H catalyst. (50 mg ZTM catalyst, 50 mL of 10 ppm phenol, 500 W Xe lamp, 0.1 mmol of scavenger into to 50 mL phenol solution, for 180 min).

4.3.3. Reversed double-beam photoacoustic spectroscopy (RDB-PAS)

In **Fig. 4.8**, the different calcination temperatures showed the different ERDT patterns (ZTM4-400H, ZTM4-500H, ZTM4-600H), while the different Zn/Ti molar ratios displayed similar ERDT patterns (ZTM2-500H, ZTM4-500H, ZTM6-500H) even with different phases in XRD. In comparison, the ZTM4-400H and ZTM4-500R displayed similar ERDT/CBB patterns which have the highest electron accumulation around 3.5 eV from VBT, implying to be due to characteristics of ZnO. The ERDT patterns for ZTM2-500H and ZTM4-500H, containing ZnO and $ZnTiO_3$, showed the highest electron accumulation around 3.1 eV near conduction band bottom (CBB).

The ERDT patterns for ZTM2-500H and ZTM4-500H compose of not only the characteristic pattern of ZnO at 3.5 eV but also new characteristic of electron accumulation at 3.1 eV derived from $ZnTiO_3$. However, the characteristic of $ZnTiO_3$ observed in ERDT for ZTM6-500H was not observed in XRD, indicating that the ZTM6-500H would contain the amorphous phase of $ZnTiO_3$. In addition, the ERDT pattern for ZTM6-500H showed the greatest electron accumulation around 3.2 eV, which can be assigned to TiO_2 (anatase) on the surface [38]. This is in good agreement with the result of XPS (**Table 4.2**) that the surface of ZTM6-500H is relatively Ti-rich. Moreover, when the calcination temperature increased to 600 °C, the largest peak in ERDT/CBB pattern for ZTM4-600H has shifted to lower energy around 2.9 eV, attributed to the formation of new phases of Zn_2TiO_4 and TiO_2 (rutile) that covered on the surface of mixed metal oxide particles which were confirmed by XRD (**Fig. 4.1a**).

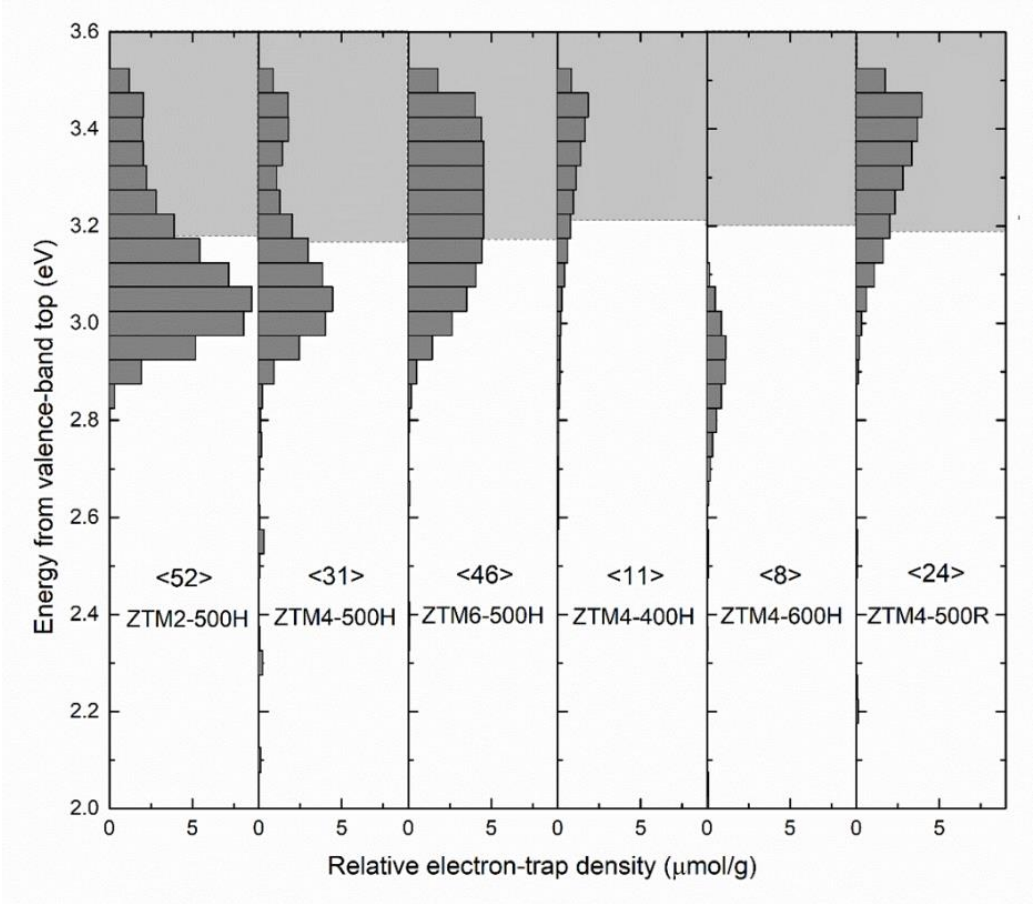

Fig. 4.8 Representative ERDT/CBB patterns of as-prepared samples plotted as a function of energy (eV) from the valence band top (VBT) combined with CBB. Numbers in brackets denote the relative total electron-trap density in the unit of μmol/g.

Table 4.3. Calculated partial and overall degrees of coincidence for ZTM samples.

		ZTM2-500H	ZTM4-500H	ZTM6-500H	ZTM4-400H	ZTM4-600H	ZTM4-500R
ZTM2-500H	ζ(a)	-	0.85	0.40	0.11	0.23	0.08
	ζ(b)	-	0.57	0.86	0.22	0.16	0.45
	ζ(c)	-	0.99	1.00	0.99	0.99	1.00
	ζ	-	**0.64**	**0.37**	0.05	0.09	0.05
ZTM4-500H	ζ(a)	0.85	-	0.47	0.14	0.16	0.08
	ζ(b)	0.57	-	0.67	0.38	0.27	0.79
	ζ(c)	1.00	-	1.00	0.98	0.99	1.00
	ζ	**0.64**	-	**0.38**	0.08	0.08	0.07
ZTM6-500H	ζ(a)	0.40	0.47	-	0.51	0.07	0.52
	ζ(b)	0.86	0.67	-	0.25	0.18	0.52
	ζ(c)	1.00	1.00	-	0.99	0.99	1.00
	ζ	**0.37**	**0.38**	-	0.25	0.03	**0.38**
ZTM4-400H	ζ(a)	0.11	0.14	0.51	-	0.07	0.89
	ζ(b)	0.22	0.38	0.25	-	0.71	0.34
	ζ(c)	0.99	0.98	0.99	-	1.01	1.01
	ζ	0.05	0.08	0.25	-	0.06	**0.52**
ZTM4-600H	ζ(a)	0.23	0.16	0.07	0.07	-	0.00
	ζ(b)	0.16	0.27	0.18	0.71	-	0.34
	ζ(c)	1.00	0.99	0.99	1.01	-	1.01
	ζ	0.09	0.08	0.03	0.06	-	0.00
ZTM4-500R	ζ(a)	0.08	0.08	0.52	0.89	0.00	-
	ζ(b)	0.45	0.79	0.52	0.34	0.34	-
	ζ(c)	0.99	1.00	1.00	1.01	1.01	-
	ζ	0.05	0.07	**0.38**	**0.52**	0.00	-

The degrees of coincidence (ζ) for each ZTM sample pair were summarized in **Table 4.3**. To evaluate the similarity of the ERDT/CBB patterns of all as-prepared ZTM samples, the degrees of coincidence (ζ) of every pair comparison can be applied by calculation based on three factors, ERDT-pattern shape ζ(a), total electron-trap density ζ(b) and CBB position ζ(c). The factor ζ(c) is reflected by the property of bulk structure, while the ζ(a) and ζ(b) is contributed by the surface structure properties. The overall degree of coincidence of different samples can be evaluated by using the equation (4.1):

$$\zeta = \zeta(a) * \zeta(b)^{\frac{1}{2}} * \zeta(c)^2 \tag{4.1}$$

Where ζ(a) is ERDT pattern matching (f) that is evaluated for two ERDT patterns f_s (ERDT-pattern profiles as a function of energy from VBT; integrated f is equal to the total density of ETs, D, $f(1)$ and $f(2)$ ($D(1) < D(2)$), as shown in equation (4.2, 4.3).

$$\zeta(a) = 1 - \frac{\int |f(1) - \alpha f(2)|}{\int f(1)} \; [\int f(1) < \int f(2)] \tag{4.2}$$

with 'α' to minimize

$$\alpha: \int \big(f(1) - \alpha f(2)\big)^2 \; (minimun) \tag{4.3}$$

ζ(b) is the total Density of Ets (D) that evaluated by using the equation (4.4):

$$\zeta(b) = \frac{D(1)}{D(2)} \; [D(1) < D(2)] \tag{4.4}$$

and ζ(c) is CBB Energy that evaluated by using the equation (4.5):

$$\zeta(c) = \frac{CBB(1)}{CBB(2)} [CBB(1) < CBB(2)] \tag{4.5}$$

In comparison with ZTM4-500H, the high overall degrees of coincidence (ζ) of ZTM2-500H and ZTM6-500H (0.64 and 0.38) were observed due to high values of ζ(a) and ζ(b), indicating that these samples might have more similar phase compositions than others. Moreover, the comparison between ZTM4-400H and ZTM4-500R showed high ζ (0.52), suggesting that it has similar phase compositions which were confirmed by XRD results (**Fig. 4.1a**). Based on the above results, the present samples can be classified into 2 groups, in which one includes ZTM2-500H, ZTM4-500H, and ZTM6-500H, and another one includes ZTM4-400H, ZTM4-600H, and ZTM4-500R. The classification based on the similarity of ERDT/CBB pattern can be well related to the photocatalytic performances of ZTM samples in phenol degradation. The former group samples (ZnTM2-500H, ZnTM4-500H, ZnTM6-500H) have always shown the high photocatalytic activities, while the latter group samples (ZTM4-400H, ZTM4-600H and ZTM4-500R) showed much lower activities (**Fig. 4.7a, b**). The reason why ZTM6-500H showed the high photocatalytic activity could be explained by the presence of amorphous $ZnTiO_3$ phase, which cannot be observed in XRD but is suggested by ERDT pattern. This suggests there is a correlative relationship between the similarity of ERDT/CBB patterns and the similarity of photocatalytic activity. Also, the subtracted pattern of ZTM6-500H by ZTM4-500H was calculated to compare with TiO_2 (anatase), as shown in **Fig. 4.9**. The results show that the subtracted pattern of ZTM6-500H show high ζ(a) suggesting that the peak around 3.2 is in good agreement with TiO_2 (anatase) (**Table 4.4**).

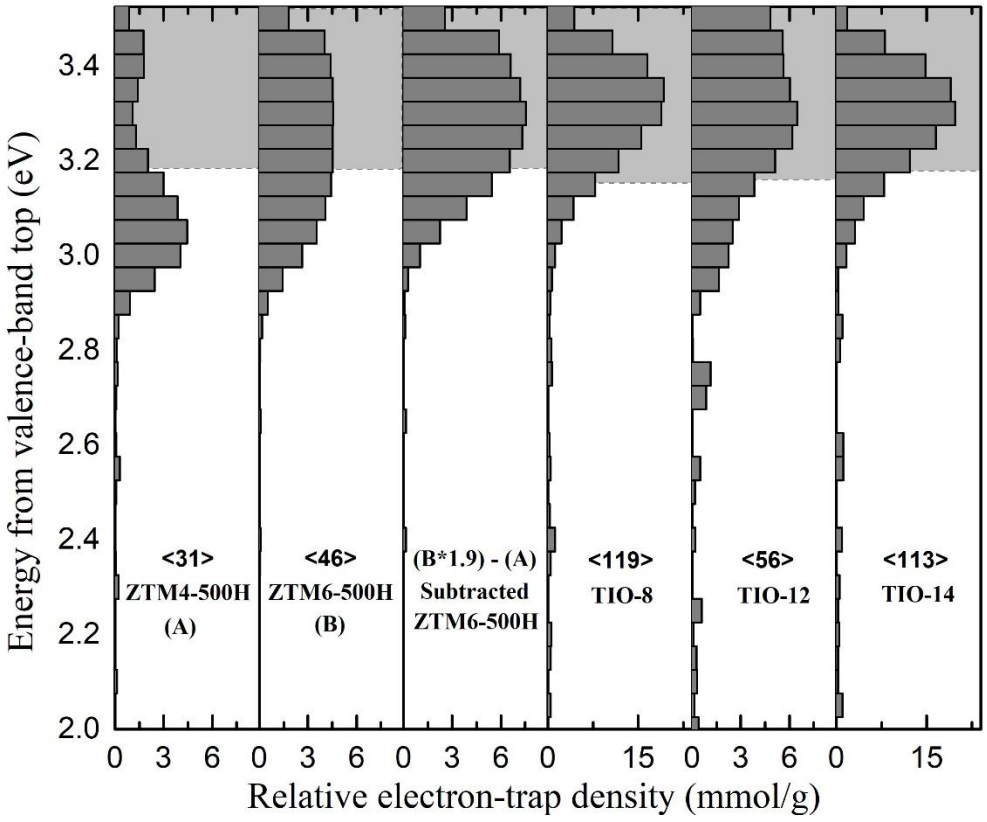

Fig. 4.9 Representative ERDT/CBB patterns of ZTM4-500H, ZTM4-500H, subtracted ZTM6-500H and references of TiO_2 (anatase) plotted as a function of energy (eV) from the valence band top (VBT) combined with CBB. Numbers in brackets denote the relative total electron-trap density in the unit of μmol/g.

Table 4.4. Calculated partial and overall degrees of coincidence for subtracted ZTM6-500H.

TiO_2 (anatase)	**ζ(a)**
TIO-8	0.74
TIO-12	0.67
TIO-14	0.71

4.3.4. Photocatalytic mechanism of phenol degradation over ZTM samples

To interpret the transfer of electron in the higher performance group, the electronic band structures of ZnO, TiO_2 (anatase) and $ZnTiO_3$ must be focused to consider. The VB and CB of ZnO have been reported about 3.05 eV and −0.12 eV *vs.* NHE, respectively [39], while the VB and CB of TiO_2 (anatase) have been reported about 3.08 eV and -0.10 eV [40]. Under the visible light irradiation, the photogenerated electron and hole were produced and separated at different electronic states. The photogenerated electron will move from VB to CB, leaving the photogenerated hole in the VB. The VB potentials of ZnO and TiO_2 (anatase) are more negative than the VB potential of $ZnTiO_3$ (2.83 eV vs. NHE), leading to the migration of hole from VB of ZnO and TiO_2 to VB of $ZnTiO_3$ [41]. The electrons can be transferred from $ZnTiO_3$ and ZnO to the surface of TiO_2 (anatase). Moreover, the responsibility of photocatalytic reactive species (hydroxyl radicals as well as superoxide radicals) has been explained based on the previous reports [42, 43]. In degradation of phenol, the electrons in the CB of TiO_2 (anatase) can be reacted with dissolved O_2 molecules in water to produce reactive oxygen species (standard redox potential $E^0(O_2/^{\bullet}O_2^-)$ = −0.046 eV *vs.* NHE), simultaneously the holes in VB of $ZnTiO_3$ can be reacted with H_2O molecules to produce hydroxyl radicals ($E^0(H_2O/^{\bullet}OH)$ = 2.38 eV *vs.* NHE). Thus, the generated reactive species ($^{\bullet}O_2^-$ and $^{\bullet}OH$) can jointly decompose phenol into smaller molecular compounds as byproducts, like fumaric acid and p-benzoquinone [7, 44], through oxidation. However, in ZTM4-600H, the production of $^{\bullet}OH$ is suppressed, since the more negative level of the VB of coexisting Zn_2TiO_4 (2.10 eV vs. NHE) than reduction potential of $^{\bullet}OH$ production. Based on the heterojunction among ZnO, TiO_2 and $ZnTiO_3$, the photocatalytic mechanism of high

activity group sample (ZnTM2-500H, ZnTM4-500H, ZnTM6-500H) can be proposed as illustrated in **Fig. 4.10.**

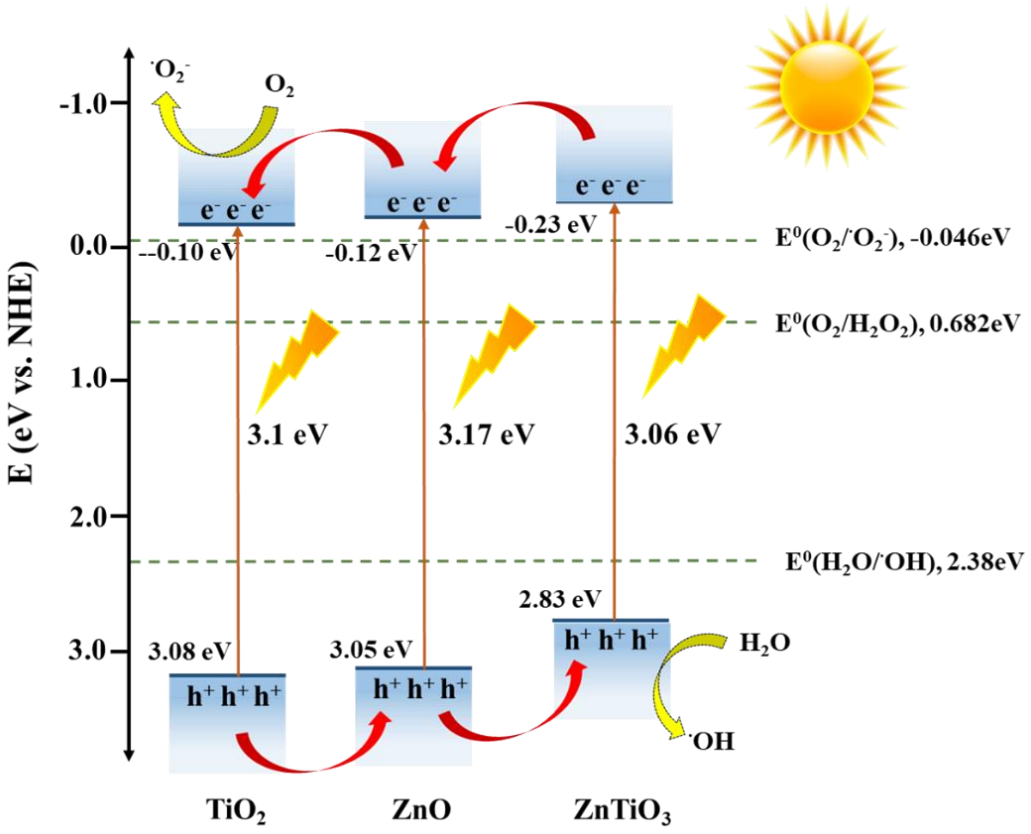

Fig. 4.10 Proposed mechanism in photocatalytic degradation of phenol on ZTM2-500H, ZTM4-500H and ZTM6-500H.

4.4 Conclusions

In the present work, we reported at the first about $ZnTiO_3$ contained in mixed metal oxide was prepared by calcination of ZnTi layered double hydroxide, synthesized from the hydrothermal method. The different calcination temperatures can control the phase component and the optical properties towards visible, active photocatalyst. The calcined products at 500 °C (ZTM2-500H, ZTM4-500H, ZTM6-500H) provided the crystalline/amorphous phase of $ZnTiO_3$, which is confirmed by

RDB-PAS technique. The high photocatalytic activity for phenol degradation of calcined products from 500 °C might be obtained from the high separation of photogenerated charge carrier and light absorption ability due to the existing of $ZnTiO_3$ phase.

References

[1] W.-J. Ong, L.-L. Tan, Y.H. Ng, S.-T. Yong, S.-P. Chai, Graphitic Carbon Nitride ($g\text{-}C_3N_4$)-Based Photocatalysts for Artificial Photosynthesis and Environmental Remediation: Are We a Step Closer To Achieving Sustainability?, Chemical Reviews, 116 (2016) 7159-7329.

[2] K. Maeda, K. Teramura, D. Lu, T. Takata, N. Saito, Y. Inoue, K. Domen, Photocatalyst releasing hydrogen from water, Nature, 440 (2006) 295-295.

[3] H. Rao, L.C. Schmidt, J. Bonin, M. Robert, Visible-light-driven methane formation from CO_2 with a molecular iron catalyst, Nature, 548 (2017) 74 –77.

[4] C.S. Ponseca, P. Chábera, J. Uhlig, P. Persson, V. Sundström, Ultrafast Electron Dynamics in Solar Energy Conversion, Chemical Reviews, 117 (2017) 10940-11024.

[5] K. Hashimoto, H. Irie, A. Fujishima, TiO_2 photocatalysis: a historical overview and future prospects, Japanese journal of applied physics, 44 (2005) 8269-8285.

[6] A. Fujishima, K. Honda, Electrochemical photolysis of water at a semiconductor electrode, nature, 238 (1972) 37-38.

[7] B. Barrocas, T.J. Entradas, C.D. Nunes, O.C. Monteiro, Titanate nanofibers sensitized with ZnS and Ag_2S nanoparticles as novel photocatalysts for phenol removal, Applied Catalysis B: Environmental, 218 (2017) 709-720.

[8] S. Yang, P. Wu, M. Chen, Z. Huang, W. Li, N. Zhu, Y. Ji, Enhanced photo-degradation of bisphenol a under simulated solar light irradiation by Zn–Ti mixed metal oxides loaded on graphene from aqueous media, RSC Advances, 6 (2016) 26495-26504.

[9] K.S. Ranjith, T. Uyar, Conscientious Design of Zn-S/Ti-N Layer by Transformation of $ZnTiO_3$ on Electrospun $ZnTiO_3@TiO_2$ Nanofibers: Stability and

Reusable Photocatalytic Performance under Visible Irradiation, ACS Sustainable Chemistry & Engineering, 6 (2018) 12980-12992.

[10] M.A. Aramendía, V. Borau, J.C. Colmenares, A. Marinas, J.M. Marinas, J.A. Navío, F.J. Urbano, Modification of the photocatalytic activity of Pd/TiO_2 and Zn/TiO_2 systems through different oxidative and reductive calcination treatments, Applied Catalysis B: Environmental, 80 (2008) 88-97.

[11] Y. Huang, Y. Wei, J. Wu, C. Guo, M. Wang, S. Yin, T. Sato, Low temperature synthesis and photocatalytic properties of highly oriented ZnO/$TiO_2^{-x}N^y$ coupled photocatalysts, Applied Catalysis B: Environmental, 123-124 (2012) 9-17.

[12] K.H. Reddy, S. Martha, K.M. Parida, Erratic charge transfer dynamics of Au/$ZnTiO_3$ nanocomposites under UV and visible light irradiation and their related photocatalytic activities, Nanoscale, 10 (2018) 18540-18554.

[13] Z.X. Chen, A. Derking, W. Koot, M.P. van Dijk, Dehydrogenation of Isobutane over Zinc Titanate Thin Film Catalysts, Journal of Catalysis, 161 (1996) 730-741.

[14] Z.-X. Li, F.-B. Shi, Y. Ding, T. Zhang, C.-H. Yan, Facile Synthesis of Highly Ordered Mesoporous $ZnTiO_3$ with Crystalline Walls by Self-Adjusting Method, Langmuir, 27 (2011) 14589-14593.

[15] A. Ali, X. Li, J. Song, S. Yang, W. Zhang, Z. Zhang, R. Xia, L. Zhu, X. Xu, Nature-Mimic ZnO Nanoflowers Architecture: Chalcogenide Quantum Dots Coupling with ZnO/$ZnTiO_3$ Nanoheterostructures for Efficient Photoelectrochemical Water Splitting, The Journal of Physical Chemistry C, 121 (2017) 21096-21104.

[16] M. Salavati-Niasari, F. Soofivand, A. Sobhani-Nasab, M. Shakouri-Arani, A. Yeganeh Faal, S. Bagheri, Synthesis, characterization, and morphological control of $ZnTiO_3$ nanoparticles through sol-gel processes and its photocatalyst application, Advanced Powder Technology, 27 (2016) 2066-2075.

[17] J.-Z. Kong, A.-D. Li, H.-F. Zhai, H. Li, Q.-Y. Yan, J. Ma, D. Wu, Preparation, characterization and photocatalytic properties of $ZnTiO_3$ powders, Journal of Hazardous Materials, 171 (2009) 918-923.

[18] A. Nitta, M. Takase, M. Takashima, N. Murakami, B. Ohtani, A fingerprint of metal-oxide powders: energy-resolved distribution of electron traps, Chemical Communications, 52 (2016) 12096-12099.

[19] C.M. Puscasu, G. Carja, M. Mureseanu, C. Zaharia, Mixed oxides derived from layered double hydroxides as novel catalysts for phenol photodegradation, IOP Conference Series: Materials Science and Engineering, 227 (2017) 012105, 1-8.
[20] M. Mureseanu, T. Radu, R.-D. Andrei, M. Darie, G. Carja, Green synthesis of g-C_3N_4/CuONP/LDH composites and derived g-C_3N_4/MMO and their photocatalytic performance for phenol reduction from aqueous solutions, Applied Clay Science, 141 (2017) 1-12.
[21] D. Sánchez-Rodríguez, M.G. Méndez Medrano, H. Remita, V. Escobar-Barrios, Photocatalytic properties of BiOCl-TiO_2 composites for phenol photodegradation, Journal of Environmental Chemical Engineering, 6 (2018) 1601-1612.
[22] C.-M. Puscasu, E.M. Seftel, M. Mertens, P. Cool, G. Carja, ZnTiLDH and the Derived Mixed Oxides as Mesoporous Nanoarchitectonics with Photocatalytic Capabilities, Journal of Inorganic and Organometallic Polymers and Materials, 25 (2015) 259-266.
[23] Z. Wei, F. Liang, Y. Liu, W. Luo, J. Wang, W. Yao, Y. Zhu, Photoelectrocatalytic degradation of phenol-containing wastewater by TiO_2/g-C_3N_4 hybrid heterostructure thin film, Applied Catalysis B: Environmental, 201 (2017) 600-606.
[24] G. Darabdhara, M.R. Das, Bimetallic Au-Pd nanoparticles on 2D supported graphitic carbon nitride and reduced graphene oxide sheets: A comparative photocatalytic degradation study of organic pollutants in water, Chemosphere, 197 (2018) 817-829.
[25] S. Perween, A. Ranjan, Improved visible-light photocatalytic activity in $ZnTiO_3$ nanopowder prepared by sol-electrospinning, Solar Energy Materials and Solar Cells, 163 (2017) 148-156.
[26] S. Karthikeyan, S. Kumar, L.J. Durndell, M.A. Isaacs, C.M.A. Parlett, B. Coulson, R.E. Douthwaite, Z. Jiang, K. Wilson, A.F. Lee, Size-Dependent Visible Light Photocatalytic Performance of Cu2O Nanocubes, ChemCatChem, 10 (2018) 3554-3563.
[27] N. Xu, Z. Shi, Y. Fan, J. Dong, J. Shi, M.Z.C. Hu, Effects of Particle Size of TiO_2 on Photocatalytic Degradation of Methylene Blue in Aqueous Suspensions, Industrial & Engineering Chemistry Research, 38 (1999) 373-379.

[28] L. Jing, B. Xin, F. Yuan, L. Xue, B. Wang, H. Fu, Effects of Surface Oxygen Vacancies on Photophysical and Photochemical Processes of Zn-Doped TiO_2 Nanoparticles and Their Relationships, The Journal of Physical Chemistry B, 110 (2006) 17860-17865.

[29] W.-K. Jo, S. Kumar, M.A. Isaacs, A.F. Lee, S. Karthikeyan, Cobalt promoted TiO_2/GO for the photocatalytic degradation of oxytetracycline and Congo Red, Applied Catalysis B: Environmental, 201 (2017) 159-168.

[30] D. Vione, T. Picatonotto, M.E. Carlotti, Photodegradation of phenol and salicylic acid by coated rutile-based pigments: A new approach for the assessment of sunscreen treatment efficiency, Journal of cosmetic science, 54 (2003) 513-524.

[31] N. Barbero, D. Vione, Why dyes should not be used to test the photocatalytic activity of semiconductor oxides, Environ. Sci. Technol, 50, 5 (2016) 2130-2131

[32] Y. Chen, W. Huang, D. He, Y. Situ, H. Huang, Construction of Heterostructured g-C_3N_4/Ag/TiO_2 Microspheres with Enhanced Photocatalysis Performance under Visible-Light Irradiation, ACS Applied Materials & Interfaces, 6 (2014) 14405-14414.

[33] W. Yin, W. Wang, S. Sun, Photocatalytic degradation of phenol over cage-like Bi_2MoO_6 hollow spheres under visible-light irradiation, Catalysis Communications, 11 (2010) 647-650.

[34] R.-C. Wang, C.-W. Yu, Phenol degradation under visible light irradiation in the continuous system of photocatalysis and sonolysis, Ultrasonics Sonochemistry, 20 (2013) 553-564.

[35] W. Shi, N. Chopra, Controlled Fabrication of Photoactive Copper Oxide–Cobalt Oxide Nanowire Heterostructures for Efficient Phenol Photodegradation, ACS Applied Materials & Interfaces, 4 (2012) 5590-5607.

[36] Y. Niu, M. Xing, J. Zhang, B. Tian, Visible light activated sulfur and iron co-doped TiO_2 photocatalyst for the photocatalytic degradation of phenol, Catalysis Today, 201 (2013) 159-166.

[37] B. Tryba, A.W. Morawski, M. Inagaki, M. Toyoda, The kinetics of phenol decomposition under UV irradiation with and without H_2O_2 on TiO_2, Fe–TiO_2 and Fe–C–TiO_2 photocatalysts, Applied Catalysis B: Environmental, 63 (2006) 215-221.

[38] A. Nitta, M. Takashima, M. Takase, B. Ohtani, Identification and characterization of titania photocatalyst powders using their energy-resolved distribution of electron traps as a fingerprint, Catalysis Today, 321-322 (2019) 2-8.
[39] T. Torimoto, N. Nakamura, S. Ikeda, B. Ohtani, Discrimination of the active crystalline phases in anatase–rutile mixed titanium(iv) oxide photocatalysts through action spectrum analyses, Physical Chemistry Chemical Physics, 4 (2002) 5910-5914.
[40] S. Lei, H. Fan, X. Ren, J. Fang, L. Ma, Z. Liu, Novel sintering and band gap engineering of $ZnTiO_3$ ceramics with excellent microwave dielectric properties, Journal of Materials Chemistry C, 5 (2017) 4040-4047.
[41] S. Manchala, L.R. Nagappagari, S. Muthukonda Venkatakrishnan, V. Shanker, Facile synthesis of noble-metal free polygonal Zn_2TiO_4 nanostructures for highly efficient photocatalytic hydrogen evolution under solar light irradiation, International Journal of Hydrogen Energy, 43 (2018) 13145-13157.
[42] Y. Cai, Y. Ye, Z. Tian, J. Liu, Y. Liu, C. Liang, In situ growth of lamellar $ZnTiO_3$ nanosheets on TiO_2 tubular array with enhanced photocatalytic activity, Physical Chemistry Chemical Physics, 15 (2013) 20203-20209.
[43] J. Liu, Y. Liu, N. Liu, Y. Han, X. Zhang, H. Huang, Y. Lifshitz, S.-T. Lee, J. Zhong, Z. Kang, Metal-free efficient photocatalyst for stable visible water splitting via a two-electron pathway, Science, 347 (2015) 970-974.
[44] L. Mino, A. Zecchina, G. Martra, A.M. Rossi, G. Spoto, A surface science approach to TiO_2 P25 photocatalysis: An in situ FTIR study of phenol photodegradation at controlled water coverages from sub-monolayer to multilayer, Applied Catalysis B: Environmental, 196 (2016) 135-141.

Chapter 5

One pot synthesis of O-doped porous graphitic carbon nitride as a photocatalyst for RhB degradation under visible light

5.1. Introduction

Nowadays, water pollution is one of the huge environmental problems that were commonly found in the industrial effluents such as manufacture dyes, electroplating, metal finishing, leather tanning, steel fabricating, photographic [1]. The organic wastewater is regarded as pollutants because it causes serious health-risk to human and threats the survival of many animals. There are many methods to remove these organic pollutants, including physical adsorption, bio-degradation, chemical precipitation, and photocatalytic degradation [1]. The oxidation of organic pollutants via photocatalytic reaction is one interesting process because it shows a cost-effective, simple, clean, convenient environmentally friendly approach for the mitigation of dye pollution

Visible light active photocatalyst has attracted interest for organic wastewater treatment due to its effective use of solar light radiation. However, the main problem of photocatalytic reaction is the recombination of photogenerated charges [2]. Recently, there are many methods to depress the charge recombination such as the deposition of noble metal nanoparticle on photocatalyst, make heterojunctions between two semiconductors. Meanwhile, non-metal doping into n-type semiconductors such as nitrogen, sulfur, and phosphorous have also been widely studied [3-9].

Graphitic carbon nitrides with two-dimensional (2D) topology great potential for the photocatalytic reaction because of their semiconductor properties, facile synthesis, suitable electronic structure (Eg = 2.7 eV), environmentally compatible composition and excellent physicochemical stability [10-12]. Moreover, this material

can absorb light up to 450 nm. Thus, it can work as a photocatalyst under visible light irradiation. However, the fast recombination of photo-generated charge carriers of graphitic carbon nitrides results in low photocatalytic efficiency.

In this work, a series of porous oxygen-doped graphitic carbon nitride (OCN) have been successfully synthesized via thermal polycondensation of melamine with a different amount of polyoxyethylene stearyl ether. The as-prepared samples were characterized by PXRD, XPS, BET, PL. Also, the photocatalytic performance was also examined for the degradation of Rhodamine B (RhB) as a model under visible light irradiation.

The previous reports regarding of photocatalytic degradation of g-C_3N_4 were summarized in **Table 5.1** to compare with the present work. From the comparative results, we observed that O doped g-C_3N_4 material could show comparable degradation of RhB. We believe that the present finding might be useful for a detailed understanding of the upcoming research scope of the O doped g-C_3N_4 photocatalyst materials for RhB degradation.

Table 5.1. Comparison of photocatalytic efficiency for RhB degradation.

Catalyst	Active compound	Target	C_0	Loading (g/L)	Efficacy (%)	Time (min)	Ref.
NiS_2 nanoparticles/sulfur-doped carbon nitride	NiS_2 nanoparticles/sulfur-doped carbon nitride	RhB	8 ppm	1.0	90	180	[13]
S doped g-C_3N_4	S doped g-C_3N_4	RhB	1 x 10^{-5} M	1.0	90	20	[14]
O functionalized S–P codoped g-C_3N_4 nanorods	O functionalized S–P codoped g-C_3N_4 nanorods	RhB	10 ppm	0.25	100	120	[15]
g-C_3N_4 nanodots as 2D/0D	g-C_3N_4 nanodots as 2D/0D	MB	12 ppm	0.2	90	60	[16]
S and O codoped g-C_3N_4	S and O codoped g-C_3N_4	RhB	10 ppm	0.1	75	180	[6]
Oxygen self-doped g-C_3N_4	Oxygen self-doped g-C_3N_4	RhB	1 x 10^{-5} M	0.5	100	45	[17]
O doped g-C_3N_4	O doped g-C_3N_4	MO	20 ppm	0.3	20	60	[18]
S doped mesoporous g-C_3N_4	S doped mesoporous g-C_3N_4	RhB	11 ppm	0.7	100	90	[19]
O doped g-C_3N_4	O doped g-C_3N_4	RhB	10 ppm	1.0	100	90	This work

5.2. Materials and Methods

5.2.1. Materials and reagents

Rhodamine B ($C_{28}H_{31}ClN_2O_3$, 97% dye content, RhB) was obtained from Sigma Aldrich Japan Co. Ltd (Tokyo, Japan). Melamine ($C_3H_6N_6$) and polyoxyethylene stearyl ether were purchased from Wako Chemicals (Osaka, Japan). All the chemicals were directly utilized without further purification. Ultrapure water was used in the preparation of the organic dye solutions and their experiments.

5.2.2. Synthesis of CN and OCN samples

The porous oxygen-doped graphitic carbon nitride samples were prepared by thermal polycondensation of melamine with polyoxyethylene stearyl ether. In details, 1 g of melamine was mixed with different amounts of polyoxyethylene stearyl ether (0.5, 1 and 5 mg) by grinding in a mortar. The mixed solid was transferred into a crucible with a cover, and then calcined at 500 ºC for two h under air condition. The obtained products were denoted as OCN-0.5, OCN-1, and OCN-5 (with the amount of the polyoxyethylene stearyl ether). The graphitic carbon nitride (CN) was prepared by the same process without adding polyoxyethylene stearyl ether in order to compare with OCN samples.

5.2.3. Characterizations

The characterizations of the solid samples were carried out by X-ray diffraction (XRD), UV–vis diffuse reflectance spectroscopy (DRS), specific surface area (BET

method), scanning electron microscopy (SEM), and X-ray photoelectron spectroscopy (XPS) and photoluminescence spectroscopy (PL). Detailes are described in **Chapter 2**.

5.2.4. Photocatalytic test

The photocatalytic performance of as-prepared samples was evaluated by the degradation of RhB under visible light irradiation (500W Xe lamp with a cut off filter (>400 nm). 50 mg as-prepared sample was suspended in a 50 mL of 10 ppm RhB solution. The solution was stirred at 500 rpm in dark condition for 30 min in order to achieve adsorption-desorption equilibrium. Then the solution was irradiated from the top while stirring, and an external cooling jacket was maintained the reaction temperature at 25 ºC. At the time interval, 1.0 mL solution was taken out and examined the remaining concentration of RhB was monitored by using UV–Vis spectrophotometer at the maximum absorption wavelength of RhB at 554 nm.

5.3. Results and Discussion

5.3.1 Characterizations

The phase structure of CN and OCN samples were confirmed by powder X-ray diffraction (XRD) measurement (**Fig. 5.1**). The diffraction peaks of all sample can be observed around 12.9° with (100) plan) which can be assigned to an interlayer distance of d =0.33 nm and the 27.6° with (002) plan corresponding to an in-plane structural packing motif with a period of 0.675 nm [20, 21]. This two main peaks can

be confirmed to successful doping of oxygen into the structure of g-C_3N_4, and no obvious impurity phase was found. The decreasing of the intensity of $I_{(002)}/I_{(100)}$ after oxygen-doping by polymer-assistance precursor can be attributed to the reduced the content of layered morphology in the porous microstructure of latter materials. The OCN-5 showed lowest the intensity, indicating that it has the highest porous microstructure properties.

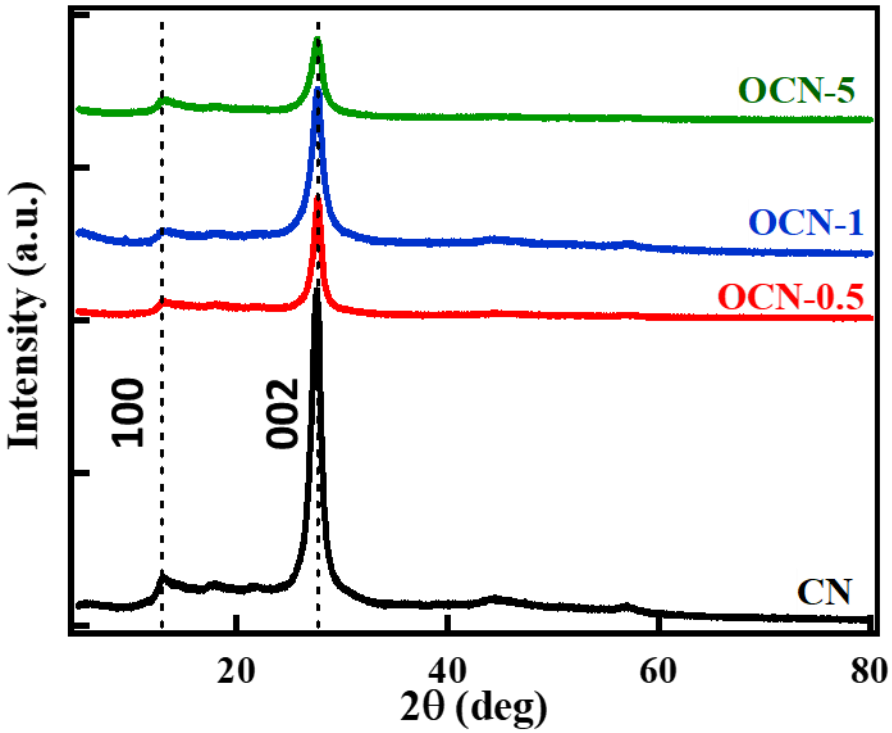

Fig. 5.1 XRD patterns of CN and OCN samples.

The chemical structure of CN and OCN samples was investigated by the FTIR spectroscopy technique. **Fig. 5.2** shows the FTIR spectra of as-prepared samples. In comparison, the Oxygen-doped sample had no distinct different of FTIR spectra compared with the undoped sample (CN). The bands observed in the range of 1200 and 1650 cm^{-1} were assigned to the C-N heterocycles stretching mode. The peak centered at 1641, 1570, and 1414 cm^{-1}, attributed to heptazine ring stretching mode

[22]. The absorption bands centered at about 1324 and 1243 cm^{-1} corresponded to the vibration mode of heptazine bending. The representative peak at 883 cm^{-1} due to the N-H deformation mode [23]. The bands at the 810 cm^{-1} were assigned to the characteristic of tri-3s-triazine breathing mode. The broad bands in the 2900-3500 cm^{-1} range was ascribed to adsorbed H_2O molecules and N-H vibration of the edge of g-C_3N_4 sheet [24]. The additional weak peak at 2377 cm^{-1} was observed, attributed to the physically adsorbed CO_2 on the surface of g-C_3N_4. The expected peaks of C-O-C stretching in OCN samples were not observed due to the low concentration of oxygen.

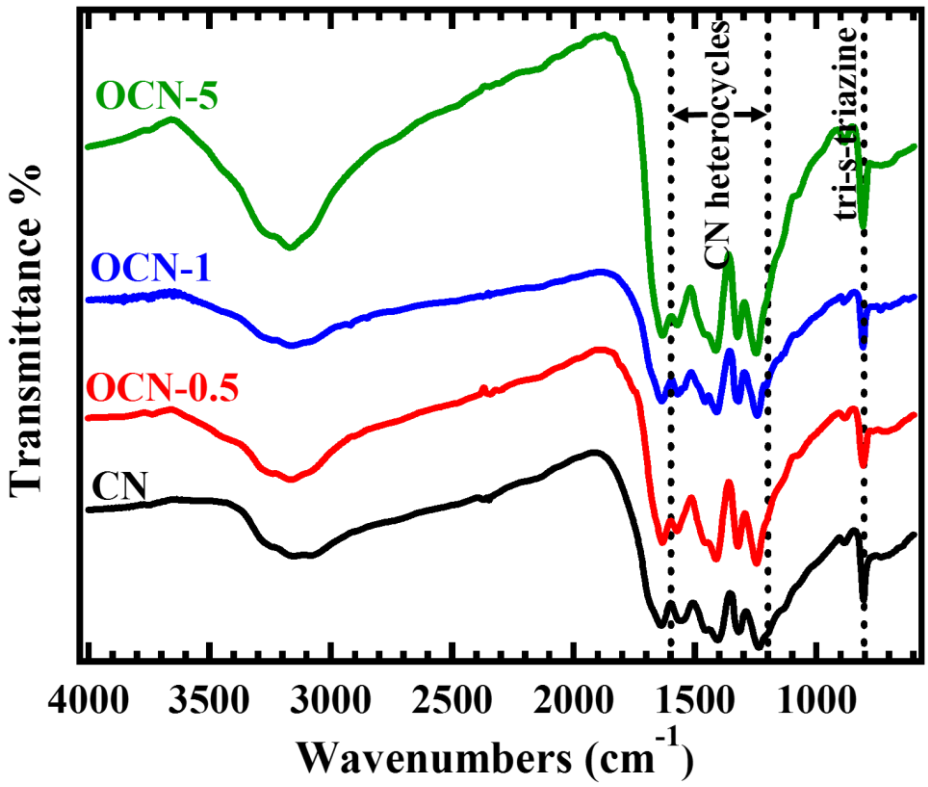

Fig. 5.2 FTIR spectra of CN and OCN samples.

To confirm the oxygen doping into g-C_3N_4 structure, reversed double-beam photoacoustic spectroscopy (RDB-PAS) was utilized because of the ERDT pattern, which is the result of this technique can be used as a fingerprint of g-C_3N_4. In **Fig. 5.3**,

the ERDT of all sample show high electron accumulation near conduction band bottom (CBB) around 2.4-3.0 eV, suggesting that the excited electron can be trapped at electron traps state close to CBB. In contrast, the OCN-0.5 and OCN-1 show high electron accumulation lower 2.4 e, which is characteristic of oxygen doped g-C_3N_4 compare to CN sample because n-type oxygen doped sample might have electron trapped donor level near CBB. However, the OCN-1 which also contains the higher oxygen than pure CN did not show the characteristic of electron traps lower 2.4 eV of donor level of oxygen because the sample has high light absorption ability at 625 nm which affect to the detection of electron accumulation of RDB-PAS experiment. These results confirm that the O element has been introduced into the g-C_3N_4 by POS assisted method.

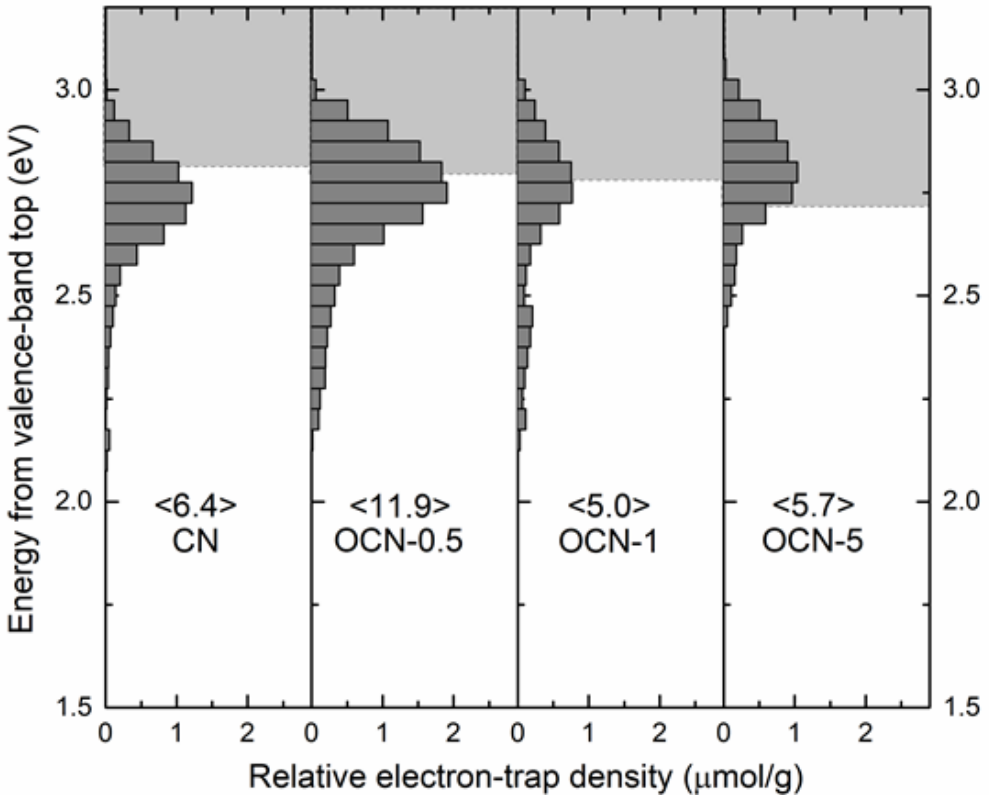

Fig. 5.3 Representative ERDT/CBB patterns of CN and OCN samples plotted as a function of energy (eV) from the valence band top (VBT) combined with CBB.

Numbers in brackets denote the relative total electron-trap density in the unit of μmol/g.

The C/N molar ratio in all samples was estimated by using CHN analysis, as shown in **Fig. 5.4**. In comparison, the C/N ratio of CN, OCN-0.5, OCN-1, and OCN-5 were 0.6553, 0.6660, 0.6643, and 0.6640, respectively. It is clear that the C/N increase after modification by polyoxyethylene stearyl ether, suggesting that the OCN samples should have the existence of O element and N vacancies in the structure of g-C_3N_4.

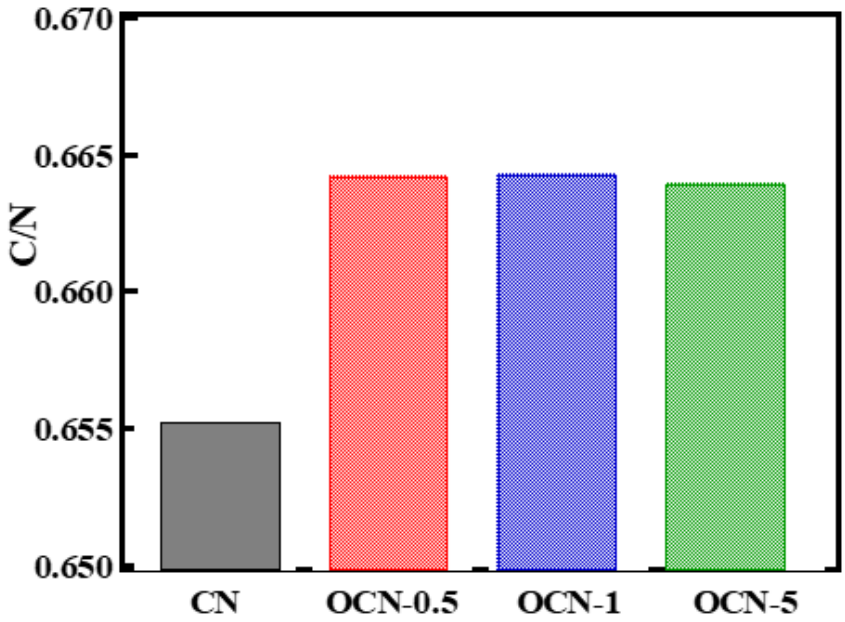

Fig. 5.4 Molar ratio of C/N of CN and OCN samples by CHN analysis.

The morphology of the CN and OCN samples were examined by scanning electron microscopy (SEM). It can be seen that both the CN and OCN sample have obvious layer and stacked structure, as shown in **Fig. 5.5**. In comparison, The CN samples showed the smooth surface of non-porous microstructure while the roughness surface of porous microstructure can be observed in OCN samples. This results suggesting that the melamine mixed with the polymer can provide the porous g-C_3N_4

because in the polymer can be decomposed at high temperature and leave the pore in the g-C_3N_4 structure.

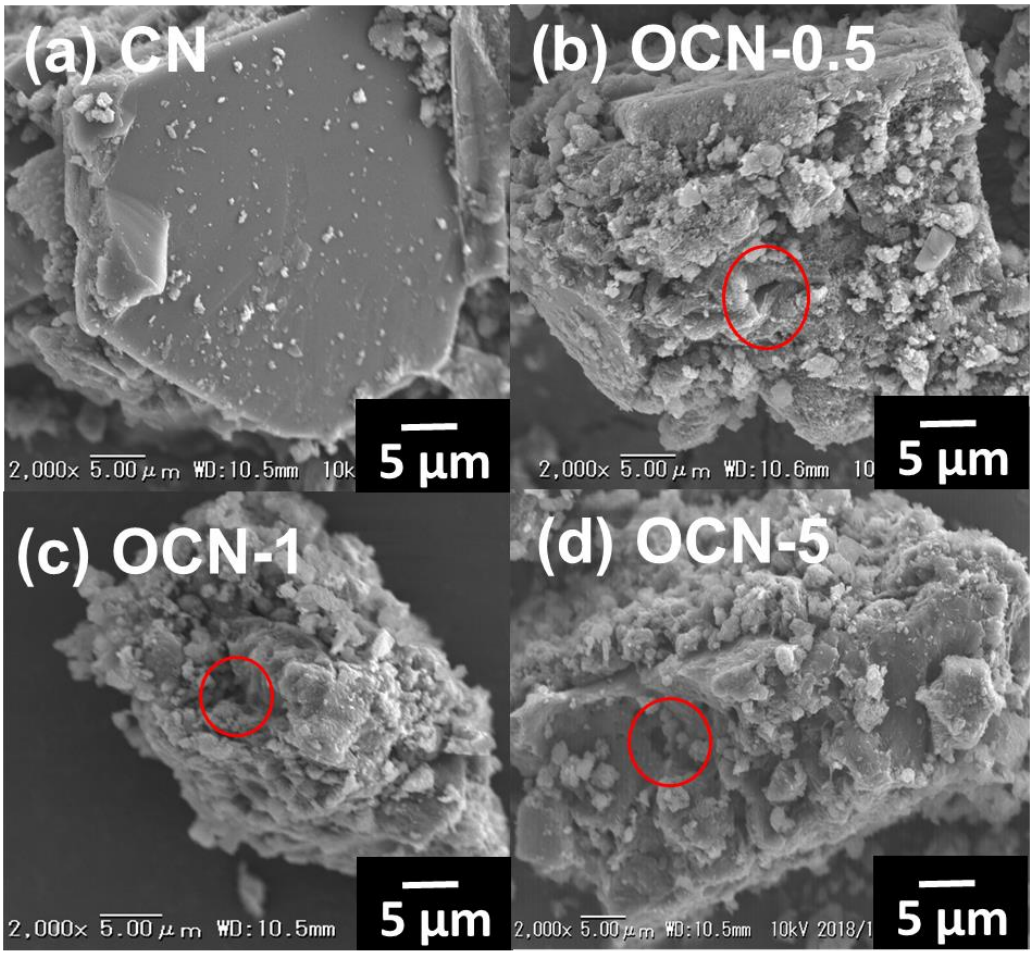

Fig. 5.5 SEM image of (a)CN, (b)OCN-0.5, (c)OCN-1 and (d)OCN-5.

The surface and textural properties of the CN and OCN samples were future investigated by adsorption-desorption of nitrogen gas porosity. The adsorption-desorption isotherms and pore size distribution for the CN and OCN are displayed in **Fig. 5.6a-b**. All of the sample shown the type-IV isotherm with H3-type hysteresis loops, which can be implied to the porous microstructure. The BET specific surface areas of the CN and OCN-0.5, 1, 5 were determined to be 5.1, 22.7, 10.4 and 18.2

m^2/g. The results show that the surface area of OCN samples was more than twice of larger compared with the original CN sample because gas production during thermal polycondensation of melamine with polyoxyethylene stearyl ether can generate the porous structure. The average pore sizes of all sample were determined by using the Barrett-Joyner-Halenda (BJH) method. All sample shows the pore size around 10-12 nm, which are closer to the previous report about 14.6 nm. Fig. 5b exhibit the BJH curve of the CN and OCN sample. The strong board peak around 2-50 nm was appeared in the OCN sample, which can be attributed to the microporous structure in the samples. The BET and BJH results are consistent with the observation from SEM, which also indicates that the adding of the polyoxyethylene stearyl ether could be improved the surface area, leading to enhance photocatalytic activity. Both of BET and BJH results are summarized in Table 1.

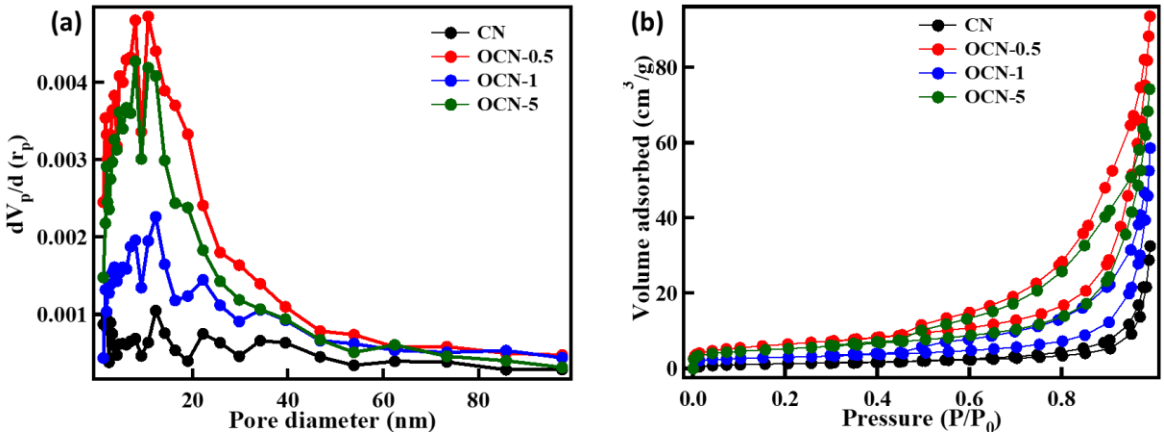

Fig. 5.6 (a) Adsorption/desorption isotherm and (b) pore size distribution of CN and OCN samples.

The light harvesting nature and energy band gap of the photocatalyst were examined by UV-Vis diffuse reflectance spectroscopy, and the results were shown in **Fig. 5.7a**. The light absorption ability of OCN samples is significantly increased and broadened in the visible light region (higher wavelength region) when the doping

amount of added polymer increased. The absorption light ability of OCN samples is higher than CN sample in the visible light region, suggested it might be effective and produce more electron in the visible light region. The band gap energies (Eg) of CN and OCN samples can be calculated through the Kubelka–Munk equation. The band gap energies estimated by the linear part of the $(\alpha h\nu)^2$ versus the energy of absorbed light affords the Eg plot as shown in **Fig. 5.7b**. The Eg values of CN, OCN-0.5, OCN-1, and OCN-5 were found to be approximately 2.81 eV, 2.78 eV, 2.76 eV, and 2.72eV, respectively. The Eg of CN is consistent with the previous report, while the decreasing of Eg was observed in OCN samples, which has oxygen doped in the g-C_3N_4 structure. Hence, the lower Eg of OCN samples may have more absorption of light, which can improve the photocatalytic activity.

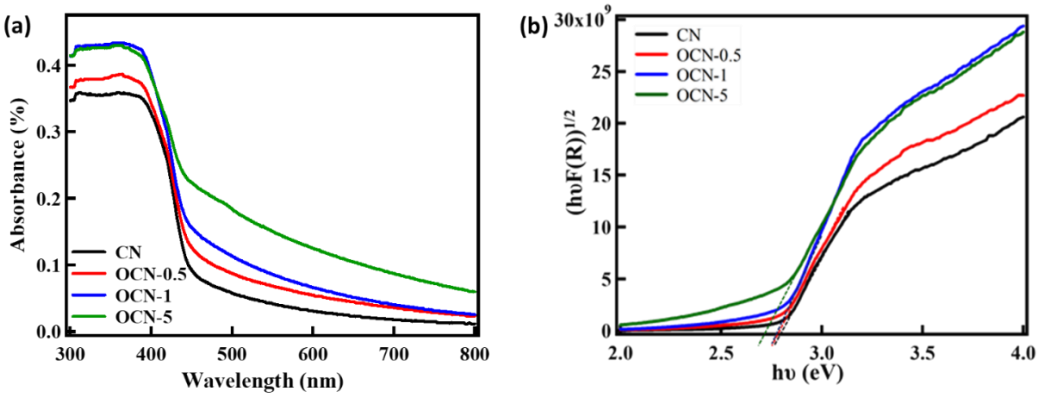

Fig. 5.7 (a) DR UV-Vis absorption spectra and (b) tauc plot of the CN and OCN samples.

The obtained CN and OCN products were further characterized by XPS in order to understand the surface molar ratio and surface speciation of N (**Table 5.2**). In **Fig. 5.8a**, the survey scans show that CN and OCN samples contain carbon and nitrogen as the main elemental components. Moreover, a small amount of oxygen is present in the CN sample, and it dramatically increased after doping O in the OCN

samples. For the narrow scanning of XPS results, the deconvoluted C 1s XPS spectrum of all synthesized sample was shown in **Fig. 5.8b**. The peaks around 288.0 and 285.9 are assigned to N-C=N and C-O bond in the g-C_3N_4 structure, respectively [25]. The peaks around 284.6 and 283.1 eV are assigned to sp^3 C-C and sp^2 C=C bond of contaminations in XPS equipment [26]. The O 1s spectra (**Fig. 5.8c**) of all samples were deconvoluted into two components around 530.0 and 532.1 eV, which are corresponding to C-O bond and molecular water [9]. The N 1s spectra of all samples illustrate in **Fig. 5.8d** can be separated into three components at 398.2, 400.0 and 404.5 eV which can be assigned to sp^2-hybridized nitrogen in triazine ring (C=N-C), tertiary nitrogen N-$(C)_3$ groups and $-NH_2$ or =NH functional groups, respectively [25, 27].

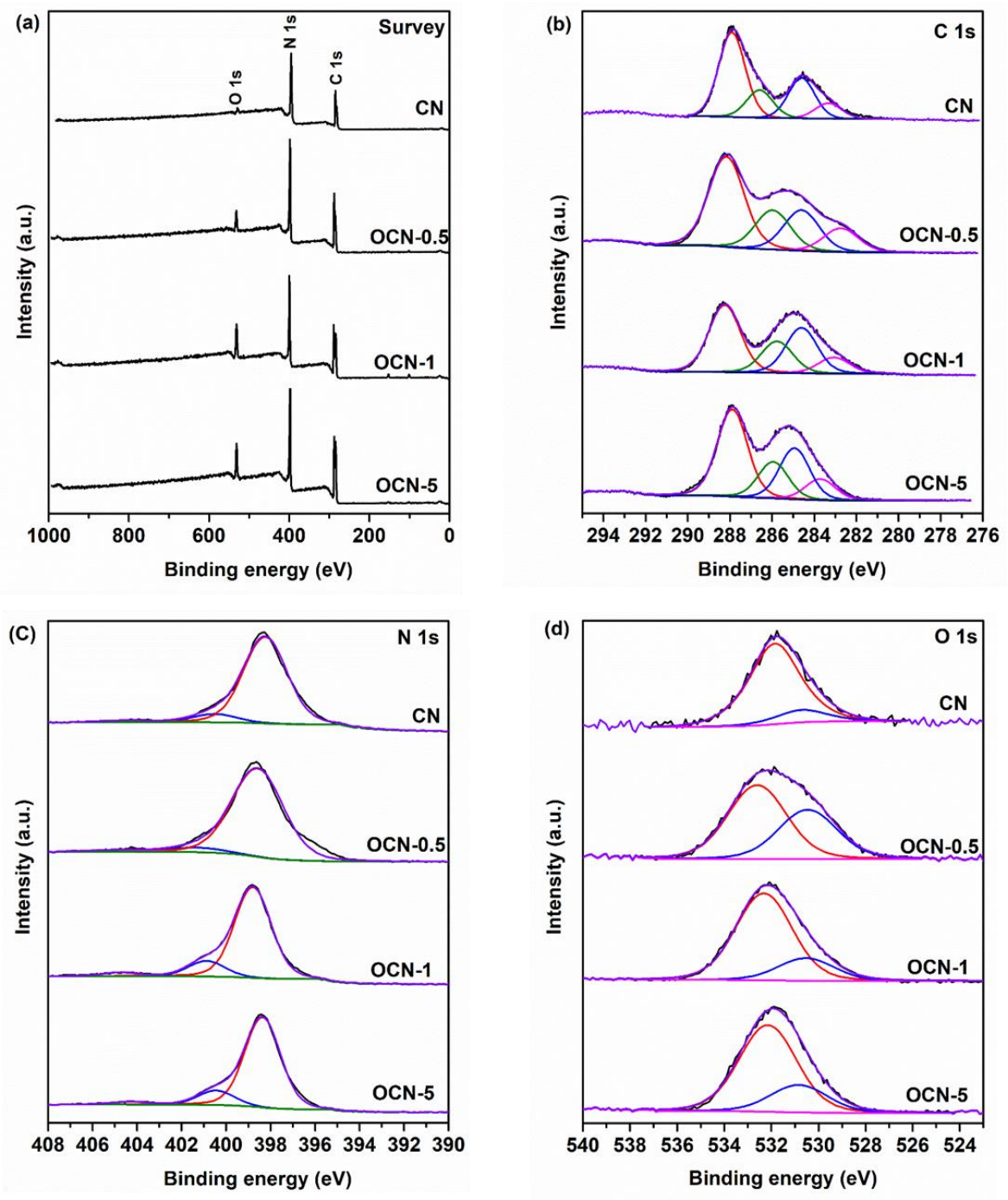

Fig. 5.8 XPS spectra of the CN and OCN samples: (a)survey, (b) C 1s, (c) N 1s and (d) O 1s.

Table 5.2 Binding energies of C 1s, O 1s, and N 1s for CN and OCN samples.

sample		**C 1s**	**C 1s**	**C 1s**	**C 1s**	**O 1s**	**O 1s**	**N 1s**	**N 1s**	**N 1s**
		N-C=N	C-O	Sp^3 C-C	sp^2 C-C	H_2O	C-O	$-NH_2$	N-$(C)_3$	C=N-C
CN	AREA	2412.8	788.1	1153.6	443.0	1509.6	233.4	282.4	1641.4	17018.4
	E_B/eV	287.9	286.5	284.6	283.6	531.8	530.7	404.5	400.5	398.2
	FWHM	1.5	1.5	1.5	1.5	2.5	2.5	2.3	2.3	2.3
OCN-0.5	AREA	6815.9	2956.2	3073.0	1716.1	2519.0	1686.0	267.0	837.0	16120.0
	E_B/eV	288.2	285.9	284.6	282.8	532.6	530.5	404.6	401.0	398.6
	FWHM	1.9	1.9	1.9	1.9	2.7	2.7	2.9	2.9	2.9
OCN-1	AREA	2927.7	1371.0	1982.0	705.0	7128.7	1857.0	494.0	2082.0	12627.0
	E_B/eV	288.2	285.7	284.6	283.1	532.3	530.5	404.7	400.8	398.8
	FWHM	1.8	1.8	1.8	1.8	2.8	2.8	1.9	1.9	1.9
OCN-5	AREA	3642.0	1520.0	1772.3	544.0	7937.0	922.0	514.0	2623.2	16905.0
	E_B/eV	288.2	285.9	284.9	283.7	532.4	530.8	404.5	400.7	398.6
	FWHM	1.7	1.7	1.7	1.7	2.9	2.9	1.9	1.9	1.9

AREA: peak area; E_B: binding energy; FWHM: full width at half maximum

From the XPS results, the surface molar ratio of O/N was calculated by the relative sensitivity factor of O1S and N1S. In this calculation, the O1s peak of C-O bond is focused for comparison of with and without added polymer in the synthesis method due to this oxygen species represent the oxygen in the backbone structure of g-C_3N_4. It was found that the O/C ratios of CN, OCN-0.5, OCN-1, and OCN-5 were 0.025, 0.058, 0.147, and 0.060, respectively. The O/N ratios of CN, OCN-0.5, OCN-1, and OCN-5 were 0.007, 0.060, 0.075, and 0.028, respectively. The surface molar ratio of O/N and O/C of the OCN-1 samples are higher CN sample that confirms the successful doping of oxygen in the main structure of g-C_3N_4 by coexisting precursor of oxygen-contained polymer and melamine. Also, the ratio of C-O/ N-C=N bond of OCN samples is higher than CN, suggesting that the polymer assisted method generated O-doped g-C_3N_4 by substitution of O in N position in the structure of g-C_3N_4.

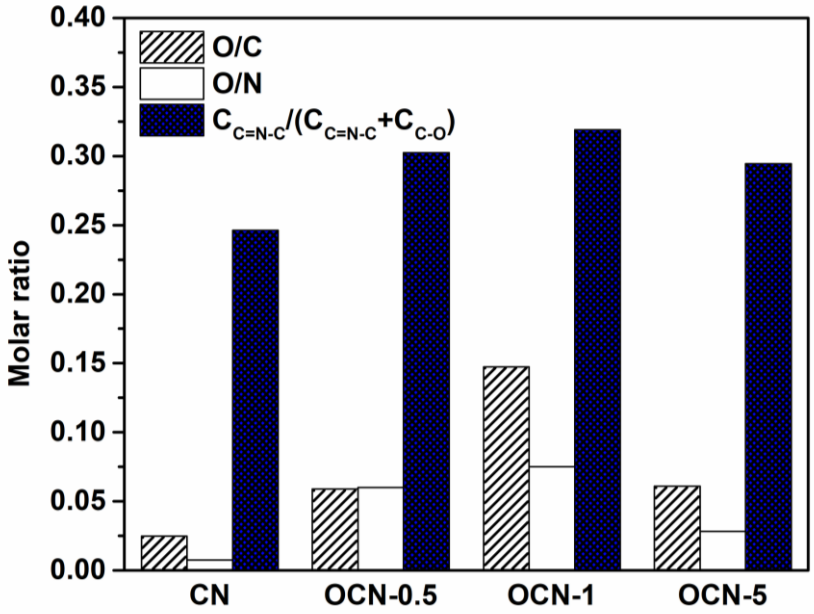

Fig. 5.9 Molar ratio O/C and O/C of CN and OCN samples by XPS analysis.

Photoluminescence emission (PL) method was utilized to evaluate the electron-hole recombination of photocatalyst because the intensity of peak PL depended on the recombination rate of electron and hole. In **Fig. 5.10**, the CN and OCN show the PL emission peak around 450 nm, which were excited under the light of 370 nm. Clearly, the OCN-1 has shown lower PL intensity than CN, suggesting that the high separation of photogenerated charge carriers due to doping oxygen in graphitic carbon nitride structure.

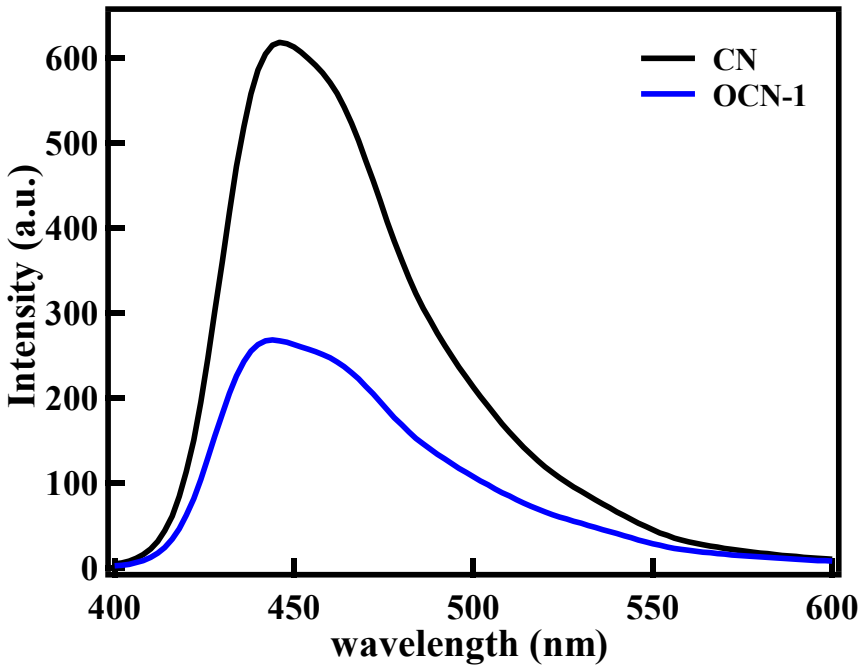

Fig. 5.10 Photoluminescence spectra of CN and OCN-1.

5.3.2 Photocatalytic degradation of RhB

The photocatalytic activity of all samples was examined by RhB degradation under visible light irradiation, as shown in **Fig. 5.11a**. The slight adsorption of RhB on the CN and OCN samples was shown for 30 min before the light irradiation. All

sample unlikely adsorbs RhB, lower than 5% RhB was removed. After 2 h-reaction, the decolorization efficiency (C/C_0) of RhB by CN, OCN-0.5, OCN-1 and OCN-5 were 0.204, 0.003, 0.006 and 0.017. In comparison, photocatalytic degradation of RhB significantly increased with the OCN sample, and the OCN-1 showed the highest photocatalytic performance because of highest oxygen content. The improving of photocatalytic efficiency of OCN sample maybe come from prolonging the lifetime of photogenerated charge carrier (electron and hole) in the photocatalytic reaction.

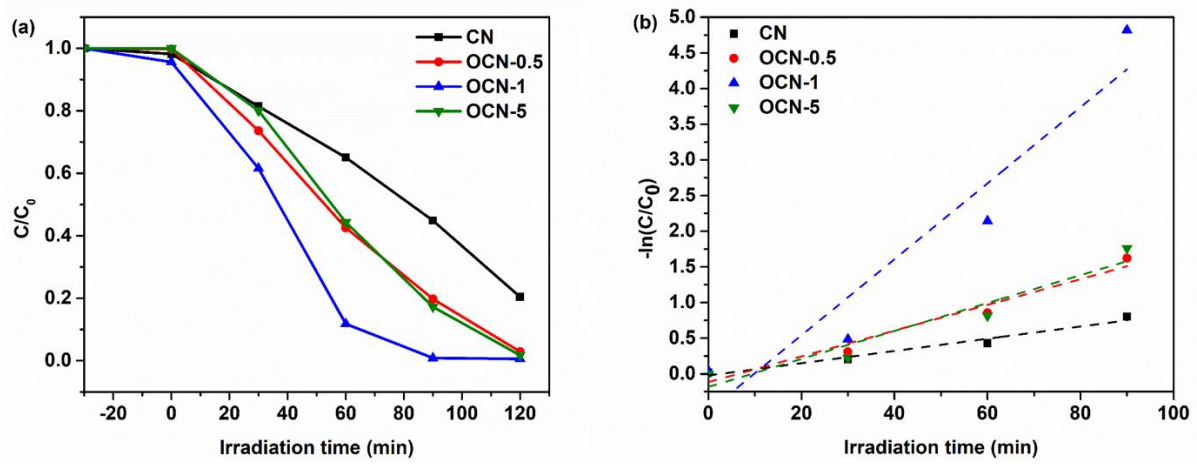

Fig. 5.11 (a) Time courses and (b) pseudo-first-order kinetics plots of photocatalytic degradation of RhB over CN and OCN samples.

It was observed that the rate of photocatalytic degradation of RhB follows the principle of kinetics pseudo-first-order reaction with regression coefficients (R^2) all over 0.9 (**Fig. 5.11b**). The photocatalytic rate constants of RhB for CN, OCN-0.5, OCN-1 and OCN-5 are 0.0085 min^{-1}, 0.0180 min^{-1}, 0.0532 min^{-1}, and 0.0196 min^{-1}, respectively. The highest rate constant was obtained from OCN-1, which was about six times as high as that of pristine CN, without oxygen doping. This results confirm that the OCN-1 is the optimum doping amount of polymer for making oxygen doped carbon nitride. Moreover, the improving of photocatalytic activity and reaction rate

constant of RhB degradation over OCN sample suggest the oxygen doped into g-C_3N_4 can enhance the separation of electron-hole pair; the facilitate of electron transportation and light absorption ability of OCN samples.

One of the important factors of photocatalyst material is reused ability. The reusability of OCN-1 was performed for the RhB degradation under the same conditions. The spent catalyst after photocatalytic degradation of RhB was used directly for the next cycle without any treatment of spent catalyst. **Fig. 5.12** displays the RhB degradation results for five runs of the OCN-1 sample. It was found that up to five cycles more than 95% degradation of RhB for 2 h was achieved. These results suggest that the OCN-1 is stable for degradation RhB, which can be applied to practical application for organically contaminated wastewater remediation.

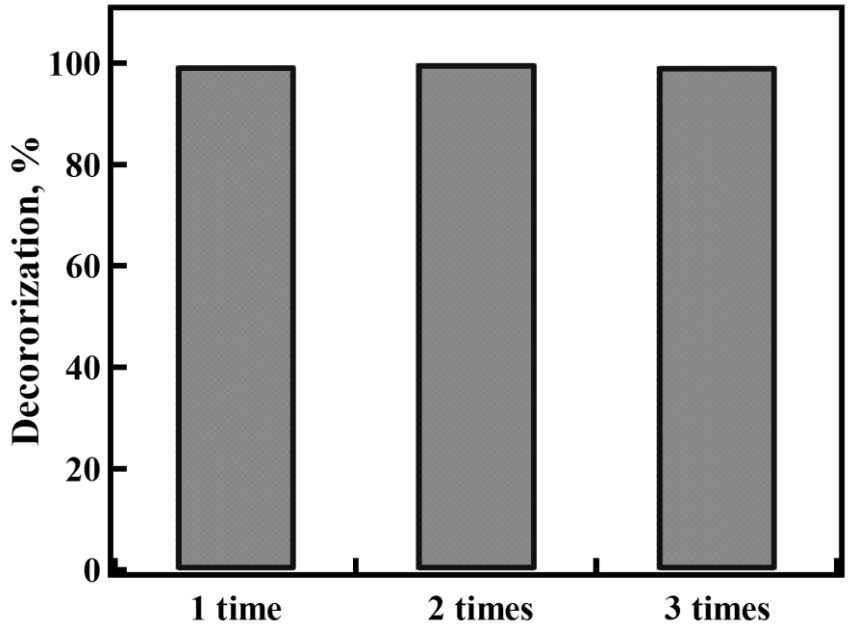

Fig. 5.12 Recycling test in the photocatalytic degradation of RhB over OCN-1 under visible light irradiation.

In order to understand the role of active species in photocatalytic degradation of RhB over OCN-1, radicals scavenging tests were performed, and the results were shown in **Fig. 5.13**. In this experiment, IPA, BQ, and EDTA-2Na were used as the hydroxyl radical scavenger, superoxide radical scavenger and hole scavenger, respectively. It was found that the photocatalytic activity decrease in the presence of BQ and EDTA-2Na, indicating that the predominant active species for RhB degradation are superoxide radical ($^{\bullet}O_2^-$) and hole (h^+).

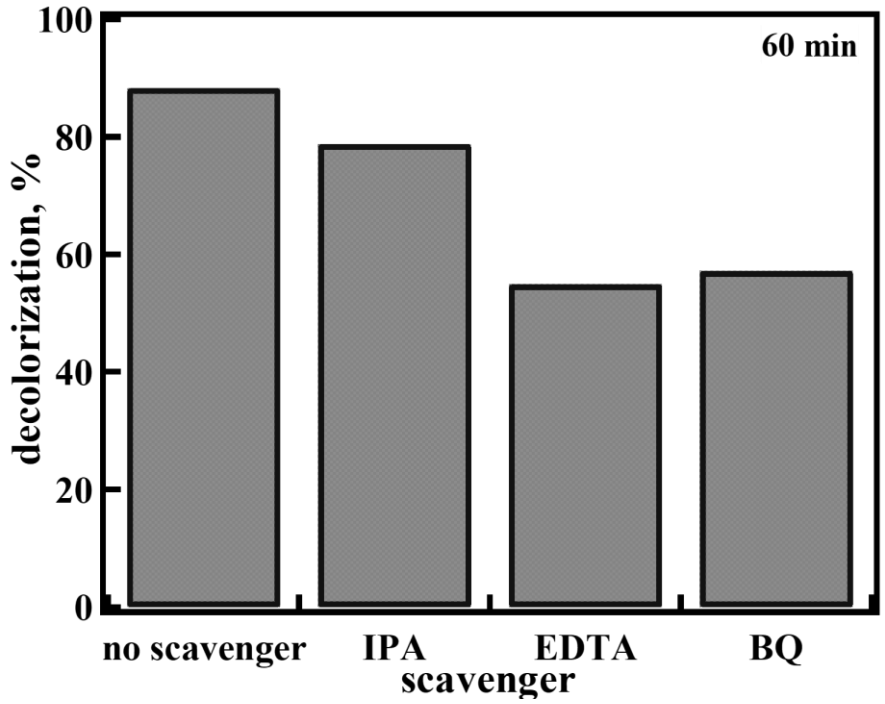

Fig. 5.13 The degradation efficiency of RhB over SC30%-Pd1% in the presence of various radical scavengers.

5.3.3 Photocatalytic mechanism of RhB degradation over OCN

According to the above results and discussion, the possible photocatalytic mechanism of RhB degradation over OCN samples was proposed, as shown in

Fig. 5.14. Under visible light irradiation, the photogenerated electron was generated and transfer to the conduction band (CB), simultaneously, producing the photogenerated hole in the valence band (VB). The accumulated electron on the surface of OCN can react the oxygen to form $^{\bullet}O_2^-$ due to more negative level than the standard reduction potential of O_2 to $^{\bullet}O_2^-$ ($E^0(O_2/^{\bullet}O_2^-) = -0.046$ eV versus NHE [28, 29]. At the same time, some of the generated $^{\bullet}O_2^-$ also can react with H^+ and e^- to provide $^{\bullet}OH$. Moreover, h^+ in the VB also can directly oxidize the RhB molecules [30, 31]. Thus, these active species are responsible for the degradation of RhB into degradation products. From the above discussions, the photocatalytic reaction for RhB degradation could be described as the following reaction of (5.1) - (5.8).

$$OCN + h\nu \rightarrow OCN\ (h_{VB}^+ + e_{CB}^-) \quad (5.1)$$

$$OCN\ (e_{CB}^-) + O_2 \rightarrow {}^{\bullet}O_2^- \quad (5.2)$$

$${}^{\bullet}O_2^- + H^+ \rightarrow {}^{\bullet}OOH \quad (5.3)$$

$${}^{\bullet}OOH + H^+ + e^- \rightarrow H_2O_2 \quad (5.4)$$

$$H_2O_2 + e^- \rightarrow {}^{\bullet}OH + OH^- \quad (5.5)$$

$${}^{\bullet}OH + RhB \rightarrow \text{degradation products} \quad (5.6)$$

$${}^{\bullet}O_2^- + RhB \rightarrow \text{degradation products} \quad (5.7)$$

$$CN\ (h^+) + RhB \rightarrow \text{degradation products} \quad (5.8)$$

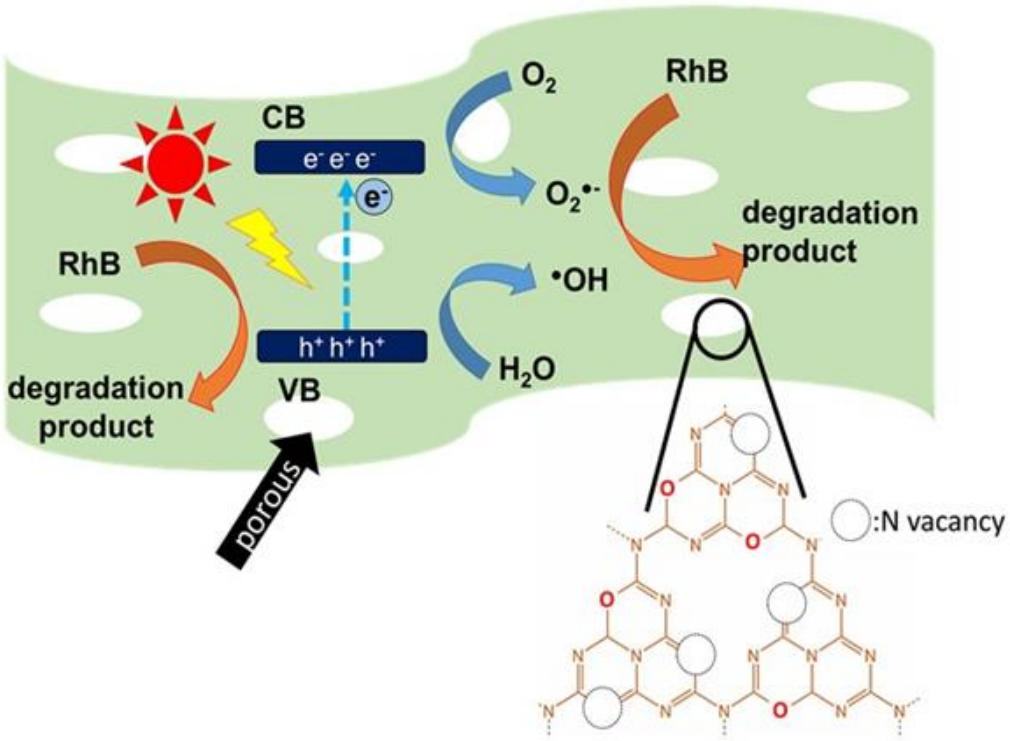

Fig. 5.14 Proposed mechanism of photocatalytic degradation RhB over OCN under the visible light irradiation.

5.4. Conclusions

In summary, O-doped porous graphitic carbon nitride was successfully synthesized by polycondensation of melamine with a polyoxyethylene stearyl ether. The sample with a 1 mg of polyoxyethylene stearyl ether showed the highest photocatalytic performance for rhodamine B degradation visible light irradiation among all these OCN samples. Moreover, the electron-hole recombination of OCN sample exhibited lower than normal graphitic carbon nitride that was confirmed by PL results. It has been demonstrated that the enhancement of photocatalytic efficiency for RhB degradation under visible light irradiation might come from not only high specific

surface area but also low photogenerated charge recombination which were attributed to the O doping and porous structure.

References

[1] B. González, R. Trujillano, M.A. Vicente, V. Rives, S.A. Korili, A. Gil, Photocatalytic degradation of trimethoprim on doped Ti-pillared montmorillonite, Applied Clay Science, 167 (2019) 43-49.

[2] Y. Zhu, R. Zhu, G. Zhu, M. Wang, Y. Chen, J. Zhu, Y. Xi, H. He, Plasmonic Ag coated Zn/Ti-LDH with excellent photocatalytic activity, Applied Surface Science, 433 (2018) 458-467.

[3] S.P. Adhikari, Z.D. Hood, Vincent W. Chen, K.L. More, K. Senevirathne, A. Lachgar, Visible-light-active g-C_3N_4/N-doped $Sr_2Nb_2O_7$ heterojunctions as photocatalysts for the hydrogen evolution reaction, Sustainable Energy & Fuels, 2 (2018) 2507-2515.

[4] F. Raziq, M. Humayun, A. Ali, T. Wang, A. Khan, Q. Fu, W. Luo, H. Zeng, Z. Zheng, B. Khan, H. Shen, X. Zu, S. Li, L. Qiao, Synthesis of S-Doped porous g-C_3N_4 by using ionic liquids and subsequently coupled with Au-TiO_2 for exceptional cocatalyst-free visible-light catalytic activities, Applied Catalysis B: Environmental, 237 (2018) 1082-1090.

[5] W. Li, E. Rodríguez-Castellón, T.J. Bandosz, Photosensitivity of g-C_3N_4/S-doped carbon composites: study of surface stability upon exposure to CO_2 and/or water in ambient light, Journal of Materials Chemistry A, 5 (2017) 24880-24891.

[6] R. You, H. Dou, L. Chen, S. Zheng, Y. Zhang, Graphitic carbon nitride with S and O codoping for enhanced visible light photocatalytic performance, RSC Advances, 7 (2017) 15842-15850.

[7] H.J. Kong, D.H. Won, J. Kim, S.I. Woo, Sulfur-Doped g-C_3N_4/$BiVO_4$ Composite Photocatalyst for Water Oxidation under Visible Light, Chemistry of Materials, 28 (2016) 1318-1324.

[8] J. Ran, T.Y. Ma, G. Gao, X.-W. Du, S.Z. Qiao, Porous P-doped graphitic carbon nitride nanosheets for synergistically enhanced visible-light photocatalytic H_2 production, Energy & Environmental Science, 8 (2015) 3708-3717.

[9] L.J. Fang, X.L. Wang, J.J. Zhao, Y.H. Li, Y.L. Wang, X.L. Du, Z.F. He, H.D. Zeng, H.G. Yang, One-step fabrication of porous oxygen-doped g-C_3N_4 with feeble nitrogen vacancies for enhanced photocatalytic performance, Chem Commun (Camb), 52 (2016) 14408-14411.

[10] P. Li, L. Huang, Y. Li, Y. Xu, S. Huang, D. Yuan, H. Xu, H. Li, Synthesis of dark orange montmorillonite/g-C_3N_4 composites and their applications in the environment, Journal of Physics and Chemistry of Solids, 107 (2017) 131-139.

[11] X. Bai, L. Wang, Y. Wang, W. Yao, Y. Zhu, Enhanced oxidation ability of g-C_3N_4 photocatalyst via C60 modification, Applied Catalysis B: Environmental, 152-153 (2014) 262-270.

[12] N. Tian, Y. Zhang, C. Liu, S. Yu, M. Li, H. Huang, g-C_3N_4/$Bi_4O_5I_2$ 2D–2D heterojunctional nanosheets with enhanced visible-light photocatalytic activity, RSC Advances, 6 (2016) 10895-10903.

[13] M. Jourshabani, Z. Shariatinia, G. Achari, C.H. Langford, A. Badiei, Facile synthesis of NiS_2 nanoparticles ingrained in a sulfur-doped carbon nitride framework with enhanced visible light photocatalytic activity: two functional roles of thiourea, Journal of Materials Chemistry A, 6 (2018) 13448-13466.

[14] Y. Zheng, Z. Yu, F. Lin, F. Guo, K.A. Alamry, L.A. Taib, A.M. Asiri, X. Wang, Sulfur-Doped Carbon Nitride Polymers for Photocatalytic Degradation of Organic Pollutant and Reduction of Cr(VI), Molecules, 22 (2017) 572, 1-17.

[15] S. Hu, L. Ma, Y. Xie, F. Li, Z. Fan, F. Wang, Q. Wang, Y. Wang, X. Kang, G. Wu, Hydrothermal synthesis of oxygen functionalized S-P codoped g-C_3N_4 nanorods with outstanding visible light activity under anoxic conditions, Dalton Trans, 44 (2015) 20889-20897.

[16] L. Fu, X. Xiao, A. Wang, Reduced graphene oxide coupled with g-C_3N_4 nanodots as 2D/0D nanocomposites for enhanced photocatalytic activity, Journal of Physics and Chemistry of Solids, 122 (2018) 104-108.

[17] F. Wei, Y. Liu, H. Zhao, X. Ren, J. Liu, T. Hasan, L. Chen, Y. Li, B.L. Su, Oxygen self-doped g-C_3N_4 with tunable electronic band structure for unprecedentedly enhanced photocatalytic performance, Nanoscale, 10 (2018) 4515-4522.

[18] Y. Wu, H. Wang, Y. Sun, T. Xiao, W. Tu, X. Yuan, G. Zeng, S. Li, J.W. Chew, Photogenerated charge transfer via interfacial internal electric field for significantly

improved photocatalysis in direct Z-scheme oxygen-doped carbon nitrogen/CoAl-layered double hydroxide heterojunction, Applied Catalysis B: Environmental, 227 (2018) 530-540.

[19] M. Jourshabani, Z. Shariatinia, A. Badiei, Sulfur-Doped Mesoporous Carbon Nitride Decorated with Cu Particles for Efficient Photocatalytic Degradation under Visible-Light Irradiation, The Journal of Physical Chemistry C, 121 (2017) 19239-19253.

[20] J. Cao, C. Qin, Y. Wang, H. Zhang, G. Sun, Z. Zhang, Solid-State Method Synthesis of SnO_2-Decorated g-C_3N_4 Nanocomposites with Enhanced Gas-Sensing Property to Ethanol, Materials, 10 (2017) 604, 1-14.

[21] A. Kumar, P. Kumar, C. Joshi, M. Manchanda, R. Boukherroub, S.L. Jain, Nickel Decorated on Phosphorous-Doped Carbon Nitride as an Efficient Photocatalyst for Reduction of Nitrobenzenes, Nanomaterials, 6 (2016) 59.

[22] M. Xu, L. Han, S. Dong, Facile fabrication of highly efficient g-C_3N_4/Ag_2O heterostructured photocatalysts with enhanced visible-light photocatalytic activity, ACS Appl Mater Interfaces, 5 (2013) 12533-12540.

[23] J. Tong, L. Zhang, F. Li, K. Wang, L. Han, S. Cao, Rapid and high-yield production of g-C_3N_4 nanosheets via chemical exfoliation for photocatalytic H_2 evolution, RSC Advances, 5 (2015) 88149-88153.

[24] M. Fu, J. Liao, F. Dong, H. Li, H. Liu, Growth of g-C_3N_4 Layer on Commercial TiO_2 for Enhanced Visible Light Photocatalytic Activity, Journal of Nanomaterials, 2014 (2014) 1-8.

[25] D. Gao, Y. Liu, P. Liu, M. Si, D. Xue, Atomically Thin B doped g-C_3N_4 Nanosheets: High-Temperature Ferromagnetism and calculated Half-Metallicity, Sci Rep, 6 (2016) 35768.

[26] A. Fujimoto, Y. Yamada, M. Koinuma, S. Sato, Origins of sp^3 C peaks in C1s X-ray Photoelectron Spectra of Carbon Materials, Anal Chem, 88 (2016) 6110-6114.

[27] M. Wang, P. Guo, Y. Zhang, C. Lv, T. Liu, T. Chai, Y. Xie, Y. Wang, T. Zhu, Synthesis of hollow lantern-like Eu(III)-doped g-C_3N_4 with enhanced visible light photocatalytic perfomance for organic degradation, J Hazard Mater, 349 (2018) 224-233.

[28] Z. Chen, F. Bing, Q. Liu, Z. Zhang, X. Fang, Novel Z-scheme visible-light-driven Ag_3PO_4/Ag/SiC photocatalysts with enhanced photocatalytic activity, Journal of Materials Chemistry A, 3 (2015) 4652-4658.

[29] Y. Peng, Q.-G. Chen, D. Wang, H.-Y. Zhou, A.-W. Xu, Synthesis of one-dimensional WO_3–Bi_2WO_6 heterojunctions with enhanced photocatalytic activity, CrystEngComm, 17 (2015) 569-576.

[30] S. Fang, K. Lv, Q. Li, H. Ye, D. Du, M. Li, Effect of acid on the photocatalytic degradation of rhodamine B over g-C_3N_4, Applied Surface Science, 358 (2015) 336-342.

[31] X. Meng, Z. Zhang, Ag/AgCl Loaded Bi_2WO_6 Composite: A Plasmonic Z-Scheme Visible Light-Responsive Photocatalyst, International Journal of Photoenergy, 2016 (2016) 1-11.

Chapter 6

Enhanced visible-light photocatalytic efficiency for rhodamine B degradation using ZnTi mixed metal oxide/g-C_3N_4 composite

6.1. Introduction

The synthetic organic dyes are an essential constituent in dyeing, printing, and textile industries. During textile processing, disorganization in dyeing result in huge quantities of the dyestuff being directly lost to the wastewater; which ultimately finds its way into the environment [1-3]. The wastewater containing chemical dyes is not only appealingly offensive but also responsible for the adverse effect on the aquatic biota and public health. The treatment of dye containing wastewater before discharge in the environment for organic pollutants is an important step and challenging for environmental research. Substantial research work has been carried out on the treatment of various types of wastewater including several types of dyes through adsorption, coagulation, flocculation, oxidation, precipitation, membrane filtration, and electrochemical processes [4]. Nevertheless, all these techniques have some benefits and limitations involving high operating costs, incapability to treatment pollutants totally, difficulties in the development of actual industrial arrangement[4, 5]. Photocatalysis is a remarkable methodology which is popular and applied in the different interdisciplinary area of the research such as, degradation of several organic and reduction of hazardous metal ions due to eco-friendly, low cost, easy to operation and energy shortages problem [6-9].

In recent years, carbon nitride (g-C_3N_4) as a metal-free π-conjugated polymeric semiconductor has attracted much interest as a promising photocatalyst due to suitable band gap about 2.70 eV, inexpensive, easily-prepared, high thermal and chemical stability [10-15]. This material has been extensively used as a visible light active photocatalyst in many photocatalytic applications, such as the environmental purification, generation of hydrogen, and conversion of carbon dioxide, due to high

photocatalytic performance for organic dye degradation. However, the photocatalytic performance of bulk g-C_3N_4 is still low due to its quick rate recombination of holes and electrons as well as relatively low quantum yield [16]. Thus, many strategies have been utilized to improve the photocatalytic activity, for instance, metal or nonmetal elements doping, controlling the shape, coupling with another semiconductor [17-19]. The g-C_3N_4 composited with another semiconductor has been considered as an effective transporter in the photocatalytic treatment of several types of pollutants including an organic dye. Wei and coauthors reported TiO_2/g-C_3N_4 hybrid heterostructure thin film for phenol degradation of pharmaceuticals in wastewater [20], while Boonprakob and coworkers developed g-C_3N_4/TiO_2 and utilized for simultaneous photocatalytic degradation of methylene blue [21]. Among g-C_3N_4 composite, both of layered double hydroxide (LDH) and mixed metal oxide derived (MMO) from LDH composite with C_3N_4 is gaining greatly attraction in the present because of the composite show the high separation of photogenerated electron and hole through two-dimensional/two-dimensional (2D/2D) charge transfer [22-27].

LDH is two-dimensional layered anionic clays, expressed by the general formula $[M^{2+}_{1-x}M^{3+}_{x}(OH)_2]^{z+}(A^n)_{z/n}\cdot yH_2O$. M^{2+} and M^{3+}, divalent and trivalent metal cations respectively, are located in the brucite-like octahedral sheet while A^n is the interlayer anion between the layer compensating for positive charge of the layer [28, 29]. The MMO can be obtained from topological decomposition of LDH at high temperature (400-1000 °C), which exhibit higher photocatalytic performance than other preparation methods. For example, Liu and coauthors reported ZnCr-LDH/N-doped g-C_3N_4 composite with improved visible-light-induced photocatalytic activity for congo red degradation [23]. Oxygen doped g-C_3N_4/CoAl LDH was utilized for the

methyl orange [25]. For the MMO derived from LDH, g-C_3N_4/CuONP/LDH composite was developed, and it shows high photocatalytic degradation of phenol under UV and visible light irradiation [24]. Bui and co-workers report the improvement of photocatalytic degradation of Rhodamine B by ZnBi MMO/g-C_3N_4 composite [30]. Moreover, the 2D/2D g-C_3N_4/MgFe MMO also was successfully synthesized, and it showed an efficient photocatalytic activity for photocatalytic H_2 production [26].

In order to enhance the photocatalytic degradation efficiency of g-C_3N_4, a new composite of ZnTi MMO and g-C_3N_4 composites was prepared by hydrothermal followed by calcination method. The obtained composites were utilized as photocatalyst for rhodamine B degradation under visible light irradiation. Furthermore, the characterization of material and photocatalytic degradation mechanism are also discussed in detail.

The previous reports regarding of photocatalytic degradation of RhB were summarized in **Table 6.1** to compare with the present work. From the comparative results, we observed that CN/ZTM composites could show comparable degradation of RhB. We believe that the present finding might be useful for a detailed understanding of the upcoming research scope of the CN/ZTM composites photocatalyst materials for RhB degradation.

Table 6.1. Comparison of photocatalytic efficiency for RhB degradation by g-C_3N_4 composites

Catalyst	Active compound	Target	C_0	Loading (g/L)	Efficacy (%)	Time (min)	Ref.
g-C_3N_4/Fe_3O_4/AgI	g-C_3N_4/Fe_3O_4/AgI	RhB	2.5 x 10^{-5} M	0.4	98	270	[31]
NiS_2 nanoparticles/sulfur-doped g-C_3N_4	NiS_2 nanoparticles/sulfur-doped g-C_3N_4	RhB	8 ppm	1.0	90	180	[32]
S doped g-C_3N_4	S doped g-C_3N_4	RhB	1 x 10^{-5} M	1.0	90	20	[33]
O functionalized S–P codoped g-C_3N_4 nanorods	O functionalized S–P codoped g-C_3N_4 nanorods	RhB	10 ppm	0.25	100	120	[34]
Ag@NiAl LDH/g-C_3N_4	Ag@NiAl LDH/g-C_3N_4	RhB	5 ppm	0.25	85	60	[35]
S and O codoped g-C_3N_4	S and O codoped g-C_3N_4	RhB	10 ppm	0.1	75	180	[36]
Oxygen self-doped g-C_3N_4	Oxygen self-doped g-C_3N_4	RhB	1 x 10^{-5} M	0.5	100	45	[37]
BiOCl/g-C_3N_4/kaolinite	BiOCl/g-C_3N_4	RhB	10 ppm	3.0	95	360	[38]
S doped mesoporous g-C_3N_4	S doped mesoporous g-C_3N_4	RhB	11 ppm	0.7	100	90	[39]
kaolinite/g-C_3N_4	g-C_3N_4	RhB	10 ppm	3.0	95	360	[40]
g-C_3N_4/kaolinite	g-C_3N_4	RhB	10 ppm	2.0	95	360	[41]
g-C_3N_4/illite	g-C_3N_4	RhB	10 ppm	2.0	80	360	[41]

Table 6.1. Comparison of photocatalytic efficiency for RhB degradation by g-C_3N_4 composites (continued)

Catalyst	Active compound	Target	C_0	Loading (g/L)	Efficacy (%)	Time (min)	Ref.
g-C_3N_4/montmorillonite	g-C_3N_4	RhB	30 ppm	2.0	85	360	[42]
Cyanuric Acid Modified g-C_3N_4/Kaolinite	Cyanuric Acid Modified g-C_3N_4	RhB	10 ppm	2.0	93	420	[43]
Mn/Co/Ti LDH	Mn/Co/Ti LDH	RhB	1 x 10-5 M	0.1	80	60	[44]
ZnTi LDH	ZnTi LDH	RhB	5 ppm	0.66	100	120	[45]
ZnCr LDH	ZnCr LDH	RhB	100 ppm	1.0	95	60	[46]
BiOCl/TiO_2/ZnCr LDH	BiOCl/TiO_2/ZnCr LDH	RhB	100 ppm	0.37	100	30	[47]
Ag coated Zn/Ti-LDH	Ag coated Zn/Ti-LDH	RhB	10 ppm	1.0	83	30	[48]
Ag/GO/g-C_3N_4	Ag/GO/g-C_3N_4	RhB	10 ppm	1.2	100	120	[49]
Pd/g-C_3N_4/Bi_2MoO_6	Pd/g-C_3N_4/Bi_2MoO_6	RhB	10 ppm	0.2	100	40	[50]
Au/Pt/g-C_3N_4	Au/Pt/g-C_3N_4	RhB	10 ppm	0.2	90	180	[51]
Sepiolite –TiO_2	Sepiolite –TiO_2	RhB	8.3×10^{-5}	0.85	~80	120	[52]
CN/ZTM	CN/ZTM	RhB	10 ppm	1.0	95	120	This work

6.2. Materials and Methods

6 2.1 Materials and reagents

Rhodamine B ($C_{28}H_{31}ClN_2O_3$, 97% dye content, RhB) was obtained from Sigma Aldrich Japan Co. Ltd (Tokyo, Japan). Melamine ($C_3H_6N_6$), zinc nitrate hexahydrate ($Zn(NO_3)_2{\cdot}6H_2O$), titanium(IV) chloride ($TiCl_4$) and urea ($CO(NH_2)_2$) were purchased from Wako Chemicals (Osaka, Japan). All the chemicals were directly utilized without further purification. Ultrapure water was used in the experiments.

6.2.2 Synthesis of ZnTi mixed metal oxide (ZTM)

The ZTM samples were synthesized by hydrothermal, followed by calcination. Typically, 1.5 g of urea was dissolved in 50 ml of 0.25 M mixed solution of $TiCl_4$ and $Zn(NO_3)_2{\cdot}6H_2O$ with molar ratios of Zn/Ti = 4/1 under vigorous stirring, the total molar concentration of [Zn] and [Ti] is set 0.25 M in all cases. The above mixture was aged at 130 °C for 24 h by hydrothermal. The obtained solid products were separated by filtration, washed several times with de-ionized water, and dried at 75 °C for 24 h. Afterward, the synthetic products were calcined at 400 °C under air for 2 h. The calcined products were denoted as ZTM.

6.2.3 Synthesis of CN

The polymeric carbon nitride structure of g-C_3N_4 fabricated by adopting widespread thermal polymerization. In a typical preparation, exactly 5 g of melamine was placed in well cleaned an alumina crucible with a cap and then transferred into a

muffle furnace. The furnace temperature was maintained at 550 °C for two hours under the continuous flow of air. After the completion of calcination, the crucible was cooled down to the room temperature. The obtained product was denoted as CN.

6.2.4 Preparation of CN/ZTM composite

The CN/ZTM composites were prepared calcination method. 1.5 g of urea was dissolved in 50 ml of 0.25 M mixed solution of $TiCl_4$ and $Zn(NO_3)_2 \cdot 6H_2O$ with molar ratios of Zn/Ti = 4/1 under vigorous stirring, the total molar concentration of [Zn] and [Ti] is set 0.25 M in all cases. After that, the CN was added into the above solution in order to make 1, 5, and 10 wt% of ZTM in the composite. The above mixture was aged at 130 °C for 24 h by hydrothermal. The obtained solid products were separated by filtration, washed several times with de-ionized water, and dried at 75 °C for 24 h. Afterward, the synthetic products were calcined at 400 °C under air for 2 h. The calcined products were denoted as CN/ZTM.

6.2.5. Characterizations

The characterizations of the solid samples were carried out by X-ray diffraction (XRD), UV–vis diffuse reflectance spectroscopy (DRS), specific surface area (BET method), scanning electron microscopy (SEM), and X-ray photoelectron spectroscopy (XPS) and photoluminescence spectroscopy (PL). Detailes are described in **Chapter 2**.

6.2.6. Photocatalytic test

The photocatalytic performance of as-prepared samples was evaluated by the degradation of RhB under visible light irradiation (500W Xe lamp with a cut off filter (>400 nm). 50 mg as-prepared sample was suspended in a 50 mL of 10 ppm RhB solution. The solution was stirred at 500 rpm in dark condition for 30 min in order to achieve adsorption-desorption equilibrium. Then the solution was irradiated from the top while stirring, and an external cooling jacket was maintained the reaction temperature at 25 ºC. At the time interval, 1.0 mL solution was taken out and examined the remaining concentration of RhB was monitored by using UV–Vis spectrophotometer at the maximum absorption wavelength of RhB at 554 nm.

6.3. Results and Discussion

6.3.1 Characterizations

Fig. 6.1a shows the PXRD patterns of the CN, ZTM, and CN/ZTM composites. The powder X-ray diffraction pattern of the CN sample shows two characteristic peaks at 2-theta 13.2 (002) and 27.3° (100), which correspond to g-C_3N_4 (JCPDS No.87-1526) [53]. The ZTM sample shows the main diffraction peaks 2θ at 31.8, 34.5, 36.3, 47.6, 56.7, 62.8, 66.4, 67.9 and 69.1, which are indicated to the ZnO phase (JCPDS No. 36-1451) [54, 55]. Moreover, the small amount of TiO_2 anatase phase (JCPDS No. 21-1272) was observed [56]. In the cases of CN/ZTM composites, the PXRD patterns clearly showed increasing of ZnO phase when the amount to ZnO in the composite increased. The existence of ZnO and g-C_3N_4 confirm the composite between ZTM and CN was formed.

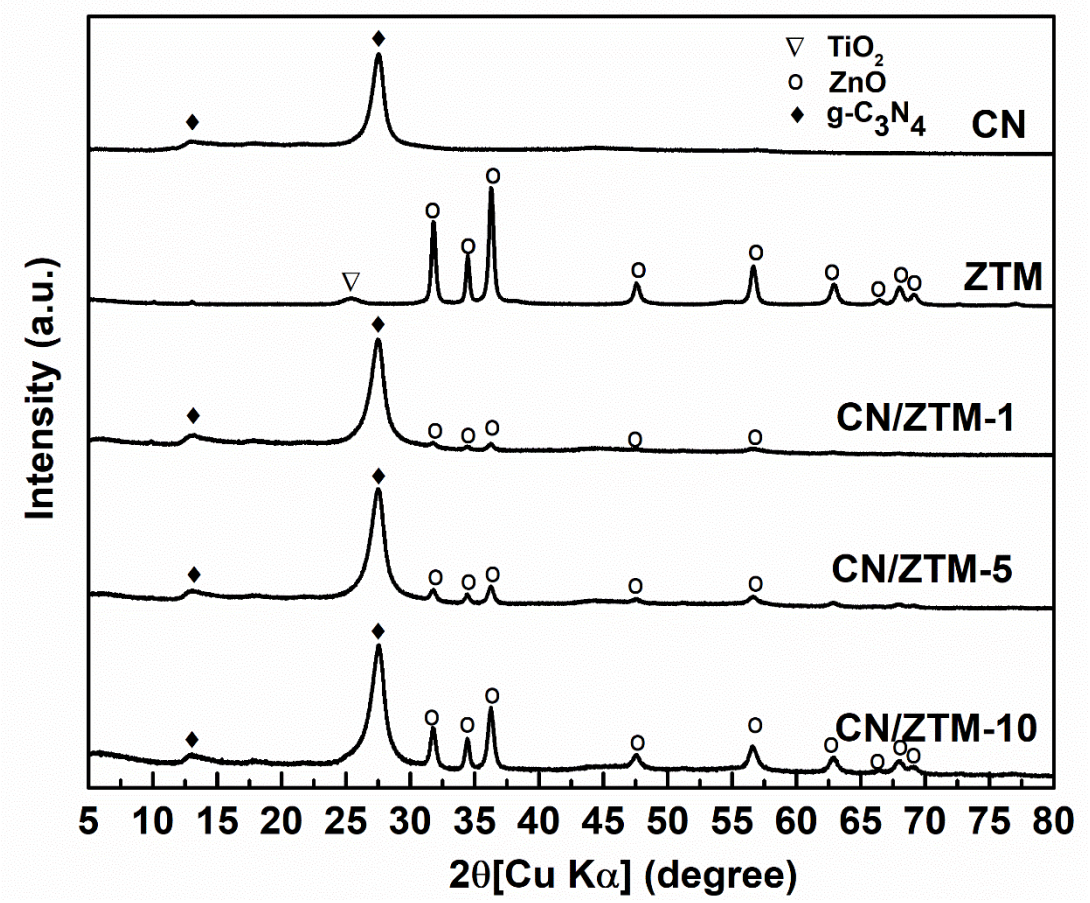

Fig. 6.1 PXRD pattern for CN, ZTM, and CN/ZTM composites.

Future more, the synthetic products were characterized by FTIR, as shown in **Fig. 6.2**. The FTIR spectra of CN and CN/ZTM composite are highlighted with characteristic aromatic C–N heterocycle stretching vibration mode in the region of 1200–1600 cm^{-1} and triazine units at 808 cm^{-1}, confirming the successful fabrication of original graphitic C–N network. Additionally, strong absorbance at 3200 cm^{-1} was observed, due to the residual N–H functional groups in the carbon nitride [57-59]. No differences among FTIR spectra for CN and CN/ZTM composite were observed. Moreover, the ZTM exhibits the broadband around 3500 $cm^{-1,}$ which can be assigned to adsorbed H_2O molecule on the surface of metal oxide particles.

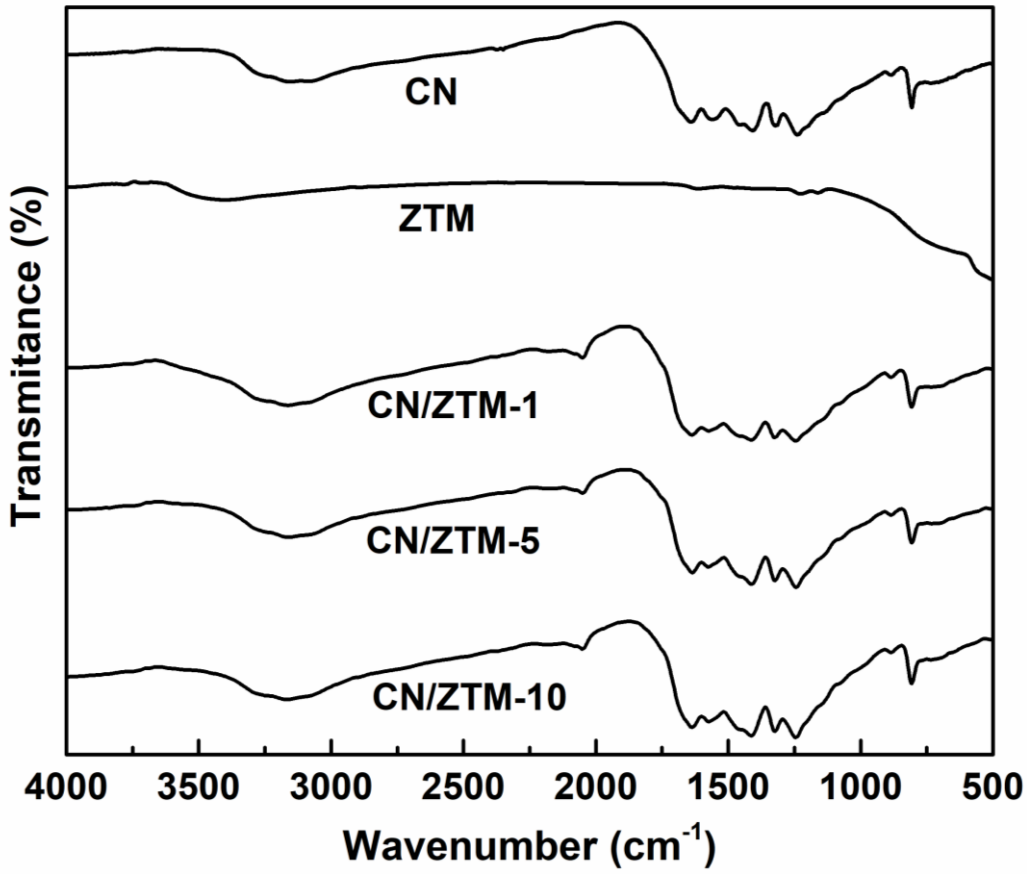

Fig. 6.2 FTIR spectra for CN, ZTM, and CN/ZTM composites.

The light absorption ability and energy band gap (Eg) of the photocatalyst was examined by UV-Vis diffuse reflectance spectroscopy, as shown in **Fig. 6.3a**. It was observed that the CN and CN/ZTM show the main photoabsorption in the visible light regions, while the ZTM showed the main light absorption in the UV region. These results are suggesting that CN and CN/ZTM composites might have higher photocatalytic activity than ZTM under visible light irradiation. The conduction band (CB) of CN and ZTM can be calculated to -0.95 eV and -1.48 eV, respectively, based on DRS-UV and VB results.

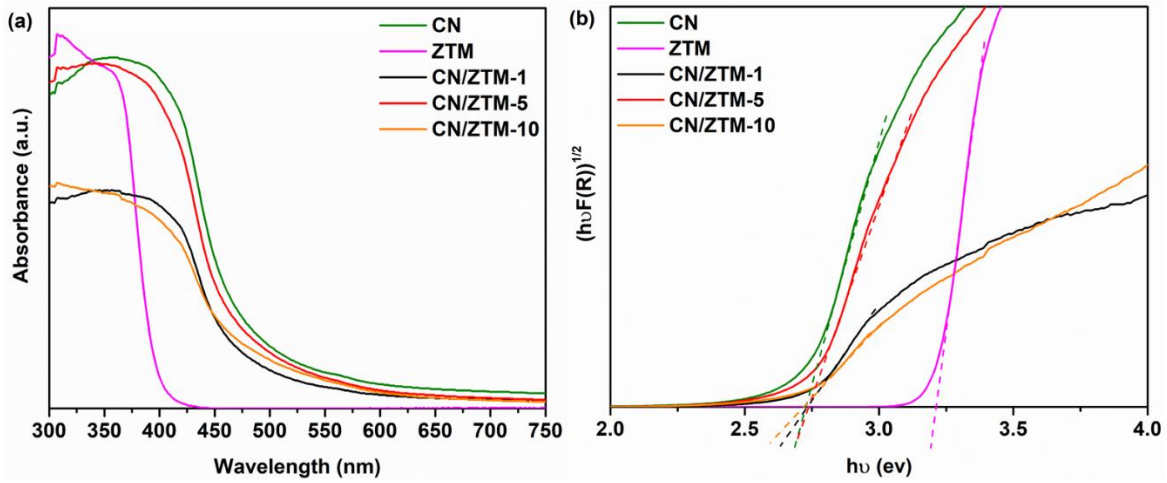

Fig. 6.3 (a) Diffuse reflectance UV-visible spectra and (b) Plots between $(h\nu F(R))^{1/2}$ vs. hν (eV) for synthetic samples.

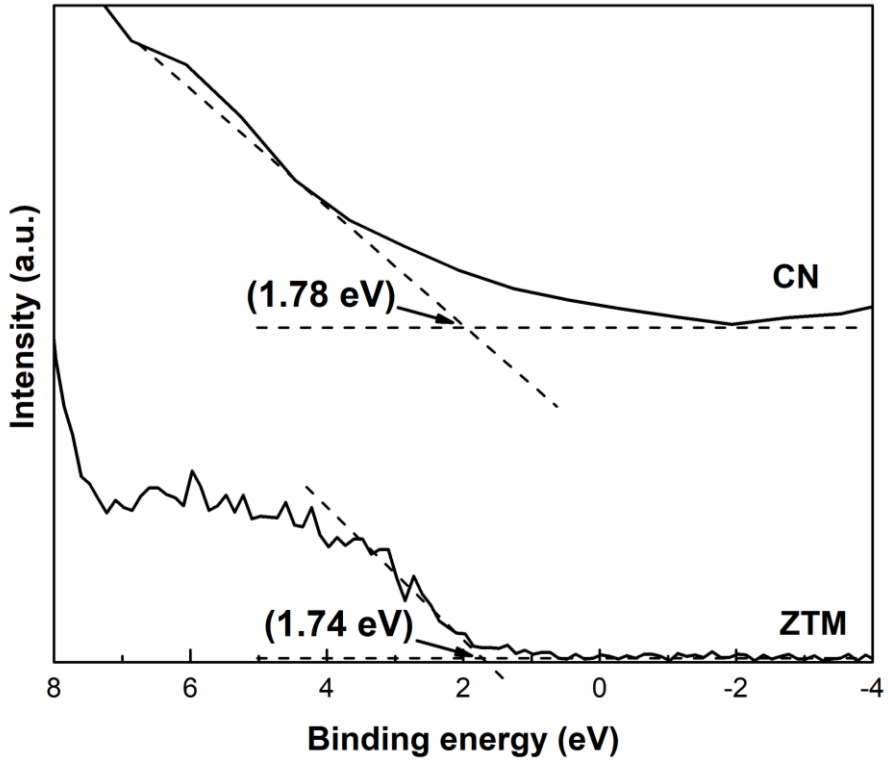

Fig. 6.4 Valence band energy region of CN and ZTM samples.

Photoluminescence spectroscopy is a useful technique to investigate the efficiency of photogenerated charge carries separation and lifetime of the photocatalyst [60-62]. In basically, the low PL intensity may indicate low recombination of

photogenerated electron and hole during light irradiation. The photoluminescence spectra (PL) of CN and CN/ZTM-5 were shown in **Fig. 6.5**. The pure CN shows the higher PL intensity than CN/ZTM-5, indicating that the fabrication of CN with ZTM can avoid the recombination of CN. The improving of separation efficiency of photogenerated charge cattier could be caused by the interfacial charge transfer between CN and ZTM through heterojunction.

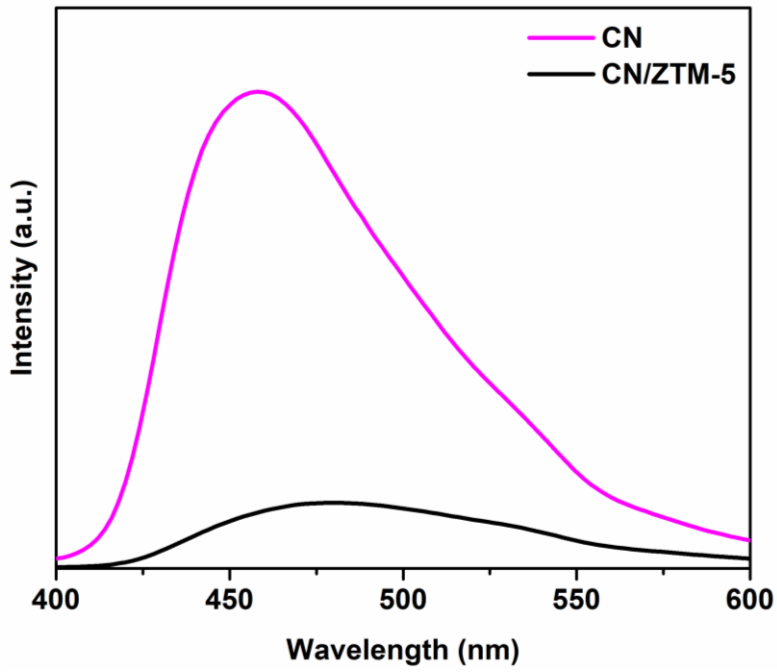

Fig. 6.5 PL curves of CN and ZTM samples.

The morphology of the CN, ZTM, and CN/ZTM samples was examined by scanning electron microscopy (SEM). It can be seen that the ZTM sample have obvious hierarchical structure while the CN is unshaped morphology (**Fig. 6.6)**. In comparison, The ZTM samples shown the mixed morphology of CN and ZTM, and it is connected, confirming the well-connected phases in the composite.

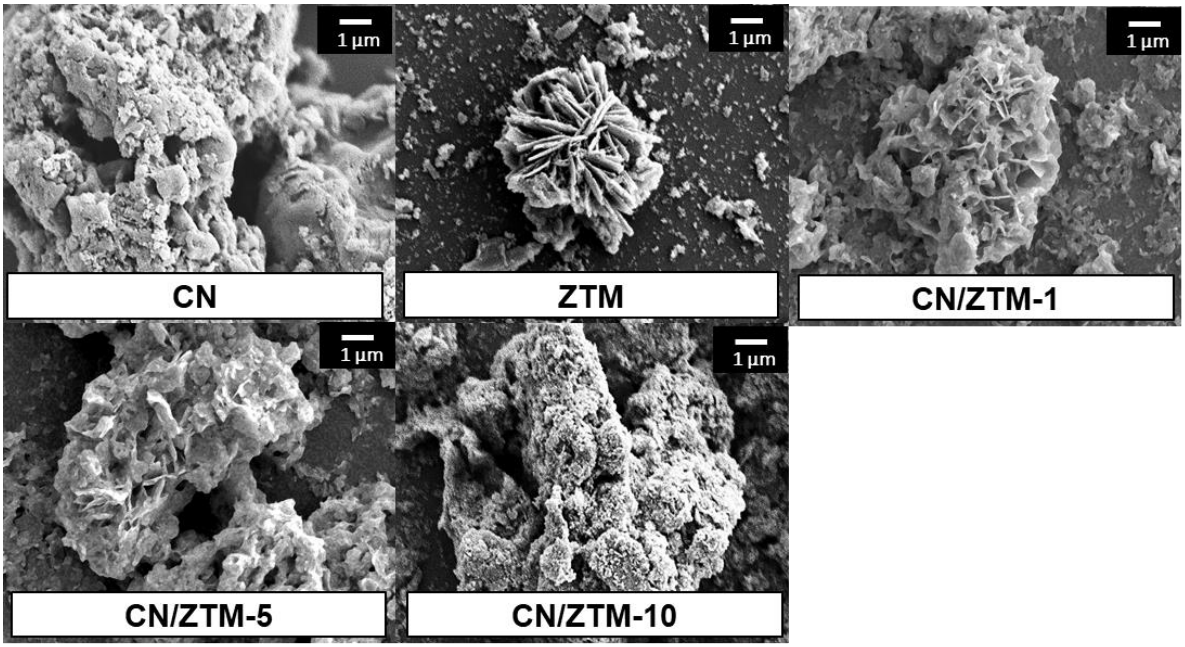

Fig. 6.6 SEM images for CN, ZTM, and CN/ZTM composites.

6.3.2 Photocatalytic degradation of RhB

The photocatalytic activity of CN, ZTM, and CN/ZTM composites was evaluated by photocatalytic degradation of RhB under visible light irradiation. **Fig. 6.7a** exhibits the time-dependent of RhB degradation of all samples. The photocatalytic activity of CN, ZTM and CN/ZTM-1, CN/ZTM-5 and CN/ZTM-10 for 2 h are 0.21, 0.42, 0.11, 0.05 and 0.15, respectively. The pristine CN show higher degradation efficiency for RhB that pure ZTM due to the higher light absorption ability in the visible region and lower energy gap. Furthermore, the CN/ZTM samples have better photocatalytic degradation performance than pure CN and ZTM, which is probably due to the formation of heterojunction between ZTM and CN can improve electron-hole separation, leading higher the photocatalytic activity for RhB degradation. The optimum loading amount of ZTM was observed at CN/ZTM -5, which contained a 5%wt of ZTM in the composite. The decreasing of photocatalytic

activity of CN/ZTM-5, which has a high content of less active ZTM in the composite. The fitting of kinetic results have high values of linear regression coefficients (R^2), confirming that the photocatalytic degradation of RhB over CN, ZTM, and CN/ZTM samples agree with the pseudo-first-order kinetic model. It was clear that the CN/ZTM sample has a higher rate constant than pristine CN and ZTM sample and the CN/ZTM-5 provide the highest rate constant that is corresponding to degradation efficiency (**Fig. 6.7b**). The degradation efficiency and kinetic study confirm that the CN/ZTM-5 is the optimized condition for CN/ZTM composite, which provides the highest photocatalytic performance for the degradation of RhB under visible light irradiation.

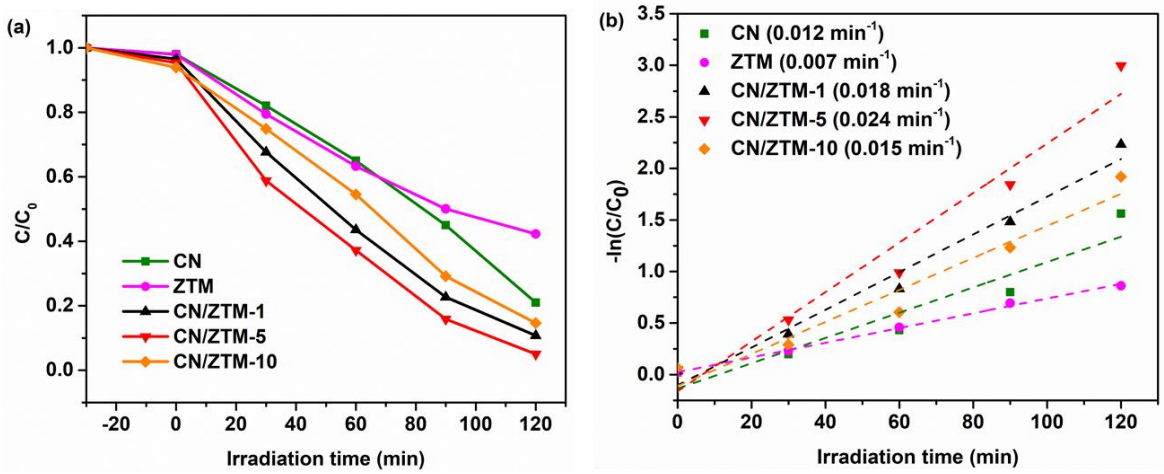

Fig. 6.7 (a) Time courses and (b) pseudo-first-order kinetics plots of photocatalytic degradation of RhB over synthetic samples.

The role of reactive species, superoxide radical ($^{\cdot}O_2^-$), hydroxyl radical ($^{\cdot}OH$) and hole (h^+), in RhB degradation over CN/ZTM-5 under visible light irradiation were examined through the radical scavenger tests. The isopropyl alcohol (IPA), p-benzoquinone(BQ) and ethylenediaminetetraacetic acid disodium salt (EDTA-2Na) were added to the RhB solution in order to remove the $^{\cdot}O_2^-$, $^{\cdot}OH$ and h^+, respectively [63, 64]. **Fig. 6.8** shows the photocatalytic degradation RhB over CN/ZTM-5 with or without a quencher. In case of adding of IPA, the degradation efficiency of RhB

decreased negligibly, indicating that the $^{\cdot}OH$ was not the main reactive free radical for the reaction. On the other hands, the dramatically decreasing of photocatalytic activity for RhB degradation was observed in the presence of BQ and EDTA-2Na, suggesting that both of $^{\cdot}O_2^-$ and h^+ were the main the reactive species and play the important role for RhB degradation in the system.

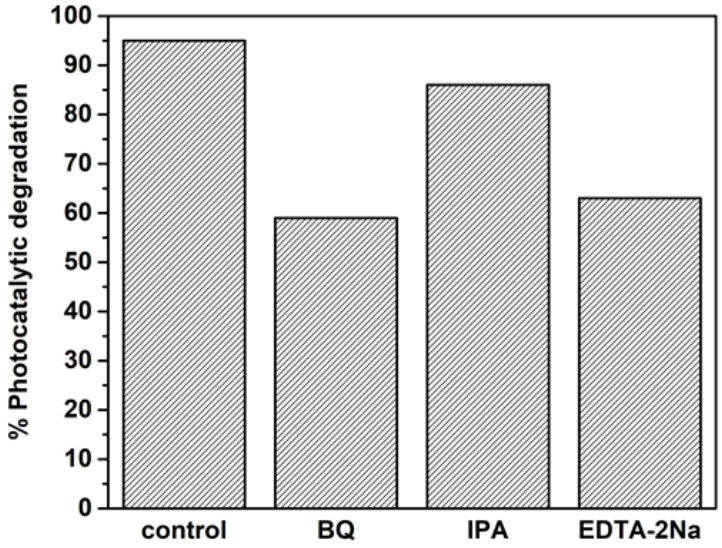

Fig. 6.8 The degradation efficiency of RhB over the CN/ZTM-5 in the presence of various radical scavengers; 120 min, catalyst loading = 1 g•L^{-1}.

6.3.3 Photocatalytic mechanism of RhB degradation over CN/ZTM

To interpret the photocatalytic degradation mechanism, the electronic band structures of CN and ZTM were focused on considering. For the above results, the VB and CB of CN are 1.78 eV and -0.95 eV *vs.* NHE, respectively, while the VB and CB of ZTM are 1.74 eV and -1.48eV. Under visible light irradiation, the photogenerated electron and hole were produced and separated at different electronic states. The photogenerated electron will move from VB to CB, leaving the photogenerated hole in the VB. The VB potentials of ZTM is more negative than the VB potential of CN, leading to the migration

of the hole from the VB of CN to the VB of ZTM. The electrons can be transferred from the CB of ZTM to the CB of CN. In the degradation of RhB, the electrons in the LUMO of RhB (E_{LUMO} = −1.10 eV versus NHE) were moved to the CB of CN due to the more positive state of the CB of CN. In this way, the electrons in the CB of CN could reduce the dissolved O_2 to $^{\bullet}O_2^-$ due to more negative level than the standard redox potential of O_2 to $^{\bullet}O_2^-$ ($E^0(O_2/^{\bullet}O_2^-)$ = −0.046 eV versus NHE [65, 66]. At the same time, h^+ in the VB of ZTM jointly decomposed RhB into degradation products through oxidation and reduction. Based on the above results, a charge transfers of each compound in CN/ZTM composites through the heterojunction can be proposed as illustrated in **Fig. 6.9**. All the photocatalytic reaction process was described the following reaction of (6.1) - (6.8).

$$\text{RhB@CN/ZTM} + h\nu \rightarrow \text{RhB*}\ (h^+ + e^-)\text{@CN/ZTM} \quad (6.1)$$

$$\text{RhB@ CN/ZTM} + h\nu \rightarrow \text{RhB*}\ (h^+)\text{@CN/ZTM}\ (e^-) \quad (6.2)$$

$$\text{CN} + h\nu \rightarrow \text{CN}\ (h^+ + e^-) \quad (6.3)$$

$$\text{ZTM} + h\nu \rightarrow \text{ZTM}\ (h^+ + e^-) \quad (6.4)$$

$$\text{ZTM}\ (h^+ + e^-) + \text{CN} \rightarrow \text{ZTM}\ (h^+) + \text{CN}\ (e^-) \quad (6.5)$$

$$\text{CN}\ (h^+ + e^-) + \text{ZTM} \rightarrow \text{CN}\ (e^-) + \text{ZTM}\ (h^+) \quad (6.6)$$

$$\text{CN}\ (e^-) + O_2 \rightarrow {}^{\bullet}O_2^- \quad (6.7)$$

$$\text{ZTM}\ (h^+) + \text{RhB} \rightarrow \text{degradation products} \quad (6.8)$$

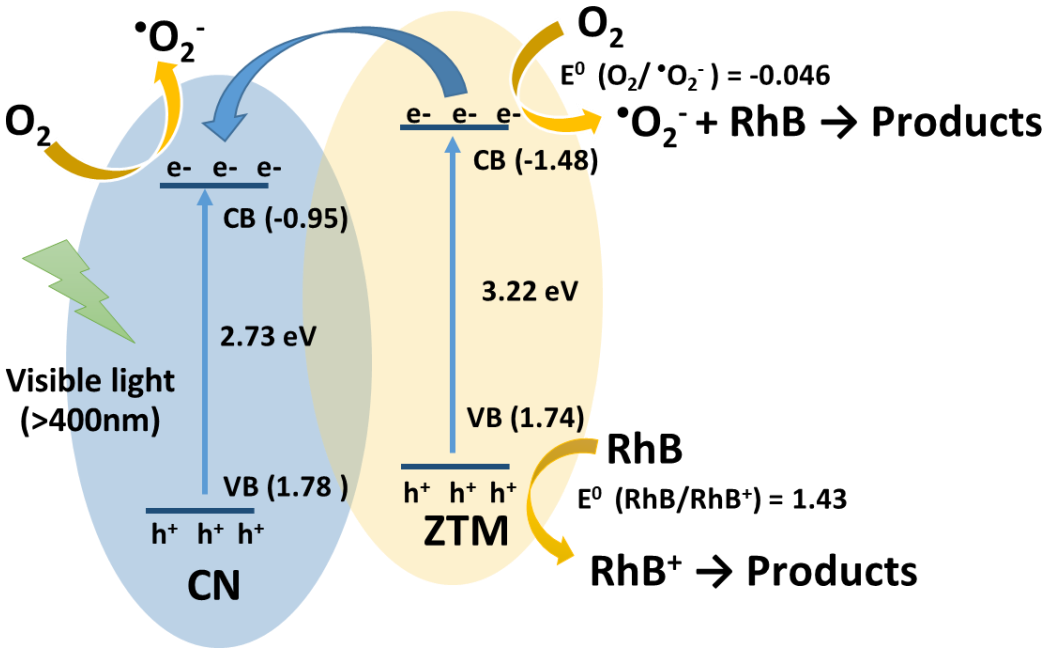

Fig. 6.9 Proposed mechanism of photocatalytic degradation phenol over CN/ZTM-5 under the visible light irradiation.

6. 4 Conclusions

CN/ZTM composites have been successfully prepared by a simple heat treatment method. In this work, the different ZTM in the composites (1-10%wt) were shown the higher photocatalytic activity for degradation of RhB than that of pristine CN and ZTM, and CN/ZTM-5 composite exhibited the highest photocatalytic activity. The results emphasize that the significant improvement in the photocatalytic performance of CN/ZTM composite might come from the highly electron-hole pair separation via heterojunction between CN and ZTM.

References

[1] N. D, K.K. Kondamareddy, H. Bin, D. Lu, P. Kumar, R.K. Dwivedi, V.O. Pelenovich, X.Z. Zhao, W. Gao, D. Fu, Enhanced visible light photodegradation activity of RhB/MB from aqueous solution using nanosized novel Fe-Cd co-modified ZnO, Sci Rep, 8 (2018) 10691, 1-12.

[2] F.H. AlHamedi, M.A. Rauf, S.S. Ashraf, Degradation studies of Rhodamine B in the presence of UV/H_2O_2, Desalination, 239 (2009) 159-166.

[3] H. Ps, L. Joseph, D. A, Photocatalytic degradation of textile dyes by hydrogel supported titanium dioxide nanoparticles, journal of Environmental Engineering and Ecological Science, 2 (2013) 2, 1-9.

[4] P. Rajasulochana, V. Preethy, Comparison on efficiency of various techniques in treatment of waste and sewage water – A comprehensive review, Resource-Efficient Technologies, 2 (2016) 175-184.

[5] W.J. Cosgrove, D.P. Loucks, Water management: Current and future challenges and research directions, Water Resources Research, 51 (2015) 4823-4839.

[6] M. Epifani, S. Kaciulis, A. Mezzi, D. Altamura, C. Giannini, R. Díaz, C. Force, A. Genç, J. Arbiol, P. Siciliano, E. Comini, I. Concina, Inorganic Photocatalytic Enhancement: Activated RhB Photodegradation by Surface Modification of SnO_2 Nanocrystals with V_2O_5-like species, Scientific Reports, 7 (2017) 44763-44770.

[7] X. Li, B. Wang, Y. Huang, J. Di, J. Xia, W. Zhu, H. Li, Boosting photocatalytic degradation of RhB via interfacial electronic effects between Fe-based ionic liquid and g-C_3N_4, Green Energy & Environment, 4 (2019) 198-206.

[8] J. Zhuang, W. Dai, Q. Tian, Z. Li, L. Xie, J. Wang, P. Liu, X. Shi, D. Wang, Photocatalytic degradation of RhB over TiO_2 bilayer films: effect of defects and their location, Langmuir, 26 (2010) 9686-9694.

[9] H. Gan, Z. Wang, H. Li, Y. Wang, L. Sun, Y. Li, CdSe QDs@UIO-66 composite with enhanced photocatalytic activity towards RhB degradation under visible-light irradiation, RSC Advances, 6 (2016) 5192-5197.

[10] S. Yin, J. Han, T. Zhou, R. Xu, Recent progress in g-C_3N_4 based low cost photocatalytic system: activity enhancement and emerging applications, Catalysis Science & Technology, 5 (2015) 5048-5061.

[11] Q. Zhao, L. Fu, D. Jiang, Y. Xi, H. Yang, A nanoclay-induced defective g-C_3N_4 photocatalyst for highly efficient catalytic reactions, Chem Commun (Camb), 54 (2018) 8249-8252.

[12] A. Naseri, M. Samadi, A. Pourjavadi, A.Z. Moshfegh, S. Ramakrishna, Graphitic carbon nitride (g-C_3N_4)-based photocatalysts for solar hydrogen generation: recent advances and future development directions, Journal of Materials Chemistry A, 5 (2017) 23406-23433.

[13] W. Zou, Y. Shao, Y. Pu, Y. Luo, J. Sun, K. Ma, C. Tang, F. Gao, L. Dong, Enhanced visible light photocatalytic hydrogen evolution via cubic CeO_2 hybridized g-C_3N_4 composite, Applied Catalysis B: Environmental, 218 (2017) 51-59.

[14] R. Ye, H. Fang, Y.Z. Zheng, N. Li, Y. Wang, X. Tao, Fabrication of $CoTiO_3$/g-C_3N_4 Hybrid Photocatalysts with Enhanced H_2 Evolution: Z-Scheme Photocatalytic Mechanism Insight, ACS Appl Mater Interfaces, 8 (2016) 13879-13889.

[15] X. Bai, L. Wang, R. Zong, Y. Zhu, Photocatalytic Activity Enhanced via g-C_3N_4 Nanoplates to Nanorods, The Journal of Physical Chemistry C, 117 (2013) 9952-9961.

[16] W. Iqbal, B. Qiu, J. Lei, L. Wang, J. Zhang, M. Anpo, One-step large-scale highly active g-C_3N_4 nanosheets for efficient sunlight-driven photocatalytic hydrogen production, Dalton Trans, 46 (2017) 10678-10684.

[17] J.X. Sun, Y.P. Yuan, L.G. Qiu, X. Jiang, A.J. Xie, Y.H. Shen, J.F. Zhu, Fabrication of composite photocatalyst g-C_3N_4-ZnO and enhancement of photocatalytic activity under visible light, Dalton Trans, 41 (2012) 6756-6763.

[18] Y. Fu, C.a. Liu, C. Zhu, H. Wang, Y. Dou, W. Shi, M. Shao, H. Huang, Y. Liu, Z. Kang, High-performance NiO/g-C_3N_4 composites for visible-light-driven photocatalytic overall water splitting, Inorganic Chemistry Frontiers, 5 (2018) 1646-1652.

[19] W.J. Ong, L.L. Tan, S.P. Chai, S.T. Yong, Heterojunction engineering of graphitic carbon nitride (g-C_3N_4) via Pt loading with improved daylight-induced photocatalytic reduction of carbon dioxide to methane, Dalton Trans, 44 (2015) 1249-1257.

[20] Z. Wei, F. Liang, Y. Liu, W. Luo, J. Wang, W. Yao, Y. Zhu, Photoelectrocatalytic degradation of phenol-containing wastewater by TiO_2/g-C_3N_4 hybrid heterostructure thin film, Applied Catalysis B: Environmental, 201 (2017) 600-606.

[21] N. Boonprakob, N. Wetchakun, S. Phanichphant, D. Waxler, P. Sherrell, A. Nattestad, J. Chen, B. Inceesungvorn, Enhanced visible-light photocatalytic activity of g-C_3N_4/TiO_2 films, J Colloid Interface Sci, 417 (2014) 402-409.

[22] S. Nayak, L. Mohapatra, K. Parida, Visible light-driven novel g-C_3N_4/NiFe-LDH composite photocatalyst with enhanced photocatalytic activity towards water oxidation and reduction reaction, Journal of Materials Chemistry A, 3 (2015) 18622-18635.

[23] J. Liu, J. Li, X. Bing, D.H.L. Ng, X. Cui, F. Ji, D.D. Kionga, ZnCr-LDH/N-doped graphitic carbon-incorporated g-C_3N_4 2D/2D nanosheet heterojunction with enhanced charge transfer for photocatalysis, Materials Research Bulletin, 102 (2018) 379-390.

[24] M. Mureseanu, T. Radu, R.-D. Andrei, M. Darie, G. Carja, Green synthesis of g-C_3N_4/CuONP/LDH composites and derived g-C_3N_4/MMO and their photocatalytic performance for phenol reduction from aqueous solutions, Applied Clay Science, 141 (2017) 1-12.

[25] S. Tonda, S. Kumar, M. Bhardwaj, P. Yadav, S. Ogale, g-C_3N_4/NiAl-LDH 2D/2D Hybrid Heterojunction for High-Performance Photocatalytic Reduction of CO_2 into Renewable Fuels, ACS Appl Mater Interfaces, 10 (2018) 2667-2678.

[26] J. Shi, S. Li, F. Wang, L. Gao, Y. Li, X. Zhang, J. Lu, 2D/2D g-C_3N_4/MgFe MMO nanosheet heterojunctions with enhanced visible-light photocatalytic H_2 production, Journal of Alloys and Compounds, 769 (2018) 611-619.

[27] Y. Wang, W. Wei, M. Li, S. Hu, J. Zhang, R. Feng, In situ construction of Z-scheme g-C_3N_4/$Mg_{1.1}Al_{0.3}Fe_{0.2}O_{1.7}$ nanorod heterostructures with high N_2 photofixation ability under visible light, RSC Advances, 7 (2017) 18099-18107.

[28] J. Yu, Q. Wang, D. O'Hare, L. Sun, Preparation of two dimensional layered double hydroxide nanosheets and their applications, Chem Soc Rev, 46 (2017) 5950-5974.

[29] L. Xue, Z. Lu, Y. Cheng, X. Sun, H. Lin, X. Xiao, X. Liu, S. Zhuo, Three-dimensional layered double hydroxide membranes: fabrication technique, growth mechanism, and enhanced photocatalytic activity, Chem Commun (Camb), 54 (2018) 8494-8497.

[30] B.T. Huy, C.T.B. Thao, V.-D. Dao, N.T.K. Phuong, Y.-I. Lee, A Mixed-Metal Oxides/Graphitic Carbon Nitride: High Visible Light Photocatalytic Activity for

Efficient Mineralization of Rhodamine B, Advanced Materials Interfaces, 4 (2017) 1700128, 1-9.

[31] A. Akhundi, A. Habibi-Yangjeh, Ternary magnetic g-C_3N_4/Fe_3O_4/AgI nanocomposites: Novel recyclable photocatalysts with enhanced activity in degradation of different pollutants under visible light, Materials Chemistry and Physics, 174 (2016) 59-69.

[32] M. Jourshabani, Z. Shariatinia, G. Achari, C.H. Langford, A. Badiei, Facile synthesis of NiS_2 nanoparticles ingrained in a sulfur-doped carbon nitride framework with enhanced visible light photocatalytic activity: two functional roles of thiourea, Journal of Materials Chemistry A, 6 (2018) 13448-13466.

[33] Y. Zheng, Z. Yu, F. Lin, F. Guo, K.A. Alamry, L.A. Taib, A.M. Asiri, X. Wang, Sulfur-Doped Carbon Nitride Polymers for Photocatalytic Degradation of Organic Pollutant and Reduction of Cr(VI), Molecules, 22 (2017) 572,1-17.

[34] S. Hu, L. Ma, Y. Xie, F. Li, Z. Fan, F. Wang, Q. Wang, Y. Wang, X. Kang, G. Wu, Hydrothermal synthesis of oxygen functionalized S-P codoped g-C_3N_4 nanorods with outstanding visible light activity under anoxic conditions, Dalton Trans, 44 (2015) 20889-20897.

[35] S. Tonda, W.-K. Jo, Plasmonic Ag nanoparticles decorated NiAl-layered double hydroxide/graphitic carbon nitride nanocomposites for efficient visible-light-driven photocatalytic removal of aqueous organic pollutants, Catalysis Today, 315 (2018) 213-222.

[36] R. You, H. Dou, L. Chen, S. Zheng, Y. Zhang, Graphitic carbon nitride with S and O codoping for enhanced visible light photocatalytic performance, RSC Advances, 7 (2017) 15842-15850.

[37] F. Wei, Y. Liu, H. Zhao, X. Ren, J. Liu, T. Hasan, L. Chen, Y. Li, B.L. Su, Oxygen self-doped g-C3N4 with tunable electronic band structure for unprecedentedly enhanced photocatalytic performance, Nanoscale, 10 (2018) 4515-4522.

[38] X. Dong, Z. Sun, X. Zhang, C. Li, S. Zheng, Construction of BiOCl/g-C_3N_4 /kaolinite composite and its enhanced photocatalysis performance under visible-light irradiation, Journal of the Taiwan Institute of Chemical Engineers, 84 (2018) 203-211.

[39] M. Jourshabani, Z. Shariatinia, A. Badiei, Sulfur-Doped Mesoporous Carbon Nitride Decorated with Cu Particles for Efficient Photocatalytic Degradation under

Visible-Light Irradiation, The Journal of Physical Chemistry C, 121 (2017) 19239-19253.

[40] Z. Sun, G. Yao, X. Zhang, S. Zheng, R.L. Frost, Enhanced visible-light photocatalytic activity of kaolinite/g-C_3N_4 composite synthesized via mechanochemical treatment, Applied Clay Science, 129 (2016) 7-14.

[41] Z. Sun, C. Li, X. Du, S. Zheng, G. Wang, Facile synthesis of two clay minerals supported graphitic carbon nitride composites as highly efficient visible-light-driven photocatalysts, J Colloid Interface Sci, 511 (2018) 268-276.

[42] C. Li, Z. Sun, W. Huang, S. Zheng, Facile synthesis of g-C_3N_4/montmorillonite composite with enhanced visible light photodegradation of rhodamine B and tetracycline, Journal of the Taiwan Institute of Chemical Engineers, 66 (2016) 363-371.

[43] Z. Sun, F. Yuan, X. Li, C. Li, J. Xu, B. Wang, Fabrication of Novel Cyanuric Acid Modified g-C_3N_4/Kaolinite Composite with Enhanced Visible Light-Driven Photocatalytic Activity, Minerals, 8 (2018) 437,1-15.

[44] P. Roy Chowdhury, K.G. Bhattacharyya, Synthesis and characterization of Mn/Co/Ti LDH and its utilization as a photocatalyst in visible light assisted degradation of aqueous Rhodamine B, RSC Adv, 6 (2016) 112016-112034.

[45] S.J. Xia, F.X. Liu, Z.M. Ni, J.L. Xue, P.P. Qian, Layered double hydroxides as efficient photocatalysts for visible-light degradation of Rhodamine B, J Colloid Interface Sci, 405 (2013) 195-200.

[46] L. Mohapatra, K.M. Parida, Zn–Cr layered double hydroxide: Visible light responsive photocatalyst for photocatalytic degradation of organic pollutants, Separation and Purification Technology, 91 (2012) 73-80.

[47] Q. Liu, J. Ma, K. Wang, T. Feng, M. Peng, Z. Yao, C. Fan, S. Komarneni, BiOCl and TiO_2 deposited on exfoliated ZnCr-LDH to enhance visible-light photocatalytic decolorization of Rhodamine B, Ceramics International, 43 (2017) 5751-5758.

[48] Y. Zhu, R. Zhu, G. Zhu, M. Wang, Y. Chen, J. Zhu, Y. Xi, H. He, Plasmonic Ag coated Zn/Ti-LDH with excellent photocatalytic activity, Applied Surface Science, 433 (2018) 458-467.

[49] Y. Zhang, J. Wu, Y. Deng, Y. Xin, H. Liu, D. Ma, N. Bao, Synthesis and visible-light photocatalytic property of Ag/GO/g-C_3N_4 ternary composite, Materials Science and Engineering: B, 221 (2017) 1-9.

[50] M. Wang, Y. Zhang, C. Jin, Z. Li, T. Chai, T. Zhu, Fabrication of novel ternary heterojunctions of Pd/g-C_3N_4/Bi_2MoO_6 hollow microspheres for enhanced visible-light photocatalytic performance toward organic pollutant degradation, Separation and Purification Technology, 211 (2019) 1-9.

[51] J. Xue, S. Ma, Y. Zhou, Z. Zhang, M. He, Facile Photochemical Synthesis of Au/Pt/g-C_3N_4 with Plasmon-Enhanced Photocatalytic Activity for Antibiotic Degradation, ACS Appl Mater Interfaces, 7 (2015) 9630-9637.

[52] D. Papoulis, D. Panagiotaras, P. Tsigrou, K.C. Christoforidis, C. Petit, A. Apostolopoulou, E. Stathatos, S. Komarneni, I. Koukouvelas, Halloysite and sepiolite –TiO_2 nanocomposites: Synthesis characterization and photocatalytic activity in three aquatic wastes, Materials Science in Semiconductor Processing, 85 (2018) 1-8.

[53] J. Cao, C. Qin, Y. Wang, H. Zhang, G. Sun, Z. Zhang, Solid-State Method Synthesis of SnO_2-Decorated g-C_3N_4 Nanocomposites with Enhanced Gas-Sensing Property to Ethanol, Materials, 10 (2017) 604, 1-14.

[54] B. Montassar Billeh, A. En Naciri, A. Moadhen, H. Rinnert, M. Guendouz, Y. Battie, C. Annick, M.A. Zaïbi, M. Oueslati, Effects of silicon porosity on physical properties of ZnO films,175 (2016) 233-240.

[55] V.P. Dinesh, P. Biji, A. Ashok, S.K. Dhara, M. Kamruddin, A.K. Tyagi, B. Raj, Plasmon-mediated, highly enhanced photocatalytic degradation of industrial textile dyes using hybrid ZnO@Ag core–shell nanorods, RSC Adv., 4 (2014) 58930-58940.

[56] W. Zhang, X. Xiao, Y. Li, X. Zeng, L. Zheng, C. Wan, Liquid-exfoliation of layered MoS2 for enhancing photocatalytic activity of TiO_2/g-C_3N_4 photocatalyst and DFT study, Applied Surface Science, 389 (2016) 496-506.

[57] M. Fu, J. Liao, F. Dong, H. Li, H. Liu, Growth of g-C_3N_4 Layer on Commercial TiO_2 for Enhanced Visible Light Photocatalytic Activity, Journal of Nanomaterials, 2014 (2014) 1-8.

[58] J. Tong, L. Zhang, F. Li, K. Wang, L. Han, S. Cao, Rapid and high-yield production of g-C_3N_4 nanosheets via chemical exfoliation for photocatalytic H_2 evolution, RSC Advances, 5 (2015) 88149-88153.

[59] M. Xu, L. Han, S. Dong, Facile fabrication of highly efficient g-C_3N_4/Ag_2O heterostructured photocatalysts with enhanced visible-light photocatalytic activity, ACS Appl Mater Interfaces, 5 (2013) 12533-12540.

[60] Y. Yang, T. Zhang, L. Le, X. Ruan, P. Fang, C. Pan, R. Xiong, J. Shi, J. Wei, Quick and facile preparation of visible light-driven TiO_2 photocatalyst with high absorption and photocatalytic activity, Sci Rep, 4 (2014) 7045-7050.

[61] A.B. Lavand, Y.S. Malghe, Visible light photocatalytic degradation of 4-chlorophenol using C/ZnO/CdS nanocomposite, Journal of Saudi Chemical Society, 19 (2015) 471-478.

[62] J. Cheng, Y. Wang, Y. Xing, M. Shahid, W. Pan, A stable and highly efficient visible-light photocatalyst of TiO_2 and heterogeneous carbon core–shell nanofibers, RSC Advances, 7 (2017) 15330-15336.

[63] T. Liu, L. Wang, X. Lu, J. Fan, X. Cai, B. Gao, R. Miao, J. Wang, Y. Lv, Comparative study of the photocatalytic performance for the degradation of different dyes by $ZnIn_2S_4$: adsorption, active species, and pathways, RSC Advances, 7 (2017) 12292-12300.

[64] Q. Zhang, Y. Zhang, Z. Meng, W. Tong, X. Yu, Q. An, Constructing the magnetic bifunctional graphene/titania nanosheet-based composite photocatalysts for enhanced visible-light photodegradation of MB and electrochemical ORR from polluted water, Sci Rep, 7 (2017) 12296-12305.

[65] Y. Peng, Q.-G. Chen, D. Wang, H.-Y. Zhou, A.-W. Xu, Synthesis of one-dimensional WO_3–Bi_2WO_6 heterojunctions with enhanced photocatalytic activity, CrystEngComm, 17 (2015) 569-576.

[66] X. Guo, L. Rao, P. Wang, L. Zhang, Y. Wang, Synthesis of Porous Boron-Doped Carbon Nitride: Adsorption Capacity and Photo-Regeneration Properties, Int J Environ Res Public Health, 16 (2019) 581, 1-16.

Chapter 7

Dye-sensitized Photocatalyst of Sepiolite for Organic Dye Degradation

7. 1 Introduction

Naturally abundant 2:1 type of clay minerals, representatively smectite, have been extensively used as support materials for semiconductors or other photocatalysts due to its natural abundant availability and characteristics features, such as, fibrous or layered morphology, large specific surface areas, superior cation exchange capacity, negative surface charge, and a hydroxyl group rooted at the bottom in the octahedral sheet [1-5]. Comprehensively, all these natural properties can be utilized for several types of organic and inorganic types of modifications which are benefited to the development of clay-based photocatalyst [6, 7]. In recent years, natural sepiolite, belonging to the 2:1 type of clay minerals, has gained great interest in different fields of application, including the development of photocatalyst [8-10]. Sepiolite is a hydrous magnesium silicate that is widespread due to its unusual fibrous morphology and intracrystalline tunnels [11, 12]. The ideal chemical formula is expressed as $Si_{12}Mg_8O_{30}(OH)_4 \cdot 12H_2O$ for the half-unit cell. In the structure of sepiolite, there is an alternation of blocks and tunnels around 200 Å in pore size that grows up in the direction of fibers belonging to a chain type of clay mineral [13]. Each structural block is composed of a central octahedral sheet containing magnesium sandwiched by two tetrahedral silicate sheets. The structure of sepiolite results in zeolite-like channels [14]. The peculiar pore structure with interior channels contributes to voluminously adsorb cationic organic molecules and ions. Also, these channels might contain zeolitic water and exchangeable metal ions. The structural and textural physicochemical properties of sepiolite offer its exclusive role compared to other clay materials.

So far, sepiolite has been considered as an effective hole transporter between known semiconductor materials and degrading targets in the photocatalytic reaction to

decompose organic pollutants, including organic dyes and pharmaceutical wastes. Many TiO_2-based composites have been developed to improve photodegradation using a sepiolite matrix: ternary heterogeneous BiOCl/TiO_2/sepiolite composite for tetracycline degradation [15], sepiolite-TiO_2 nanocomposites for the orange G dye degradation [16], TiO_2/sepiolite composites for the degradation of acid red G and 4-nitrophenol [17], and TiO_2/sepiolite composites to decompose phenol [18]. Composites with other metallic oxides and hydroxides have also been synthesized for photodegradation of organic dye compounds: Sepiolite@LDH composite for simultaneous photocatalytic degradation of methyl orange (MO) and methylene blue (MB) dye [19], ternary ZnO/Fe_3O_4-sepiolite nanostructured material for MB dye degradation [20, 21], and quantum-sized ZnO particles on sepiolite for the degradation of reactive blue 4 [22]. So far, from the above reports, sepiolite has been generally utilized as an efficient supporting material for well-known semiconductors and other types of active species under UV light irradiation.

Fibrous morphologies of sepiolite offer the rigid and active surfaces for the adsorption of cationic dye molecules through electrostatic interaction or complexation. Successful adsorption of dye molecules on clay surfaces is indispensably the first step for photocatalytic reactions [23-25]. Siloxane bonds are existing at the edge of the outer surface, and broken and terminated Si–O, and Mg–O bonds are on lateral surfaces of sepiolite. Since these unprotected metallic ions at the edges are electron-deficient, they are expected to act as natural electron acceptors. The adsorbed cationic dye species, which are electro-statistically bound with the broken bond surface, should be responsible for the generation of dye radical species. It is predictable that the formed dye radicals can react with active oxygen species present within the system, which

may lead to a disintegration of the dyes [26]. Also, it is well-known that the highly polar surface of the clay material is advantageous to stabilize the generated radical species, which prolongs the lifetime and ultimately causes better photocatalytic performance [6].

As aforementioned, sepiolite was utilized as supporting material for well-known photocatalysts (TiO_2, BiOCl, ZnO). As per our knowledge, there was no report available on the dye-sensitization of natural sepiolite. In this work, we tried to fulfill the understanding of natural sepiolite as a dye-sensitized photocatalyst for dyes degradation. The observed phenomenon was proved by several physiochemical and photocatalytic experimental studies in the presence of different dyes with various size and charges, e.g., anionic or cation colorants organic pollutants. One of the important findings in the present work was that natural sepiolite material without any modification could be utilized for the photocatalytic degradation of organic dye via the dye-sensitization mechanism.

The detail objectives in the present study were to investigate the visible light-driven photocatalytic degradation performance of the natural, pristine sepiolite for cationic (rhodamine B (RhB) and methylene blue (MB)) and anionic (orange II (OII) and trypan blue (TB)) dyes and to propose the mechanism based on the experimental results.

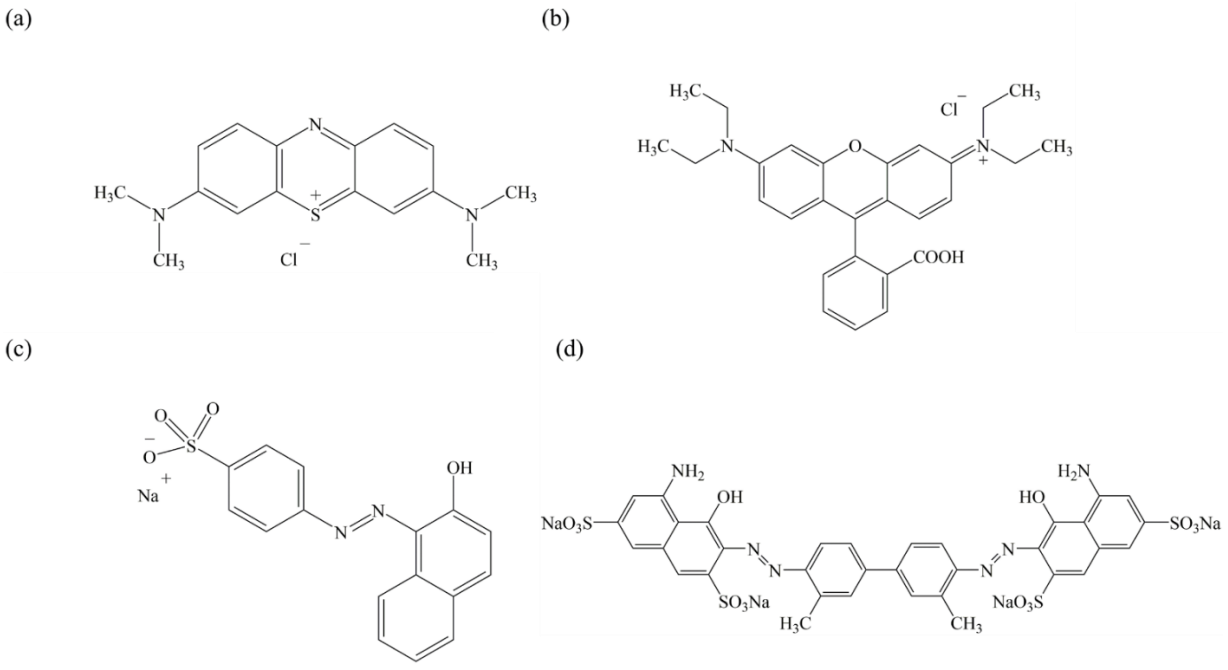

Fig. 7.1 Chemical structures of dyes: (a) methylene blue (MB); (b) rhodamine B (RhB); (c) orange II (OII); (d) trypan blue (TB).

The previous reports regarding of photocatalytic degradation of organic dyes using composites, including sepiolite, were summarized in **Table 7.1** to compare with the present work. From the comparative results of dye degradation, we could clearly signify our research work from the reported results. In the previous reports, sepiolite was utilized as supporting material for known photocatalysts, such as TiO_2, and showed ~80% RhB dye degradation, whereas we observed that pristine sepiolite material could show comparable degradation efficiency under visible light irradiation. We believe that the present finding might be useful for a detailed understanding of the upcoming research scope of the sepiolite-based photocatalyst materials for organic dye degradation.

Table 7.1. Comparison of photocatalytic efficiency of sepiolite composites with other reported photocatalysts for organic dye degradation.

Catalyst	Active compound	Target	C_0 (mol/L)	Loading (g/L)	Efficacy (%)	Time (min)	Ref.
Bi_2O_3/sepiolite	Bi_2O_3	Malachite green	14×10^{-5}	0.5	98.2	180	[27]
Sepiolite-TiO_2	TiO_2	Orange G	2.2×10^{-5}	0.8	97.8	150	[28]
Sepiolite/Cu_2O/Cu	Cu_2O/Cu	Congo red	1.4×10^{-5}	0.2	95.1	50	[29]
Eu-TiO_2/sepiolite	Eu-TiO_2	Orange G	2.2×10^{-5}	0.8	~70	600	[30]
ZnCr LDH/Sepiolite	ZnCr LDH	MB	3.1×10^{-5}	1.25	93.1	120	[19]
Sepiolite –TiO_2	TiO_2	RhB	8.3×10^{-5}	0.85	~80	120	[31]
Sepiolite	Adsorbed MB on sepiolite	MB	2.0×10^{-5}	0.25	83.3	120	This work
Sepiolite	Adsorbed RhB on sepiolite	RhB	2.0×10^{-5}	0.25	65.5	120	This work

7.2 Materials and Methods

7.2.1 Materials and reagents

Sepiolite (13% Mg, ≤ 10% loss on drying) was obtained from Sigma Aldrich Japan Co. Ltd (Tokyo, Japan) with the color of grayish white. RhB ($C_{28}H_{31}ClN_2O_3$, 97% dye content, RhB) was also obtained from Sigma Aldrich Japan. MB ($C_{16}H_{18}N_3SCl\cdot 3H_2O$, MB) was purchased from Waldeck GmbH & Co. KG (Münster, Germany). Orange II ($C_{16}H_{11}N_2NaO_4S$, OII) and TB ($C_{34}H_{28}N_6O_{14}S_4$, TB) were purchased from Wako Chemicals (Osaka, Japan). The chemicals were directly utilized without further purification. Ultrapure water was used in the preparation of the organic dye solutions and their experiments.

7.2.2 Characterizations

The characterizations of the solid samples were carried out by X-ray diffraction (XRD), UV–vis diffuse reflectance spectroscopy (DRS), specific surface area (BET method), X-ray photoelectron spectroscopy (XPS) and photoluminescence spectroscopy (PL). Detailes are described in **chapter 2**.

7.2.3 Photocatalytic test

Photocatalytic performances were evaluated toward the photocatalytic degradation of various organic dyes under the visible light ($\lambda > 400$ nm) irradiation. Typically, 50 mg of sepiolite powder was magnetically stirred in 50 mL of 2×10^{-5} M organic dye solution in the dark condition for 30 min to reach the adsorption-desorption equilibrium. The suspensions were then irradiated using a 500 W Xe lamp

with a cut-off filter. During the light illumination, solutions were collected and filtrated by 0.45 μm membrane filters to remove the suspended particles. The concentrations of the remaining organic dyes of MB, RhB, OII, and TB were determined by UV-Vis spectrometry at 665, 554, 483, and 575 nm, respectively. Moreover, photocatalytic stability of sepiolite for RhB degradation under visible light irradiation was examined by the recycling test for three cycles. After every cycle, the spent sepiolite was separated from the suspension by centrifugation, followed by a wash with ethanol and water three times to remove covered, unreacted RhB and degradation products. The spent sepiolite was dried and used in the next cycle under identical photocatalytic experiment.

7. 3 Results and Discussion

7.3.1 Characterizations

As received, the sepiolite was confirmed by several characterization techniques, including XRD, FTIR, TEM, XRF, specific surface area measurement, and XPS analysis. As shown in **Fig. 7.3a**, the specimen had a single phase of sepiolite in the XRD pattern (Joint Committee on Powder Diffraction Standards (JCPDS) 13-0595). There were trace amounts of impurities of Ti, Fe, and Al, confirmed by XRF (**Table 7.2**). The purity as sepiolite ($Si_{12}Mg_8O_{30}(OH)_4$) could be estimated to 89.9%, based on Mg content. The XRD results showed several reflections, such as the strong diffraction peaks, for pure sepiolite observed around d-spacing value 1.2 nm at $2\theta = 7.3°$ (110), which represent the characteristics interlayer distance reflection for sepiolite clay. And another characteristics reflection peaks for the pure phases of sepiolite clay was

observed at 0.75 nm.at 2θ 11.83° (130), 0.66 nm at 2θ 13.12°, (040), 0.45 nm.at 2θ 19.71° (060), 0.43 nm.at 2θ 20.66° (031), 0.375 nm.at 2θ 23.74° (221), 0.334 nm.at 2θ 26.71° (400), and 0.25 nm.at 2θ 35.01° (191), which confirmed the presence of pure phases of sepiolite [32].

Table 7.2. The elemental compositions of sepiolite in wt%.

Component	**C**	**N**	**O**	**F**	**Na**	**Mg**	**Al**	**Si**	**P**	**S**
wt.%	6.817	0.339	53.459	0.864	0.047	13.182	1.087	23.235	0.007	0.011
Component	Cl	K	Ca	Ti	Mn	Fe	Cu	Zn	Zr	Ba
wt.%	0.017	0.435	0.135	0.054	0.011	0.265	0.002	0.009	0.001	0.019

The FTIR spectrum of the pristine sepiolite clay mineral was observed in **Fig. 7.2b** similarly to that reported in the literature for 2:1 smectite clay minerals by a slight variation in the frequencies [33, 34]. The bands observed in the range of 3000 and 3800 cm^{-1} were assigned to the stretching vibration mode of the hydroxyl groups in Mg–OH. The peak centered at 3625 cm^{-1}, attributed to OH stretching mode. The absorption bands centered at about 3423 and 3251 cm^{-1} corresponding to the vibration mode of physisorbed water (surface and zeolitic); a band at 1673 cm^{-1} due to the bending mode of zeolitic water; bands in the 1200–400 cm^{-1} range characteristic of silicate; bands centered at 1014 and 462 cm^{-1} due to stretching in the vibration mode of Si–O–Si groups in the tetrahedral sheet; bands at 1217 and 975 cm^{-1} due to Si–O bonds; and bands at 690 and 639 cm^{-1} corresponding to the vibration mode of Mg–OH bond [34].

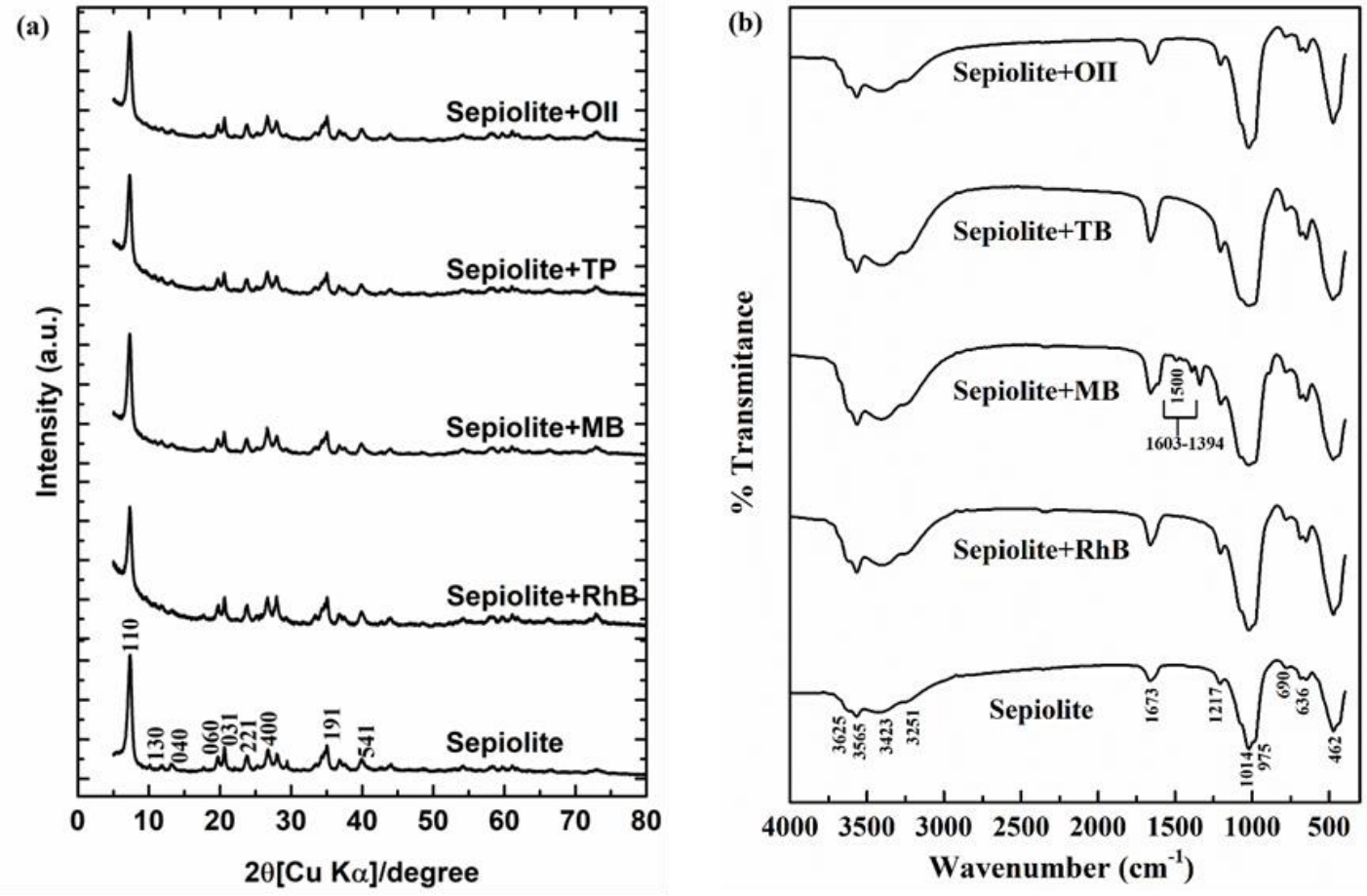

Fig. 7.2 (**a**) PXRD patterns and (**b**) FTIR spectra of sepiolite and the spent sepiolite after photocatalytic degradation in various organic dye compounds.

TEM images for the pristine sepiolite showed straightly fibrous shapes with several hundred nm to 1 μm in length and 50–60 nm in width (**Fig. 7.3**). It was clear that the crystal was developed in a one-dimensional direction [35]. The nitrogen sorption isotherm plot is presented in **Fig. 7.4a**. The isotherms represented type IV isotherm nature, with a narrow H3-type of the hysteresis loop, according to the International Union of Pure and Applied Chemistry (IUPAC) classification [36, 37]. The H3 type of hysteresis loop is characteristic of the pore channels in the layers of smectite clay minerals [34, 38, 39]. A comparative pressure range from 0.7 to 1.0 would indicate that a crack-type mesoporous structure exists in pristine sepiolite [40]. Additionally, the isotherm was unsaturated near to 1.0 relative pressure (P/P_0). The Barrett, Joyner, and Halenda method (BJH) pore size distribution plot is presented in **Fig. 7.4b**, suggesting that the pore structure in the sepiolite was an irregular type. The Brunauer–Emmett–Teller (BET), the specific surface area of pristine sepiolite, was observed around 230 m^2/g, and the total pore volume of 0.686 cm^3/g was determined by the BET method.

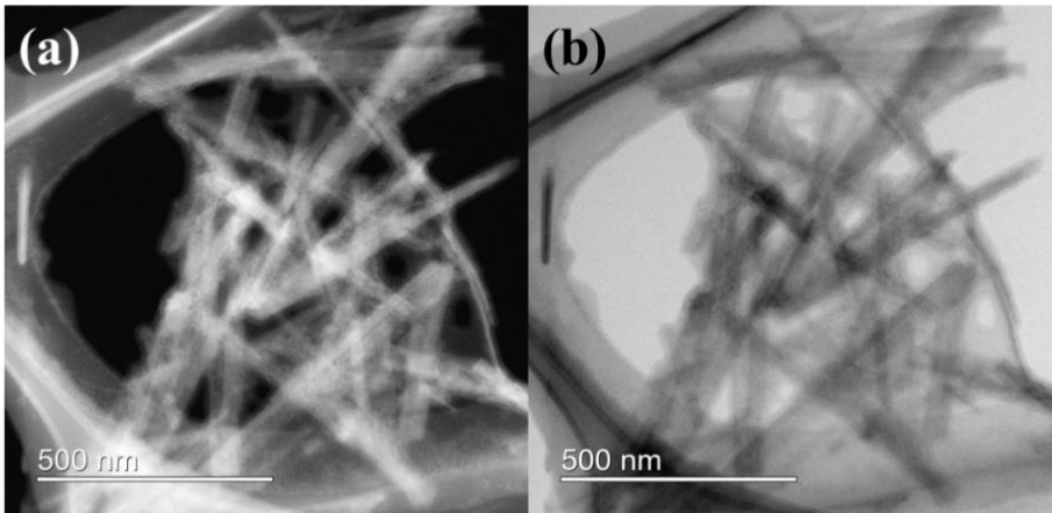

Fig. 7.3 TEM images of sepiolite. (**a**) Bright-field and (**b**) dark-field; scale bars indicate 500 nm.

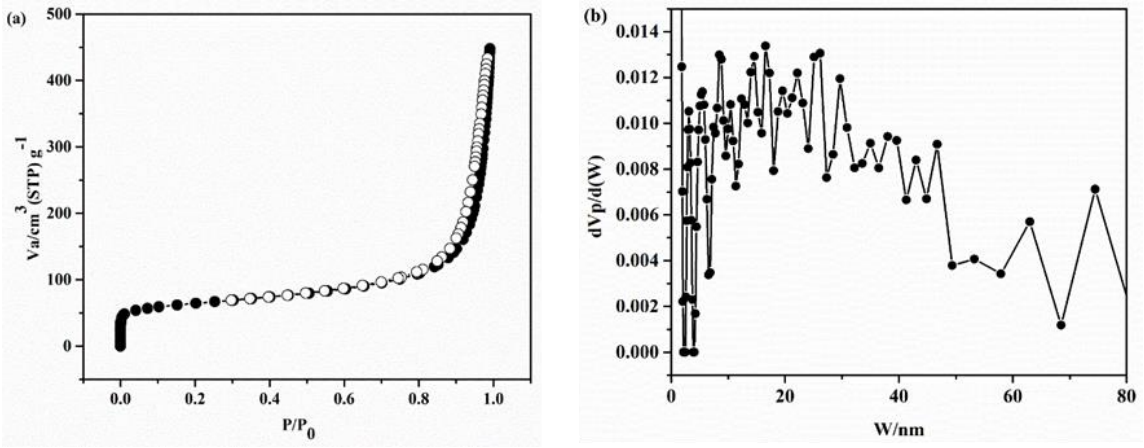

Fig. 7.4 (**a**) Nitrogen adsorption-desorption isotherm and (**b**) BJH pore size distribution for sepiolite.

The XPS measurements were carried out to elucidate the elemental compositions and electronic properties of sepiolite. In **Fig. 7.5a**, the survey spectrum for the pristine sepiolite shows the predominant peaks assigned to Si 2p, O 1s, and Mg 2p orbitals and a small peak assigned to Al 2p. The valence band (VB) energy can be estimated to around 2.81 eV by drawing the straight tangent line to the VB spectrum of the sepiolite, as shown in Fig. 7.5b [41, 42].

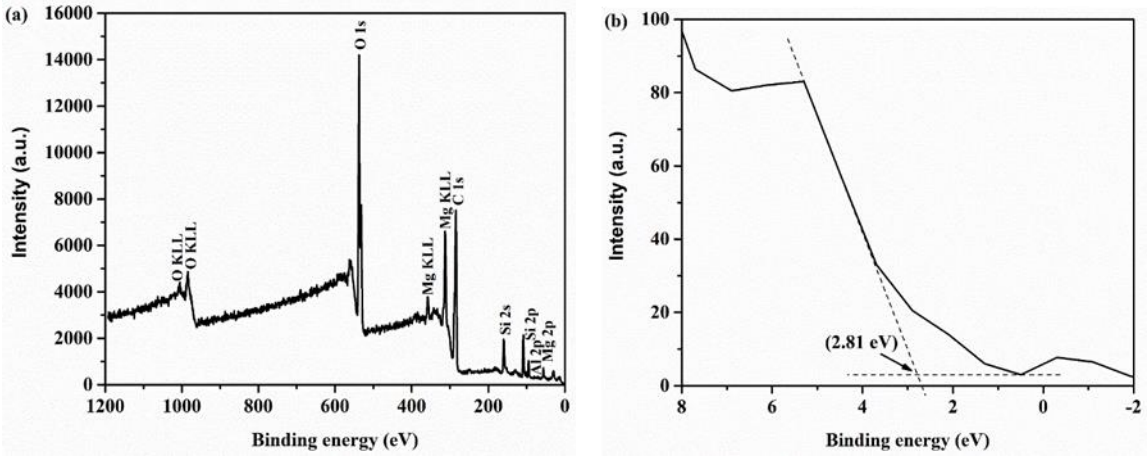

Fig. 7.5 XPS spectrum of sepiolite. (**a**) Survey scan and (**b**) valence band (VB) energy region.

Fig. 7.6a shows the UV-Vis diffuse reflectance spectrum (UV-DRS) of sepiolite. It was observed that the absorption of sepiolite had photo-responses from the UV to the visible light region. In addition, sepiolite has shown a light absorption predominantly around 300–350 nm, indicating that sepiolite can be excited under the ultraviolet light irradiation. The band gap energy value was calculated by the linear part of the $(\alpha hv)^2$ versus energy (Eg) plot. Based on the UV-DRS results, the band gap energy of sepiolite could be estimated to be 3.7 eV through the Tauc plot (**Fig. 7.6b**). Therefore, the conduction band energy (CB) of sepiolite could be calculated to be −0.89 eV.

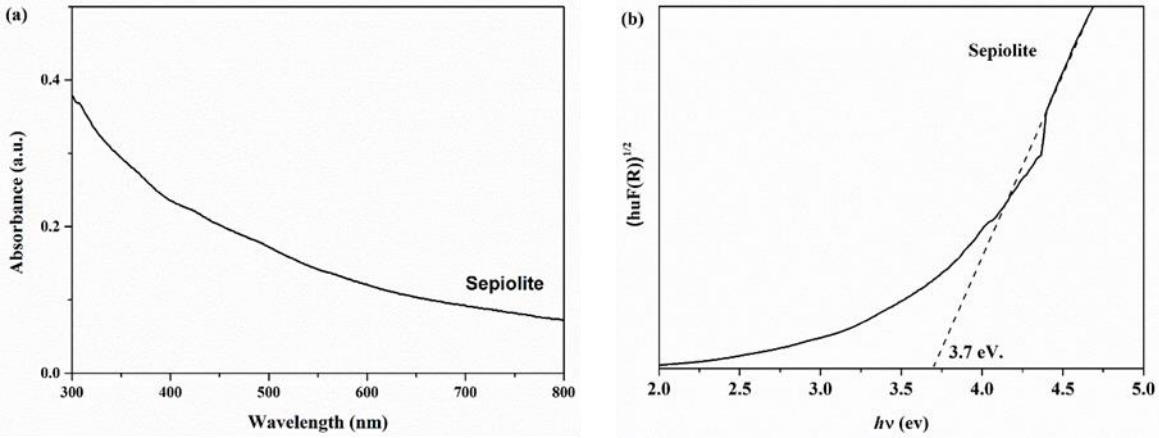

Fig. 7.6 UV-Vis spectrum of sepiolite. (a) Diffuse reflectance spectrum (DRS) spectrum and (b) Tauc plo.

7.3.2 Photocatalytic degradation of organic dyes

Organic dyes, MB, RhB, OII, and TB, were used as models of organic pollutants to estimate the photocatalytic performance of sepiolite under the visible light irradiation. The adsorption capacity of each organic dye compound on sepiolite was

determined under the dark condition without the visible light irradiation. **Fig. 7.7a** displays the removal efficiency results of organic dyes by sepiolite under the dark (dotted lines) and visible light (solid lines) irradiation. In dark control, the sepiolite showed a higher adsorption capacity of cationic dyes, MB and RhB, than anionic dyes, OII and TB. It could be explained by electrostatic interaction of the cationic dyes with sepiolite, which is negatively charged so that the cationic dye molecules are strongly attracted through ion exchange with mainly K^+ [3, 4, 43]. However, the adsorption density was saturated within 30 min under the dark condition. Prior to photocatalytic reaction under the visible light, the suspension of sepiolite particles was well-dispersed by stirring under dark for 30 min in order to achieve the adsorption-desorption equilibrium. Immediately after the visible light was irradiated, sepiolite particles exhibited the photocatalytic degradation of cationic dyes in contrast to anionic dye molecules.

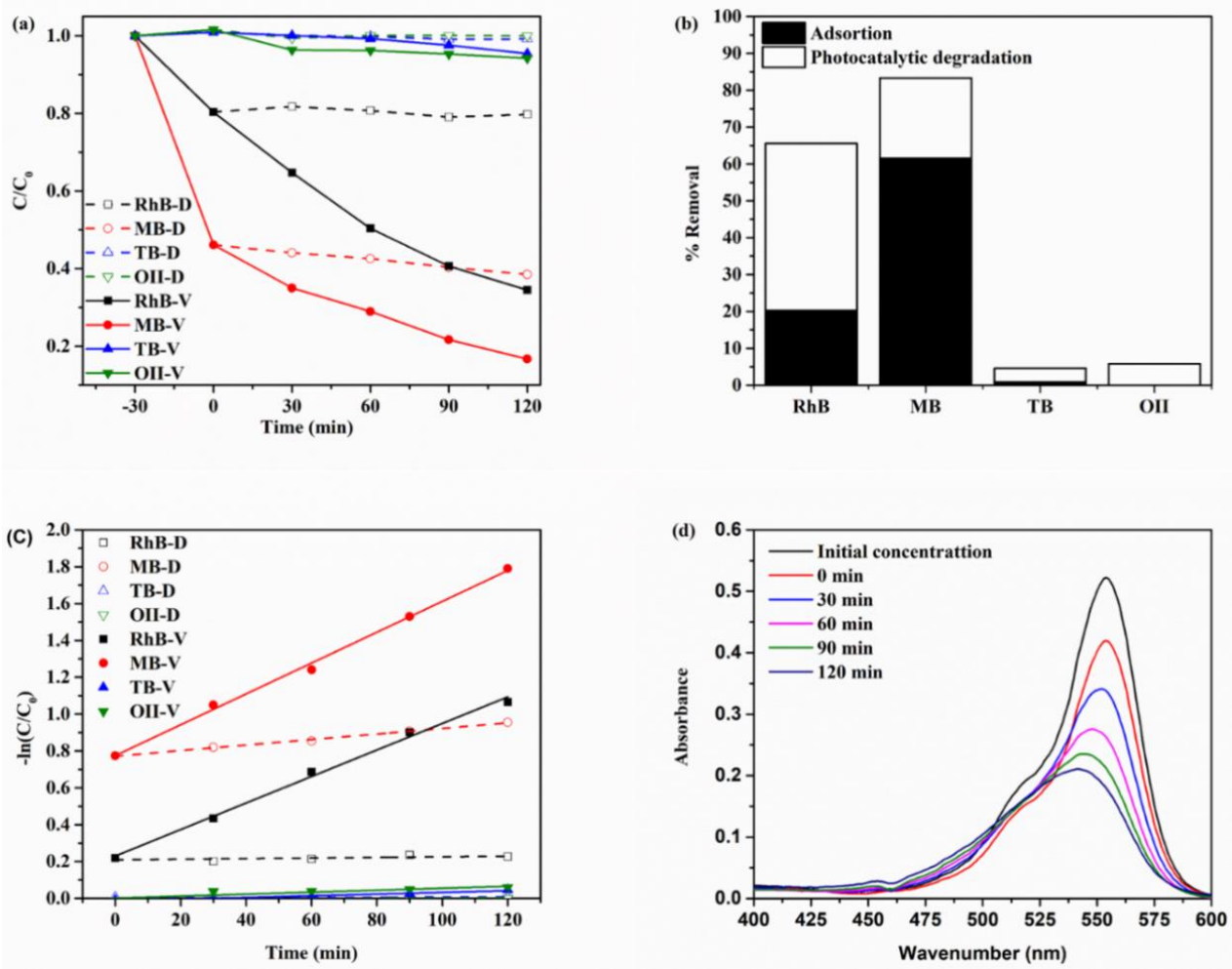

Fig. 7.7 (**a**) Adsorption and photocatalytic degradation of various organic dyes over sepiolite as a function of time; (**b**) removal efficiency of various organic dyes over sepiolite after 120 min; (**c**) pseudo-first-order kinetic plot of various organic dyes over sepiolite; and (**d**) time-dependent changes in UV-Vis spectra of rhodamine B (RhB) in suspension of sepiolite under the visible light irradiation.

Fig. 7.7b summarized the final organic dye removal (%) after 120 min of irradiation time under the visible light. The highest removal efficiency of MB was observed with 83.3%, in which 61.5% was from adsorption, and 21.7% was from photocatalytic degradation. The reason why RhB was less adsorbed on sepiolite despite the same charge as MB would be the larger molecular size of RhB than MB and the higher electron density localized in S of MB than N of RhB (**Fig. 7.1**). Regarding of photocatalytic degradation, RhB was the most effectively photocatalytically-degraded, with 45.3%. The lower photocatalytic performance of MB than RhB was caused by the shielding effect from supernumerary adsorbed dye molecules, which may have changed the rate of production of active species (e.g., $^{\bullet}O_2^-$). Negligibly trace degradation was observed with anionic dyes (OII and TB), indicating photodegradation of dyes hardly happens without adsorption. The kinetic plots of reaction time (t) versus $-\ln(C/C_0)$ provided a linear line, suggesting that the organic dye degradations were well fitted to the pseudo-first-order kinetic model, as shown in **Fig. 7.7c** (R^2 = 0.9938 and 0.9956 for MB-V and RhB-V). In addition, it could be seen that the degradation rate constants under the visible light irradiation were greater than those under the dark conditions about 45 and 6 times in case of RhB and MB, respectively, indicating a synergetic effect of cationic dye and sepiolite under visible light irradiation. Moreover, the synergistic effect was more excellent for the degradation of RhB than MB over sepiolite.

By focusing on the photocatalytic degradation of RhB on sepiolite, time-dependent UV-Vis absorption spectra were observed (**Fig. 7.7d**). After photocatalytic degradation of RhB on sepiolite happened, the adsorption intensity decreased around 554 nm, and the absorption peak position of RhB had shifted to the lower

wavenumbers, indicating that the degradation of ethyl groups in RhB occurred during the photocatalytic degradation [44-47]. Moreover, the decomposition of RhB was monitored over time by HPLC, as shown in **Fig. 7.8**. The peak at 18.5 min of retention time was assigned to RhB, and the peak intensity relatively decreased over time. A distinctive new peak at 14.6 min of retention time was observed within 30 min after photocatalytic degradation, and its intensity increased relatively with time. The other tiny peaks around 8.9 min and 11.8 min of the retention time were gradually observed over time. The appearance of the new peaks in HPLC was in accordance with the degradation of RhB, which could be confirmed by the determination of the remaining RhB by UV-Vis spectrometry (**Fig. 7.7a**) and the wavenumber-shift of an absorption peak in UV-Vis spectrum (**Fig. 7.7d**). In the previous reports, *N*-deethylated byproducts (*N*,*N*-diethyl-*N*'-ethylrhodamine, *N*,*N*-diethylrhodamine, and *N*-ethylrhodamine) were confirmed as byproducts in photocatalytic degradation of RhB using LC-MS [48-50], suggesting decomposition of ethyl groups from xanthene rings in the molecular structure of RhB.

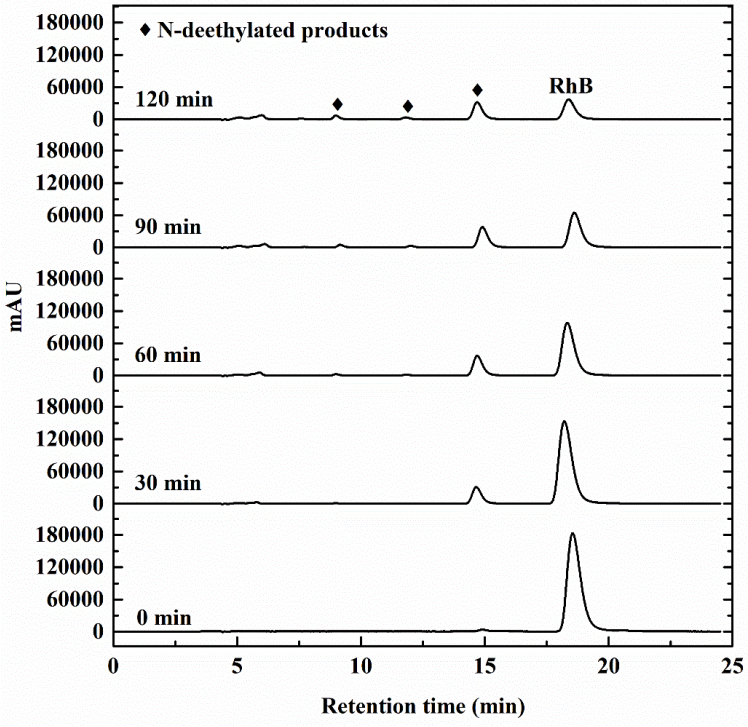

Fig. 7.8 Time-dependent changes in HPLC spectra of RhB and degradation products on sepiolite under the visible light irradiation.

After 120 min-photoreaction, XRD patterns and FTIR spectra for the solid resides were collected in the same manner as the pristine sepiolite (**Fig. 7.2a**). XRD patterns were mostly identical with the pristine sepiolite. In FTIR for the solid resides after reaction with MB, there were additional peaks in a region of 1300 to 1600 cm^{-1}, which were assigned to the aromatic ring structure in MB molecule, and the peaks at 1500 cm^{-1} were attributed to C=N stretching vibration mode (**Fig. 7.2b**). It was consistent with the largest amounts of MB, which were adsorbed on sepiolite (**Fig. 7.7b**). In other FTIR spectra, there were no significant changes. These results supported that the photocatalytic reaction happened without any degradation of sepiolite.

In order to elucidate the role of responsible reactive species for RhB degradation, several scavenger reagents were tested, as shown in Fig. 7.9, where isopropyl alcohol (IPA), benzoquinone (BQ), and potassium iodide (KI) were used as the scavenger

reagents for h^+, $^{\bullet}O_2^-$, and $^{\bullet}OH$, respectively [51-54]. The photocatalytic degradation efficiency of RhB significantly decreased after trapping $^{\bullet}O_2^-$ by BQ, but the presence of KI and IPA had shown negligibly small decreases in RhB degradation efficiency, indicating that $^{\bullet}O_2^-$ was dominantly responsible for the photocatalytic degradation of RhB, but the h^+ and $^{\bullet}OH$ did not play an important role in the degradation of RhB over sepiolite under the visible light irradiation. These results implied that $^{\bullet}O_2^-$ was the main oxidant species in the photocatalytic degradation of RhB.

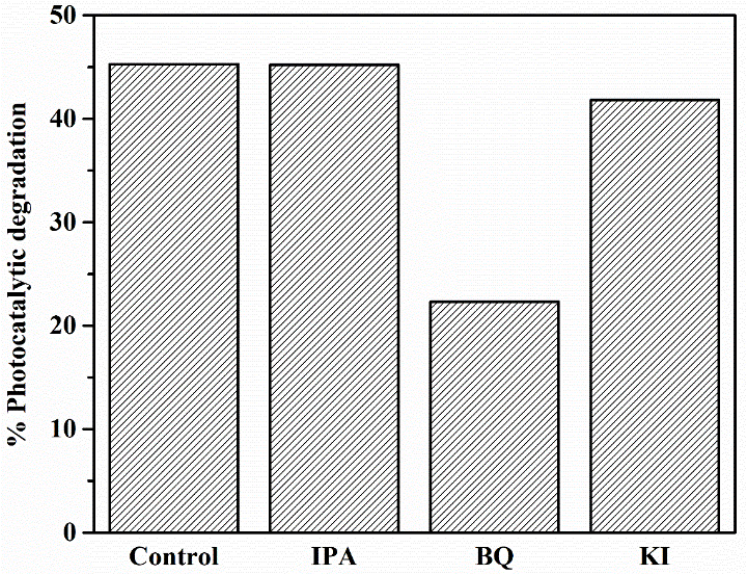

Fig. 7.9 Photocatalytic degradation of RhB over sepiolite in the presence of different radical scavengers. IPA: isopropyl alcohol; BQ: benzoquinone; and KI: potassium iodide.

One of the important factors of photocatalyst material is stability. The photocatalytic stability of sepiolite for RhB degradation under visible light irradiation was examined by the recycling test three times. From the observed results in **Fig. 7.10**, it could be seen that the photocatalytic efficiency of sepiolite for RhB degradation still maintained for three cycles, suggesting the sepiolite showed high stability for photocatalytic degradation of organic dye.

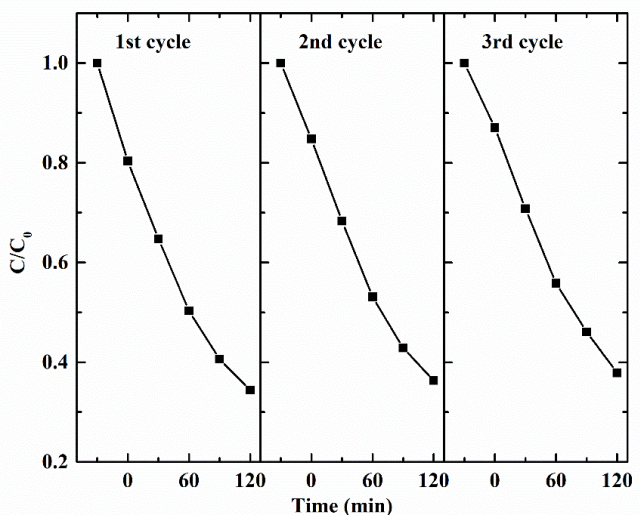

Fig. 7.10 Recycling test in the photocatalytic degradation of 2×10^{-5} M RhB over sepiolite (catalyst loading = 0.25 g/L) under visible light irradiation.

Moreover, the reusability of spent sepiolite after adsorption of RhB for 30 min in dark condition without any pretreatment was examined by applying to photocatalytic degradation of an anionic dye, TB, under the visible light irradiation. TB can be utilized for staining of cells in cytotoxicity measurements due to the negative charge of TB. The removal efficiency of TB after 2 h was displayed in **Fig. 7.11**. Little adsorption capacity (~1%) of TB was observed on sepiolite and spent RhB–sepiolite under the dark condition. However, after the visible light irradiation, the spent RhB–sepiolite shows greater than twice photocatalytic degradation than pristine sepiolite. This suggests that the RhB adsorbed on the surface of sepiolite enhanced the photocatalytic degradation of TB through photosensitization property of RhB–sepiolite. Based on the results, the sequential photodegradation of cationic and anionic dye molecules are possible on sepiolite under the visible light to contribute to green chemistry in dye-contaminated water treatment.

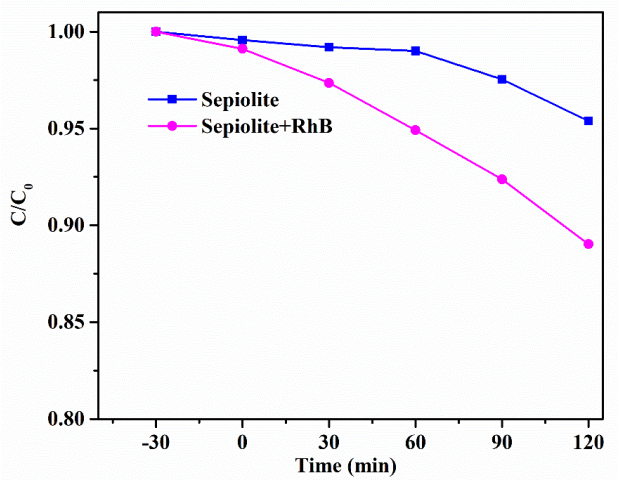

Fig. 7.11 Removal efficiency of TB by sepiolite and spent RhB-sepiolite after adsorption of RhB under the visible light irradiation. The initial concentrations of RhB and TB were 2×10^{-5} M.

7.3.3 Photocatalytic mechanism of organic dye degradation over sepiolite

The photosensitization of organic dye molecules is an important step for starting the photocatalytic reaction because the dye molecule can provide the electron to sepiolite through the photo-irradiation process [55-58]. In the case of RhB degradation over sepiolite under the visible light irradiation, the electron in the pristine sepiolite could not be excited under the visible light due to the wide energy band gap (Eg = 3.7 eV, Fig. 7.6b). Firstly, cationic organic dye molecules (RhB) were adsorbed on the surface of the sepiolite, and then the electrons of RhB were excited under the visible light to generate the excited electrons. The electrons in the LUMO of RhB (E_{LUMO} = −1.10 eV versus NHE) were transferred to the CB of sepiolite (E_{CB} = −0.89 eV) due to the more positive energy level of the CB of sepiolite, compared with LUMO state of RhB [59]. The photo-excited electron on the CB of sepiolite could reduce the dissolved O_2 to $^{\bullet}O_2^-$ because the standard reduction potential of O_2 to $^{\bullet}O_2^-$ ($E^0(O_2/^{\bullet}O_2^-)$ = −0.046

eV versus NHE [60, 61]) was more positive than the CB potential of sepiolite. Then, the oxidation of RhB by $^{\bullet}O_2^-$ occurred to degrade RhB to smaller molecules. Based on the above results, the mechanism for degradation of RhB over sepiolite under the visible light irradiation could be proposed as follows:

$$\text{RhB@sepiolite} + h\nu \rightarrow \text{RhB*}\ (h^+ + e^-)\text{@sepiolite}, \quad (7.1)$$

$$\text{RhB*}\ (h^+ + e^-)\text{@sepiolite} \rightarrow \text{RhB*}\ (h^+)\text{@sepiolite}\ (e^-), \quad (7.2)$$

$$\text{sepiolite}\ (e^-) + O_2 \rightarrow {}^{\bullet}O_2^-, \quad (7.3)$$

$$^{\bullet}O_2^- + \text{RhB} \rightarrow \text{degradation products}. \quad (7.4)$$

The obtained degradation results of anionic dyes (OII and TB) showed less degradation efficiency by using sepiolite. This was explained due to the less adsorption behavior of anionic dyes on the negative surface of sepiolite. This reconfirmed the role of adsorbed cationic dye, which is influenced by the dye photosensitized degradation mechanism. For the confirmation of this phenomena, the RhB adsorbed solid residual sepiolite from the dark conditions is further used for the degradation of anionic dye (TB) and showed better photocatalyst efficiency than pristine sepiolite. Here adsorbed RhB residue showed similar dye-sensitized mechanistic approach (as explained in Equation (7.1–7.4)) providing an electron to sepiolite and generated the $^{\bullet}O_2^-$ species responsible for the degradation of TB as in Equation (7.5):

$$^{\bullet}O_2^- + \text{TB} \rightarrow \text{degradation products}. \quad (7.5)$$

According to the above sequence, photocatalytic degradation mechanisms of organic dye (both cationic and anionic dyes) over sepiolite under the visible light irradiation, as illustrated in **Fig. 7.12**. Consequently, the cooperative function through the combination of cationic organic dye molecules with sepiolite through electrostatic

interaction resulted in the improved photocatalytic degradation of organic dye molecules. The electrostatic interaction of cationic organic dye (i.e., RhB) with sepiolite was much more favorable than anionic dye (i.e., TB). Although anionic dye was less favorable for adsorption on sepiolite, a small amount of adsorbed anionic dye would still have been involved in photocatalytic degradation by $^{\bullet}O_2^-$ species on the surface of the sepiolite.

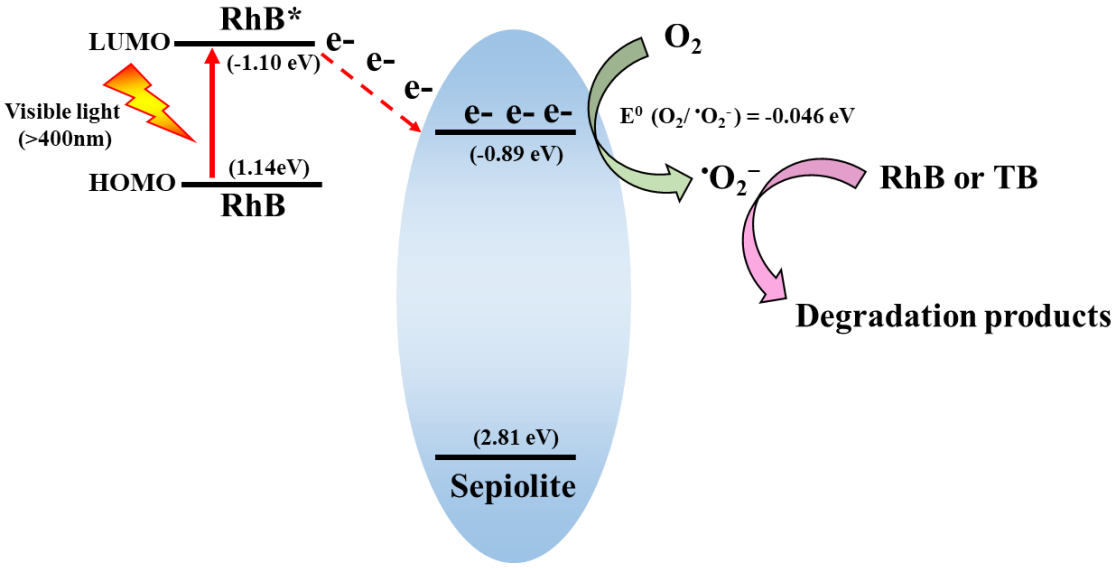

Fig. 7.12 Proposed mechanism of photocatalytic degradation RhB over sepiolite and TB over spent sepiolite after adsorption of RhB under the visible light irradiation.

7. 4 Conclusions

In the present work, we reported the photocatalytic activity of natural sepiolite by the dye-sensitized process to degrade organic dyes under the visible light irradiation. The photocatalytic activity of sepiolite was shown through electrostatic coverage on the surface of sepiolite by the cationic organic dye compound. The role of covered cationic organic dye molecules on the surface of sepiolite was to produce the excited

electrons under the visible light. Then the electrons could be transferred to CB of sepiolite, enhancing the photocatalytic degradation efficiency of organic dyes mainly through oxidation by $^{\bullet}O_2^-$ which was generated by reduction of O_2. The function of RhB-adsorbed sepiolite in the system is called as "photosensitizer". RhB was the most efficiently photo-degraded on the sepiolite compared with MB, TB, and OII. All the kinetic data of removal of RhB, MB, TB, and OII on sepiolite were fitted to the pseudo-first-order reaction model. The greatest kinetic constant was found with RhB. The photocatalytic degradation of RhB on sepiolite under the visible light irradiation could be explained by adsorption and E_{LUMO} and E_{HOMO} in RhB. The spent sepiolite after adsorption of RhB successfully acted to photocatalytically degrade even anionic organic dye (TB) through dye-sensitization of RhB on sepiolite. Especially, we confirmed that the natural sepiolite represents a new class of visible light-responsive photocatalyst from naturally occurring minerals. It is unique as it absorbs visible light without modification. The acceptable performance with regard to photocatalytic activity and its low-cost characteristics make it a suitable candidate for application in environmental treatments.

References

[1] A. Sun, J.B.D. Delacaillerie, J.J. Fripiat, A New Microporous Material - Aluminated Sepiolite, Microporous Materials, 5 (1995) 135-142.

[2] G. Rytwo, S. Nir, M. Crespin, L. Margulies, Adsorption and Interactions of Methyl Green with Montmorillonite and Sepiolite, J Colloid Interface Sci, 222 (2000) 12-19.

[3] A. Jacobo-Azuara, R. Ramos, E. Padilla, A. Aragon-Piña, R. Maria Guerrero-Coronado, J. Mendoza-Barron, Adsorption of heavy metals on Sepiolite,29 (2011) 569-584.

[4] Y. Ozdemir, M. Dogan, M. Alkan, Adsorption of cationic dyes from aqueous solutions by sepiolite, Microporous and Mesoporous Materials, 96 (2006) 419-427.
[5] F. Bergaya, G. Lagaly, Chapter 1 General Introduction: Clays, Clay Minerals, and Clay Science, 5 (2006) 1-19.
[6] J. Liu, G. Zhang, Recent advances in synthesis and applications of clay-based photocatalysts: a review, Physical chemistry chemical physics : PCCP, 16 (2014) 8178-8192.
[7] A. Álvarez, J. Santaren, A. Esteban, Current Industrial Applications of Palygorskite and Sepiolite, 3 (2011) 281-298.
[8] A. Alvarez, Sepiolite: Properties and Uses, in: A. Singer, E. Galan (Eds.) Developments in Sedimentology, Elsevier, 1984, 253-287.
[9] H.H. Murray, Overview — clay mineral applications, Applied Clay Science, 5 (1991) 379-395.
[10] E. Ruiz-Hitzky, P. Aranda, A. Álvarez, J. Santarén, A. Esteban-Cubillo, Chapter 17 - Advanced Materials and New Applications of Sepiolite and Palygorskite, in: E. Galàn, A. Singer (Eds.) Developments in Clay Science, Elsevier, 2011, 393-452.
[11] S. Guggenheim, M.P.S. Krekeler, Chapter 1 - The Structures and Microtextures of the Palygorskite–Sepiolite Group Minerals, in: E. Galàn, A. Singer (Eds.) Developments in Clay Science, Elsevier, 2011, 3-32.
[12] J.A. Cecilia, E. Vilarrasa-Garcia, C.L. Cavalcante, D.C.S. Azevedo, F. Franco, E. Rodriguez-Castellon, Evaluation of two fibrous clay minerals (sepiolite and palygorskite) for CO_2 Capture, Journal of Environmental Chemical Engineering, 6 (2018) 4573-4587.
[13] M.F. Brigatti, E. Galan, B.K.G. Theng, Chapter 2 Structures and Mineralogy of Clay Minerals, in: F. Bergaya, B.K.G. Theng, G. Lagaly (Eds.) Developments in Clay Science, Elsevier, 2006, 19-86.
[14] M. Brigatti, D. Malferrari, A. Laurora, C. Elmi, Structure and mineralogy of layer silicates: recent perspectives and new trends,11 (2011), 1-71.
[15] X. Hu, Z. Sun, J. Song, G. Zhang, C. Li, S. Zheng, Synthesis of novel ternary heterogeneous BiOCl/TiO_2/sepiolite composite with enhanced visible-light-induced photocatalytic activity towards tetracycline, J Colloid Interface Sci, 533 (2019) 238-250.

[16] S. Kaur, V. Singh, Visible light induced sonophotocatalytic degradation of Reactive Red dye 198 using dye sensitized TiO_2, Ultrason Sonochem, 14 (2007) 531-537.

[17] Y. Zhang, D. Wang, G. Zhang, Photocatalytic degradation of organic contaminants by TiO_2/sepiolite composites prepared at low temperature, Chemical Engineering Journal, 173 (2011) 1-10.

[18] M. Uğurlu, M.H. Karaoğlu, TiO_2 supported on sepiolite: Preparation, structural and thermal characterization and catalytic behaviour in photocatalytic treatment of phenol and lignin from olive mill wastewater, Chemical Engineering Journal, 166 (2011) 859-867.

[19] L. Jin, H.Y. Zeng, S. Xu, C.R. Chen, H.Z. Duan, J.Z. Du, G. Hu, Y.X. Sun, Facile preparation of sepiolite@LDH composites for the visible-light degradation of organic dyes, Chinese Journal of Catalysis, 39 (2018) 1832-1841.

[20] M. Akkari, P. Aranda, C. Belver, J. Bedia, A. Ben Haj Amara, E. Ruiz-Hitzky, ZnO/sepiolite heterostructured materials for solar photocatalytic degradation of pharmaceuticals in wastewater, Applied Clay Science, 156 (2018) 104-109.

[21] M. Akkari, P. Aranda, A. Mayoral, M. Garcia-Hernandez, A. Ben Haj Amara, E. Ruiz-Hitzky, Sepiolite nanoplatform for the simultaneous assembly of magnetite and zinc oxide nanoparticles as photocatalyst for improving removal of organic pollutants, J Hazard Mater, 340 (2017) 281-290.

[22] W.G. Xu, S.F. Liu, S.X. Lu, S.Y. Kang, Y. Zhou, H.F. Zhang, Photocatalytic degradation in aqueous solution using quantum-sized ZnO particles supported on sepiolite, J Colloid Interface Sci, 351 (2010) 210-216.

[23] R. Giustetto, K. Seenivasan, F. Bonino, G. Ricchiardi, S. Bordiga, M.R. Chierotti, R. Gobetto, Host/Guest Interactions in a Sepiolite-Based Maya Blue Pigment: A Spectroscopic Study, J Phys Chem C, 115 (2011) 16764-16776.

[24] A.S. Bhatt, P.L. Sakaria, M. Vasudevan, R.R. Pawar, N. Sudheesh, H.C. Bajaj, H.M. Mody, Adsorption of an anionic dye from aqueous medium by organoclays: equilibrium modeling, kinetic and thermodynamic exploration, Rsc Advances, 2 (2012) 8663-8671.

[25] A. Rodriguez, G. Ovejero, M. Mestanza, J. Garcia, Removal of Dyes from Wastewaters by Adsorption on Sepiolite and Pansil, Industrial & Engineering Chemistry Research, 49 (2010) 3207-3216.

[26] P. Wang, M.M. Cheng, Z.H. Zhang, On different photodecomposition behaviors of rhodamine B on laponite and montmorillonite clay under visible light irradiation, Journal of Saudi Chemical Society, 18 (2014) 308-316.

[27] L. Guishui, C. Lijun, Z. Bing, L. Yi, Novel Bi_2O_3 loaded sepiolite photocatalyst: Preparation and characterization, Materials Letters, 168 (2016) 143-145.

[28] F. Zhou, C.J. Yan, T. Liang, Q. Sun, H.Q. Wang, Photocatalytic degradation of Orange G using sepiolite-TiO_2 nanocomposites: Optimization of physicochemical parameters and kinetics studies, Chemical Engineering Science, 183 (2018) 231-239.

[29] P.S. Wang, C.X. Qi, L.Y. Hao, P.C. Wen, X. Xu, Sepiolite/Cu_2O/Cu photocatalyst: Preparation and high performance for degradation of organic dye, Journal of Materials Science & Technology, 35 (2019) 285-291.

[30] F. Zhou, C.J. Yan, Q. Sun, S. Komarneni, TiO_2/Sepiolite nanocomposites doped with rare earth ions: Preparation, characterization and visible light photocatalytic activity, Microporous and Mesoporous Materials, 274 (2019) 25-32.

[31] D. Papoulis, D. Panagiotaras, P. Tsigrou, K.C. Christoforidis, C. Petit, A. Apostolopoulou, E. Stathatos, S. Komarneni, I. Koukouvelas, Halloysite and sepiolite –TiO_2 nanocomposites: Synthesis characterization and photocatalytic activity in three aquatic wastes, Materials Science in Semiconductor Processing, 85 (2018) 1-8.

[32] M. Hassan, A.S. Afify, J.M. Tulliani, Synthesis of ZnO Nanoparticles onto Sepiolite Needles and Determination of Their Sensitivity toward Humidity, NO_2 and H_2, Journal of Materials Science & Technology, 32 (2016) 573-582.

[33] R.R. Pawar, Lalhmunsiama, H.C. Bajaj, S.-M. Lee, Activated bentonite as a low-cost adsorbent for the removal of Cu(II) and Pb(II) from aqueous solutions: Batch and column studies, Journal of Industrial and Engineering Chemistry, 34 (2016) 213-223.

[34] R.R. Pawar, P. Gupta, Lalhmunsiama, H.C. Bajaj, S.M. Lee, Al-intercalated acid activated bentonite beads for the removal of aqueous phosphate, The Science of the total environment, 572 (2016) 1222-1230.

[35] M.P.S. Krekeler, S. Guggenheim, Defects in microstructure in palygorskite–sepiolite minerals: A transmission electron microscopy (TEM) study, Applied Clay Science, 39 (2008) 98-105.

[36] K.S.W. Sing, R.T. Williams, Physisorption Hysteresis Loops and the Characterization of Nanoporous Materials, Adsorption Science & Technology, 22 (2004) 773-782.

[37] K.S.W. Sing, D.H. Everett, R.A.W. Haul, L. Moscou, R.A. Pierotti, J. Rouquérol, T. Siemieniewska, Reporting Physisorption Data for Gas/Solid Systems With Special Reference to the Determination of Surface Area and Porosity, Pure & App. Chem., 57 (1985) 4, 603-619.

[38] R.R. Pawar, B.D. Kevadiya, H. Brahmbhatt, H.C. Bajaj, Template free synthesis of mesoporous hectorites: Efficient host for pH responsive drug delivery, International Journal of Pharmaceutics, 446 (2013) 145-152.

[39] R.R. Pawar, H.A. Patel, G. Sethia, H.C. Bajaj, Selective adsorption of carbon dioxide over nitrogen on calcined synthetic hectorites with tailor-made porosity, Applied Clay Science, 46 (2009) 109-113.

[40] B. Hubbard, W. Kuang, A. Moser, G.A. Facey, C. Detellier, STRUCTURAL STUDY OF MAYA BLUE: TEXTURAL, THERMAL AND SOLID-STATE MULTINUCLEAR MAGNETIC RESONANCE CHARACTERIZATION OF THE PALYGORSKITE-INDIGO AND SEPIOLITE-INDIGO ADDUCTS, Clays and Clay Minerals, 51 (2003) 318-326.

[41] F. Dong, Z. Zhao, T. Xiong, Z. Ni, W. Zhang, Y. Sun, W.K. Ho, In situ construction of g-C_3N_4/g-C_3N_4 metal-free heterojunction for enhanced visible-light photocatalysis, ACS Appl Mater Interfaces, 5 (2013) 11392-11401.

[42] X.D. Su, J.J. Yang, X. Yu, Y. Zhu, Y.M. Zhang, In situ grown hierarchical 50%BiOCl/BiOI hollow flowerlike microspheres on reduced graphene oxide nanosheets for enhanced visible-light photocatalytic degradation of rhodamine B, Applied Surface Science, 433 (2018) 502-512.

[43] C. Wan, B. Chen, Synthesis and characterization of biomimetic hydroxyapatite/sepiolite nanocomposites, Nanoscale, 3 (2011) 693-700.

[44] D. Zhang, Effectiveness of photodecomposition of rhodamine B and malachite green upon coupled tricomponent TiO_2(Anatase-Rutile)/ZnO nanocomposite, Acta Chimica Slovaca, 6 (2013) 245-255.

[45] R.L. Halterman, J.L. Moore, L.M. Mannel, Disrupting aggregation of tethered rhodamine B dyads through inclusion in cucurbit[7]uril, J Org Chem, 73 (2008) 3266-3269.

[46] M. Pica, S. Calzuola, A. Donnadio, P. Gentili, M. Nocchetti, M. Casciola, De-Ethylation and Cleavage of Rhodamine B by a Zirconium Phosphate/Silver Bromide Composite Photocatalyst, Catalysts, 9 (2018) 3, 1-15.

[47] A. Mishra, A. Mehta, S. Kainth, S. Basu, Effect of g-C_3N_4 loading on TiO_2/Bentonite nanocomposites for efficient heterogeneous photocatalytic degradation of industrial dye under visible light, Journal of Alloys and Compounds, 764 (2018) 406-415.

[48] W. Zhang, J. Xing, Z. Yang, M. Kong, H. Yao, A chemical etching route to controllable fabrication of TiO_2 hollow nanospheres for enhancing their photocatalytic activity,7 (2013) 192-201.

[49] K. Yu, S. Yang, H. He, C. Sun, C. Gu, Y. Ju, Visible light-driven photocatalytic degradation of rhodamine B over $NaBiO_3$: pathways and mechanism, The journal of physical chemistry. A, 113 (2009) 10024-10032.

[50] X. Hu, T. Mohamood, W. Ma, C. Chen, J. Zhao, Oxidative decomposition of rhodamine B dye in the presence of VO^{2+} and/or Pt(IV) under visible light irradiation: N-deethylation, chromophore cleavage, and mineralization, The journal of physical chemistry. B, 110 (2006) 26012-26018.

[51] D.B. Hernández-Uresti, A. Vázquez, D. Sanchez-Martinez, S. Obregón, Performance of the polymeric g-C_3N_4 photocatalyst through the degradation of pharmaceutical pollutants under UV–vis irradiation, Journal of Photochemistry and Photobiology A: Chemistry, 324 (2016) 47-52.

[52] B. Luo, M. Chen, Z. Zhang, J. Xu, D. Li, D. Xu, W. Shi, Highly efficient visible-light-driven photocatalytic degradation of tetracycline by a Z-scheme g-C_3N_4/Bi_3TaO_7 nanocomposite photocatalyst, Dalton Trans, 46 (2017) 8431-8438.

[53] C.T. Hou, B. Hu, J.M. Zhu, Photocatalytic Degradation of Methylene Blue over TiO_2 Pretreated with Varying Concentrations of NaOH, Catalysts, 8 (2018) 575.

[54] L. Wang, C.B. Zhang, R. Cheng, J. Ali, Z.B. Wang, G. Mailhot, G. Pan, Microcystis aeruginosa Synergistically Facilitate the Photocatalytic Degradation of Tetracycline Hydrochloride and Cr(VI) on PAN/TiO_2/Ag Nanofiber Mats, Catalysts, 8 (2018) 628.

[55] Z.Q. Bai, Z.W. Liu, A broadband photodetector based on Rhodamine B-sensitized ZnO nanowires film, Sci Rep, 7 (2017) 11384.

[56] T.T. Le, M.S. Akhtar, D.M. Park, J.C. Lee, O.B. Yang, Water splitting on Rhodamine-B dye sensitized Co-doped TiO_2 catalyst under visible light, Appl Catal B-Environ, 111 (2012) 397-401.

[57] H.P. Zhao, Y.F. Zhang, G.F. Li, F. Tian, H. Tang, R. Chen, Rhodamine B-sensitized BiOCl hierarchical nanostructure for methyl orange photodegradation, Rsc Advances, 6 (2016) 7772-7779.

[58] M.A.I. Molla, I. Tateishi, M. Furukawa, H. Katsumata, T. Suzuki, S. Kaneco, Photocatalytic Decolorization of Dye with Self-Dye-Sensitization under Fluorescent Light Irradiation, ChemEngineering, 1 (2017) 8, 1-10.

[59] P. Ruankham, C. Sae-Kung, N. Mangkorntong, P. Mangkorntong, S. Choopun, Photoelectrochemical Characteristic of ZnO Dye-sensitized Solar Cell with Platinum Nanoparticle as a Counterelectrode, Journal of Scientific Review,2 (2008) 96-100.

[60] S. Huang, J. Chen, J. Zhong, J. Li, W. Hu, M. Li, K. Huang, R. Duan, Enhanced photocatalytic performance of Ag/AgCl/SnO_2 originating from efficient formation of $^{\cdot}O^{2-}$, Materials Chemistry and Physics, 201 (2017) 35-41.

[61] M. Watanabe, Dye-sensitized photocatalyst for effective water splitting catalyst, Sci Technol Adv Mater, 18 (2017) 705-723.

Chapter 8

Fabrication of sepiolite/graphitic carbon nitride/Pd nanoparticles composites with enhanced photocatalytic degradation of rhodamine B under visible light irradiation

8.1 Introduction

Over the last decade, a graphitic carbon nitride (g-C_3N_4) as a metal-free conjugated semiconductor photocatalyst has fascinated massive attention in the photocatalysis research [1, 2]. This material (g-C_3N_4) has some interesting properties that give it advantages over traditional semiconductor photocatalyst materials [3]. Most importantly, it is composed of highly abundant earth elements carbon and nitrogen, a structural arrangement similar to graphene which provides highly physicochemical stability, simple synthesis approaches to solve the cost issues, the absorption band favorably placed in the visible light region (the development of photocatalyst which works in the visible light region also a big challenge) [4]. Considering all these features, g-C_3N_4 has rapidly become a popular material in photocatalysis fields. However, the main intrinsic limitation in practical applications of the use of original g-C_3N_4 due to its high recombination rate of photogenerated electron-hole pairs, low electronic conductivity, and small specific surface areas [3]. Thus, researchers have devoted considerable efforts to modify g-C_3N_4 by different aspects such as by ions doping, noble metals deposition, construction with other semiconductors, and heterojunction construction [5]. The photocatalytic activity of g-C_3N_4 has been improved as above mentioned modifications even though additional improvement is necessary to avoid fast recombination of electron-hole pair, low degradation efficiency, difficulty in separation, and low adsorption ability [6]. Bearing in mind these difficulties, researchers have focused on hybridizing g-C_3N_4 with natural minerals diatomite [7], zeolite [8], and including several recognized clay minerals loke kaolinite [9], attapulgite [10], montmorillonite[11], bentonite [12], and rectorite [13].

These all reports that the minerals could be useful as carrier support and also convenient to avoid recombination of electron and hole due to interfacial charge transfer between the positively photogenerated hole and the negatively charged electron on the clay surfaces. Currently, natural sepiolite, belonging to the 2:1 type of clay minerals, has gained significant interest in different fields of application, including the development of photocatalyst materials. Sepiolite is a hydrous magnesium silicate that is widespread due to its unusual fibrous morphology and intracrystalline tunnels, which are the difference from other clays like layered phyllosilicate [14]. To the best of our knowledge, the photocatalytic performance of fibrous sepiolite combined with g-C_3N_4 has not been yet reported previously.

Recently, the loading of metal nanoparticles on the surface of photocatalyst has been interested in enhancing the photocatalytic activity [15]. The metal nanoparticles on the surface of photocatalyst can induce the oscillation of the conducted electrons with a resonance frequency, called the surface plasmon resonance, which can improve the visible light absorption ability [16]. Also, the separation of photogenerated electron and hole of photocatalyst also can be facilitated through the Schottky barrier [17], which is the heterojunction between the photocatalytic semiconductor and metal nanoparticle. In this work, we have developed for the first time a natural sepiolite/g-C_3N_4 by varying the compositions of well-dispersed Pd nanoparticles to enable the efficient photodegradation RhB. The structural properties, optical properties, and photocatalytic efficiency of products were characterized. The possible mechanism of the enhanced photocatalyst was proposed.

Moreover, reversed double-beam photoacoustic spectroscopy (RDB-PAS) was applied to interpret the charge transfer in the composite.

The previous reports regarding of photocatalytic degradation of RhB were summarized in **Table 8.1** to compare with the present work. From the comparative results, we observed that SC30%-Pd1%composites could show comparable degradation of RhB. We believe that the present finding might be useful for a detailed understanding of the upcoming research scope of the SC30%-Pd1%composites photocatalyst materials for RhB degradation.

Table 8.1 Comparison of clay-based photocatalysts for photocatalytic removal of toxic pollutants

Catalyst	Active compound	Target	C_0	Loading (g/L)	Efficacy (%)	Time (min)	Ref.
BiOCl/g-C_3N_4/kaolinite	BiOCl/g-C_3N_4	RhB	10 ppm	3.0	95	360	[18]
g-C_3N_4/TiO_2/kaolinite	g-C_3N_4/TiO_2	ciprofloxacin	10 ppm	2.0	90	240	[19]
kaolinite/g-C_3N_4	g-C_3N_4	RhB	10 ppm	3.0	95	360	[9]
g-C_3N_4/kaolinite	g-C_3N_4	RhB	10 ppm	2.0	95	360	[20]
g-C_3N_4/illite	g-C_3N_4	RhB	10 ppm	2.0	80	360	[20]
g-C_3N_4/montmorillonite	g-C_3N_4	RhB	30 ppm	2.0	85	360	[11]
Dark orange montmorillonite/g-C_3N_4	g-C_3N_4	MB	20 ppm	0.5	95	150	[21]
Cyanuric Acid Modified g-C_3N_4/Kaolinite	Cyanuric Acid Modified g-C_3N_4	RhB	10 ppm	2.0	93	420	[22]
TiO_2-montmorillonite	TiO_2	Cr(VI)	30 ppm	0.2	~15	240	[23]
TiO_2-montmorillonite with tartaric acid	TiO_2 with tartaric acid	Cr(VI)	30 ppm	0.2	100	120	[23]
Bi_2O_3/sepiolite	Bi_2O_3	Malachite green	14×10^{-5}	0.5	98.2	180	[24]
Sepiolite-TiO_2	TiO_2	Orange G	2.2×10^{-5}	0.8	97.8	150	[25]

Table 8.1. Comparison of clay-based photocatalysts for photocatalytic removal of toxic pollutants (continued)

Catalyst	Active compound	Target	C_0	Loading (g/L)	Efficacy (%)	Time (min)	Ref.
Sepiolite/Cu_2O/Cu	Cu_2O/Cu	Congo red	1.4×10^{-5}	0.2	95.1	50	[26]
Eu-TiO_2/sepiolite	Eu-TiO_2	Orange G	2.2×10^{-5}	0.8	~70	600	[27]
ZnCr LDH/Sepiolite	ZnCr LDH	MB	3.1×10^{-5}	1.25	93.1	120	[28]
Sepiolite –TiO_2	TiO_2	RhB	8.3×10^{-5}	0.85	~80	120	[29]
Sepiolite	Adsorbed MB on sepiolite	MB	2.0×10^{-5}	0.25	83.3	120	[14]
Sepiolite	Adsorbed RhB on sepiolite	RhB	2.0×10^{-5}	0.25	65.5	120	[14]
SC30%-Pd1%	SC30%-Pd1%	RhB	10 ppm	1.0	95	90	This work

8.2 Materials and Methods

8.2.1 Materials and reagents

The natural sepiolite clay (13% Mg, ≤ 10% mass loss on drying), Rhodamine B ($C_{28}H_{31}ClN_2O_3$, with 97% of dye content) and palladium(II) chloride ($PdCl_2$) obtained from Sigma Aldrich Japan Co. Ltd (Tokyo, Japan). Melamine ($C_3H_6N_6$, special grade) and hydrochloric acid (HCl, special grade) were purchased from Wako Chemicals (Osaka, Japan). All the chemicals were utilized without further purification. Ultrapure water was used in the preparation of the organic dye solutions and their experiments.

8.2.2 Synthesis of g-C_3N_4

The polymeric carbon nitride structure of g-C_3N_4 was fabricated by adopting widespread thermal polymerization. In a typical preparation, exactly 5 g of melamine was placed in well cleaned an alumina crucible with a cap and then transferred into a muffle furnace. The furnace temperature was maintained at 550 °C for 2 h under the continuous flow of air. After the completion of calcination, the crucible was cooled down to the room temperature. The obtained product was denoted as CN.

8.2.3 *Preparation of sepiolite/g-C_3N_4 and sepiolite/g-C_3N_4 /Pd nanoparticles composites*

Sepiolite/g-C_3N_4/Pd nanoparticles composites were produced by ultrasound-mediated borohydride reduction. In details, precisely 140 mg of sepiolite and 60 mg

of g-C_3N_4 powder, which is equivalent to the 30wt% of g-C_3N_4 in the mixture, was well dispersed in 80 ml of water under vigorous magnetic stirring for 30 min. Then the stock solution of 17.6 ~ 88.1 mM $PdCl_4^{2-}$ was prepared into 320 ml 0.1% HCl, then the prepared solution was added into the above-described suspension under magnetic stirring for 30 min in order to obtain 0.5, 1 and 5%wt of Pd in the composite. After that, 28 ml of 0.1 M $NaBH_4$ was slowly dropped to the mixture solution under magnetic stirring, following by sonication for 180 min. Then observed gray colored solid was separated by filtration using membrane filters with 0.45 μmϕ, washed several times with water and dried at 75°C for overnight. The sepiolite/g-C_3N_4/Pd nanoparticles composite with different amounts of Pd was denoted as SC30%-Pd0.5%, SC30%-Pd1%, and SC30%-Pd5% for 0.5wt%, 1wt% and 5wt% of Pd nanoparticle in the composites respectively. For the sake of comparison, the sepiolite/g-C_3N_4 (SC30%) composite was fabricated by following the same procedure without the addition of palladium in the synthesis.

8.2.4 Characterizations

The characterizations of the solid samples were carried out by X-ray diffraction (XRD), UV–vis diffuse reflectance spectroscopy (DRS), specific surface area (BET method), scanning electron microscopy (SEM), X-ray photoelectron spectroscopy (XPS), Reversed double-beam photoacoustic spectroscopy (RDB-PAS) and photoluminescence spectroscopy (PL). Detailes are described in **chapter 2**.

8.2.5 Photocatalytic test

The photocatalytic performances for degradation of rhodamine B (RhB) on the original and developed composites were evaluated under the visible light ($\lambda > 400$ nm) irradiation. In details, typically 50 mg of the synthesized composite was magnetically stirred in 50 mL of 10 ppm RhB in the dark condition for 30 min to reach the adsorption-desorption equilibrium. The suspensions were then irradiated using a 500 W Xe lamp with a cut-off filter. During the light illumination, solutions were collected and filtrated by 0.45 μm membrane filters to remove the suspended particles. The concentrations of the remaining RhB were determined by UV-Vis spectrometry at 554 nm. Separately photolysis of RhB was also examined without adding any sorbents as the background in the same manner as above.

Moreover, the role of reactive species, superoxide radical ($^{\cdot}O_2^-$), hydroxyl radical ($^{\cdot}OH$) and hole (h^+), in photocatalytic degradation of RhB under visible light irradiation were examined through the radical scavenger tests. The isopropyl alcohol (IPA), p-benzoquinone (BQ) and ethylenediaminetetraacetic acid disodium salt (EDTA-2Na) were added to the RhB solution in order to remove the superoxide radical ($^{\cdot}O_2^-$), hydroxyl radical ($^{\cdot}OH$) and hole (h^+), respectively.

8.3 Results and Discussion

8.3.1 Characterizations

Fig. 8.1a shows the PXRD patterns of the original sepiolite, CN and fabricated composites of sepiolite/g-C_3N_4 with/ without Pd nanoparticles. The observed XRD pattern for the original sepiolite sample is in good agreement with sepiolite (JCPDS No. 13-0595) without other phases. The powder X-ray diffraction pattern of the CN

sample shows two characteristic peaks at 2θ 13.2 (002) and 27.3° (100), which correspond to g-C_3N_4 (JCPDS No.87-1526). In the cases of synthesized sepiolite/C_3N_4/Pd nanoparticles composites, the PXRD patterns clearly showed collective patterns of sepiolite and g-C_3N_4. According to the previous reports, the distinct peak for the Pd nanoparticles observed around at d = 0.224 nm indexed to the (111) plane of Pd [30]. The PXRD patterns of the present composite did not show any distinguished peaks for dispersed Pd nanoparticle. The reason could be explained as due to the less content of metallic Pd nanoparticle in the composites, and also possibility might be the concern peak of metallic Pd nanoparticle might be overlapped with d = 0.226 nm in sepiolite.

The FTIR spectra for the original sepiolite, CN, SC30% and SC30%-PdX% composites are presented in **Fig. 8.1b**. The FTIR spectrum for sepiolite has been already explained in our previous report [14]. The FTIR spectrum for CN is highlighted with characteristic aromatic C–N heterocycle stretching vibration mode in the region of 1200–1600 cm^{-1} and triazine units at 808 cm^{-1}, confirming the successful fabrication of original graphitic C–N network. Additionally, a strong absorbance at 3200 cm^{-1} was observed, due to the residual N–H functional groups in the carbon nitride [31]. The FTIR spectra for the composites showed characteristics frequencies for sepiolite as well as CN. No differences among FTIR spectra for three different Pd content-dispersed composites were observed.

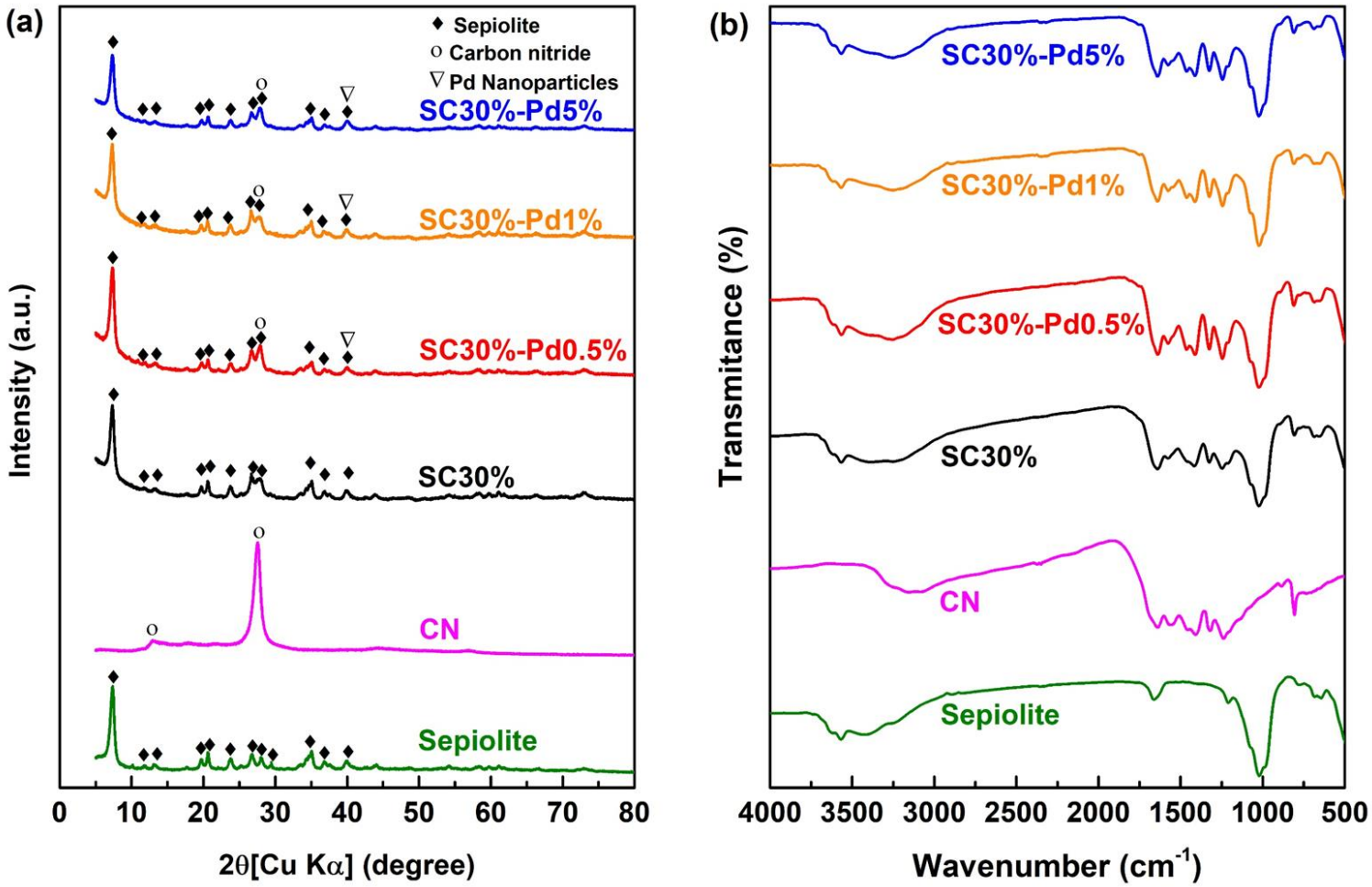

Fig. 8.1 (a) PXRD and (b) FTIR spectra for sepiolite, CN, and SC30% and SC30%-PdX% nanoparticle composites.

The light absorption ability and energy band gap (*E*g) of the photocatalyst was examined by UV-Vis diffuse reflectance spectroscopy, as shown in **Fig. 8.2a** The CN shows the highest photoabsorption in the UV and visible light regions, while the notable light absorption of sepiolite is around UV region. It is clear that the SC30%-Pd composite displays higher light absorption ability in the visible region than CN and SC30%. **Fig. 8.2b** exhibits the estimated Eg by the linear part of the $(\alpha h\nu)^2$ versus the energy of absorbed light. The Eg values of sepiolite, CN, SC30%, SC30%-Pd0.5%, SC30%-Pd1% and SC30%-Pd5% were 3.70 eV, 2.73 eV, 2.97 eV, 2.76 eV, 2.70 eV and 2.64 eV, respectively. It is clear that the adding of Pd nanoparticle in the composites affected the optical properties such as light absorption ability and Eg. The enhancing of light absorption ability and decreasing of *E*g of SC30%-Pd composite suggest that the Pd composite can generate the number of photogenerated charge carrier (electron and hole) under visible light irradiation, resulting in higher photocatalytic efficiency.

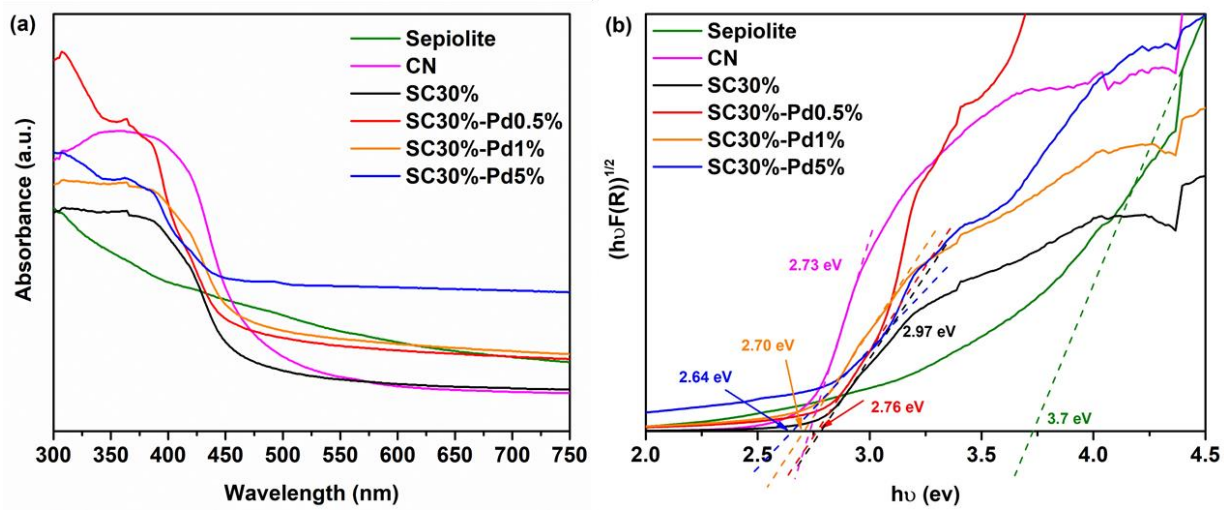

Fig. 8.2 (a) Diffuse reflectance UV-visible spectra and (b) Plots between $(h\nu F(R))^{1/2}$ vs. hν (eV) for as-prepared samples.

8.3.2 Photocatalytic degradation of RhB

The photocatalytic activity of the developed photocatalysts was investigated by the degradation of RhB under visible light irradiation, as shown in **Fig. 8.3a**. It was observed that the sepiolite composites show a higher adsorption capacity of RhB than CN since the surface charges of sepiolite and CN should be negative and RhB is charged positively in the solution. After visible light irradiation for 90 min, RhB remaining ratio of RhB (C/C_0) were achieved 0.21, 0.45, 0.13, 0.05, 0.04 and 0.07 over sepiolite, CN, SC30%, SC30%-Pd0.5%, SC30%-Pd1% and SC30%-Pd5%, respectively. These results indicate that the combinations of sepiolite, CN, and Pd nanoparticle improved the photocatalytic performance in RhB degradation. Further, the greatest photocatalytic activity was observed with Pd content (1%), due to the good dispersion and proper amount of Pd on the surface of CN. The lower photocatalytic efficiency of SC30%-Pd5% than SC30%-Pd1% might have come from the overloaded Pd nanoparticle on the surface of CN, which may act as the recombination centers, leading to suppression ability of electron-hole recombination. The kinetic results of all samples are in good agreement with the pseudo-first-order model, which have the linear regression coefficients (R^2) all over 0.95 (**Fig. 8.3b**). The rate constants for sepiolite, CN, SC30%, SC30%-Pd0.5%, SC30%-Pd1% and SC30%-Pd5% were calculated to be 0.010 min^{-1}, 0.009 min^{-1}, 0.016 min^{-1}, 0.027 min^{-1}, 0.032 min^{-1} and 0.027 min^{-1}, respectively. The highest rate constant was obtained from SC30%-Pd1%, which was about three times as high as that of pristine sepiolite and CN.

To better understand the removal mechanism, three different experiments (photolysis, adsorption, and photocatalysis) for RhB removal with/without SC30%-Pd1% were carried out and shown in **Fig. 8.3(c)**. The concentration of RhB was not

significantly changed during visible light irradiation without the catalyst (photolysis), indicating that RhB is stable and not degraded under only visible light irradiation. The adsorption test in the dark condition was also performed to check the adsorption and oxidation of RhB without light. The adsorption capacity of RhB on SC30%-Pd1% was observed with C/C_0 = 0.3, and it was not changed after 30 min, indicating that the suspension reaches the adsorption-desorption equilibrium within 30 min. However, the presence of the photocatalyst and light (photocatalysis) in the reaction displays dramatically decrease in RhB concentration after stirring in the dark condition for 30 min. These results indicate that the primary process for RhB degradation over SC30%-Pd1% is through the photocatalytic reaction.

Fig. 8.3d shows the photocatalytic degradation of RhB over SC30%-Pd1% with or without quenchers. In case of adding of IPA, the degradation efficiency of RhB decreased by approximately 14%, indicating that the $^{\bullet}OH$ was not the predominant reactive free radical for the whole reaction. On the other hands, the dramatic decrease in photocatalytic degradation of RhB was observed in the presence of BQ (25.3%) and EDTA-2Na (28.6%), suggesting that both of $^{\bullet}O_2^-$ and h^+ were the more reactive species to play the vital role in RhB degradation in the system

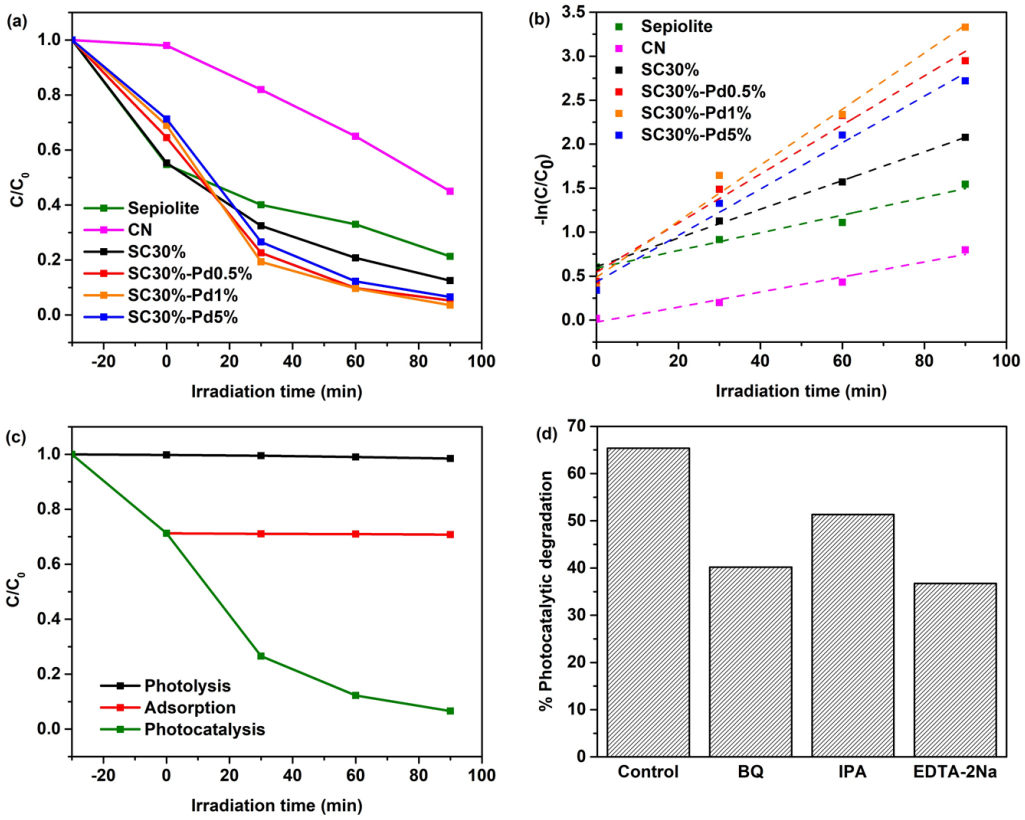

Fig. 8.3 (a) Time courses and (b) pseudo-first-order kinetics plots of photocatalytic degradation of RhB over as-prepared samples. (c) Time courses of visible light photocatalytic degradation of 10 mg/L RhB (catalyst dose= 1 g•L^{-1}) and without catalyst (represent the photolysis) and reaction in the dark over SC30%-Pd1% (represent the adsorption), (d) The degradation efficiency of RhB over the SC30%-Pd1% in the presence of various radical scavengers ; 120 min, catalyst loading = 1 g•L^{-1}.

The nitrogen adsorption-desorption isotherms and detailed textural properties results (BET surface area, total pore volume, and average pore diameter) for pure sepiolite, CN, and SC30%-Pd1% are shown in **Fig. 8.4** and summarized in **Table 8.1**. The adsorption isotherm plot of N_2 for all three samples exhibited a typical type-IV with an H_3-type hysteresis loop indicating that a slit type mesoporous arrangement occurs in the original sepiolite [32], CN and composite SC30%-Pd1%. As presented in the adsorption of N_2 volume on sepiolite and composite SC30%-Pd1% at the maximum relative pressure (P/P_0 = 0.9901) is observed around 450 cm^3g^{-1} which noticed 5.32 fold higher than the pure CN. After CN is fabricated with sepiolite, the average pore size significantly decreased from 37.40 nm to 16.84 nm. As seen in Table 1, the BET surface area and total pore volume for sepiolite, C, and SC30%-Pd1% were 230.15, 165.33, 13.12 m^2g^{-1} and 0.686, 0.696, 0.123 cm^3/g, respectively.

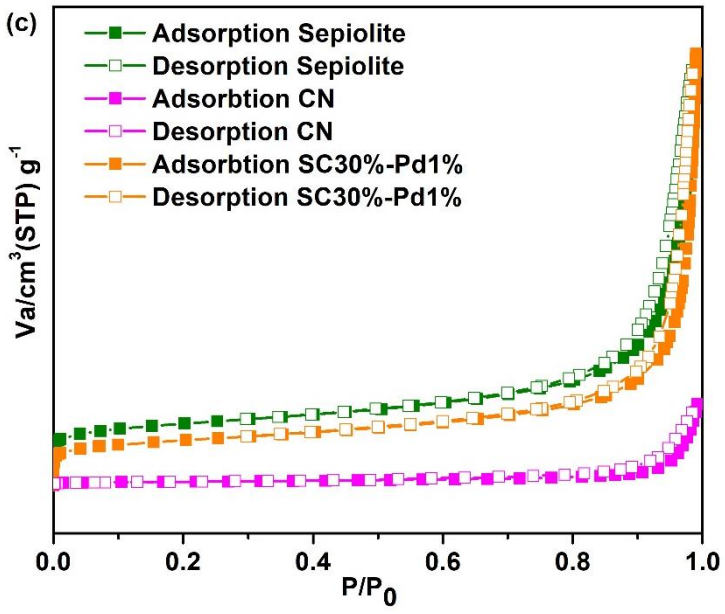

Fig. 8.4 Nitrogen adsorption-desorption isotherms for pure sepiolite, carbon nitride, and composite SC30%-Pd1%.

Therefore, SC30%-Pd1% should be focused on further characterization. TEM-EDX images for SC30%-Pd1% were observed in **Fig. 8.5**. Nanoparticles are dispersed on the fibrous network of nanorods of sepiolite with 1 μm in length and 50-60 nm in width, whereas the CN in the composite showed irregular shapes of platelet-like morphology with some thin layers. Interestingly we observed that the nanorods of sepiolite are partially covered with irregular shapes of thin layers of CN and that black dots of Pd(0) nanoparticles around 10 nm sizes mainly located on the surface of CN. The corresponding elemental mapping confirmed the location of Pd nanoparticle in the composite, as shown in **Fig. 8.5c**. The distribution of Pd is mainly overlapped with C and N from CN not but with Mg, Si and Al from sepiolite, suggesting that the presence of Pd nanoparticles on the surface of CN.

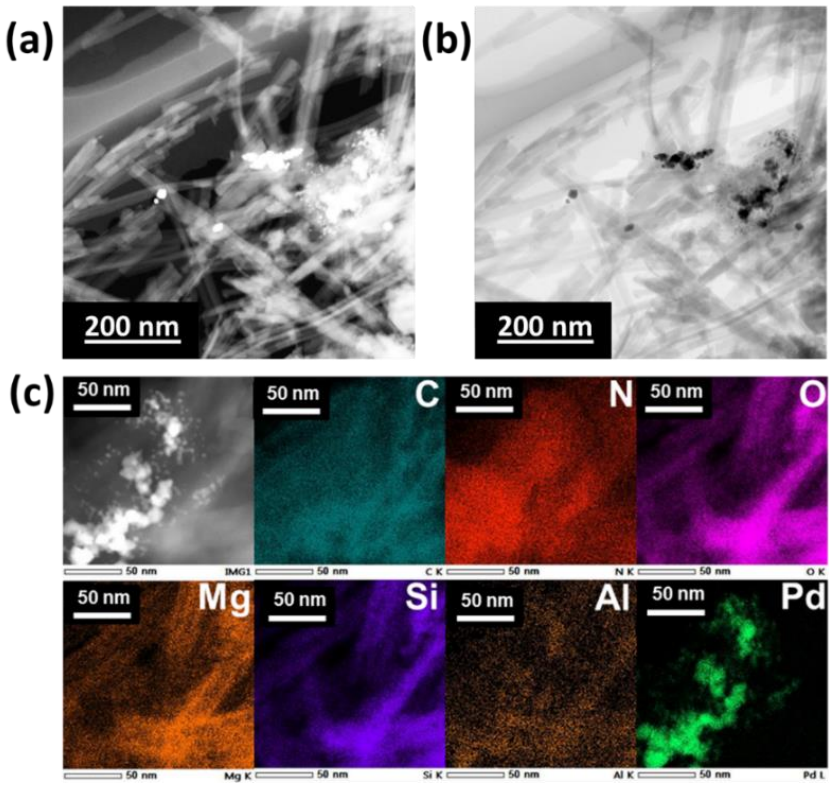

Fig. 8.5 TEM images of SC30%-Pd1%. (a) Bright-field and (b) dark-field; scale bars indicate 200 nm. (c) TEM-EDX elemental mapping of C, N, O, Mg, Si, Al, and Pd in SC30%-Pd1%.

The XPS spectrum of Pd 3d shows the peak at E_B[Pd $3d_{5/2}$] = 334.80 eV, which is ascribed to Pd(0) [33] in **Fig. 8.6b,** indicating the successful reduction of Pd^{2+} to Pd^0 by $NaBH_4$. The survey spectrum (**Fig. 8.6a**) also shows that there are several distinctive peaks of Mg 2p, Al 2p, Si 2p from sepiolite and C 1, N 1s from CN in addition to Pd 3d. The valence bands (VB) of sepiolite and CN were estimated to around 2.81 eV and 1.78 eV, respectively (**Fig. 8.6c**). The conduction band (CB) of sepiolite and CN can be calculated to -0.89 eV and -0.95 eV, respectively, based on DRS-UV and VB results.

The photoluminescence spectra (PL) of CN, SC30% and SC30%-Pd1% have shown that the pure CN show the highest PL intensity, which indicates the highest the recombination of electron-hole pair (**Fig. 8.6d**). By fabrication with sepiolite, the PL intensity decreased in SC30%, and by further combination with Pd(0), the PL intensity additionally decreased in SC30%-Pd1%, implying that SC30%-Pd1% avoids the recombination most effectively. The improving of separation efficiency of photogenerated charge carrier could be caused by the interfacial charge transfer between sepiolite and CN and the electron transfer from CN to Pd nanoparticles through Schottky barrier.

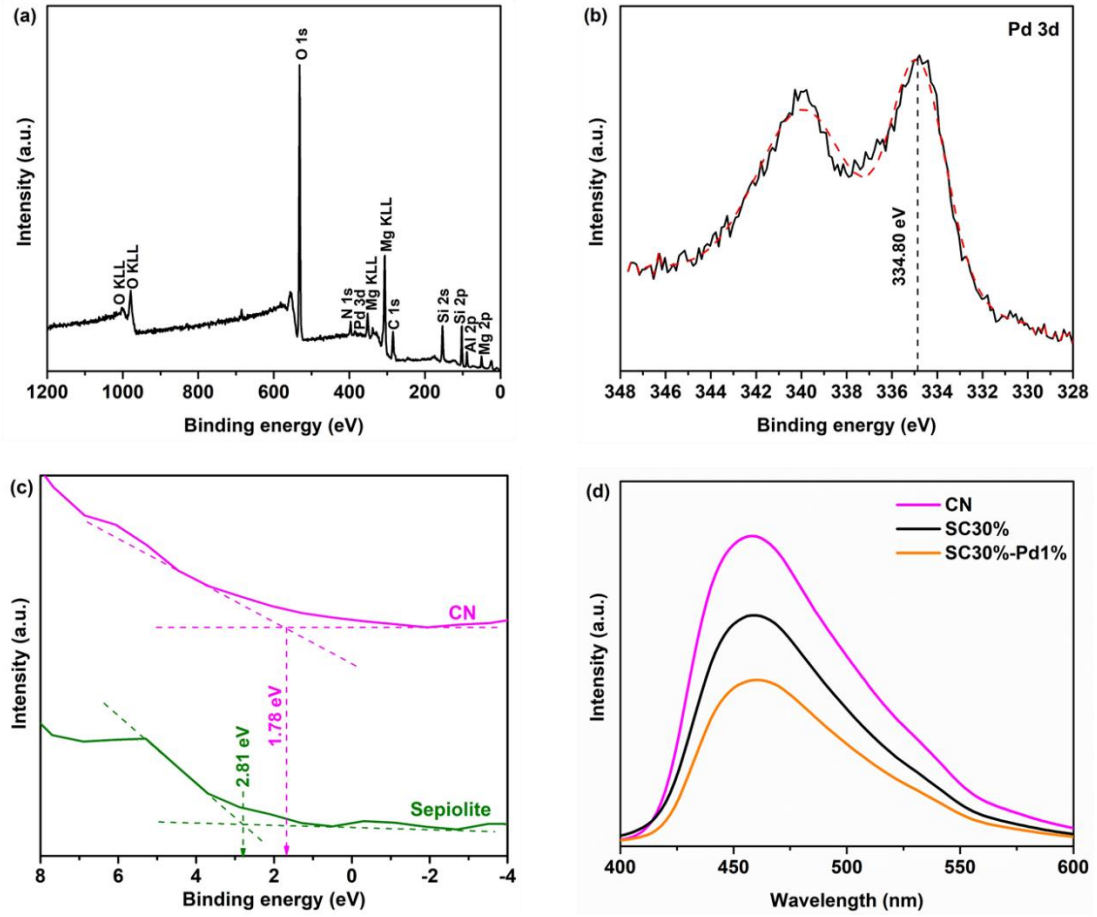

Fig. 8.6 XPS results of (a) survey spectrum, (b) Pd3d of SC30%-Pd1% and (c) valence band energy region and (d) PL curves of CN, SC30% and SC30%-Pd1%.

To understand the electron transfer behavior in original and composite materials, electron accumulation in trapping levels was observed by advanced reversed double-beam photoacoustic spectroscopy. **Fig. 8.7** provides the ERDT/CBB patterns for all materials which are plotted as a function of energy (eV) from the valence band top (VBT) against electron-trap density. The pure sepiolite and CN samples show the ERDT/CBB patterns located in the energy range of 2.2-3.0 eV and 2.3-2.9 eV, respectively, but the signal intensity in sepiolite is much lower than CN due to larger energy band gap in sepiolite (~3.7 eV in **Fig. 8.2b**). In comparison, the SC30% has a relative total density (5.2) of ETs close to CN (5.3), indicating that the heterojunction between the sepiolite and CN can avoid the recombination of electron and hole of CN through the interfacial charge transfer process. ERDT pattern for SC30% shows three predominant peaks at 2.50 eV, 2.75 eV and 2.95 eV. The most intensive peak at 2.75 eV would be caused by CN. By focusing on the SC30%-Pd composite series, the relative total density of ETs decreased from 3.1 to 1.4, with an increase in the content of Pd nanoparticle in the composite. This phenomenon is attributed to the migration of electron from the CB of CN to the Pd nanoparticle through the Schottky barrier, metal-semiconductor junction [17]. The electron from the CB of CN prefers to transfer to Pd nanoparticle than sepiolite due to the high electrical conductivity of Pd nanoparticle which is confirmed by a decrease in electron accumulation in the energy range of characteristic of sepiolite at 2.50 eV and 2.95 eV. This result of charge separation in this work is different from the previous reports about C_3N_4/clay composites which are explained about the transfer of hole from the VB of C_3N_4 to the negative surface of the clay [9, 11].

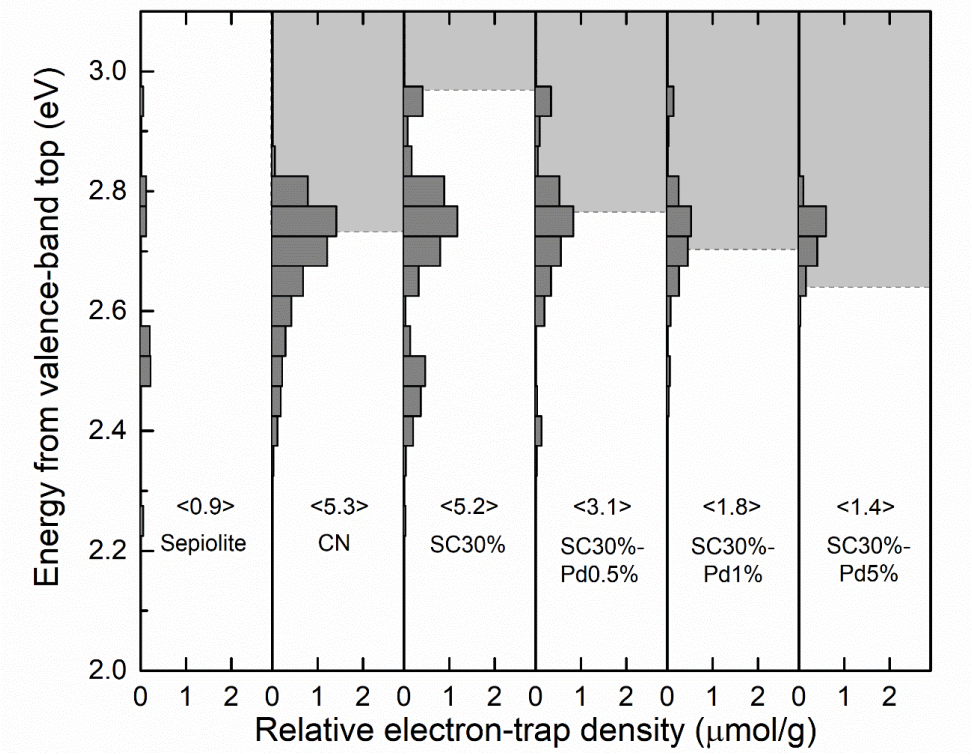

Fig. 8.7. Representative ERDT/CBB patterns of SC30%-Pd1%. Figures in < > denote the relative total density of ETs in units of μmol.

8.3.3 Photocatalytic mechanism of RhB degradation over SC30%-Pd

According to the TEM-EDX observation, the Pd nanoparticles were formed through heterojunction on the surface of C, which exists on the surface of sepiolite. In general, electrons on the higher CB level can be transferred to lower CB through the heterojunction or the interfacial charge transfer process. Under light irradiation, the photogenerated charge carriers (electron and hole) were generated and separated at different electronic states; the photogenerated electron will move to CB leaving the photogenerated hole in the VB. From the DRS and VB-XPS results, the CB potential of CN (-0.95 eV vs. NHE) is more negative than the CB potential of sepiolite (-0.89 eV vs. NHE), leading to the migration of electron from the CB of the CN to the CB of the sepiolite. After fabricating the composite with Pd nanoparticles, most of the

electrons in the CB of CN move to the Pd nanoparticle through Schottky barrier. The existence of Pd nanoparticles on the surface of CN can not only avoid the photogenerated charge separation but also improve the energy of trapped electrons by the strong local electron field of surface plasmon resonance effect (SPR). The high energy of trapped electrons on the surface of Pd nanoparticles is quickly transferred and react with electron acceptors such as dissolved O_2 gas in water. In the photocatalytic degradation of RhB, the adsorbed RhB on the surface of the sepiolite can produce the electrons under the visible light due to the dye-sensitized photocatalytic process. The electrons in the LUMO of RhB (E_{LUMO} = −1.10 eV VS. NHE) were moved to the CB of sepiolite (E_{CB} = −0.89 eV) due to the more positive state of the CB of sepiolite. In this way, electron on the surface of Pd and in the CB of sepiolite and CN could reduce the dissolved O_2 to $^{\bullet}O_2^-$ due to more negative level than the standard redox potential of O_2 to $^{\bullet}O_2^-$ ($E^0(O_2/^{\bullet}O_2^-)$ = −0.046 eV VS. NHE. At the same time, the generated $^{\bullet}O_2^-$ also can react with H^+ or H_2O to produce $^{\bullet}OH$. Thus, the generated reactive species ($^{\bullet}O_2^-$ and $^{\bullet}OH$) and h^+ in the VB of CN jointly decomposed RhB into degradation products through oxidation and reduction. Based on the above results, a charge transfers of each compound in SC30%-Pd composites through the heterojunction can be proposed as illustrated in **Fig. 8. 8.** All the photocatalytic reaction process was described the following reaction of (8.1) - (8.12).

$$\text{RhB@sepiolite} + h\nu \rightarrow \text{RhB*}\ (h^+ + e^-)\text{@sepiolite} \quad (8.1)$$

$$\text{RhB@sepiolite} + h\nu \rightarrow \text{RhB*}\ (h^+)\text{@sepiolite}\ (e^-) \quad (8.2)$$

$$\text{CN} + h\nu \rightarrow \text{CN}\ (h^+ + e^-) \quad (8.3)$$

$$\text{sepiolite/CN}\ (h^+ + e^-)\text{/Pd} \rightarrow \text{sepiolite}\ (e^-)\text{/CN}\ (h^+)\text{/Pd}\ (e^-) \quad (8.4)$$

$$Pd\ (e_{Pd}^{-}) + h\nu \rightarrow Pd\ (e_{SPR}^{-}) \quad (8.5)$$

$$\text{sepiolite}\ (e^{-}) + O_2 \rightarrow {}^{\bullet}O_2^{-} \quad (8.6)$$

$$Pd\ (^{*}e^{-}) + O_2 \rightarrow {}^{\bullet}O_2^{-} \quad (8.7)$$

$$H_2O \rightarrow H^{+} + OH^{-} \quad (8.8)$$

$${}^{\bullet}O_2^{-} + H^{+} \rightarrow {}^{\bullet}OOH \quad (8.9)$$

$${}^{\bullet}OOH + H^{+} + e^{-} \rightarrow H_2O_2 \quad (8.10)$$

$$H_2O_2 + e^{-} \rightarrow {}^{\bullet}OH + OH^{-} \quad (8.11)$$

$${}^{\bullet}OH + {}^{\bullet}O_2^{-} + CN\ (h^{+}) + RhB \rightarrow \text{degradation products} \quad (8.12)$$

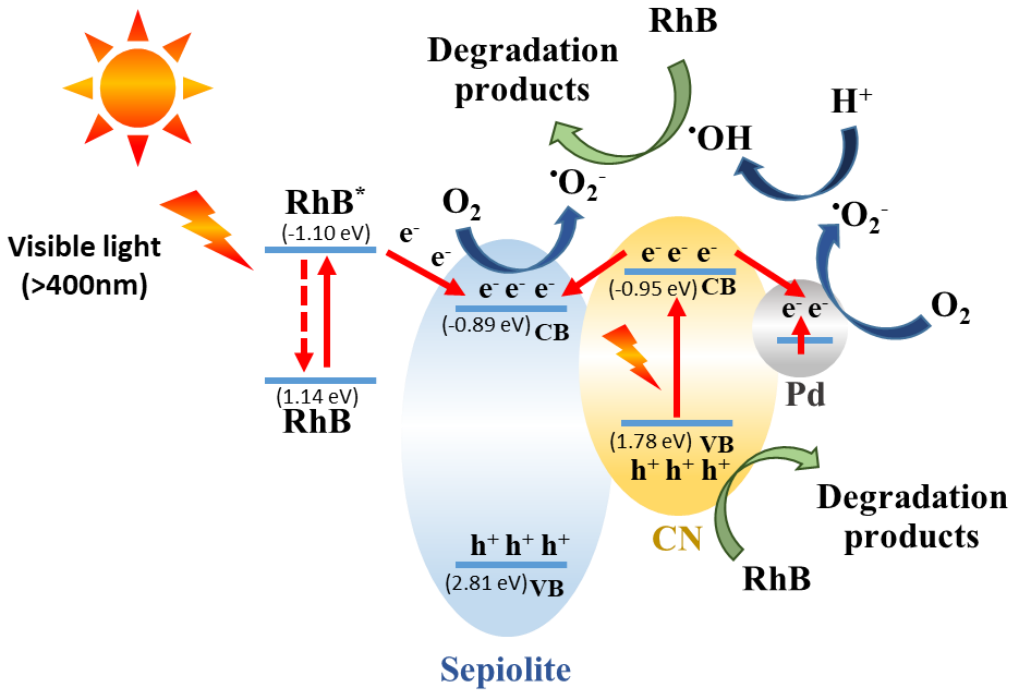

Fig. 8.8 Proposed mechanism of photocatalytic degradation RhB over SC30%-PD1% under the visible light irradiation.

8. 4 Conclusions

A series of plasmonic Pd dispersed C_3N_4/sepiolite composites (SP30%-Pd) have been successfully developed through reduction. In this work, the new role of sepiolite in the composite is proposed that "sepiolite" can be utilized not only for avoiding the electron-hole recombination but also responsible for the degradation of organic dye (RhB) by a dye-sensitized mechanism on the surface of sepiolite. Moreover, it is the first time to report the electron transfer between sepiolite and CN confirmed by ERDT patterns, which show different mechanism from previous reported CN and clay composites. The as-prepared SC30% composite exhibit higher photocatalytic activity for RhB degradation than the pristine materials (sepiolite and CN). The degradation efficiency of SC30% has shown a dramatic increase when combined with 1% Pd nanoparticle. The results emphasize that the significant improvement in the photocatalytic performance of SC30%-Pd composite might come from the enhancing of visible light adsorption ability form the surface plasmon resonance effect and highly electron-hole pair separation via heterojunction between sepiolite and CN, and the Schottky barriers between CN and Pd nanoparticle. Thus, the investigated results provide a new concept to understand the photocatalytic mechanism of sepiolite-based photocatalyst for organic dye degradation.

References

[1] W.-J. Ong, L.-L. Tan, Y.H. Ng, S.-T. Yong, S.-P. Chai, Graphitic Carbon Nitride (g-C_3N_4)-Based Photocatalysts for Artificial Photosynthesis and Environmental Remediation: Are We a Step Closer To Achieving Sustainability?, Chemical Reviews, 116 (2016) 7159-7329.

[2] L. Zhou, H. Zhang, H. Sun, S. Liu, M.O. Tade, S. Wang, W. Jin, Recent advances in non-metal modification of graphitic carbon nitride for photocatalysis: a historic review, Catalysis Science & Technology, 6 (2016) 7002-7023.

[3] Z. Yang, Y. Zhang, Z. Schnepp, Soft and hard templating of graphitic carbon nitride, Journal of Materials Chemistry A, 3 (2015) 14081-14092.

[4] A. Wang, C. Wang, L. Fu, W. Wong-Ng, Y. Lan, Recent Advances of Graphitic Carbon Nitride-Based Structures and Applications in Catalyst, Sensing, Imaging, and LEDs, Nano-Micro Letters, 9 (2017) 47, 2-21.

[5] L. Jiang, X. Yuan, Y. Pan, J. Liang, G. Zeng, Z. Wu, H. Wang, Doping of graphitic carbon nitride for photocatalysis: A reveiw, Applied Catalysis B: Environmental, 217 (2017) 388-406.

[6] Z. Zhao, Y. Sun, F. Dong, Graphitic carbon nitride based nanocomposites: a review, Nanoscale, 7 (2015) 15-37.

[7] B. Li, H. Huang, Y. Guo, Y. Zhang, Diatomite-immobilized BiOI hybrid photocatalyst: Facile deposition synthesis and enhanced photocatalytic activity, Appl Surf Sci, 353 (2015) 1179-1185.

[8] A. Kumar, S. Samanta, R. Srivastava, Systematic Investigation for the Photocatalytic Applications of Carbon Nitride/Porous Zeolite Heterojunction, ACS Omega, 3 (2018) 17261-17275.

[9] Z. Sun, G. Yao, X. Zhang, S. Zheng, R.L. Frost, Enhanced visible-light photocatalytic activity of kaolinite/g-C_3N_4 composite synthesized via mechanochemical treatment, Applied Clay Science, 129 (2016) 7-14.

[10] Z. Zhu, Y. Yu, H. Dong, Z. Liu, C. Li, P. Huo, Y. Yan, Intercalation Effect of Attapulgite in g-C_3N_4 Modified with Fe_3O_4 Quantum Dots To Enhance Photocatalytic Activity for Removing 2-Mercaptobenzothiazole under Visible Light, ACS Sustainable Chemistry & Engineering, 5 (2017) 10614-10623.

[11] C. Li, Z. Sun, W. Huang, S. Zheng, Facile synthesis of g-C_3N_4/montmorillonite composite with enhanced visible light photodegradation of rhodamine B and tetracycline, Journal of the Taiwan Institute of Chemical Engineers, 66 (2016) 363-371.

[12] Y. Li, J. Zhan, L. Huang, H. Xu, H. Li, R. Zhang, S. Wu, Synthesis and photocatalytic activity of a bentonite/g-C_3N_4 composite, Rsc Adv, 4 (2014) 11831-11839.

[13] Z. Sun, X. Zhang, R. Zhu, X. Dong, J. Xu, B. Wang, Facile Synthesis of Visible Light-Induced g-C_3N_4/Rectorite Composite for Efficient Photodegradation of Ciprofloxacin, Materials (Basel, Switzerland), 11 (2018) 2452.

[14] C. Chuaicham, R. Pawar, K. Sasaki, Dye-sensitized Photocatalyst of Sepiolite for Organic Dye Degradation, Catalysts, 9 (2019) 235, 1-16.

[15] M. Vadai, D.K. Angell, F. Hayee, K. Sytwu, J.A. Dionne, In-situ observation of plasmon-controlled photocatalytic dehydrogenation of individual palladium nanoparticles, Nature Communications, 9 (2018) 4658, 1-8.

[16] W. Hou, S.B. Cronin, A Review of Surface Plasmon Resonance-Enhanced Photocatalysis, Advanced Functional Materials, 23 (2013) 1612-1619.

[17] N. Lu, Y. Wang, S. Ning, W. Zhao, M. Qian, Y. Ma, J. Wang, L. Fan, J. Guan, X. Yuan, Design of plasmonic Ag-TiO_2/$H_3PW_{12}O_{40}$ composite film with enhanced sunlight photocatalytic activity towards o-chlorophenol degradation, Sci Rep, 7 (2017) 17298, 1-17.

[18] X. Dong, Z. Sun, X. Zhang, C. Li, S. Zheng, Construction of BiOCl/g-C_3N_4 /kaolinite composite and its enhanced photocatalysis performance under visible-light irradiation, Journal of the Taiwan Institute of Chemical Engineers, 84 (2018) 203-211.

[19] F. Ji, J. Li, X. Cui, J. Liu, X. Bing, P. Song, Hierarchical C-doped $BiPO_4$/ZnCoAl-LDO hybrid with enhanced photocatalytic activity for organic pollutants degradation, Applied Clay Science, 162 (2018) 182-191.

[20] Z. Sun, C. Li, X. Du, S. Zheng, G. Wang, Facile synthesis of two clay minerals supported graphitic carbon nitride composites as highly efficient visible-light-driven photocatalysts, J Colloid Interface Sci, 511 (2018) 268-276.

[21] P. Li, L. Huang, Y. Li, Y. Xu, S. Huang, D. Yuan, H. Xu, H. Li, Synthesis of dark orange montmorillonite/g-C_3N_4 composites and their applications in the environment, Journal of Physics and Chemistry of Solids, 107 (2017) 131-139.

[22] Z. Sun, F. Yuan, X. Li, C. Li, J. Xu, B. Wang, Fabrication of Novel Cyanuric Acid Modified g-C_3N_4/Kaolinite Composite with Enhanced Visible Light-Driven Photocatalytic Activity, Minerals, 8 (2018) 437, 1-15.

[23] R. Djellabi, M.F. Ghorab, C.L. Bianchi, G. Cerrato, S. Morandi, Recovery of hexavalent chromium from water using photoactive TiO_2-montmorillonite under sunlight, Mediterranean Journal of Chemistry, 5 (2016) 442-449.

[24] L. Guishui, C. Lijun, Z. Bing, L. Yi, Novel Bi_2O_3 loaded sepiolite photocatalyst: Preparation and characterization, Materials Letters, 168 (2016) 143-145.

[25] F. Zhou, C.J. Yan, T. Liang, Q. Sun, H.Q. Wang, Photocatalytic degradation of Orange G using sepiolite-TiO_2 nanocomposites: Optimization of physicochemical parameters and kinetics studies, Chemical Engineering Science, 183 (2018) 231-239.

[26] P.S. Wang, C.X. Qi, L.Y. Hao, P.C. Wen, X. Xu, Sepiolite/Cu_2O/Cu photocatalyst: Preparation and high performance for degradation of organic dye, Journal of Materials Science & Technology, 35 (2019) 285-291.

[27] F. Zhou, C.J. Yan, Q. Sun, S. Komarneni, TiO_2/Sepiolite nanocomposites doped with rare earth ions: Preparation, characterization and visible light photocatalytic activity, Microporous and Mesoporous Materials, 274 (2019) 25-32.

[28] L. Jin, H.Y. Zeng, S. Xu, C.R. Chen, H.Z. Duan, J.Z. Du, G. Hu, Y.X. Sun, Facile preparation of sepiolite@LDH composites for the visible-light degradation of organic dyes, Chinese Journal of Catalysis, 39 (2018) 1832-1841.

[29] D. Papoulis, D. Panagiotaras, P. Tsigrou, K.C. Christoforidis, C. Petit, A. Apostolopoulou, E. Stathatos, S. Komarneni, I. Koukouvelas, Halloysite and sepiolite –TiO_2 nanocomposites: Synthesis characterization and photocatalytic activity in three aquatic wastes, Materials Science in Semiconductor Processing, 85 (2018) 1-8.

[30] R. Zhang, Z. Huang, C. Li, Y. Zuo, Y. Zhou, Monolithic g-C_3N_4/reduced graphene oxide aerogel with in situ embedding of Pd nanoparticles for hydrogenation of CO_2 to CH_4, Appl Surf Sci, 475 (2019) 953-960.

[31] J. Fang, H. Fan, M. Li, C. Long, Nitrogen self-doped graphitic carbon nitride as efficient visible light photocatalyst for hydrogen evolution, Journal of Materials Chemistry A, 3 (2015) 13819-13826.

[32] R.R. Pawar, B.D. Kevadiya, H. Brahmbhatt, H.C. Bajaj, Template free synthesis of mesoporous hectorites: Efficient host for pH responsive drug delivery, International Journal of Pharmaceutics, 446 (2013) 145-152.

[33] M. Peng, Y. Liu, H. Jiang, R. Chen, W. Xing, Enhanced catalytic properties of Pd nanoparticles by their deposition on ZnO-coated ceramic membranes, RSC Adv., 6 (2016) 2087-2095.

Chapter 9

Conclusions

Photocatalysis is a remarkable methodology which is popular and applied in the degradation of several organic pollutants and reduction of hazardous metal ions in wastewater due to eco-friendly, easy to operation and energy shortages problem. According to that fact, this thesis represents the development of various two-dimensional geomimetic photocatalytic composites for the removal of phenol, organic dyes and hexavalent chromium (Cr(VI)) under the UV and visible light irradiation. The composites exhibit higher photocatalytic activity than the pristine materials, suggesting that the introduction of two dimensional geomimetic resulted in the well distribution of the photocatalyst and the formation of the heterojunction between the two dimensional geomimetic and the main photocatalyst. In addition, the two dimensional geomimetic material are assumed to play an important role in the separation of electron-hole pair, leading to prolong the lifetime of excited electron and the enhanced photocatalytic activity. It is clear that the roles of two dimensional geomimetic in the composite are not only supporting material but also it can avoid the recombination of electron-hole pair of the photocatalyst.

The treatment of Cr(VI) containing wastewater is gradually becoming the most concerning issues due to their great threat to human health. Two-dimensional/two-dimensional (2D/2D) photocatalytic composite have been received considerable attention for photocatalytic application because it has high electron-hole mobility across the heterojunction interface, which can impede the electron-hole recombination rate. In **chapter 3,** The 2D/2D ZnTi layer double hydroxide/montmorillonite composites (ZTL/MT) were prepared a simply precipitation method and utilized the composites as a photocatalyst for the photocatalytic reduction of Cr(VI) under UV light irradiation. The ZTL/MT20% composite displayed the highest reduction

efficiency and reaction rate constant for Cr(VI), which could be attributed to the efficient light adsorption ability and low recombination rate of electron and hole in ZTL. Moreover, the photocatalytic reduction mechanism of Cr(VI) and electronic state of MT and ZTL were confirmed by DFT calculation. The Fe impurity in the layer structure of MT generates the middle state level between the VB and CB leading to provide the multi gap state in MT. Thus, the electron in the mid-gap state can be excited by light and the excited electron can be recombined with h^+ in VB of ZTL to enhancing the charge separation of ZTL, leading to enhance the photocatalytic reduction of Cr(VI). Moreover, the Cr(III) after photocatalytic reduction could be adsorbed on the surface of MT and intercalated between the layer of MT. Cr(III), which can keep the active surface of ZTL catalyst and eliminate the toxic Cr(III) from the water.

The topotactic transformation from layer double hydroxide to mixed metal oxide (MMO) has been considered to be an effective photocatalyst for degradation of organic pollutants because of being grafted within an amorphous matrix; has high dispersion of immobilized semiconductor nanoparticles; has a large specific surface area; and there are possible synergistic effects between the components of MMO. **In Chapter 4**, The ZnTi mixed metal oxide samples (ZTM) were prepared by calcination of ZnTi layered double hydroxide from different synthetic conditions. It was found that the different calcination temperatures can control the phase component and the optical properties towards visible active photocatalyst. Moreover, the surface structure and phase composition including amorphous phase of different ZTM samples were characterized by newly technique reversed double-beam photoacoustic spectroscopy technique (RDB-PAS). The calcined products at 500 °C (ZTM2-500H, ZTM4-500H,

ZTM6-500H) provided the crystalline/amorphous phase of $ZnTiO_3$ which is confirmed by RDB-PAS technique. The high photocatalytic activity for phenol degradation of calcined products from 500 °C might be obtained from high separation of photogenerated charge carrier and light absorption ability due to the existing of $ZnTiO_3$ phase. This finding indicate that the present of $ZnTiO_3$ phase in ZTM could be enhanced the photocatalytic degradation of phenol over ZTM.

Nowadays, the utilization of visible light have been focused for photocatalysis due to the solar spectrum constitutes about 47% visible light. Graphitic carbon nitrides with two-dimensional (2D) topology was wildly used as visible light active photocatalyst because of their semiconductor properties, facile synthesis, suitable electronic structure (Eg = 2.7 eV), environmentally compatible composition and excellent physicochemical stability. In this thesis, the graphitic carbon nitride was modified to by heteroatom doping or making a composite with the two-dimensional geomimetic to enhance the photocatalytic performance for organic dye degradation. **In chapter 5,** O-doped porous graphitic carbon nitride (OCN) was successfully synthesized by polycondensation of melamine with a polyoxyethylene stearyl ether. The sample with a 1 mg of polyoxyethylene stearyl ether showed the highest photocatalytic performance for rhodamine B (RhB) degradation under visible light irradiation among all these OCN samples. The electron-hole recombination of OCN sample exhibited lower than normal graphitic carbon nitride which is in good agreement with its low PL intensity. It has been demonstrated that the enhancement of photocatalytic efficiency for RhB degradation under visible light irradiation might come from not only high specific surface area but also low photogenerated charge recombination which were attributed to the O doping and porous structure. These

findings indicate that the preparation method of OCN by polyoxyethylene stearyl ether assisted method may give a new insight for the development of advanced visible light driven photocatalysts for organic dye degradation.

The formation of the heterojunction between graphitic carbon nitrides and two-dimensional geomimetic is one of the way to enhance the separation of photogenerated charge carrier. **In chapter 6**, graphitic carbon nitrides/ZnTi mixed metal oxide (CN/ZTM) composites have been successfully prepared by a simple calcination of the mixture of graphitic carbon nitrides and ZnTi layer double hydroxide. The different ZTM in the composites (1-10%wt) were shown the higher photocatalytic activity for degradation of RhB than that of pristine CN and ZTM, and CN/ZTM-5 composite exhibited the highest photocatalytic activity. The results emphasize that the significant improvement in the photocatalytic performance of CN/ZTM composite might come from the highly electron-hole pair separation via heterojunction between CN and ZTM which is corresponding with the decreasing of PL intensity of the composite. Moreover, the role of active species during the RhB degradation over CN/ZTM composite were investigated by scavenger test. The superoxide anion radical is a main active species for rhodamine B degradation. Thus, the CN/ZTM composites can be potential catalysts for the degradation of organic pollutants in wastewater.

Understanding of photocatalytic degradation of organic dye by and sepiolite which are a kind of the two-dimensional geomimetic is an important issue for organic dye degradation, since sepiolite has been used as a support for clay-based photocatalyst. **In chapter 7**, the photocatalytic activity of natural sepiolite by the dye-sensitized process to degrade organic dyes under the visible light irradiation. The photocatalytic activity of sepiolite was shown through electrostatistic coverage on the

surface of sepiolite by the cationic organic dye compound. The role of covered cationic organic dye molecules on the surface of sepiolite was to produce the excited electrons under the visible light. Then the electrons could be transferred to CB of sepiolite, enhancing the photocatalytic degradation efficiency of organic dyes mainly through oxidation by $^{\bullet}O_2^-$ which was generated by reduction of O_2. The function of RhB-adsorbed sepiolite in the system is called as "photosensitizer". RhB was the most efficiently photo-degraded on the sepiolite compared with orange II (OII) and trypan blue (TB) and methylene blue (MB). All the kinetic data of removal of RhB, MB, TB, and OII on sepiolite were fitted to the pseudo-first-order reaction model. The greatest kinetic constant was found with RhB. The photocatalytic degradation of RhB on sepiolite under the visible light irradiation could be explained by adsorption and E_{LUMO} and E_{HOMO} in RhB. The spent sepiolite after adsorption of RhB successfully acted to photocatalytically degrade even anionic organic dye (TB) through dye-sensitization of RhB on sepiolite. Especially, we confirmed that the natural sepiolite represents a new class of visible light-responsive photocatalyst from naturally occurring minerals. It is unique as it absorbs visible light without modification. The acceptable performance with regard to photocatalytic activity and its low-cost characteristics make it a suitable candidate for application in environmental treatments.

In **Chapter 8**, a series of plasmonic Pd dispersed C_3N_4/sepiolite composites (SP30%-Pd) have been successfully developed through reduction to improve the photocatalytic performance for RhB degradation. The new role of sepiolite in the composite is proposed that "sepiolite" can be utilized not only for avoiding the electron-hole recombination but also responsible for the degradation of organic dye (RhB) by a dye-sensitized mechanism on the surface of sepiolite. Moreover, it is the

first time to report the electron transfer between sepiolite and CN, which show different mechanism from previous reported CN and clay composites. The as-prepared SC30% composite exhibit higher photocatalytic activity for RhB degradation than the pristine materials (sepiolite and CN). The degradation efficiency of SC30% has shown a dramatic increase when combined with 1% Pd nanoparticle. The results emphasize that the significant improvement in the photocatalytic performance of SC30%-Pd composite might come from the enhancing of visible light adsorption ability form the surface plasmon resonance effect and highly electron-hole pair separation via heterojunction between sepiolite and CN, and the Schottky barriers between CN and Pd nanoparticle. Thus, the investigated results provide a new concept to understand the photocatalytic mechanism of sepiolite-based photocatalyst for organic dye degradation.

In the last chapter, the conclusions of this work were summarized. It was found that the two dimensional geomimetic photocatalytic composite showed the improvement of photocatalytic activity for degradation of organic pollutants and reduction of Cr(VI). Based on this research, the role of two dimensional geomimetic are not only enhance the distribution of the photocatalyst as a supported material but also prolong the lifetime of excited electron by avoiding the recombination of electron-hole pair. Moreover, in case of organic dye degradation, the covered molecule of organic dye on the surface of two dimensional geomimetic material can generate electron, leading to decompose its self by photocatalytic dye-sensitized process. Thus, the two dimensional geomimetic photocatalytic composite could be an alternative way to treat the wastes waters, especially for organic dye due to dye-sensitized mechanism.

Acknowledgement

First of all, I would like to thank and express my deepest sincere gratitude to my supervisor, Prof. Keiko Sasaki, for her guidance, continuous support, constructive criticism, and encouragement throughout this work. During my Ph.D. study, she spent valuable time and energy on my research, presentation practice, and manuscript. I could not finish this work without her support. It is my honor to be her student. I'm grateful and consider myself fortunate for having the chance to learn from you. Working with you has been a great life experience, and it has made me a better researcher and most importantly a better person. Thank you for believing in me.

Sincere gratitude shall also be paid to my committee members, Prof. Hiroshige Matsumoto at International Institute for Carbon-Neutral Energy Research (I2CNER), Kyushu University and Assoc. Prof. Hajime Miki at Department of Earth Resources Engineering, Kyushu University, for their precious advice, comments, and encouragement in my research, but also the inspirations for other research applications.

I would like to thank the help from Assoc. Prof. Ismaila Dabo at Department of Materials Science and Engineering, Pennsylvania State University, The United States of America, for density functional theory calculation. Meanwhile, I would also like to express my thanks to Prof. Bunsho Ohtani at Institute for Catalysis, Hokkaido University, for reversed double-beam photoacoustic spectroscopy experiment. Without their help and suggestion, I do not have such important data to support my results.

I am also grateful to Assoc. Prof. Siwaporn Meejoo Smith at Department of Chemistry, Mahidol University, Thailand, who introduced me to Prof. Keiko Sasaki and always gave me kind supports and encouragement.

Besides, I have great pleasure in acknowledging Prof. Tsuyoshi Hirajima and Assoc. Prof. Naoko Okibe for advice, insightful comments, and kind supports. Of course, it is also important to appreciate the help of Ms. Makiko Samba.

My deepest appreciation goes to the members of mineral processing, recycling and environmental remediation laboratory, Dr. Koilraj Paulmanickam, Dr. Subbaiah Muthu Prabhu, Dr. Srinivasarao Kancharla, Dr. Radheshyam Pawar, Dr. Binglin Guo, Dr. Karthikeyan Sekar, Dr. Xiangchun Liu, Dr. Gde Pandhe Wisnu Suyantara, Kojo Twum Konadu, Santisak Kitjanukit, Quanzhi Tian, Mengmeng Wang, Zhang Li, Niko Dian Pahlevi, Shunsuke Imamura, Shingou Nakama, Yuta Kamura, Yoshikazu Hayashi, Shugo Nagato, Akihiro Inoue, Yuna Watanabe and others at mineral processing lab members for helping, discussions, suggestions and friendship. I will never forget the long office and laboratory hours we spent together. Believe it or not, I came to love it and will definitely miss the time spent together.

My sincere thanks to my Thai best friends for their assistance, contributions, efforts in helping me, sharing the best moment, cooking, traveling, and partying hard together.

My special thanks to the biggest source of my strength, my family. I could not have done it with your continued support and encouragements.

Last but not the least, I am grateful to the scholarship provided by the Ministry of Education, Culture, Sports, Science and Technology, Japan (MEXT) for providing

me this prestigious scholarship for supporting my degree. In addition, I also thank the Institute for Catalysis, Hokkaido University for financial support for reversed double-beam photoacoustic spectroscopy experiment.

Chitiphon Chuaicham